

BEHAVIOUR OF SHORT-SPAN CONCRETE-FILLED COMPOSITE
TUBES WITH $\pm 55^\circ$ FIBER ORIENTATION UNDER BENDING AND
SHEAR

by

Subharajit Roy

Submitted in partial fulfilment of the requirements
for the degree of Master of Applied Science

at

Dalhousie University
Halifax, Nova Scotia
December 2021

© Copyright by Subharajit Roy, 2021

I dedicate this thesis wholeheartedly to my beloved parents and elder brother.

Without their continuous encouragement, love, and support, achieving this graduate degree would not have been possible. I am truly thankful to my family for teaching me to dream big and that quitting is never an option.

TABLE OF CONTENTS

LIST OF TABLES.....	vi
LIST OF FIGURES	vii
ABSTRACT	xiv
LIST OF ABBREVIATIONS and SYMBOLS USED	xv
ACKNOWLEDGEMENTS.....	xvii
CHAPTER 1 INTRODUCTION.....	1
1.1 MOTIVATION.....	1
1.2 PROBLEM STATEMENT.....	3
1.3 OBJECTIVES.....	4
1.4 RESEARCH SCOPE.....	4
1.5 THESIS LAYOUT	5
CHAPTER 2 LITERATURE REVIEW.....	6
2.1 BACKGROUND.....	6
2.2 BEHAVIOR OF $\pm 55^\circ$ GFRP TUBES.....	7
2.3 BEHAVIOR OF CFPT.....	16
2.3.1 Behavior of Short-Span CFPT Under Lateral Load.....	16
2.3.2 Behavior of Long-Span CFPT Under Lateral Load.....	34
2.4 INFERENCE FROM THE LITERATURE and RESEARCH GAP.....	47
2.5 FIELD APPLICATION OF CFPTS.....	48
CHAPTER 3 EXPERIMENTAL STUDY.....	51
3.1 GENERAL.....	51
3.2 MATERIAL PROPERTIES	51
3.2.1 GFRP Tube.....	51
3.2.2 Concrete	53
3.2.3 Steel Reinforcement	55
3.3 TEST MATRIX.....	57
3.4 SPECIMEN FABRICATION.....	60
3.5 INSTRUMENTATION and TEST SET-UP.....	62
3.6 TEST RESULTS and DISCUSSION.....	66
3.6.1 Failure Modes.....	68
3.6.2 Load-Deflection Behavior.....	73
3.6.3 Effect of Shear Span to Depth Ratio	76
3.6.4 Effect of Internal Longitudinal Reinforcement	78
3.6.5 Effect of Pressure Rating.....	80
3.6.6 Moment Capacity.....	82
3.6.7 Load-Strain and Moment-Curvature	86

3.6.8 Neutral Axis Depth and Compositeness	89
CHAPTER 4 FINITE ELEMENT MODELING	92
4.1 MODEL DESCRIPTION	93
4.1.1 GFRP Tube.....	93
4.1.2 Concrete Core.....	95
4.1.3 Steel Reinforcement	95
4.1.4 Auxiliary Parts	96
4.2 MATERIAL MODELS	96
4.2.1 GFRP Tube.....	96
4.2.1.1 Without Stress Limiting Factors	98
4.2.1.2 With Stress Limiting Factors.....	99
4.2.2 Concrete	101
4.2.3 Steel Reinforcement	102
4.2.4 Auxiliary Materials	102
4.3 CONTACTS and BOUNDARY CONDITIONS	102
4.3.1 Contacts.....	102
4.3.2 Boundary Conditions.....	103
4.4 CONTROL PARAMETERS	105
4.4.1 Hourglass	105
4.4.2 Stability, Material, and Contact.....	107
4.5 MODEL ASSUMPTIONS and LIMITATIONS.....	108
4.6 MODEL VERIFICATION	109
4.6.1 Model without Stress Limiting Factors	109
4.6.2 Model with Stress Limiting Factors	125
CHAPTER 5 CONCLUSIONS and RECOMMENDATIONS.....	142
5.1 CONCLUSIONS.....	142
5.2 RECOMMENDATIONS FOR FUTURE STUDIES	144
BIBLIOGRAPHY	145
APPENDIX A: EXPERIMENTAL TEST DATA	150
A.1 LOAD vs. MID-SPAN STRAIN RESULTS	151
A.2 LOAD vs. STRAIN ROSETTE RESULTS	152
A.3 MOMENT vs. CURVATURE RESULTS.....	153
A.4 NEUTRAL AXIS DEPTH vs. MOMENT RESULTS.....	154
A.5 LOAD vs. SLIP BETWEEN GFRP TUBE and CONCRETE	155
A.6 LOAD vs. SLIP BETWEEN CONCRETE and STEEL REBARS	156
APPENDIX B: SAMPLE LS-DYNA MATERIAL and CFFT CODES	157
B.1 GFRP TUBE MODELING CODE	157
B.2 CONCRETE MODELING CODE	158
B.3 15 M STEEL REBAR MODELING CODE	158
B.4 10 M STEEL REBAR MODELING CODE	159

B.5	STEEL SUPPORT MODELING CODE	159
B.6	RUBBER PAD MODELING CODE	159
B.7	SAMPLE LS-DYNA CODE FOR P50-b-AD0.5 SPECIMEN	159
B.8	AUTO GENERATED CONCRETE PARAMETERS IN LS-DYNA	165

LIST OF TABLES

Table 2-1	Test Matrix (Betts et al. 2019).....	8
Table 2-2	Test Matrix (Betts et al. 2020).....	12
Table 2-3	FRP Laminate Architecture (Burgueño and Bhide 2006).....	16
Table 2-4	Carbon/Epoxy Ply Properties (Burgueño and Bhide 2006).....	18
Table 2-5	Equivalent Orthotropic Plate Properties (Burgueño and Bhide 2006).....	18
Table 2-6	Test Matrix for beam shear specimens (Fam and Cole 2007).....	22
Table 2-7	Details of Specimens and Summary of Test Results (Fam et al. 2007).....	26
Table 2-8	Properties of FRP Tubes Used in CFFT Beam Tests (Ahmad et al. 2008).....	30
Table 2-9	Test Matrix of CFFT Beams (Ahmad et al. 2008).....	31
Table 2-10	Test Matrix of Beam Specimens (Cole and Fam 2006).....	35
Table 2-11	Dimension, Details and Mechanical Properties of GFRP tubes (Mohamed and Masmoudi 2010).....	44
Table 2-12	Test Matrix and Summary of Test Results (Mohamed and Masmoudi 2010).....	44
Table 2-13	Experimental and Predicted Cracking Moments for RCFE beams (Mohamed and Masmoudi 2010).....	46
Table 3-1	Physical Properties of GFRP tubes as per the manufacturer and previous study.....	52
Table 3-2	Mechanical Properties of GFRP tubes from a previous study by Betts et al. (2019).....	52
Table 3-3	Experimental results of uniaxial tensile test of steel rebars.....	57
Table 3-4	Test matrix for CFFT.....	58
Table 3-5	Summary of CFFT Specimens' test results.....	67
Table 3-6	Summary of CFFT Specimens' reinforcement ratio.....	83
Table 4-1	Mechanical properties of GFRP lamina (Betts et al. 2019).....	98
Table 4-2	Mechanical property inputs for MAT_058 without non-physical parameters.....	99
Table 4-3	Mechanical property inputs for MAT_058 with non-physical parameters.....	100
Table 4-4	Non-physical parameters for MAT_058.....	101
Table 4-5	Verification of FE Models without SILM factors Using Test Data.....	110
Table 4-6	Verification of FE Models with SILM factors Using Test Data.....	126

LIST OF FIGURES

Figure 1-1	Environmental impact on marine structures: (a) Worn out timber piles (QuakeWrap Inc.); (b) Typical corrosion of precast prestressed concrete piles (Moser et al., GODT 2011).....	1
Figure 1-2	Recent marine infrastructure rehabilitation projects in Canada: (a) Halifax waterfront, NS (Develop Nova Scotia); (b) Port of Oshawa, ON (Piling Canada); (c) Cape Croker Park, ON (Piling Canada).....	2
Figure 2-1	Compression specimen and test set-up (Betts et al. 2019).....	8
Figure 2-2	Tension specimen and test set-up (Betts et al. 2019).....	8
Figure 2-3	Stress-strain behavior of compression tests (Betts et al. 2019).....	9
Figure 2-4	Stress-strain behavior of tension tests (Betts et al. 2019).....	10
Figure 2-5	Stress-strain analysis for compression specimens (Betts et al. 2019).....	11
Figure 2-6	Test set-up (Betts et al. 2020).....	13
Figure 2-7	Typical failure modes: (a) Bottom face progressive tensile failure; (b) Top face ultimate compression failure; (c) Side view of P350-D203 after failure; (d) Side view of P1050-D76 after failure (Betts et al. 2020).....	14
Figure 2-8	Load-Deflection behavior of test specimens: (a) P350-D76; (b) P1050-D76; (c) P350-D203; (d) P700-D203; (e) P1050-D203 (Betts et al. 2020).....	15
Figure 2-9	Shear stresses in CFFT (Burgueño and Bhide 2006).....	17
Figure 2-10	Four-point bending test set-up for large scale specimens (Burgueño and Bhide 2006).....	19
Figure 2-11	Analytical and experimental comparison between shear load vs. shear strain for SS-2 specimen (Burgueño and Bhide 2006).....	20
Figure 2-12	Analytical and experimental comparison between influence of composite action (Burgueño and Bhide 2006).....	20
Figure 2-13	Stress-strain curve for GFRP tube (Fam and Cole 2007).....	21
Figure 2-14	Test set-up and instrumentation (Fam and Cole 2007).....	22
Figure 2-15	Load-deflection behavior for specimens of $a/D = 1$ (Fam and Cole 2007).....	24
Figure 2-16	Analytical model: (a) Strut-and-tie model; (b) Mechanism of dowel action; (c) Diagonal tension field in the tube (Fam and Cole 2007).....	25

Figure 2-17	Stress-strain curves of GFRP tubes in longitudinal direction (Fam et al. 2007)	27
Figure 2-18	Normalized shear versus deflection of test beam B5 and B6 (Fam et al. 2007)	27
Figure 2-19	Normalized shear versus strain of test beam B6 (Fam et al. 2007)	28
Figure 2-20	Different failure modes: (a) Beam B1, crushing and spalling of concrete cover; (b) Beam B2, failure of GFRP tubes under bi-axial stresses on compression side; (c) Beam B3, crushing and spalling of concrete cover; (d) Beam B4, GFRP tube failed in longitudinal tension, then in longitudinal compression, followed by hoop tension; (e) Beam B5, shear-bond failure; (f) Beam B6, shear-bond failure (Fam et al. 2007)	29
Figure 2-21	Various crack patterns in different CFFT specimens (Ahmad et al. 2008).....	32
Figure 2-22	Typical load-deflection response of deep CFFT beams (Ahmad et al. 2008).....	32
Figure 2-23	Comparison of load-deflection response of deep, short, and slender CFFT beams (Ahmad et al. 2008).....	33
Figure 2-24	Effect of a/D ratio on diagonal tension and flexural strains (Ahmad et al. 2008).....	34
Figure 2-25	Test set-up (Cole and Fam 2006).....	36
Figure 2-26	Various failure modes in beam specimens (Cole and Fam 2006).....	36
Figure 2-27	Stress strain behavior: (a) GFRP tube; (b) Internal rebars (Cole and Fam 2006).....	37
Figure 2-28	Load-deflection curves for specimens: (a) B1, B2, and B3; (b) B3-B7 (Cole and Fam 2006).....	38
Figure 2-29	Analytical model based on strain compatibility (Cole and Fam 2006).....	39
Figure 2-30	Stress-strain curves of unconfined and confined concrete (Cole and Fam 2006).....	39
Figure 2-31	CFT test: (a) Test matrix; (b) Test setup and instrumentation (Fam et al. 2007)	40
Figure 2-32	Failure mode: (a) CFT-G and CFT-GS; (b) CFT-S (Fam et al. 2007).....	41
Figure 2-33	Load-deflection behavior of CFT-G and CFT-GS test beams (Fam et al. 2007)	42

Figure 2-34	A simplified strut-and-tie model for CFT beams (Fam et al. 2007).....	43
Figure 2-35	Test Setup and instrumentation (Mohamed and Masmoudi 2010)	45
Figure 2-36	Typical failure modes; (b) Load-deflection behavior (Mohamed and Masmoudi 2010)	45
Figure 2-37	Kings Stormwater Channel Bridge (HPWREN, UCSD/CalTrans).....	49
Figure 2-38	Various piling applications of CFFT: (a) Fender piling; (b) Dauphins; (c) Light structure support pile groups; (d) Bridge pier protection (Fam et al. 2003)	49
Figure 2-39	(a) Fender piles and dauphin clusters in Naval Station Ingleside Project; (b) Structural piles in Belmar Municipal Marina Project (Fam et al. 2003)	50
Figure 3-1	Variation in wall thickness of GFRP tubes: (a) P50; (b) P100; (c) P150.....	53
Figure 3-2	Schematic diagram of fiber orientation with respect to longitudinal axis.....	53
Figure 3-3	Three stages of concrete compressive test: (a) Initial; (b) Intermediate; (c) Final	54
Figure 3-4	Schematics representation of tensile test of steel rebar specimens	55
Figure 3-5	Tensile stress vs. strain behavior of steel rebars: (a) 10M; (b) 15M	56
Figure 3-6	Uniaxial tensile test: (a) 10M rebar; (b) Failed 10M rebars; (c) 15M rebar; (d) Failed 15M rebars.....	56
Figure 3-7	Layout of typical cross sections of CFFT specimen: (a) P150-15M; (b) P150-10M; (c) P100-15M; (d) P100-10M; (e) P50-15M; (f) P50-10M.....	59
Figure 3-8	CFFT specimen fabrication: (a) Dimension layout; (b) Cage assembly; (c) Specimen before rebar installation; (d) Fixing of steel rebars; (e) Full assembly; (f) Top view of the full assembly; (g) Assembled formwork before concreting.....	61
Figure 3-9	Figure 3-9: CFFT specimen casting: (a) Concrete pouring; (b) Concrete compaction during specimen casting; (c) CFFT specimens ready for curing process; (d) Longitudinal view of CFFT; (e) Cross-sectional view of CFFT	62
Figure 3-10	Schematic representation of test set-up and instrumentation details: (a) Overall test set-up; (b) Orientation of strain rosette; (c) Cross-sectional view of CFFT at mid-span	63
Figure 3-11	Actual test set-up and instrumentation details: (a) Overall test set-up; (b) Test set-up and Instrumentation	65

Figure 3-12	Instrumentation details for bond-slip: (a) Linear potentiometer arrangement (Left side of CFFT); (b) Linear potentiometer arrangement (Right side of CFFT).....	66
Figure 3-13	Test timelapse of the CFFT specimen P50-a-AD1: (a) At load about 0 kN; (b) At load about 270 kN; (c) At load about 400 kN; (d) At load about 415 kN	69
Figure 3-14	Various failure region of CFFT specimens: (a) P50-a-AD1; (b) P150-b-AD0.5; (c) P100-a-AD2.25; (d) Bottom surface of P50-b-AD0.5; (e) Front face of P50-b-AD0.5; (f) Bottom surface of P150-b-AD2.25; (g) Top surface of P150-b-AD2.25	71
Figure 3-15	Failure modes in P100-a-AD0.5 specimen: (a) Longitudinal cross-section of CFFT; (b) Inner concrete core and outer layer of GFRP tube; (c) Inner layer of GFRP tube.....	72
Figure 3-16	Failure modes in P100-a-AD1 specimen: (a) Longitudinal cross-section of CFFT; (b) Inner concrete core and outer layer of GFRP tube; (c) Inner layer of GFRP tube.....	72
Figure 3-17	Failure modes in P100-a-AD2.25 specimen: (a) Longitudinal cross-section of CFFT; (b) Inner concrete core; (c) Outer layer of GFRP tube; (d) Inner layer of GFRP tube.....	73
Figure 3-18	Load vs. Mid-span deflection for a/D_i of 0.5 specimens: (a) 10M; (b) 15M	74
Figure 3-19	Load vs. Mid-span deflection for a/D_i of 1 specimens: (a) 10M; (b) 15M	75
Figure 3-20	Load vs. Mid-span deflection for a/D_i of 2.25 specimens: (a) 10M; (b) 15M	76
Figure 3-21	Influence of a/D_i ratios on the load capacity of CFFTs: (a) 10M; (b) 15M	77
Figure 3-22	Effect of longitudinal reinforcement ratio on CFFTs: (a) P50; (b) P100; (c) P150	79
Figure 3-23	Effect of pressure rating of GFRP tubes on 10M steel-reinforced CFFTs: (a) Load-deflection behavior; (b) Percentage increase in load capacity	80
Figure 3-24	Effect of pressure rating of GFRP tubes on 15M steel-reinforced CFFTs: (a) Load-deflection behavior; (b) Percentage increase in load capacity	81
Figure 3-25	Effect of pressure ratings of GFRP tube on moment capacity of CFFTs: (a) 10M; (b) 15M; (b) Ratio of 15M and 10M specimens	82
Figure 3-26	Effect of reinforcement ratio on moment capacity of CFFTs: (a) 15M; (b) 10M; (c) Both 15M, and 10M specimen	85

Figure 3-27	10M steel-reinforced CFFT specimens with a/D_i of 1: (a) Load vs. mid-span strain; (b) Load vs. strain rosette; (c) Moment-curvature response at mid-span.....	86
Figure 3-28	10M steel-reinforced CFFT specimens with a/D_i of 0.5: (a) Load vs. mid-span strain; (b) Load vs. strain rosette; (c) Moment-curvature response at mid-span.....	88
Figure 3-29	Location of neutral axis vs. moment at mid-span: (a) 10M steel-reinforced CFFTs with a/D_i of 1; (b) 10M steel-reinforced CFFTs with a/D_i of 0.5.....	89
Figure 3-30	Compositeness of 10M steel-reinforced CFFTs with a/D_i of 1 based on slip: (a) Between concrete core-steel rebar; (b) Between concrete core-GFRP tube.....	90
Figure 3-31	Compositeness of 10M steel-reinforced CFFTs with a/D_i of 0.5 based on slip: (a) Between concrete core-steel rebar; (b) Between concrete core-GFRP tube.....	91
Figure 4-1	FE model of internally steel-reinforced CFFT with a/D_i of 2.25: (a) Isometric view; (b) Cross-sectional view	94
Figure 4-2	Steel rebar arrangement: (a) Isometric view; (b) Cross-sectional view	95
Figure 4-3	Composite ply orientation: (a) $+55^\circ$ layer; (b) -55° layer	97
Figure 4-4	Tied contact between concrete core and GFRP tube.....	104
Figure 4-5	Modeling of boundary conditions: (a) SPC reaction supports; (b) Prescribe motion set for top support.....	105
Figure 4-6	Hourglassing pattern and hourglass control in CFFT: (a) Various locations; (b) In GFRP tube; (c) In Steel supports; (d) In concrete core	106
Figure 4-7	GFRP tube architecture (Measurement provided in Betts et al. 2019)	108
Figure 4-8	Progression of failure in CFFT model without stress limiting factors: (a) Before applied load; (b) Stress concentration in GFRP tube before failure; (c) Tension failure – sudden load-drop in the load-midspan deflection curve.....	111
Figure 4-9	Visual comparison of P100-a-AD0.5 CFFT specimen: (a) Simulation of failure in GFRP tube; (b) Simulation of damage in concrete	113
Figure 4-10	Load versus mid-span deflection verification: a/D_i of 0.5 CFFT FE models	114
Figure 4-11	Load versus strain verification: a/D_i of 0.5 CFFT FE models.....	115
Figure 4-12	Moment versus curvature verification: a/D_i of 0.5 CFFT FE models	116
Figure 4-13	Visual comparison of P100-a-AD1 CFFT specimen: (a) Simulation of failure in GFRP tube; (b) Simulation of damage in concrete	117

Figure 4-14	Load versus mid-span deflection verification: a/D_i of 1 CFFT FE models	118
Figure 4-15	Load versus strain verification: a/D_i of 1 CFFT FE models	119
Figure 4-16	Moment versus curvature verification: a/D_i of 1 CFFT FE models	120
Figure 4-17	Visual comparison of P100-a-AD2.25 CFFT specimen: (a) Simulation of failure in GFRP tube; (b) Simulation of damage in concrete	121
Figure 4-18	Load versus mid-span deflection verification: a/D_i of 2.25 CFFT FE models	122
Figure 4-19	Load versus strain verification: a/D_i of 2.25 CFFT FE models	123
Figure 4-20	Moment versus curvature verification: a/D_i of 2.25 CFFT FE models	124
Figure 4-21	Progression of failure in CFFT model with stress limiting factors: (a) Before applied load; (b) Stress concentration in GFRP tube before failure; (c) Tension failure – sudden load-drop in the load-midspan deflection curve.....	128
Figure 4-22	Visual comparison of P100-a-AD0.5 CFFT specimen: (a) Simulation of failure in GFRP tube; (b) Simulation of damage in concrete	129
Figure 4-23	Load versus mid-span deflection verification: a/D_i of 0.5 CFFT FE models	130
Figure 4-24	Load versus strain verification: a/D_i of 0.5 CFFT FE models	131
Figure 4-25	Moment versus curvature verification: a/D_i of 0.5 CFFT FE models	132
Figure 4-26	Visual comparison of P100-a-AD1 CFFT specimen: (a) Simulation of failure in GFRP tube; (b) Simulation of damage in concrete	133
Figure 4-27	Load versus mid-span deflection verification: a/D_i of 1 CFFT FE models	134
Figure 4-28	Load versus strain verification: a/D_i of 1 CFFT FE models	135
Figure 4-29	Moment versus curvature verification: a/D_i of 1 CFFT FE models	136
Figure 4-30	Visual comparison of P100-a-AD2.25 CFFT specimen: (a) Simulation of failure in GFRP tube; (b) Simulation of damage in concrete	137
Figure 4-31	Load versus mid-span deflection verification: a/D_i of 2.25 CFFT FE models	138
Figure 4-32	Load versus strain verification: a/D_i of 2.25 CFFT FE models	139
Figure 4-33	Moment versus curvature verification: a/D_i of 2.25 CFFT FE models	140
Figure A.1	Load vs. mid-span strains for CFFT specimens: (a) a-AD0.5; (b) b-AD0.5; (c) a-AD1; (d) b-AD1; (e) a-AD2.25; (f) b-AD2.25	151
Figure A.2	Load vs. strain rosette for CFFT specimens: (a) a-AD0.5; (b) b-AD0.5; (c) a-AD1; (d) b-AD1; (e) a-AD2.25; (f) b-AD2.25	152

Figure A.3	Moment vs. curvature for CFFT specimens: (a) a-AD0.5; (b) b-AD0.5; (c) a-AD1; (d) b-AD1; (e) a-AD2.25; (f) b-AD2.25	153
Figure A.4	N.A depth vs. moment for CFFT specimens: (a) a-AD0.5; (b) b-AD0.5; (c) a-AD1; (d) b-AD1; (e) a-AD2.25; (f) b-AD2.25	154
Figure A.5	Load vs. slip between GFRP tube and concrete for CFFT specimens: (a) a-AD0.5; (b) b-AD0.5; (c) a-AD1; (d) b-AD1; (e) a-AD2.25; (f) b-AD2.25.....	155
Figure A.6	Load vs. slip between concrete and steel rebars for CFFT specimens: (a) a-AD0.5; (b) b-AD0.5; (c) a-AD1; (d) b-AD1; (e) a-AD2.25; (f) b-AD2.25.....	156

ABSTRACT

Concrete-filled fiber-reinforced polymer (FRP) tubes (CFFTs), an alternative to conventional systems, emerged as innovative and sustainable infrastructure systems for various structural applications. Due to their capability to resist significant axial, shear, and flexural loads and excellent corrosion resistance offered in harsh environments, CFFTs are viable for major structural applications such as bridge piers and marine piles. The main objective of this thesis was to investigate the shear and flexural behavior of steel-reinforced CFFTs with $\pm 55^\circ$ fiber orientation. An extensive study was performed by fabricating and testing a total of eighteen, 1219.2 mm long steel-reinforced CFFTs under three-point bending by varying three different parameters: pressure ratings of the GFRP tube, internal reinforcement ratios, and shear span to depth ratio. The filament-wound GFRP tubes made of glass fibers and vinyl-ester resin had a fiber orientation of $\pm 55^\circ$ with respect to the longitudinal axis. Three different GFRP tubes were used with varying wall thicknesses of 2.7, 4.7, and 6.7 mm, with a constant inner diameter of 203.2 mm. Two internal reinforcement ratios of 1.85% and 3.70% were adopted by introducing 6-10M and 6-15M steel rebars, respectively, with similar cross-sectional configurations for all CFFTs. The CFFT beams tested were under three different shear span to depth ratios (a/D_i) of 0.5, 1, and 2.25. Irrespective of their testing parameters, all CFFT specimens failed in flexure by rupturing the GFRP tube in the bottom tension region at mid-span. The study demonstrates that the increase in the total normalized reinforcement ratio resulted in a significant enhancement in the strength and stiffness of CFFTs. Additionally, no significant slip between the GFRP tube-concrete core and concrete core-steel rebars was detected, showing the superior composite action in the CFFT system. A nonlinear finite element model was developed and analyzed in LS-DYNA using its dynamic solver to predict the complete behavior of CFFTs. Overall, the FE models successfully predicted the failure mode, nonlinear response of CFFTs, and showed a good agreement with the experimental results.

LIST OF ABBREVIATIONS and SYMBOLS USED

<i>a</i>	= Shear span
<i>ACI</i>	= American Concrete Institute
<i>ASTM</i>	= American Society for Testing and Materials
<i>c</i>	= y-intercept of St. line
<i>CFFT</i>	= Concrete-filled fiber-reinforced-polymer tube
<i>CFRP</i>	= Carbon fiber reinforced polymer
<i>CIRC</i>	= Canadian Infrastructure Report Card
<i>CLT</i>	= Classical lamination theory
<i>CSA</i>	= Canadian Standards Association
<i>D</i>	= Depth
<i>D_i</i>	= Inner diameter of GFRP tube
<i>DAQ</i>	= Data Acquisition System
<i>DIREC</i>	= Coupling direction for constraint keyword in LS-DYNA
<i>E₁</i>	= Elastic modulus in fiber direction
<i>E₂</i>	= Elastic modulus in matrix direction
<i>E_A</i>	= Elastic modulus in longitudinal direction in LS-DYNA
<i>E_B</i>	= Elastic modulus in transverse direction in LS-DYNA
<i>ECR</i>	= Electrical/chemical resistant
<i>ELFORM</i>	= Element formulation in LS-DYNA
<i>EQ.</i>	= Equation for failure surface for MAT058 in LS-DYNA
<i>ERODS</i>	= Maximum effective strain for element layer failure in LS-DYNA
<i>ε_p</i>	= Principal tensile strain
<i>ε_H</i>	= Longitudinal Strain
<i>ε_V</i>	= Circumferential Strain
<i>ε_D</i>	= Diagonal Strain
<i>FE</i>	= Finite element
<i>FEA</i>	= Finite element analysis
<i>FEM</i>	= Finite element modeling
<i>FRP</i>	= Fiber Reinforced Polymer

f_t	= Tensile strength of concrete
f_c'	= Unconfined compressive strength of concrete
G_{12}	= Shear modulus
<i>GFRP</i>	= Glass fiber reinforced polymer
G_{AB}/G_{CA}	= Shear modulus in major direction in LS-DYNA
G_{BC}	= Shear modulus in minor direction in LS-DYNA
<i>HGEN</i>	= Hourglass energy calculation option in LS-DYNA
k	= Coefficient for concrete strength relation
<i>LAMSHT</i>	= Laminated shell theory in LS-DYNA
<i>LMT</i>	= Linear motion transducers
<i>LP</i>	= Linear potentiometer
M_u	= Peak moment at mid-span
m	= Gradient of St. line
n	= Coefficient for concrete strength relation
PR_{BA}/PR_{CA}	= Major Poisson's ratio in LS-DYNA
PR_{CB}	= Minor Poisson's ratio in LS-DYNA
<i>QB</i>	= Hourglass coefficient for shell bending in LS-DYNA
<i>QM</i>	= Hourglass coefficient in LS-DYNA
<i>RO</i>	= Mass density in LS-DYNA
S^c	= In-plane shear strength in LS-DYNA
S_C	= In plane shear strength
<i>SFM</i>	= Scale factor for master penalty stiffness in LS-DYNA
<i>SFS</i>	= Scale factor for slave penalty stiffness in LS-DYNA
<i>SLIM</i>	= Stress limiting factors in LS-DYNA
<i>SLIMC1</i>	= Factor to determine the minimum stress limit after stress maximum (fiber compression) in LS-DYNA
<i>SLIMC2</i>	= Factor to determine the minimum stress limit after stress maximum (matrix compression) in LS-DYNA
<i>SLIMS</i>	= Factor to determine the minimum stress limit after stress maximum (shear) in LS-DYNA
<i>SLIMT1</i>	= Factor to determine the minimum stress limit after stress maximum (fiber tension) in LS-DYNA

$SLIMIT2$	= Factor to determine the minimum stress limit after stress maximum (matrix tension) in LS-DYNA
$SLSFAC$	= Scale factor for sliding interface penalties in LS-DYNA
$SOFT$	= Soft constraint option in LS-DYNA
$SOFT(MAT058)$	= Softening reduction factor for strength in the crashfront in LS-DYNA
$SOFSCCL$	= Scale factor for constraint forces in LS-DYNA
SP	= String potentiometer
t	= Wall thickness of GFRP tubes
t_{fw}	= Thickness of the filament wound section
$TSSFAC$	= Scale factor for computed timestep in LS-DYNA
ULF	= Ultimate laminate failure
v	= Component vector in LS-DYNA
V_f	= Volume fraction
x	= Location of neutral axis
X_C	= Compressive strength in fiber direction
X^C	= Compressive strength in longitudinal direction in LS-DYNA
X_T	= Tensile strength in fiber direction
X^T	= Tensile strength in longitudinal direction in LS-DYNA
Y_C	= Compressive strength in matrix direction
Y^C	= Compressive strength in transverse direction in LS-DYNA
Y_T	= Tensile strength in matrix direction
Y^T	= Tensile strength in transverse direction in LS-DYNA
ν_{12}	= Major Poisson's ratio
ν_{21}	= Minor Poisson's ratio
γ_{xy}	= Shear strain
θ	= Angle of principal tensile strain
φ	= Curvature at mid-span of CFFT specimen
σ_{min}	= Minimum stress in the composite post-failure in LS-DYNA

ACKNOWLEDGEMENTS

I would like to express my sincere gratitude to Dr. Pedram Sadeghian, my research supervisor, for his invaluable guidance, encouragement, and patience throughout my graduate studies and for helping me complete this achievement. I feel very fortunate for this excellent research opportunity and to be a part of his Canada Research Chair in Sustainable Infrastructure research team. I'm grateful to him for sharing his immense knowledge and many valuable skills that I have learned and will take with me. I would also like to thank my supervisory committee members, Dr. Kyle Tousignant and Dr. Alex Kalamkarov, for giving their valuable time for review and feedback, which improved the quality of this thesis.

The laboratory work of my research would not have been possible without the dedicated support of the excellent lab technicians in our department, Jesse Keane, Jordan Maerz, Brian Kennedy, and Dean Grijm. I thank them for their willingness to assist me by coming up with unique ideas for fabrication, test setup, and data acquisition which allowed me to complete the lab experiments easily and safely.

I would also like to acknowledge and thank Dalhousie University for in-kind and financial support. Additionally, I'm highly grateful to RPS Composites, Inc. (Mahone Bay, NS, Canada) for providing the GFRP tubes used in this research.

I wish to acknowledge my colleagues: Senthil K. Velkumar, Thomas J. Goill, Dillon Betts, and Raghad Kassab, for their support in the lab activities. My special thank is extended to my colleague Brock Jeans for helping me explore Nova Scotia by taking me to hiking trails every once in a while.

CHAPTER 1 INTRODUCTION

1.1 MOTIVATION

Efficient and sustainable infrastructure systems such as bridges, buildings, pipelines, flood control systems, and utilities are necessary for a healthy economy and comfortable standard of living. Reinforced concrete and steel structures are the backbones of our current civil infrastructures. The long-term structural durability of reinforced concrete has been a long-term issue for the infrastructure industry. Corrosion of steel reinforcement and degradation in the wooden structures causes major rehabilitation problems to the infrastructures worldwide. The released Canadian infrastructure report card (CIRC, 2019) in 2019 states that a significant percentage of public infrastructure in Canada is in poor condition. The report also suggested that 80% of the roads and bridges are more than 20 years old, and 40% of them are in fair, poor, or very poor condition. Climate change also has major physical impacts on the aging infrastructure, as the harsh environment accelerates the deterioration of a structure's structural performance, serviceability, and lifespan, as shown in figure 1-1.

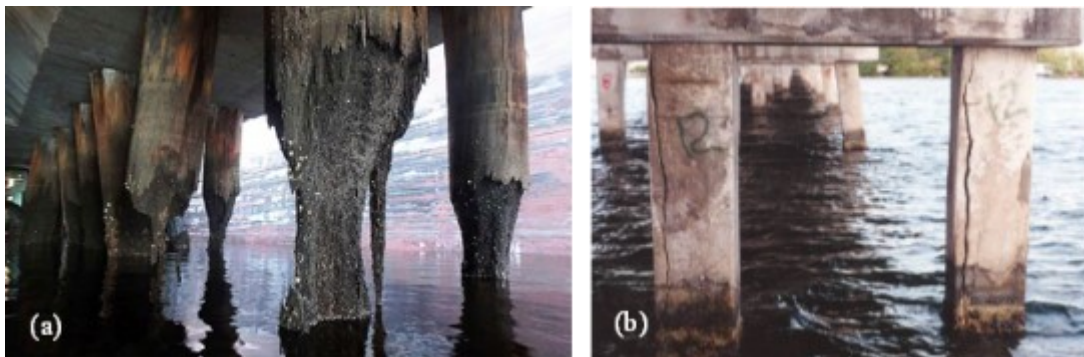


Figure 1-1. Environmental impact on marine structures: (a) Worn out timber piles (QuakeWrap Inc.); (b) Typical corrosion of precast prestressed concrete piles (Moser et al., GODT 2011)

Due to these combined factors of deteriorating conditions, age, and change in the environment, it is now more than ever necessary to rehabilitate the existing infrastructures or upgrade them into new ones. As a result, there are ongoing efforts to improve the existing marine infrastructure in Canada. Few projects, namely, improvement of Halifax Waterfront, NS as shown in figure 1-2 (a) by upgrading and replacing the existing wharves

and piers near foundation place, Figure 1-2 (b) exhibits Port of Oshawa consolidation project in Ontario, which improved east dock face by adding 98 concrete-filled steel pipe piles. Cape Crocker Park rehabilitation project in Sydney Bay, Ontario, the rehabilitation of an old concrete-capped timber crib wharf at the park by adding additional sheet pile bulkhead walls as shown in figure 1-2 (c).



Figure 1-2. Recent marine infrastructure rehabilitation projects in Canada: (a) Halifax waterfront, NS (Develop Nova Scotia); (b) Port of Oshawa, ON (Piling Canada); (c) Cape Crocker Park, ON (Piling Canada)

In the last decade, hybrid systems such as concrete-filled fiber-reinforced-polymer (FRP) tubes (CFFTs) are emerging as a promising alternative for various structural applications such as structural columns, piles, poles, signaling posts, bridge components, etc. Their fascinating features include durability, concrete confinement, resistance towards chemical attacks, etc., grabbed the attention of the researchers and the infrastructure industry. The CFFT members are usually used as an alternative to conventional reinforced concrete and

steel components, mainly in the tidal areas for marine piles and the de-icing zones, effectively solving the corrosion issue and saving millions of dollars spent yearly for rehabilitation of the concrete structures. Hence, the application of the CFFT members in the above-stated projects would have been a much more effective and appropriate replacement, particularly in terms of life span to the traditional concrete and steel members. The CFFT member does not always require the internal reinforcements in the concrete as depending on the fiber orientation, the FRP tube acts as the confinement material and provides a significant amount of reinforcement in the axial and hoop direction. However, the addition of internal longitudinal reinforcement can enhance the bending stiffness of CFFTs, resulting in a smaller deflection of CFFTs under service loads compared to conventional reinforced concrete members while reserving the contribution FRP tube to a larger extent for confinement and shear resistance. Furthermore, the FRP tubes can be designed and reinforced according to the requirement of individual applications based on the types of fibers, their orientation, fiber volume fraction, and the number of layers to achieve the optimum design. Most of the current design provisions incorporated in the codes and design guidelines are based on the existing design formulas of members reinforced with conventional steel and considering modifications factors in the equations to differentiate between FRP and steel such as Mirmiran et al. (1998) and Ahmad et al. (2008) on shear resistance and Mohamed and Masmoudi (2010) on cracking moment of CFFT members.

1.2 PROBLEM STATEMENT

Currently, the advancement in the construction industry allows the successful field applications of innovative materials such as GFRP composites. In addition to providing confinement, due to the high corrosion resistance nature of the filament-wound fiber-reinforced polymer tubes, which act as a protective barrier for the internal concrete, the potential of field applications of CFFT in the marine environment cannot be ignored. Furthermore, GFRP tubes also provide stay-in-place formwork, reducing the requirement of temporary formwork and increasing sustainability by reducing construction waste. However, CFFTs are yet to be frequently adopted by engineers in the field of construction due to limited design guidelines and information regarding the behavior of the individual material and the overall system.

$\pm 55^\circ$ filament-wound GFRP tubes are frequently used for piping applications in the municipal sectors, gas and oil industries, aerospace, and aeronautics industries due its corrosion resistance, lightweight, high strength, and resistance to both the internal pressure and axial loads. In the piping applications, the GFRP tubes are often subjected to internal pressure loads, which results in a hoop stress to axial stress ratio of 2:1. The $\pm 55^\circ$ winding angle with respect to the axial direction of the filament wound GFRP tube holds a significant advantage in these applications, as this fiber orientation makes the tube ideal for resisting this type of internal pressure loading. For these above-stated reasons, $\pm 55^\circ$ filament-wound GFRP tubes are commercially available and can be adopted as CFFT members in the construction industry. However, limited theoretical and experimental studies and design guidelines on CFFTs, prevent the potential widespread structural applications of CFFT as structural members. In addition, there is currently a gap in the literature with regards to the shear and flexural behavior of steel-reinforced CFFTs with $\pm 55^\circ$ fiber orientation which will be further explored in Chapter 2.

1.3 OBJECTIVES

The main objectives of this research aim to study and provide a deeper understanding of the shear and flexural behavior and the failure mode of reinforced concrete-filled glass-fiber-reinforced-polymer tubes (CFFTs) with $\pm 55^\circ$ fiber orientation for use in sustainable infrastructure applications. The main objectives will be achieved by completing specific objectives in this study, which are summarized as follows:

- i) To evaluate the effect of shear span to depth ratio on the behavior of the CFFT members.
- ii) To examine the effect of the internal reinforcement ratio on the behavior of CFFTs.
- iii) To evaluate the effect of the wall thickness of the GFRP tubes on the performance of the CFFT members.
- iv) To predict the load-deflection responses, nonlinear strain, moment-curvature behavior, and failure mode of the CFFT specimens via finite element modeling.

1.4 RESEARCH SCOPE

The objectives discussed in the previous section will be achieved by fabricating and preparing a total of eighteen CFFT beam members with GFRP tubes with three different wall thicknesses and two different internal steel reinforcement ratios. The prepared CFFT specimens will be tested under three-point bending with varying shear span to depth ratios. The experimental results will be analyzed, compared, and verified by developing a finite element (FE) model using the LS-DYNA software program.

1.5 THESIS LAYOUT

The contents of the thesis are briefly discussed in the following:

Chapter 2 will present reviews of previous research on the behavior of GFRP tubes with $\pm 55^\circ$ fiber orientation, concrete-filled fiber-reinforced-polymer tubes under different loading conditions. The literature will investigate the effect of internal reinforcement and their varieties, shear span to depth ratios, and fiber orientations, major inferences from the previous studies, as well as different field application of CFFTs.

Chapter 3 will describe the experimental program, including the material properties, and provide a detailed description of the fabrication procedure, test matrix, test set-up, instrumentation, and test procedure. Finally, chapter 3 will conclude with a comprehensive study of the experimental results and the behavior of CFFTs, including failure modes, the effect of various parameters such as shear span to depth ratio, the wall thickness of the GFRP tube, and internal reinforcement ratio, as well as auxiliary material tests.

Chapter 4 will explain the procedure, material models, and various parameters used in developing a finite element model in a commercially available FE software program, LS-DYNA. Finally, the FE model's analyzed results, and failure modes will be verified against the experimental results from Chapter 3.

Finally, the thesis concludes with Chapter 5, which summarizes the significant findings of this research and provides recommendations for future research into CFFTs, based on this research experience.

CHAPTER 2 LITERATURE REVIEW

2.1 BACKGROUND

The advancement in innovative materials in the field of civil engineering has seen a growth in the application of fiber-reinforced polymer (FRP) composites in the construction industry. In recent years, FRP has been extensively used for the rehabilitation and strengthening of existing structures by means of external confinement techniques with plates, sheets, and wraps. However, with an alarming rate of rapidly aging infrastructure growing worldwide, it is becoming more and more important to replace those with improved structural systems. The main advantages of concrete-filled fiber-reinforced-polymer tubes (CFFTs) over conventional structural systems with timber, reinforced or prestressed concrete, structural steel, and concrete-filled steel tubes could be as summarized as follows:

- High strength to weight ratios due to lightweight and superior strength of FRPs.
- Impressive durability in severe environments due to their low chemical reactivity.
- High energy absorption.
- Design adaptability in terms of fabrication, stay-in-place formwork, achievement of the optimum design for individual applications.

Apart from major structural applications such as bridge pier, girders, fender piles, CFFTs can also be used in highway traffic lights and sign-supporting structures, light, and hydro pole applications (Qasrawi and Fam 2008).

The common manufacturing techniques for fabricating FRP tube includes hand layup, filament-winding, spin-casting, pultrusion, and resin transfer molding. A study by (Ozbakkaloglu and Vincent 2014) suggested that FRP tubes manufactured by automatic filament winding technique provide greater strength and strain enhancement for CFFTs compared to the tubes manufactured manually using a wet layup method.

This chapter reviews experimental and analytical work conducted previously on the compression, tension, and flexural behavior of hollow GFRP tubes with $\pm 55^\circ$ fiber

orientation along with behavior short and long span of CFRTs, with or without internal reinforcement. This chapter also summarizes the major factors influencing the behavior of CFRTs and identifies potential research gaps. Finally, a few real-life field applications of CFRTs are also explored.

2.2 BEHAVIOR OF $\pm 55^\circ$ GFRP TUBES

In 2019, Betts et al. studied compression and tension behavior of $\pm 55^\circ$ filament wound GFRP tubes. The nonlinear stress-strain behavior of the GFRP tubes was studied using 25 (5 identical for each case) and 6 (3 identical for each case) specimens, which were tested under compression and tension, respectively. The GFRP pipes were manufactured using continuous roving ECR glass fibers and a BIS-A vinyl-ester resin. The tubes had a fiber volume fraction of 50.2% and had a fiber orientation of $\pm 55^\circ$ with an error of $\pm 2^\circ$. Five different GFRP tube specimens were selected based on their pressure rating and their inner diameter. The GFRP tubes' three nominal pressure ratings were 350, 700, and 1050 kPa, influenced by their filament wind layup. The two inner diameters of the compression specimens were 76.2 and 203.2 mm, and the specimen length was twice its outer diameter. The 2:1 length to diameter ratio was adopted to avoid a premature failure in the gauge length. Also, the local crushing at the pipe end was avoided by reinforcing the end using a basalt-FRP wrap. The strain data were collected from each compression specimen using four strain gauges, two of them were orientated to the axial loading direction, and the other two strain gauges were orientated in the transverse direction. The compression specimens were tested based on ASTM D5449. In comparison, the tension specimens had an inner diameter of 76.2 mm. The tension specimens were prepared by a novel method to avoid premature failure due to the slippage by fitting the end with steel cores and manually tightened by cap screws. In addition, the specimens were made into a dumbbell shape to avoid any failure in the gauge length. Total six strain gauges: four in the axial direction and two in the hoop direction were used to record the strain data from each specimen.

Table 2-1. Test Matrix (Betts et al. 2019)

Specimen Group	Nominal Pressure Rating (kPa)	No. of Specimens	Inner Diameter (mm)	Cross Sectional Area (mm ²)	Wall Thickness (mm)	Diameter-Thickness Ratio (DTR)	Filament Wind Layup (°)
P350-D76-C	350	5	76.2	416.5	1.7	44.8	[±55] ₂
P1050-D76-C	1050	5	76.2	964.4	3.8	20.1	[(±55) ₂ /+55/-55] ₅
P350-D203-C	350	5	203.2	1741.5	2.7	75.3	[±55/+55] ₅
P700-D203-C	700	5	203.2	3103.0	4.7	43.2	[±55] ₄
P1050-D203-C	1050	5	203.2	4404.6	6.7	30.3	[±55] ₅
P350-D76-T	350	3	76.2	416.5	1.7	44.8	[±55] ₂
P1050-D76-T	1050	3	76.2	964.4	3.8	20.1	[±55] ₇

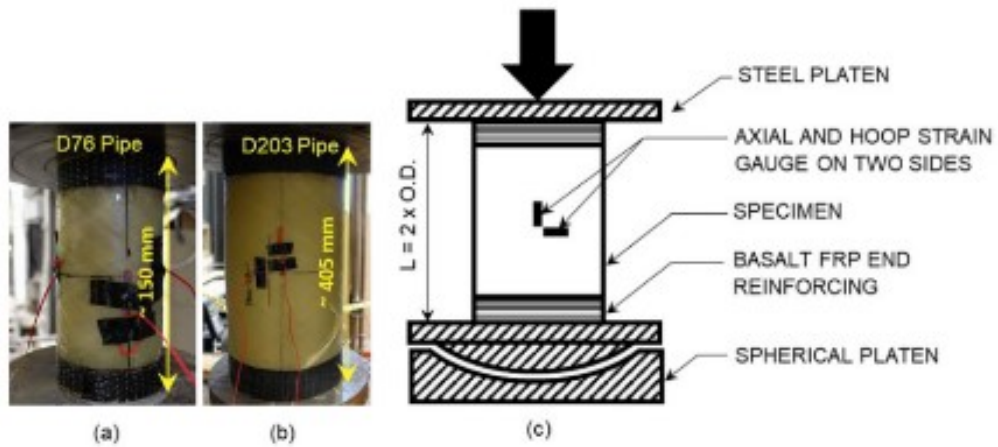


Figure 2-1. Compression specimen and test set-up (Betts et al. 2019)

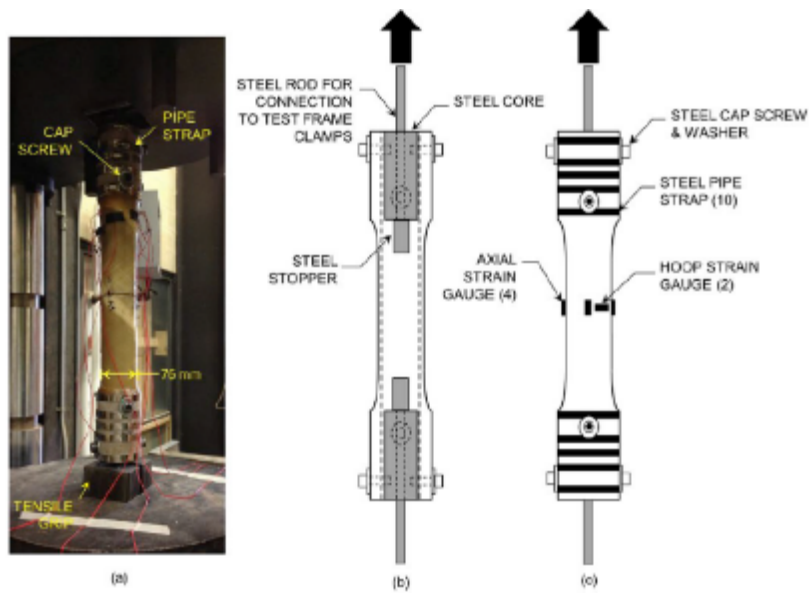


Figure 2-2. Tension specimen and test set-up (Betts et al. 2019)

The diameter-wall thickness ratio (DTR) had an essential effect on the results of both compression and tension tests. The diameter to wall thickness ratio for the compression

specimens was in the range of 20.1 to 75.3. The compression specimens with a DTR of 75.3 showed a significantly lower strength than lower DTR specimens caused by premature local buckling. The only compression specimen set did not follow the general trend of failure, matrix cracking parallel to the fiber direction, and ultimately failed by crushing. A single-factor analysis of variance (ANOVA) with a confidence of 95% was used to compare and determine variation in the specimens' strength, stress, and moduli. The compression specimens with a DTR of 75.3 had average compressive stress of 73.3 MPa. In comparison, the specimens with a DTR of 43.2 and 30.3 had exhibited a stress increment of 56% and 60%, respectively. This variation in stress was a general trend for the compression specimens; as the DTR value increased, the strength decreased. The sole significant effect in pipe modulus was seen for 203.2 mm diameter specimens. The specimens with a DTR of 75.3, 43.2, and 30.3 had a decreasing trend in the pipe modulus of 8.32, 10.03, and 11.5, respectively.

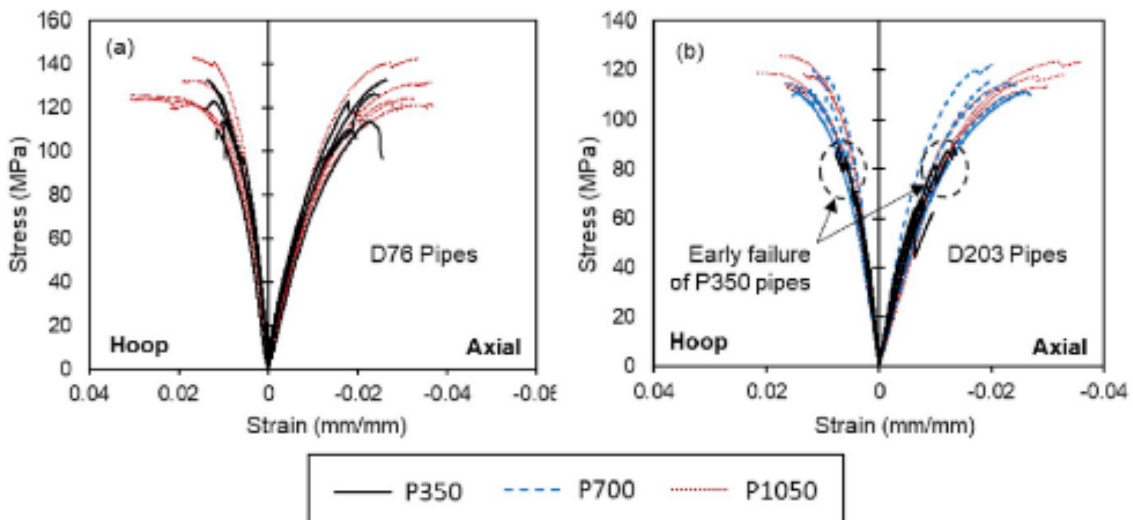


Figure 2-3. Stress-strain behavior of compression tests (Betts et al. 2019)

In contrast, the two different tensile specimens had a diameter to wall thickness of 20.1 to 44.8. The tension specimens did not experience an ultimate failure. The tubes with lower DTR showed higher strength and stiffness compared to a higher DTR specimen. The average tensile strength and pipe modulus increased 49% and 23%, respectively, for the lower DTR specimens. Two hypotheses were drawn from this behavior, thinner-walled tubes suffered a reduction in specimens' diameter at the midheight, which influenced the longitudinal bending of the wall. Another speculation for this behavior was the variation

in the amount of fibers present. The higher DTR specimens did not have enough fibers, which was the primary reason behind the premature softening of the tubes due to matrix cracking of the resin-rich area. Compared to the compression test specimens, the tensile specimens showed a lower strain level before the failure. Overall, from the tests, it was notably observed that the tubes were stronger in compression compared to tension. The 1050 and 350 kPa tubes were 83% and 167% stronger in compression, respectively, compared to their tensile counterpart.

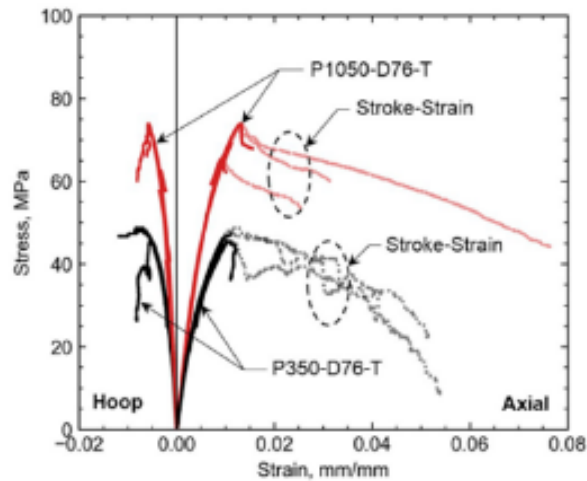


Figure 2-4. Stress-strain behavior of tension tests (Betts et al. 2019)

The stress-strain behavior of $\pm\Theta^\circ$ FRP pipes under axial compression and tension was predicted using a computer program, developed based on incremental classical lamination theory (CLT) to perform nonlinear analysis. The program considered nonlinear transverse and shear behavior of lamina and modeled as parabolic and cubic relationships, respectively. The tangent moduli of the material were used for the CLT analysis. The programming model effectively calculated the critical buckling stress for compression specimens based on tangential axial pipe modulus, thickness, the radius of the pipe wall, and Poisson's ratio. Due to the unavailability of the strength properties of the tubes, the tube strengths were calculated based on a 55% volume fraction of a unidirectional E-glass and epoxy resin lamina. The cubic model was developed based on constants with different boundary conditions to determine the shear stress-strain relationship. Similarly, a parabolic relationship was established based on ultimate transverse tensile strength, strain, and initial transverse modulus. Due to limited data of ultimate shear strain, a value of 0.04 mm/mm was considered. Also, due to limited information, the compressive behavior of the

composite in the transverse direction was considered linear-elastic until failure. The program with an iterative method calculated shear strength, shear modulus, and transverse tensile strength, transverse tensile modulus based on shear strain and transverse tensile strain at any level, respectively. The tension specimens showed an important near-linear post-peak behavior, which was recaptured in the model based on a 60% post-peak decrease of ultimate tensile stress at a slope of 8% of the ultimate stress-strain ratio. As part of the verification, the nonlinear model was able to capture the nonlinear behavior of the tubes. The 350 kPa pressure-rated tubes under both compression and tension showed an overprediction of failure. This variation in the test and model was assumed due to the premature failure or lower number of uniform fibers distributed in each tube layer. A parametric study by changing the fiber angle showed that a decrease in fiber angle resulted in an increase in strength and stiffness of the composite pipes.

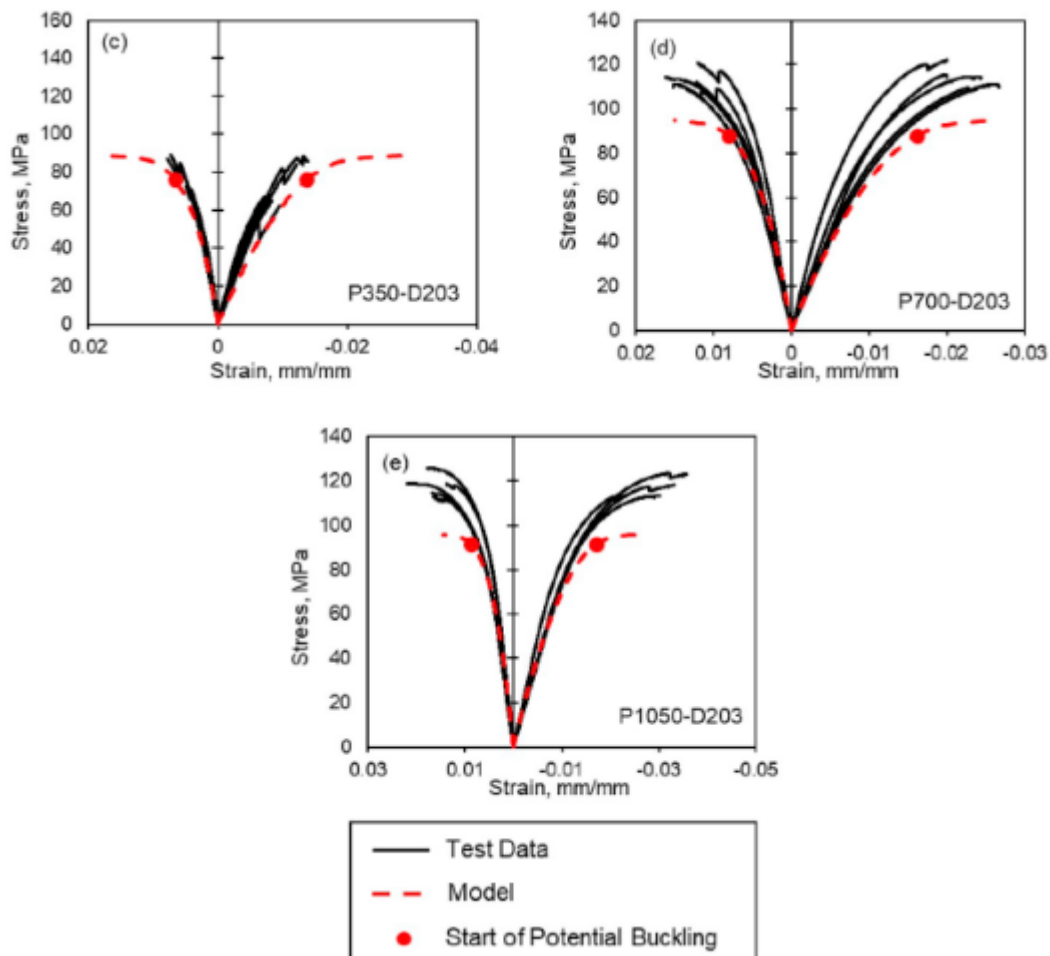


Figure 2-5. Stress-strain analysis for compression specimens (Betts et al. 2019)

More recently, Betts et al. (2020) studied the flexural behavior of hollow $\pm 55^\circ$ filament wound GFRP tubes. The study consisted of four-point bending tests of 15 filament-wound GFRP tubes with three and two different tube wall thicknesses and internal diameter. The FRP tubes were manufactured using electrical/chemical resistant (ECR) glass fibers and a vinylester resin and had a fiber volume fraction of 50.2%. The fiber orientation in the GFRP tubes had an error of $\pm 2^\circ$. The wall thickness of the tubes was directly related to their pressure ratings. The pressure rating varied from 300, 700, and 1050 kPa. The wall thickness for 76.2 mm inner diameter tubes was 1.7 and 3.8 mm, whereas 203.2 mm inner diameter tubes varied from 2.7 to 6.7 mm. The span length of smaller and larger diameter tube specimens was 1143 and 3048 mm, respectively. The main parameter of these tests was to understand the effect of inner diameter to wall thickness ratio (D/t) for the tubes. All of the specimens in this test showed a similar ductile failure pattern, and audible cracking originated from the bottom tension region at the midspan due to flexural loading. In the early stages, audible cracking was reported due to matrix cracking in the resin-rich areas. In the consecutive stages, the progressive transverse matrix cracks were noticed, and those progressed towards the top. Finally, at a certain critical point, a sudden ultimate failure occurred at the top compression face.

Table 2-2. Test Matrix (Betts et al. 2020)

Specimen Group	Nominal Pressure Rating (kPa)	No. of Identical Specimens	Inner Diameter (mm)	Span (mm)	Constant Moment Zone (mm)	Cross Sectional Area (mm ²)	Wall Thickness (mm)	Diameter-Thickness Ratio (D/t)	Fiber Architecture ^a (°)
P350-D76	350	3	76.2	1143	171	416.5	1.7	45	$[\pm 55]_2$
P1050-D76	1050	3	76.2	1143	171	964.4	3.8	20	$[\pm 55]_2/+55$
P350-D203	350	3	203.2	3048	457	1741.5	2.7	75	$[\pm 55]_2/+55$
P700-D203	700	3	203.2	3048	457	3103.0	4.7	43	$[\pm 55]_4$
P1050-D203	1050	3	203.2	3048	457	4404.6	6.7	30	$[\pm 55]_5$

^a fiber architecture degrees with respect to the longitudinal axis of the tubes.

The effect of inner diameter to the tube wall thickness was noticeable in the flexural capacity of the tubes. As the D/t ratio decreased from 45 to 20 for the 76 mm, and 75 to 30 for the 203 mm diameter tubes, the observable flexural load capacity of the tubes increased by 132% and 205%, respectively. All of the GFRP tubes exhibited a nonlinear moment-curvature, load-deflection, and a prolonged post-peak behavior. The prolonged post-peak behavior was mostly due to the observable progressive tensile failure of the tubes. Although the ultimate deflection for most of the specimen does not affect by the wall

thickness, the tube with an inner diameter of 203 mm and thickest among the other tubes with the wall thickness of 6.7 mm, showed a rather significant increase of 37% in ultimate deflection compared to the following thickest tubes with a wall thickness of 4.7 mm. The author noted that this variation was not due to the stability failure but rather a material failure and suggested that this ultimate compression failure might be due to a different failure mechanism.

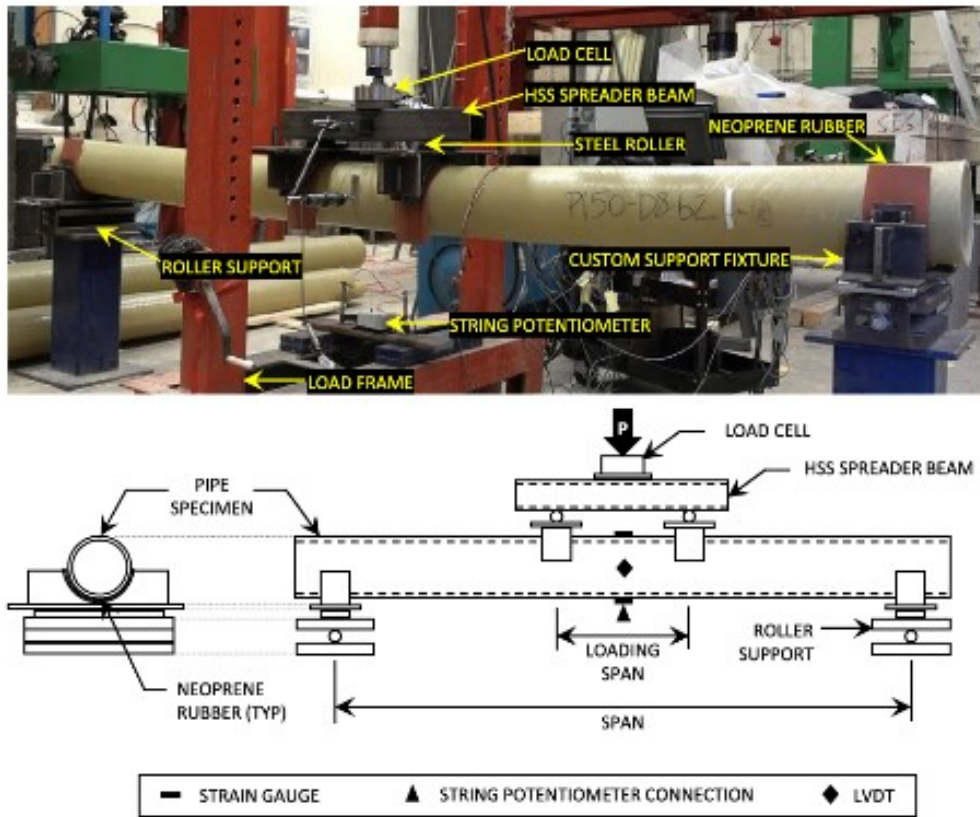


Figure 2-6. Test set-up (Betts et al. 2020)

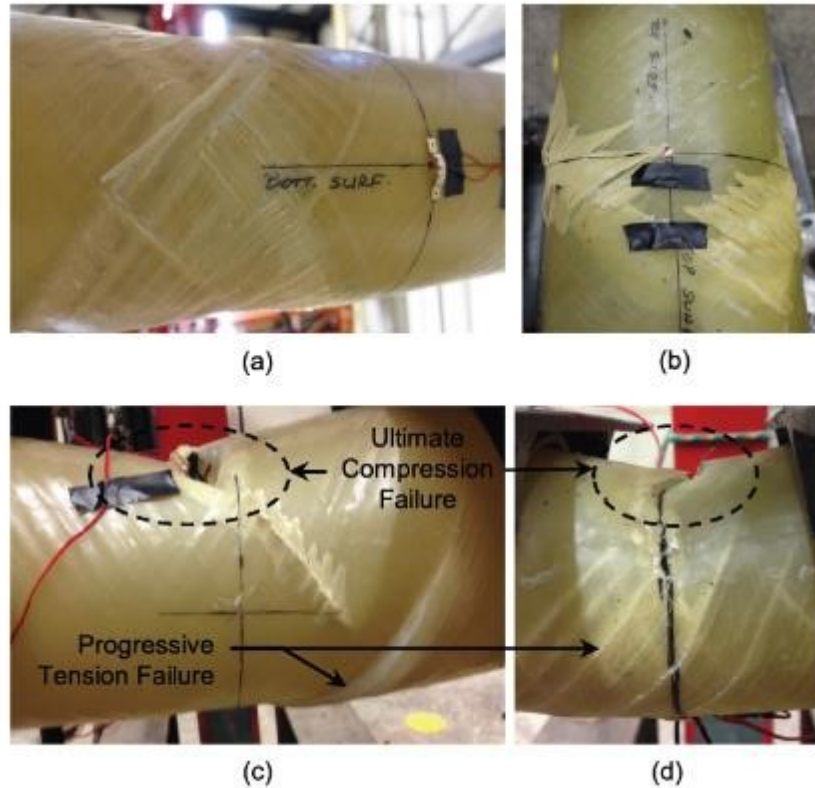


Figure 2-7. Typical failure modes: (a) Bottom face progressive tensile failure; (b) Top face ultimate compression failure; (c) Side view of P350-D203 after failure; (d) Side view of P1050-D76 after failure (Betts et al. 2020)

The nonlinear load-deflection and moment-curvature behavior of the hollow GFRP tubes were successfully captured based on a cross-sectional based analytical model. In addition to failure load, the developed model was also able to capture an agreeable post-peak tensile behavior of the tubes. The model incorporated both material failure and stability failure due to premature wall buckling. Due to the inclusion of premature instability failure in the model, the comparison study between model and test results showed a higher degree of accuracy. Whereas if the premature failure aspect was not incorporated into the model, it would have overpredicted the behavior of the GFRP tubes. Based on the model, the parametric study showed that the increase in the D/t ratio decreases the ultimate load capacity, flexural rigidity, stiffness, and ultimate deflection. Also, the decrease in the D/t ratio prolongs the post-peak behavior due to the progressive tensile failure mechanism. Additionally, it was observed that with the decrease in the span length, the ultimate load capacity and stiffness were increased.

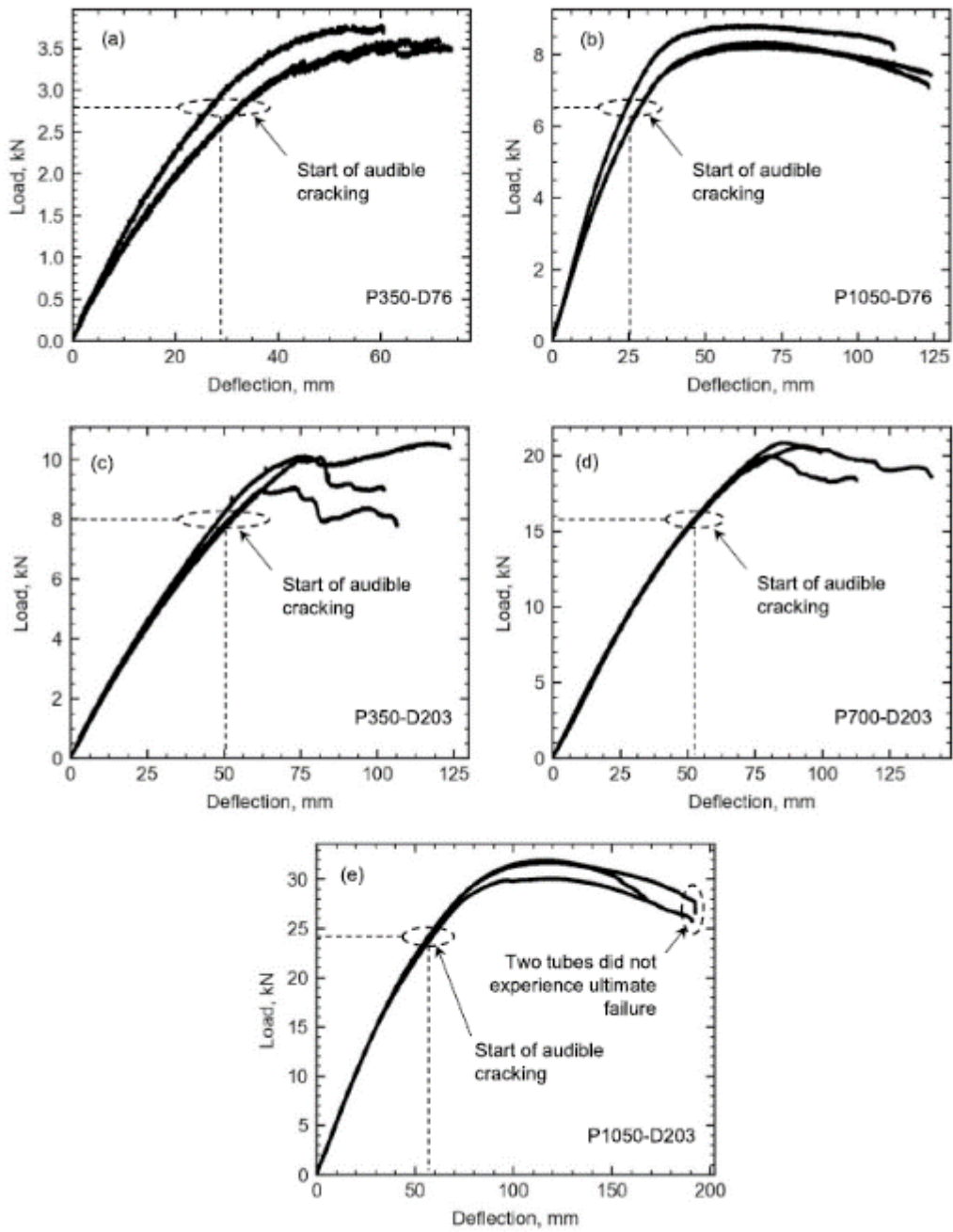


Figure 2-8. Load-Deflection behavior of test specimens: (a) P350-D76; (b) P1050-D76; (c) P350-D203; (d) P700-D203; (e) P1050-D203 (Betts et al. 2020)

2.3 BEHAVIOR OF CFFT

2.3.1 Behavior of short-span CFFT under lateral load

Burgueño and Bhide (2006) studied the shear behavior of concrete-filled carbon/epoxy fiber-reinforced polymer composite cylindrical shells and developed a shear responsive analytical model. To develop their analytical model, they considered five significant factors, shear stress distribution, FRP shell behavior, concrete core behavior, FRP and concrete system behavior, and finally, shear force transfer across cracks. According to older studies, for the stress distribution, major assumptions were considered that the line of action of all shear stresses at a given horizontal level acts directional towards a single point and that their vertical component was equal for all points along the chord line (Timoshenko and Gere 1972) and, shear stresses at the boundary must be tangential (Love 1944). With these assumptions in place, they used the generalized shear stress formula to obtain the true shear stress component in the vertical direction for the cross-section of the elastic isotropic material, which showed a 5% error, compared to the elastic theory solution. Furthermore, though the obtained results from the generalized formula satisfied the equilibrium criteria, they failed to satisfy the compatibility condition between the concrete core and FRP shell. Hence another assumption was considered to satisfy the compatibility condition between the concrete core and FRP shell. The existence of tangential shear strain at the direct proportion to the tangential shear stress at the boundary and they developed a relation for the true shear strains of the general elastic isotropic beam based on true shear stress, material shear modulus, and a defined angle between the vertical line of the section symmetry and the line from the common point of the stress intersection to the location of the interest at a certain section level.

Table 2-3. FRP Laminate Architecture (Burgueño and Bhide 2006)

Test unit	Layup	Thickness [mm (in.)]
LS-1	$[90, \pm 10_2, 90, \pm 10_2, 90]_s$	10 (0.38)
LS-2	$[90_2, \pm 10_2, 90_2, \pm 10_2, 90_2, \pm 10, 90_2, \pm 10, 90_3]$	9 (0.35)
SS-1	$[90, \pm 10, \pm 10, 90]$	2.54 (0.1)
SS-2	$[90, \pm 10, \pm 10, 90]_s$	5.08 (0.2)

Note: 10° ply=0.5 mm (0.02 in.), 90° ply=0.25 mm (0.01 in.)

For modeling the FRP cylindrical shell, they considered that the thickness of the FRP shell was smaller compared to the section. Hence, they ignored the strain gradient through the wall thickness and in-plane axial-shear coupling. This consideration made the FRP material an orthotropic laminate, and the in-plane coupling coefficients were taken as zero. As for the concrete core behavior, they modeled it based on the isotropic elastic cylinder with a varying modulus of elasticity, and the nonlinear compression behavior of the concrete was considered for the active confinement effect. They assumed that the CFFT follows Bernoulli's hypothesis, and full compositeness between the FRP shell and concrete core was considered. These assumptions established strain compatibility with longitudinal, radial, and shear strains in the FRP shell and concrete. Under compressive stresses, the FRP tube acted as a thin shell. The confinement effect of the FRP tube on the concrete was considered similar to that of a pressure vessel. Furthermore, under normal tensile stress, concrete restrains the shrinking of the FRP shell due to its Poisson ratio. With the help of modified compression field theory, the shear force transfer across the cracks was implemented. The section was regarded as a sandwich element with FRP laminates as face sheets and concrete core as an internal element, and it was subjected to in-plane stresses. The verification of the shear capacity of the concrete core was determined from its ability to transfer forces across the cracks. The crack direction was considered perpendicular to the principal strain direction.

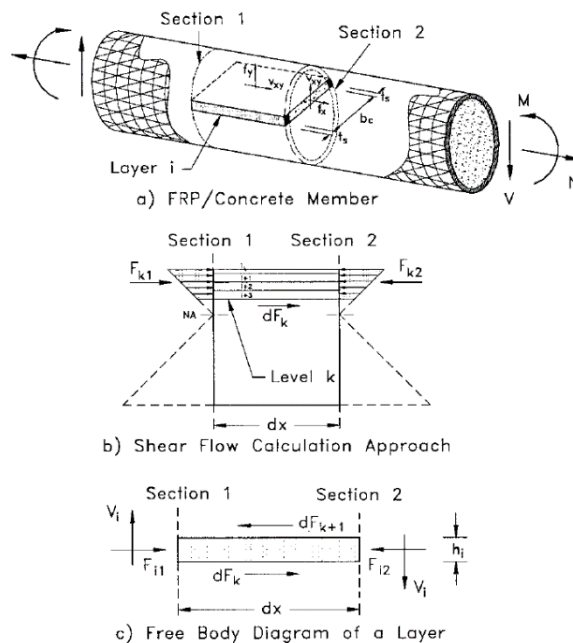


Figure 2-9. Shear stresses in CFFT (Burgueño and Bhide 2006)

They followed the analytical procedure to analyze the shear load-deformation response of FRP and concrete members, considering the extreme conditions of full composite and non-composite behavior. Also, considering that the different materials acted as a composite system, the equilibrium conditions (shear, moment, and axial load) and compatibility condition (plane section remains plane in the presence of full composite action between FRP and concrete) were satisfied. An iterative process was adopted to determine forces and stresses in each layer for both concrete and FRP shell. This process continued until the first fiber failure was encountered under the Tsai-Hill failure criterion. As Tsai-Hill quadratic failure criteria cannot accurately determine the shear failure, they considered the limit state method. The limit state method understands that when the term associated with shear was greater than 50% of the quadratic stress combination in the first ply failure equation, shear failure governs. The CFFT system behaved as a full composite system, with no shear interaction between FRP shell and concrete core. Once the shear capacity of the concrete core was exceeded, the additional shear force was then carried by the FRP shell, and it behaved as a thin elastic pipe. Though the FRP shell tried to buckle due to the additional shear force, it was resisted by the inner concrete core.

Table 2-4. Carbon/Epoxy Ply Properties (Burgueño and Bhide 2006)

Properties	Values
E_{11}	120.7 GPa (17.5 Msi)
E_{22}	6.89 GPa (1.0 Msi)
G_{12}	4.83 GPa (0.7 Msi)
ν_{12}	0.3

Note: Msi=million pounds per square inch.

Table 2-5. Equivalent Orthotropic Plate Properties (Burgueño and Bhide 2006)

Test unit	E_L GPa (ksi)	E_T GPa (ksi)	G_{LT} GPa (ksi)	ν_{LT}
LS-1	97.2(14,100)	25.1(3,700)	7.4(1,100)	0.18
LS-2	80.7(11,700)	42.9(6,200)	6.9(1,000)	0.10
SS-1, SS-2	101 (14,700)	19.8(2,870)	7.5(1,090)	0.24

They carried out four-point bending tests on large-scale and small-scale samples to understand and compare concrete-filled carbon/epoxy FRP cylindrical shells' flexural and shear behavior. Around the specimen's circumference, eight and six strain rosettes were applied to acquire the shear strain rate for the large and small-scale specimens, respectively. As the cracking in the concrete developed for the large-scale specimens, the shear strain profile showed the stress concentration in concrete at the compression zone and increment in the stress in the FRP shell at the tension zone. Though the observed shear stress in the concrete was negligible compared to the stress concentration in the FRP shell, the concrete core carried a significant amount of the vertical shear force (53%) due to its larger area. The small-scale test specimens showed a similar trend compared to the analytical results, but as the cracking in the concrete progressed, it showed a significant amount of deviation from the analytical results. This variation was due to the partial to non-composite behavior of the CFFT system. This partial to non-composite behavior was assumed due to the slip between the concrete core and FRP shell. The experimental and analytical also concurred that the principal strain angle at the mid-section started approximately at 45° and dropped sharply after the crack progress in the concrete core. The sharp decline in the principal strain angle was increased towards a stabilized level during the later stage of the loading history.

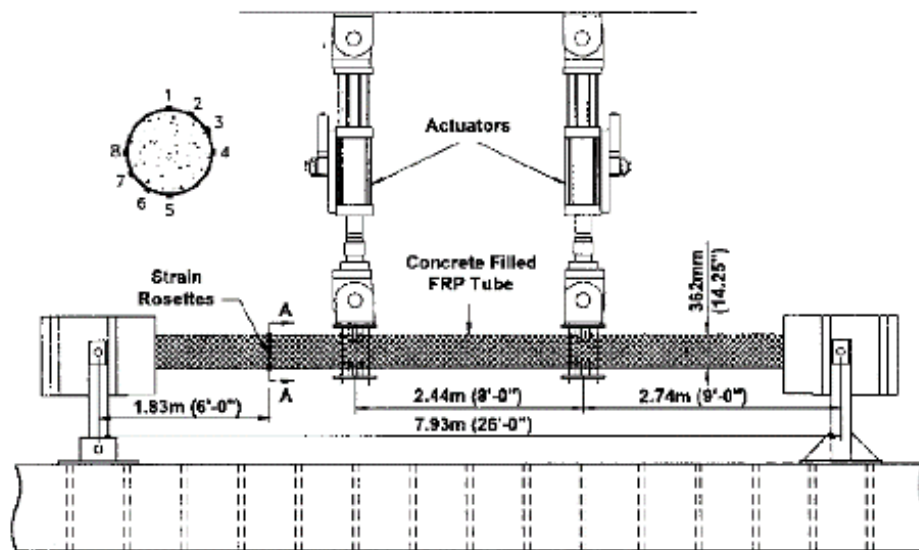


Figure 2-10. Four-point bending test set-up for large scale specimens
(Burgueño and Bhide 2006)

Finally, they justified the use of a composite and non-composite behavior, particularly for the small-scale CFFT specimens. The concrete core was influential to both the shear strength and stiffness of the CFFT specimens. The behavior was also significantly influenced by the bond between the concrete core and FRP shell and the design of the FRP laminate. One of the limitations of this analytical procedure was the assumption of compatibility rule for the composite system, which cannot determine the local effect from the concentrated load and reaction. Another prominent limitation was the low shear span to depth ratio of the CFFT specimens', which was critical in determining the shear strength.

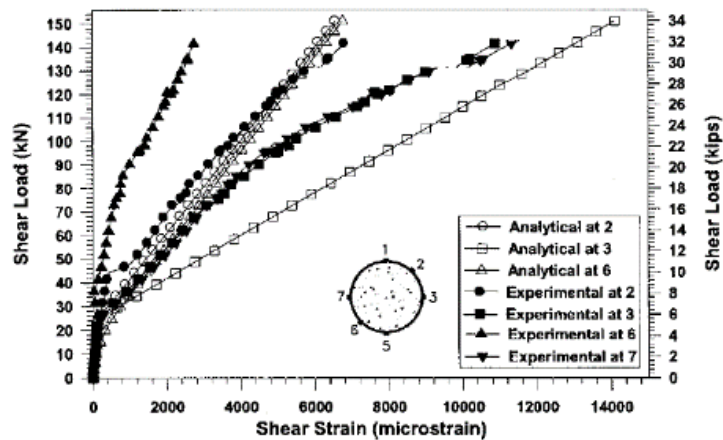


Figure 2-11. Analytical and experimental comparison between shear load vs shear strain for SS-2 specimen (Burgueño and Bhide 2006)

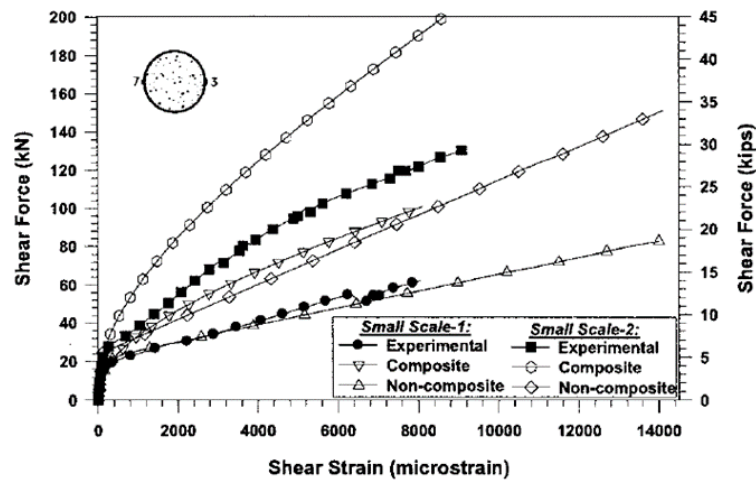


Figure 2-12. Analytical and experimental comparison between influence of composite action (Burgueño and Bhide 2006)

In their studies, Fam and Cole (2007) investigated and compared the shear capacity and behavior of CFFTs reinforced with steel, GFRP, and CFRP rebars in different shear spans. For their studies, they have considered a total of seven sets of specimens which can be further subdivided based on their critical span to depth ratio (a/D) and the internal reinforcement types and sizes, out of seven sets, two sets of specimens whose formwork was prepared with the help of cardboard tubes. These two sets were considered as control specimens. These two sets of specimens, one of which was internally reinforced longitudinal steel rebars without any confinement or lateral reinforcement, and another type was laterally reinforced with steel spirals. The CFFT specimens were divided into two categories for testing based on two different shear spans, 440 mm and 880 mm, with 30 mm and 260 mm overhangs on both sides, respectively. These specimens were tested under three-point bending. The outer diameter of the control specimens was 203 mm. The remaining five sets of CFFT test specimens were confined with GFRP tubes having a diameter of 219 mm. These specimens were internally reinforced with longitudinal steel, GFRP, and CFRP rebars, respectively. Their study used the GFRP tubes, which were prepared with eight layers of asymmetric ($+5^\circ/-88^\circ$) laminate E-glass epoxy composite. The laminate had fiber oriented at 5° and 2° towards the longitudinal and hoop direction with a ratio of 1:2, respectively.

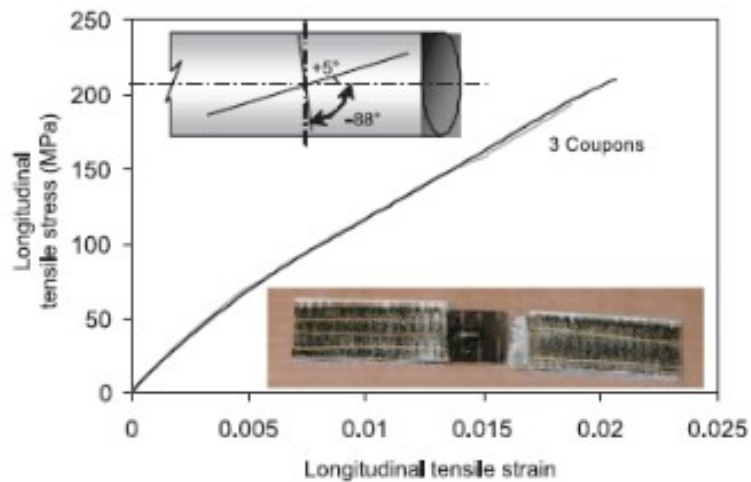
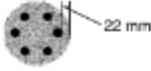



Figure 2-13. Stress-strain curve for GFRP tube (Fam and Cole 2007)

Table 2-6. Test Matrix for beam shear specimens (Fam and Cole 2007)


Specimen No.	a/D ratio ^a	Layout ^b	Confinement type	Outer diameter (mm)	Rebar type	Rebar cross-sectional area (mm ²)	Rebar reinforcement ratio (%)
B1-a	1:1	A	None	203	Steel	1200 (6 No. 15M)	3.7
B1-b	2:1						
B2-a	1:1	B	Steel spiral	203	Steel	1200 (six 6 No. 15M)	3.7
B2-b	2:1						
B3-a	1:1	C	GFRP tube	219	Steel	1200 (6 No. 15M)	3.2
B3-b	2:1						
B4-a	1:1	C	GFRP tube	219	Steel	600 (6 No. 10M)	1.6
B4-b	2:1						
B5-a	1:1	C	GFRP tube	219	GFRP	1200 (6 No. 5/8 in.)	3.2
B5-b	2:1						
B6-a	1:1	C	GFRP tube	219	GFRP	426 (6 No. 3/8 in.)	1.1
B6-b	2:1						
B7-a	1:1	C	GFRP tube	219	CFRP	426 (6 No. 3/8 in.)	1.1
B7-b	2:1						



22 mm



22 mm
Steel Spiral



30 mm
GFRP tube

^aShear span to depth ratio.

^bA, graphic 1; B, graphic 2; C, graphic 3.

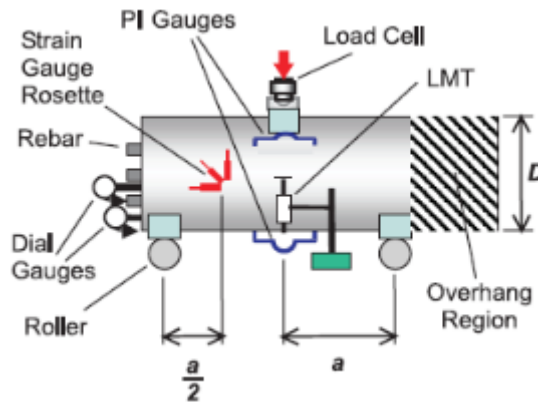


Figure 2-14. Test set-up and instrumentation (Fam and Cole 2007)

All specimens with a shear span to depth (a/D) ratio of 1 predominantly failed in shear. Apart from the specimens reinforced with CFRP rebar, all specimens with an a/D ratio of 2 failed due to flexure. In contrast, the specimens reinforced with CFRP rebar failed in shear. From this test and results, they concluded that the shear span to depth ratio was a critical factor in the failure of CFFT specimens, and the critical shear span to depth ratio for specimens reinforced with longitudinal steel and GFRP rebar lie between 1 and 2. Whereas, for the specimens reinforced with CFRP rebar, the critical a/D ratio belongs to a slightly higher range than 2.

From their test results, it can be clearly observed that the control specimens with an a/D of 1, which was reinforced with the steel rebars and confined with steel spirals, increased the shear strength by 66% and made the specimens more ductile compared to specimens without any confinements. From the results, the effect of GFRP tubes was also observed notably when subjected to shear. The CFFT specimens' shear capacity was 70% and 183% higher when compared to the control specimens with spirally confined and uncaged specimens, respectively. The introduction of internal longitudinal reinforcement and their types also showed their effect on load-carrying capacity. The results highlighted that, though the dimensional properties of both carbon and glass FRP rebars and steel rebars were similar, the capacity of the steel-reinforced CFFTs was significantly higher than that of both CFRP and GFRP reinforced CFFTs irrespective of their critical span to depth ratio. This considerable decrease in the load-carrying capacity in the specimens was due to the lower dowel resistance offered by both GFRP and CFRP rebars. As a result, the ultimate moment carrying capacity of both the CFRP and GFRP reinforced CFFTs was drastically reduced compared to steel rebar reinforced CFFTs. The CFFT specimens reinforced with a similar type of internal reinforcement showed a significant increase in shear capacity for specimens reinforced with a higher internal reinforcement ratio. No mechanical anchorage was provided for the rebars at the end of the specimens to make the testing parameters more similar to the field condition. The absence of the end anchorage caused a considerable amount of slip between longitudinal rebars-concrete core, and concrete core-GFRP tubes. Due to the lack of compositeness between the rebars and the concrete core, bond-slip cracks were developed before the development of any shear failure. Furthermore, slip between the concrete core and the GFRP tubes coincided with the slip between rebar and concrete core substantially reduced the stiffness of the specimens.

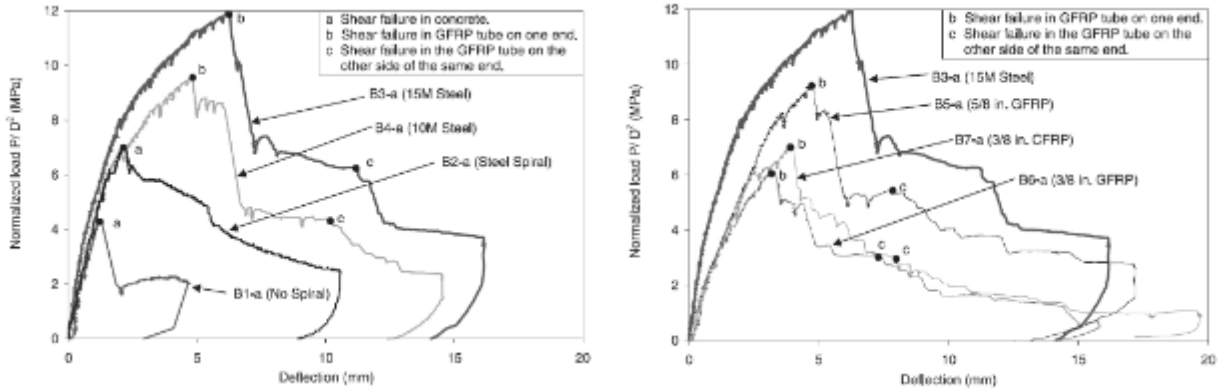


Figure 2-15. Load-deflection behavior for specimens of $a/D = 1$ (Fam and Cole 2007)

A simplified strut-tie model was developed to predict and compare the shear capacity for the specimens with an a/D ratio of 1 as part of their analytical study. Based on assumptions and equilibrium at midspan, a reasonable starting point of the total internal compressive and tensile forces was considered at a distance of 0.4 and 0.35 of the depth from the center of the CFFT specimens. The direction of the diagonal tension tie was considered as 48° based on the results of the direction of the principal strains. In the absence of the experimental results regarding principal strain, their study recommended that the direction of the diagonal tension tie can be assumed as 45° . Based on classical laminate theory (CLT)- ultimate laminate failure, and the direction of the diagonal tension tie as 48° , the in-plane strength of the GFRP laminate was considered as 112 MPa. Their strut-tie model also considered the dowel action of the internal rebar system in the shear resistance. The bottom layered tension rebars had the most contribution in the shear resistance than the other rebars. The comparison between the simplified strut-tie model prediction and the experimental results showed promise as the variation in the results was considerable, with the maximum observed error for the GFRP rebar reinforced CFFT specimens not exceeding 25%.

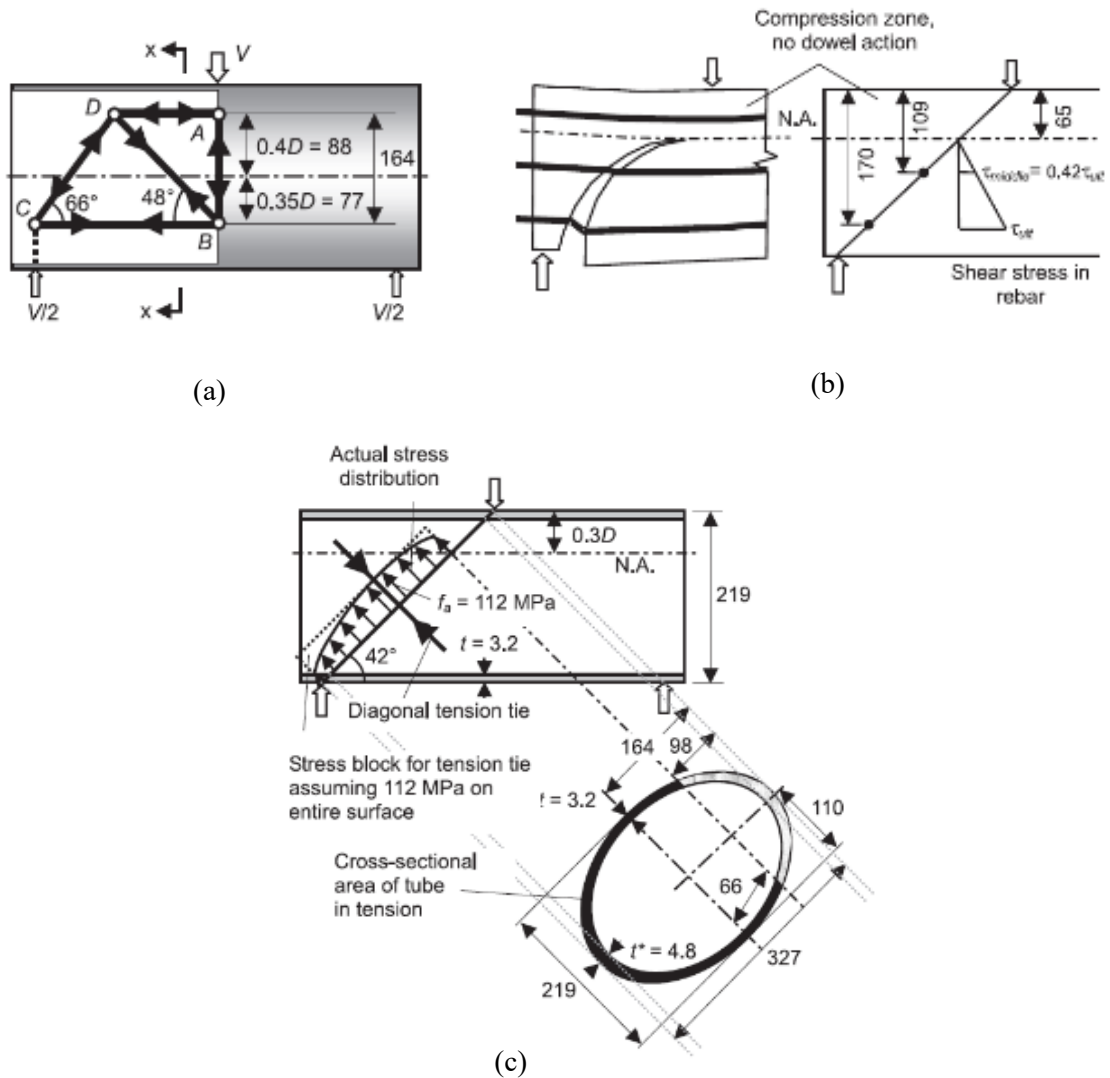


Figure 2-16. Analytical model: (a) Strut-and-tie model; (b) Mechanism of dowel action; (c) Diagonal tension field in the tube (Fam and Cole 2007)

Fam et al. (2007) examined and compared the effect of GFRP tubes as an alternative to the steel spiral confinement in the concrete members. The effect and contribution of GFRP tubes in the test specimens were compared based on shear and flexural tests. In their study, two types of filament-wound E-glass/epoxy GFRP tubes were used. Type-I and type-II tubes were made out of nine FRP layers of [88/8/88/8/88/8/88/8/88] and eight layers of [88/5/88/88/5/88/5/88] stacking sequence with respect to the longitudinal axis, respectively. In the case of type-I tubes, the average thickness of layer [88] and [8] were

0.37 mm and 0.8 mm, respectively. Whereas for the type-II GFRP tubes, the average thickness of the layer [88] and [5] were 0.43 mm and 0.35 mm, respectively. Total six test specimens were prepared in which three control test specimens were prepared with steel spiral as transverse reinforcement to compare the contribution of the GFRP tubes. Type-I tubes were used to prepare prestressed beams and were tested under flexure. Conventional beams with type-II GFRP tubes as confinement and internally reinforced with six longitudinal steel rebars were prepared and tested under both shear and flexure. Dimensional dissimilarity in the specimen diameters did not significantly impact the results as the normalized moments, strengths, and deflections were considered.

Table 2-7. Details of Specimens and Summary of Test Results (Fam et al. 2007)

Beam ID	X-section	Test type	Transverse Reinforc.	Longitudinal Reinforc.	Diam. D (mm)	Span (m)	Reinforce-ment index	f'_c (MPa)	M_u (kN.m)	V_u (kN)	$\frac{M_u}{D^2 f'_c}$	$\frac{V_u}{D^2 f'_c}$	% age increase
B1		Flexure	Spiral	8 -13 mm 7-wire strands	285	3.6	0.54	45	88	-	0.084	-	
B2			Type I tube		324	3.6	1.00	42	257	-	0.179	-	113 %
B3		Flexure	Spiral		203	2.2	0.65	39	36	-	0.108	-	
B4			Type II tube		219	2.2	0.9	39	61	-	0.148	-	37 %
B5		Shear	Spiral	6 - 15M rebar	203	0.41	0.65	39	-	147	-	0.091	
B6			Type II tube		219	0.44	0.9	39	-	289	-	0.154	69 %

Out of six test specimens, four specimens were tested under flexure with a four-point bending arrangement. The shear span to depth ratio for the flexural specimens was in the range of 4.1 to 5.4. Both precast control and type-I GFRP tube specimens were prepared with the pre-tensioning process, where both of internally reinforced with eight number of 13 mm, seven-wire strands. These two specimens had a span of 3.6 m, and the load was applied over the whole span with a 0.5 m spreader. The experimental results showed that the contribution of the GFRP tube was noteworthy as the flexural strength had an increase of 113% for the GFRP tube confined specimen. They concluded that the contribution in the increase in strengthening was mainly due to two reasons, primarily the fiber orientation in the longitudinal direction type-I GFRP tube, which positively influenced the reinforcement effect in the specimen. Secondly, the large cross-sectional area of the concrete core confined by the GFRP tube also played an essential part in the strength enhancement.

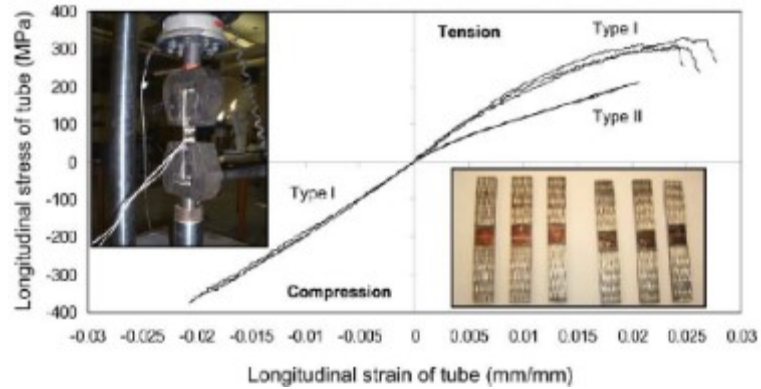


Figure 2-17. Stress-strain curves of GFRP tubes in longitudinal direction (Fam et al. 2007)

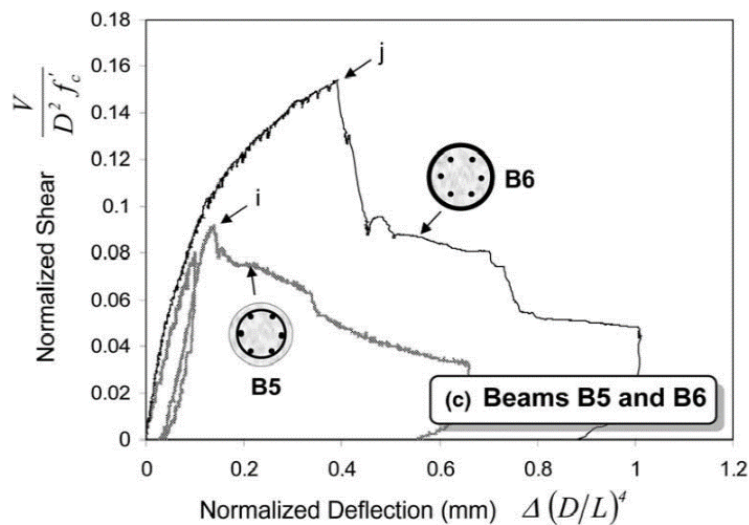


Figure 2-18. Normalized shear versus deflection of test beam B5 and B6 (Fam et al. 2007)

Another set of flexural specimens consisted of a control specimen, and the type-II GFRP tube specimen was internally reinforced with six number of 15M steel rebars. The span of these two specimens was 2.2 m, and the load was applied over the whole span with a 0.4 m spreader. From the experimental results, it was observed a similar trait as the precast specimens. The specimen confined with the GFRP tube had a 37% increase in flexural strength compared to the control specimen. The flexural strength increment was not as high as the prestressed specimen, but the reason behind the strength increase was similar to the prestressed specimens. The difference in the strength enhancement for type-I GFRP (113%) and type-II GFRP (37%) specimens was mainly due to differences in the internal reinforcement types, overall reinforcement ratios, and GFRP ply stacking.

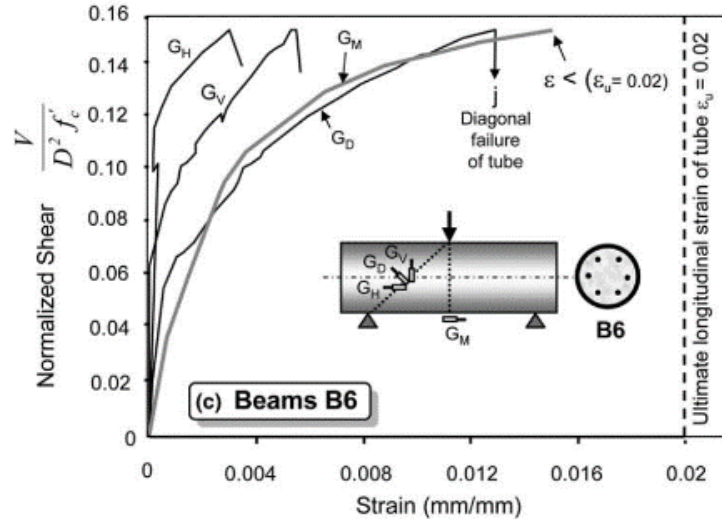


Figure 2-19. Normalized shear versus strain of test beam B6 (Fam et al. 2007)

Finally, after comparing the result of four flexural test specimens, they established that apart from the contribution of GFRP tubes, prestressing increased the confinement of the concrete. In addition to the longitudinal compressive stresses, the prestressing helped develop hoop tensile stresses in the type-I GFRP test specimens. Though this hoop stress development had a positive effect on the strength of the specimen, it weakened the tube. As a result, the specimen failed by crushing at the longitudinal direction and fracturing in the hoop direction before reaching its ultimate longitudinal compressive strain of -0.02. In the type-II GFRP beam specimens, the longitudinal compressive strain reached -0.02, which was substantially higher than its prestressed counterpart. With the higher strain value, it was also evident that the failure of the reinforced specimen was very similar to the prestressed specimen.

Furthermore, the type-II GFRP specimens failed in a sequential progressive manner which indicated pseudo ductile behavior. In the beginning, the tube was ruptured in the tension side but still withstood the load increment due to the intact compression side and steel rebars. The specimen was then crushed in the compression side longitudinally, followed by tube rupture in the hoop direction.

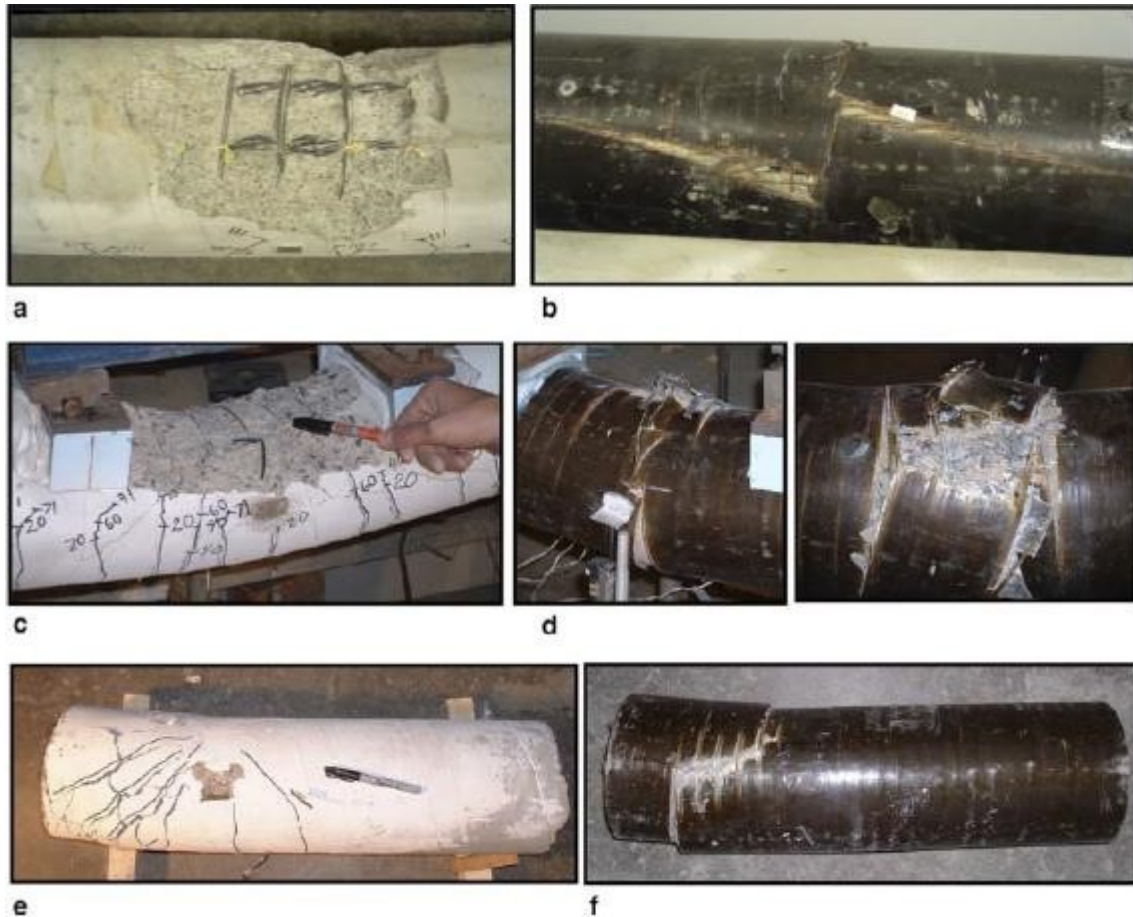


Figure 2-20. Different failure modes: (a) Beam B1, crushing and spalling of concrete cover; (b) Beam B2, failure of GFRP tubes under bi-axial stresses on compression side; (c) Beam B3, crushing and spalling of concrete cover; (d) Beam B4, GFRP tube failed in longitudinal tension, then in longitudinal compression, followed by hoop tension; (e) Beam B5, shear-bond failure; (f) Beam B6, shear-bond failure (Fam et al. 2007)

Two three-point bending tests with a shear span to depth ratio of 1 were carried out on control and type-II GFRP specimens to understand the effect of shear behavior. The specimen spans were 0.41 m and 0.44 m for the control and type-II GFRP specimen, respectively. The varying dimensional properties of both the specimen was introduced to equate the stiffness properties of the specimens. The specimens were internally reinforced with six 15M steel rebars. The control and GFRP tube specimen were failed due to bond-shear failure through diagonal tension cracking. The type-II GFRP confined specimen showed an increase of 69% in its shear strength compared to the controlled counterpart.

When a comparison of longitudinal tensile strain between flexural and shear type-II GFRP specimens was drawn, it was observed that the specimen tested under lower shear span to depth ratio only attained 0.015 longitudinal strain at midspan, which was lower compared to the ultimate tensile strain of the GFRP tube. Furthermore, this increase in shear strength indicated that the GFRP tube successfully confined the internal concrete core and resisted diagonal tension cracking to a certain extent.

Recently, Ahmad et al. (2008) studied the flexural and shear behavior of slender, short, and deep beams made of concrete-filled fiber-reinforced polymer tubes. In this study, four different types of FRP tubes were used based on fiber orientation. The tubes were designated as type I, II, III, and IV, and had fiber orientations of $[\pm 55^\circ]$ (17 layers), $[0^\circ/0^\circ/+45^\circ/-45^\circ]_{15}$ (60 layers), $[\pm 34^\circ + 80^\circ \pm 34^\circ]$ (5 layers), and $[\{-88^\circ + 3^\circ - 88^\circ\}_2 \{+3^\circ\}_1 \{-88^\circ + 3^\circ - 88^\circ\}_1]$ (10 layers), respectively. These four types of tubes were used to prepare ten short, deep, and slender beam specimens were prepared. The deep beams had a critical shear span to depth ratio of 0.9 and 1. The adopted shear span to depth ratio for short beams was 1.93, 2, and 2.04. In contrast, slender beams had a shear span to depth ratio of 6.14 and 6.25. The specimens had a diameter to thickness ratio ranged from 16 to 63, and the adopted range of reinforcement index was 0.11 to 2.2. The flexural and shear behavior and failure patterns were compared based on the specimen shear span to depth ratio, diameter to thickness ratio, and reinforcement index. The three-point bending test method was adopted for testing the deep beams. Short and slender beams were tested under four-point bending.

Table 2-8. Properties of FRP Tubes Used in CFFT Beam Tests (Ahmad et al. 2008)

Tube Type (designated color)	Fiber lay-up	Number of layers	FRP fiber volume fraction (%)	Tensile strength (MPa)	Tensile modulus (GPa)	Compressive strength (MPa)	Compressive modulus (GPa)	Hoop strength (MPa)	Hoop modulus (GPa)
I (Yellow)	$[\pm 55^\circ]$	17	75.5	71	12.5	229.6	8.69	234.5	N/A
II (White)	$[0^\circ/0^\circ/+45^\circ/-45^\circ]_{15}$	60	51.2	399.5	15.5	384.7	23.3	N/A	N/A
III ^a (Grey)	$[\pm 34^\circ + 80^\circ \pm 34^\circ]$	5	51	178	14.7	238 ^b	N/A	131 ^b	9.0 ^b
IV ^a (Red)	$[\{-88^\circ + 3^\circ - 88^\circ\}_2 \{+3^\circ\}_1 \{-88^\circ + 3^\circ - 88^\circ\}_1]$	10	51	237	17.6	343	N/A	402 ^b	19.7

^aCoupon testing done by Fam and Rizkalla (2002).

^bPredicted by the classical laminate theory.

Table 2-9. Test Matrix of CFFT Beams (Ahmad et al. 2008)

Tube type	Beam No.	Tube outside diameter D_o (mm)	Tube thickness t_f (mm)	D_o/t_f	Reinforcement ratio ρ (%)	Reinforcement index ω	Span length l (mm)	Type of bending test	a/D_0	Concrete compressive strength f'_c (MPa)	Beam type
I	S-1	322	5.1	63.1	6.3	0.11	579	three point	0.9	40.7	Deep
	S-2	168.6	3.43	49.2	8.1	0.14	338	three point	1.0	40.7	Deep
	S-3 ^a	368.8	6.6	55.9	7.2	0.22	2,286	four point	1.93	23.4	Short
	S-4	322	5.1	63.1	6.3	0.15	1,829	four point	2.0	31.0	Short
II	S-5	305	19.0	16.1	24.8	1.97	610	three point	1.0	50.3	Deep
	S-6 ^a	347.7	13.9	25.0	16.0	2.20	2,286	four point	2.04	29	Short
III	S-7	319	7.1	44.9	8.9	0.24	640	three point	1.0	66.9	Deep
	S-8 ^a	319	7.1	44.9	8.9	0.24	5,500	four point	6.25	66.9	Slender
IV	S-9	326	7.20	45.3	8.8	0.51	653	three point	1.0	40.7	Deep
	S-10 ^a	326	7.20	45.3	8.8	0.35	5,500	four point	6.14	60	Slender

^aBeams S-3 and S-6 from Mirmiran et al. (2000), and Beams S-8 and S-10 from Fam and Rizkalla (2002).

The results showed that the typical load-deflection behavior of the deep specimens was linear until the first flexural cracking. As soon as the beam underwent the first failure crack, the significant amount of stiffness reduction in the beam and the increase in the slip between the concrete core and the FRP tubes were noticed, which altered the linear load-deflection behavior to a nonlinear one. The variation in the fiber lamination and orientation was a significant contributor towards the level of nonlinearity. It was also concluded that the beams with fiber orientations along the longitudinal axis showed a lesser degree of nonlinearity. In general, the separation between the concrete core and the FRP tube was observed in specimens at 25% of its ultimate capacity. Test specimens with a higher diameter to thickness ratio experienced concrete core bulge out from the FRP tube at 80% of their ultimate strength. More specifically, a necking phenomenon at the bottom midspan section close to its ultimate capacity affected the type-I specimen with the highest diameter to thickness ratio. This phenomenon occurred due to the Poisson's effect in the FRP tube with $\pm 55^\circ$ fiber orientation. The tube rupture in the extreme tension fiber failed the tested specimens, which was a typical flexural failure.

From the tested specimens' failure pattern, it was clear that the test specimens predominantly failed in flexure. The crack patterns in the inner concrete core were studied by removing the tube. The specimens with low reinforcement indices (0.11 to 0.51) typically failed by rupture by developing of two dominant flexural cracks. These flexural cracks developed under the load point. In contrast, the test specimens with high reinforcement index showed flexural cracks, web shear, and flexural-shear cracks due to the formation of compression struts which allowed direct shear transfer to the support and progressive cracks in both tube matrix and inner concrete core. Though wide flexural

cracks were the prime reason for the specimen failure, the development of the shear cracks and their patterns in the tested specimen proved the significance of the reinforcement index factor in the CFFTs.

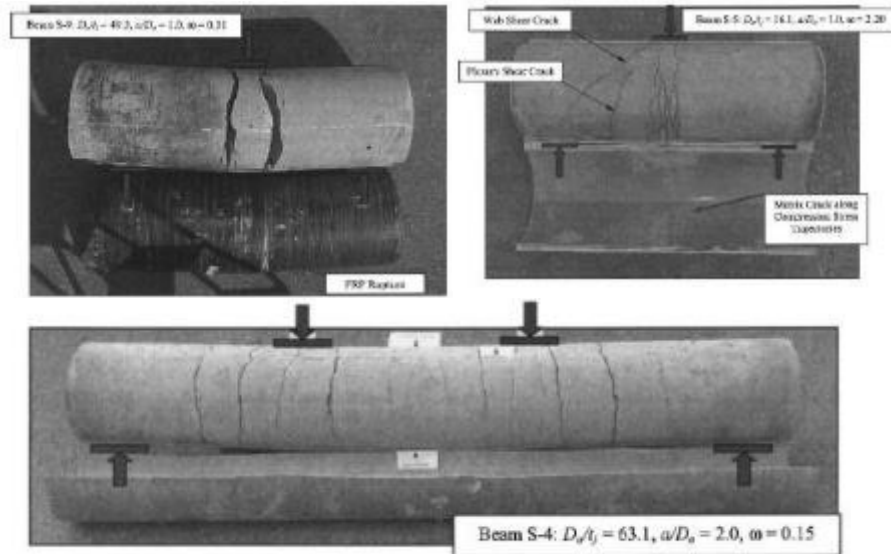


Figure 2-21. Various crack patterns in different CFFT specimens (Ahmad et al. 2008)

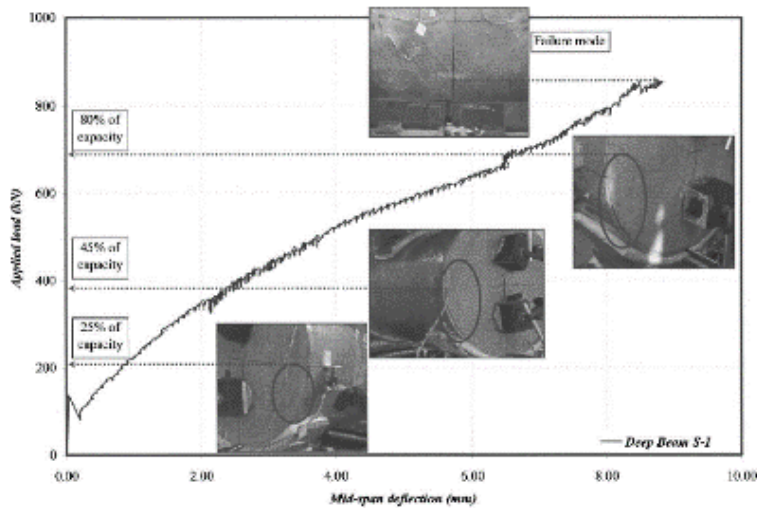


Figure 2-22. Typical load-deflection response of deep CFFT beams (Ahmad et al. 2008)

For similar CFFTs, comparisons in the tested specimens were drawn based on the effect of different shear span to depth ratios. It was explicitly observed that the deep beams developed the flexural crack under the load point, in contrast to the slender beams, where flexural cracks were distributed along the entire span of the specimen. The diagonal tension strain caused due to shear was evaluated at the midheight of the beam in the middle shear span with the help of a strain rosette. The flexural tensile strains were recorded in the mid-shear span and at the bottom midspan of the beam. This study observed that the flexural tensile and diagonal shear strains were nearly equal prior to the first crack. However, as soon as the specimen suffered the first flexural crack, the flexural strain at the midspan became significantly higher than the diagonal shear strain with its critical position. Also, the deep beams were more susceptible to premature failure than the short beams with similar material properties. These collective factors concluded that the CFFTs were predominantly affected by flexural failure rather than shear failure, where the critical shear span to depth ratios played an important role. The study also concluded that as the shear span to depth ratio decreases and the reinforcement index factor increases, the probability of the CFFTs undergoing shear failure gets higher.

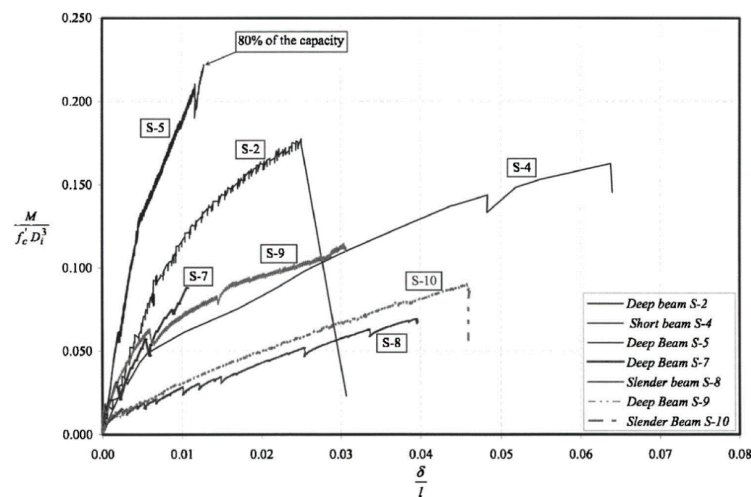


Figure 2-23. Comparison of load-deflection response of deep, short, and slender CFFT beams (Ahmad et al. 2008)

Finally, the slip between the concrete core and FRP tubes was also a prominent factor in understanding the flexural and shear behavior of CFFTs. The slip between the concrete core and the FRP tubes occurred due to a lack of compositeness and was observed just

after the beam experienced its first flexural crack. The amount of slip in the deep, short, and slender beams was observed to understand the specimens' failure modes and load capacity. The results were then compared to the theoretical models. This observation contradicted Bernoulli's beam theory for the deep beams, which supports that the bending capacity of the deep beam ($a/D \leq 1$) should not be greater than its slender counterparts. However, the results confirmed that the deep beams failed at a higher flexural capacity in contrast to their slender counterpart. The increase in the deep beams' flexural capacity was mainly due to the direct diagonal compression struts, which developed in the concrete core through the arching action. This revelation supported and confirmed that the strut-tie model was a far more convincing method to predict the load capacity and induced stress level for the CFFTs.

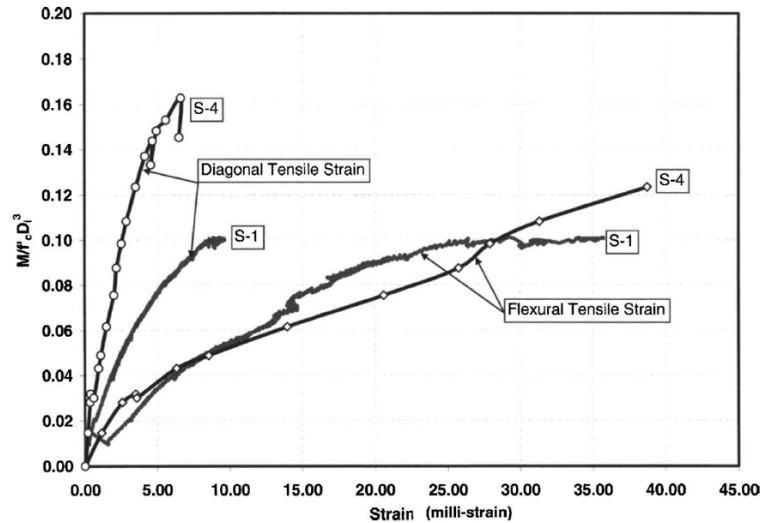


Figure 2-24. Effect of a/D ratio on diagonal tension and flexural strains
(Ahmad et al. 2008)

2.3.2 Behavior of Long-span CFFT under lateral load

Cole and Fam (2006) studied the flexural performance of seven beam specimens under flexural loading. Out of the total seven beam specimens, two controlled beam specimens, without GFRP tubes and internally reinforced with steel rebars, the rest of the five beam specimens were CFFT beams. The concrete-filled GFRP tube specimens were 2.43 m long and internally reinforced with either steel, GFRP, or CFRP rebars of various cross-sections.

The GFRP filament-wound tubes had a wall thickness of 3.2 mm and were made out of E-glass/epoxy composite with eight layers of asymmetric laminate. The laminate had a fiber orientation of 5° in longitudinal and 2° in the hoop direction. Three types of confinement configurations were used in this study, without any confinement, steel spiral and GFRP tube. Strain gauges were attached at the bottom layer rebar at mid-span and the outer surface of the GFRP tubes at the extreme compression and tension fibers. Two linear motion transducers (LMT) and dial gauges were used to record mid-span deflection and monitor any relative slippage between the GFRP tube and concrete core. The specimens had a span of 2200 mm as 60 mm wide steel channel sections were used to support the CFFT test specimens. The load was applied with a constant moment zone of 400 mm at a 2 mm/min rate. The CFFT specimens with different internal rebar were unloaded and reloaded at various stages of testing to assess the stiffness at various load levels. The results were compared with three aspects, the effect of different confining systems, conventional steel rebars against GFRP and CFRP rebars, and the overall effect of rebar reinforcement ratio.

Table 2-10. Test Matrix of Beam Specimens (Cole and Fam 2006)

Specimen number	Configuration	Confinement type	Outer diameter (mm)	Longitudinal rebar	Rebar cross-sectional area (mm ²)	Rebar reinforcement ratio (%)
B1	A	None	203	Steel	1200 (6 No. 15)	3.7
B2	B	Steel spiral	203	Steel	1200 (6 No. 15)	3.7
B3	C	GFRP tube	219	Steel	1200 (6 No. 15)	3.2
B4	C	GFRP tube	219	Steel	600 (6 No. 10)	1.6
B5	C	GFRP tube	219	GFRP	1200 (6 No. 5/8 in.)	3.2
B6	C	GFRP tube	219	GFRP	426 (6 No. 3/8 in.)	1.1
B7	C	GFRP tube	219	CFRP	426 (6 No. 3/8 in.)	1.1

All three specimens with different confinement systems, namely, no spiral, steel spiral, and GFRP tubes, started failing by yielding bottom steel rebars. The control specimen without any confining system experienced a gradual decrease in load due to crushing of concrete cover and finally failed due to buckling of the top rebar. Although the other control specimen with steel spiral experienced a similar failure pattern, the rebars were able to achieve strain hardening due to the presence of the steel spiral. Furthermore, the comparison study showed that the steel spiral successfully increased the specimen's ductility; however, the flexural strength remained unaltered. In contrast, the CFFT

specimen showed a higher stiffness and strength compared to the control specimens. In addition, the load capacity was increased by 69% compared to the specimen confined with steel spiral. The increase in ductility and load capacity was mainly due to the contribution of the GFRP tube, where the longitudinal fibers increased the flexural capacity, and the circumferential fibers helped in shear resistance and provided necessary confinement.

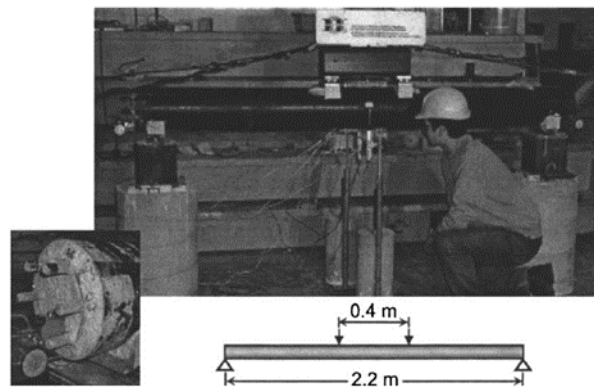


Figure 2-25. Test set-up (Cole and Fam 2006)

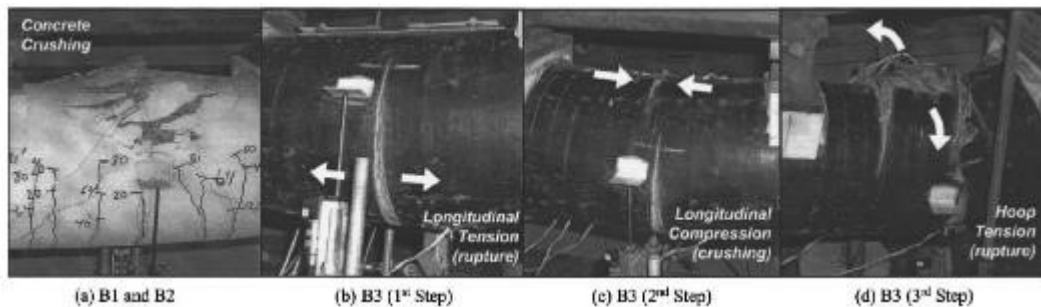


Figure 2-26. Various failure modes in beam specimens (Cole and Fam 2006)

The comparison study in the load-deflection behavior between different types of longitudinal reinforcement in CFFT showed the difference in load capacity, stiffness, ductility. Due to the similar tensile strength of GFRP and steel rebar, the difference in the load capacity between steel rebar reinforced CFFT, and GFRP rebar reinforced CFFT was similar, with 5% higher strength for the later one. In contrast, the CFRP rebar reinforced CFFT showed 43% higher strength and 32% higher stiffness when compared to the GFRP rebar reinforced CFFT. Though the study showed an increase in load capacity for the FRP rebar reinforced CFFT, the authors suggested that the increased strength and stiffness were greatly dependent on the superior properties of FRP rebars. The FRP rebar reinforced CFFTs did not exhibit any significant structural advantage over their steel reinforced

counterpart; instead, they showed disadvantages due to CFFT beams' sudden and complete failure. This sudden load drop was directly related to the failure in the FRP rebar. In comparison, the steel rebar reinforced CFFT experienced a sequential progressive failure over an extended deflection range, which offered greater ductility and sufficient warning of failure.

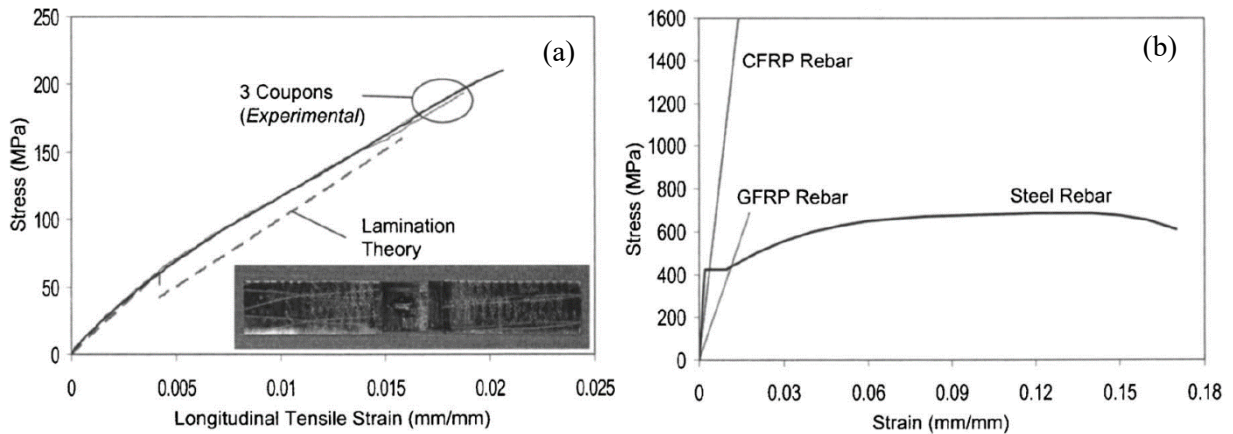


Figure 2-27. Stress strain behavior: (a) GFRP tube; (b) Internal rebars
(Cole and Fam 2006)

Additionally, the effect of the internal rebar ratio was compared in this study. The CFFT specimens of 15M and 10M steel rebars had 3.2 and 1.6% reinforcement ratios, respectively. The overall load-deflection behavior of the specimens was quite similar. However, the CFFT specimen with the lower steel reinforcement ratio showed 28% lower strength and 44% lower stiffness. The CFFT specimens reinforced with GFRP rebars had a reinforcement ratio of 3.2 and 1.1%, respectively. Like the steel-reinforced CFFTs, the higher GFRP rebar reinforced CFFT specimen exhibited 53% higher strength and 33% higher stiffness than its counterpart. This study also showed that the CFFT specimens with steel rebars failed in a sequential progressive, unlike FRP reinforced CFFT specimens.

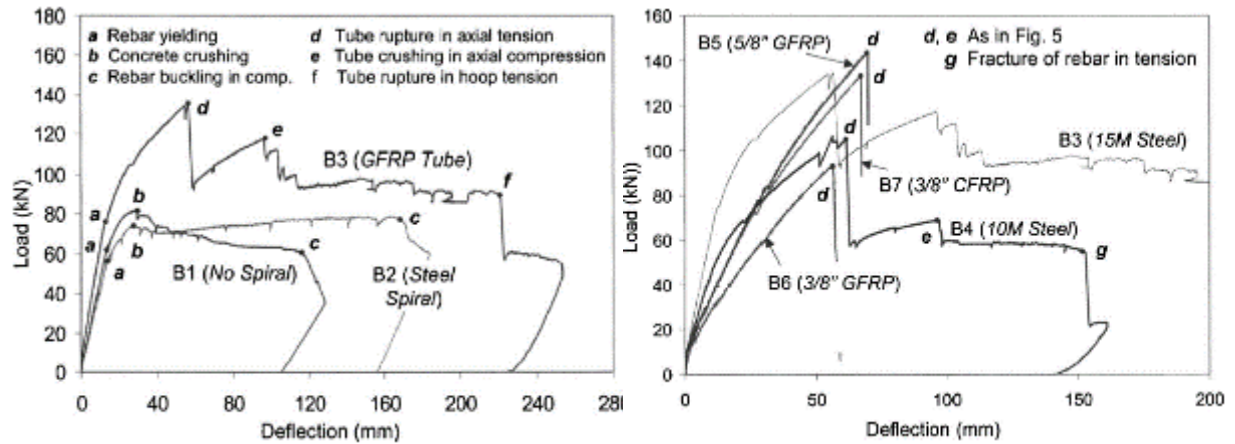


Figure 2-28. Load-deflection curves for specimens: (a) B1, B2, and B3; (b) B3-B7
(Cole and Fam 2006)

A strain compatibility/equilibrium model was developed to predict the moment-curvature relationship of CFFT members. The cross-sectional analytical model adopted a layer-by-layer approach to integrating stresses in the cross-sectional areas of concrete, rebar, and GFRP tubes by dividing them into n number strips of equal thickness. The stress-strain relationship of GFRP tubes was obtained using coupon tests and classical laminate theory (CLT-ULF). The steel reinforcement was modeled with the help of a fifth-order polynomial into three parts, a linear elastic range, followed by yield plateau, and a strain-hardening range. Both the GFRP and CFRP rebars were modeled as linear elastic until failure. Two different concrete models, namely, Popovics (1973), an unconfined concrete model with extended strain softening, and a modified version of Popovics (1973) model, a partially confined concrete model was used to model and compare the concrete in this analytic study. The analytical model was able to predict the overall behavior of reinforced CFFTs. The CFFT behavior responses improved when the partially confined concrete model was used with the FRP coupon test results.

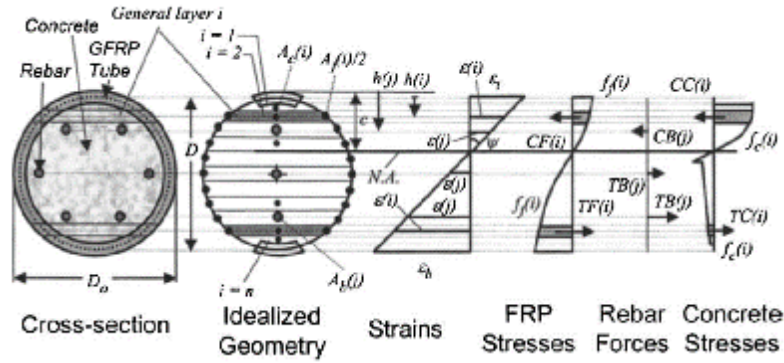


Figure 2-29. Analytical model based on strain compatibility (Cole and Fam 2006)

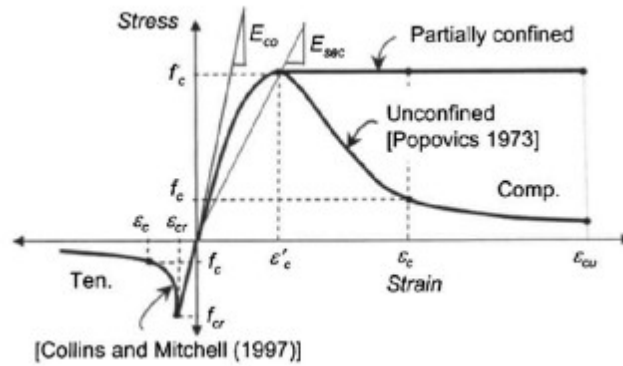


Figure 2-30. Stress-strain curves of unconfined and confined concrete (Cole and Fam 2006)

Fam et al. (2007) tested concrete filled rectangular tube beams under different moment gradients and observed the cracking patterns of the beams. Ten beams were tested under three-point bending at different shear-span to depth ratios (a/D). Out of ten test specimens, four were reinforced with steel tubes (CFT-S), six were with pultruded GFRP tubes (CFT-G). Additionally, three pultruded GFRP tubes were internally reinforced with a no. 10 steel rebar (CFT-SG). The dimension of the conventional steel tubes was 150 x 102 x 3.4 mm, and it had a nominal yield of 380 MPa and ultimate strength of 480 MPa. Whereas dimensions of the rectangular GFRP tubes were 150 x 150 x 7 mm, and it contained layers of E-glass roving (type- 366-113(4400 TEX)) sandwiched between layers of E-glass filament mats of randomly oriented continuous fiber (type M-8643). The GFRP tubes had tensile strength and moduli of 207 MPa and 17.2 MPa in the longitudinal direction and 48 MPa and 5.5 MPa in the transverse direction. The deflection at the beams' midspan was

measured using two linear potentiometers (LP), and additional LPs were used to monitor the slip between the tube and concrete core. Also, electric resistance strain gauges were used in the rosette pattern to measure the longitudinal tensile strains at the midspan.

Specimen ID	Configuration	Span (mm)	a/d	f'_c (MPa)	P_u (kN) (Exp.)	P_u (kN) (Model)
CFT-S1	150x102x3.4mm Steel tube	300	1	31	451	477
CFT-S2		600	2	31	282	238
CFT-S3		900	3	31	182	159
CFT-S4		1500	5	31	106	95
CFT-G1	150x100x7mm GFRP tube	300	1	34	92	81
CFT-G2		600	2	34	65	54
CFT-G3		900	3	34	67	56
CFT-SG1	150x100x7mm GFRP tube No.10 Steel rebar	300	1	32	142	152
CFT-SG2		600	2	32	112	90
CFT-SG3		900	3	32	96	77

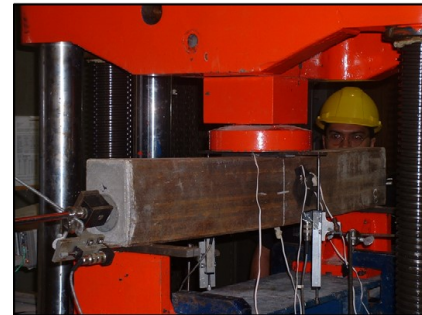
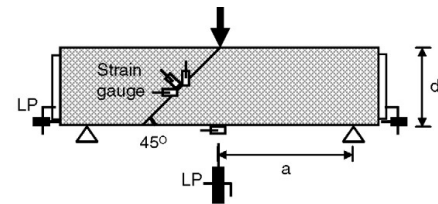
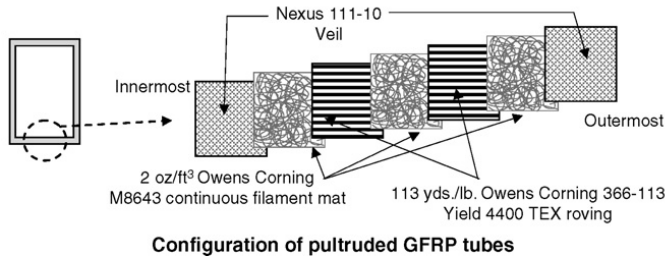
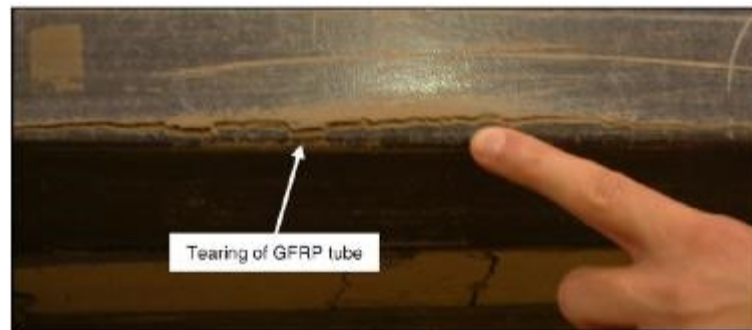


Figure 2-31. CFT test: (a) Test matrix; (b) Test setup and instrumentation
(Fam et al. 2007)

All the CFT-S test specimens were failed due to outward local buckling of the compression flange and the webs. After the yielding of the steel tube, the test beams showed plastic behavior. The reduction in the beam ductility was significant in the lower shear span to depth ratio. The maximum slip between the concrete core and the steel tube was 1 mm for the deep beams and negligible for the larger spans. This behavior explained that the composite action between the concrete core and the steel tube was adequate. For beams with an a/D ratio ranging between 1 to 3, the principal tensile strain at ultimate was less than its yield strain. The moment capacity remained remarkably stable in the specimens with an a/D ratio of 2 to 5. The significant moment capacity was reduced due to shear cracking in the specimens with an a/D ratio of 1. The cracking pattern in the concrete was observed. The deep CFT-S specimen developed a clear diagonal cracking pattern. It was

also noticed that the concrete was locally crushed in the compression zone due to confinement loss as the flange buckling took place.



(a)



(b)

Figure 2-32. Failure mode: (a) CFT-G and CFT-GS; (b) CFT-S (Fam et al. 2007)

The low elastic modulus of the GFRP tube compared to the steel tube showed a significant change in the stiffness of the beam specimens. The excessive slip between concrete core and GFRP tube was observed as high as 2 mm during the peak load, which significantly reduced the compositeness of the system. This lack of compositeness contributed to the nonlinear behavior of the tube specimens near the peak load. All the CFT-G and CFT-SG test beams failed by splitting GFRP tubes at the junction between the flange and the web. Similar to the CFT-S beams, CFT-G and CFT-SG beam failure tensile strains were lower than the ultimate strain of the GFRP tube in tension. Both the CFT-G and CFT-SG exhibited higher moment capacity as the a/D ratio increased. Also, it was noted that the inclusion of internal reinforcement increased the strength of CFT-SG beams by about 44 to 53% compared to CFT-G beams. In the FRP tube specimens, flexural cracks were

visible in the concrete without developing any diagonal cracking in the beams, which was further confirmed due to the presence of slip. Though the full depth flexural cracks were developed in the concrete core, it was noticed that the flexural crack patterns were different for the CFT-G beams and CFT-SG beams, respectively. A distinct major diagonal crack with some minor flexural crack was developed in the CFT-SG beams. The bond improvement between the concrete core and the GFRP tube was due to the additional internal reinforcement, which reduced the slippage between them.

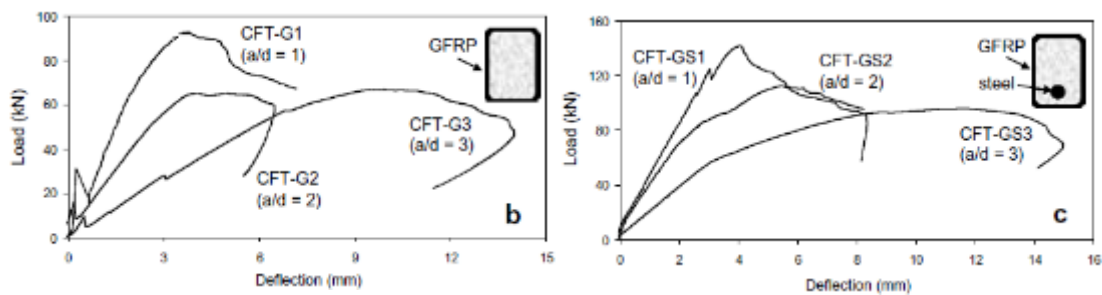


Figure 2-33. Load-deflection behavior of CFT-G and CFT-GS test beams
(Fam et al. 2007)

Finally, they developed a model to predict the strength of CFT based on a simplified strut-tie model for an a/D ratio of 1. For the CFT-G and CFT-SG beams, they considered the upper nodal point at the top surface of the beam as the beams showed full depth cracks. The depth of centroid was varied for the CFT-G and CFT-SG beams due to the internal reinforcement. The tension force in the tie depended on the strain level in the GFRP tube at the centroid. For the CFT-S beams, considered equilibrium relation between the force generated by the concrete in the compression zone and the tension force provided by the yielded part of the steel tube in tension. This assumption was due to the observations such as local buckling of steel flange and development of partial depth cracks. Their developed model showed a reasonable prediction of ultimate loads.

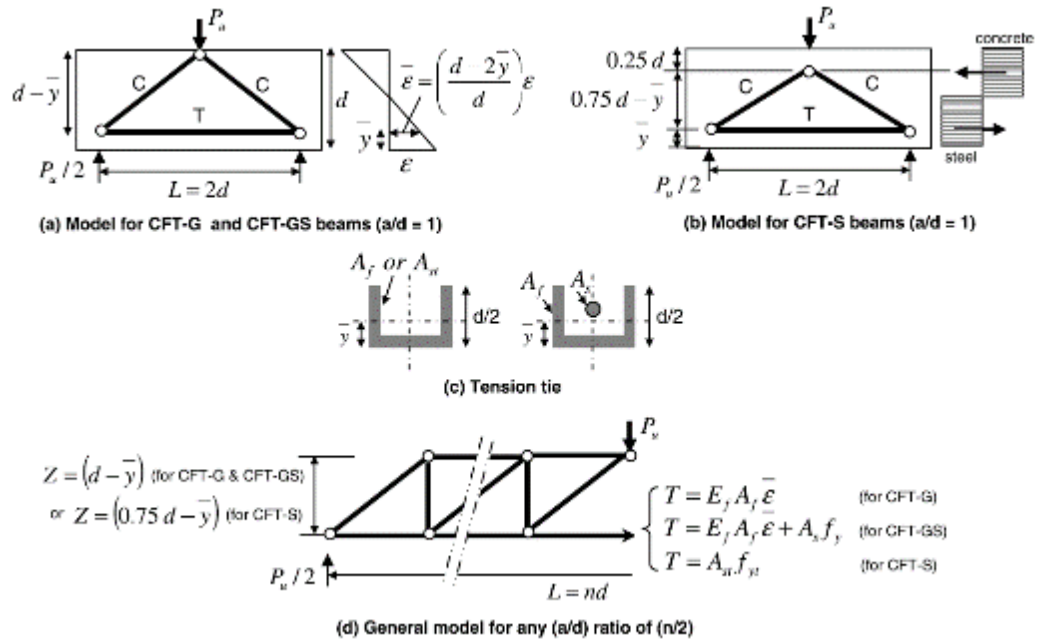


Figure 2-34. A simplified strut-and-tie model for CFT beams (Fam et al. 2007)

Mohamed and Masmoudi (2010) tested ten beams to investigate the flexural strength and behavior of reinforced concrete-filled fiber-reinforced polymer tubes under four-point bending. The test specimens had a total length and a span length of 2000 mm and 1920 mm. The GFRP tubes used to prepare the CFFTs had two different thicknesses, 2.9 and 6.4 mm. The test parameters varied with respect to internal reinforcement types, type of confinements, and compressive strength of concrete. Each specimen contained either two internal reinforcement types, 15M steel rebars or No. 5 GFRP rebars. Two types of confinement methods, steel spiral and GFRP tubes were used as a stay-in-place formwork to prepare the test specimens. Two specimen groups A and B had two different types of concrete with regards to their compressive strength. Group A and B specimens were casted concrete with a compressive strength of 30 and 45 MPa, respectively. The mid-span and quarter span deflection during the testing were measured with the help of linear variable displacement transducers. The strain in the specimens was recorded at the reinforcing bars, concrete surface, and FRP tube surface with the help of electrical resistance strain gauges.

Table 2-11. Dimension, Details and Mechanical Properties of GFRP tubes
(Mohamed and Masmoudi 2010)

Tube type	D (mm)	t_{FRP} (mm)	No. of layers	Stacking sequence	E_{xy} (MPa)	F_{ly} (MPa)	E_{rx} (MPa)	F_{rx} (MPa)	F_c (MPa)
A	213	2.90	6	[60, 90 ₄ , 60]	32 260 ^a	537 ^a	8865 ^b	55.16 ^b	135 ^b
B	213	6.40	12	[±60, 90 ₂ , ±60, 90 ₆]	30 200 ^a	498 ^a	7897 ^b	59.24 ^b	138 ^b

E_{rx} and E_{ry} are, respectively, the Young modulus in the longitudinal and hoop directions; F_{rx} and F_{ry} are, respectively, the ultimate tensile strength in the longitudinal and hoop directions.

^a Calculated using lamination theory.

^b Based on coupon test.

Table 2-12. Test Matrix and Summary of Test Results (Mohamed and Masmoudi 2010)

ID	Diameter (D=mm)	Shear reinforcement	Flexural reinforcement (ratio)	Concrete strength (MPa)	Moment (kN m)			Deflection ^a (mm)	Comp strain ^b ($\mu\epsilon$)	Failure mode	Ductility (kN m)	
					Crack	Yield	Ultimate					
Group No. 1	C30S	203	–	6 No. 15M Steel bars (3.65)	30	3.84	24.86	32.85	11.99	2.633	DT	0.78
	CS30S	203	Steel spiral	6 No. 15M Steel bars (3.65)	30	4.88	26.40	48.95	136.25	3.959	SC	17.75
	A30S	213	Tube A	6 No. 15M Steel bars (3.65)	30	6.36	37.21	75.75	124.91	15.516	FL	32.40
	A30G	213	Tube A	6 No. 5 GFRP bars (3.65)	30	5.09	–	46.33	43.13	6.017	FL	5.78
	B30G	213	Tube B	6 No. 5 GFRP bars (3.65)	30	5.55	–	56.68	38.68	6.479	FL	8.77
Group No. 2	C45G	203	–	6 No. 5 GFRP bars (3.65)	45	4.24	–	24.67	24.33	2.628	DT	1.09
	CS45G	203	Steel spiral	6 No. 5 GFRP bars (3.65)	45	4.40	–	44.55	57.47	3.124	SC	5.53
	A45G	213	Tube A	6 No. 5 GFRP bars (3.65)	45	5.09	–	48.53	45.14	5.415	FL	5.92
	B45G	213	Tube B	6 No. 5 GFRP bars (3.65)	45	6.24	–	64.78	43.75	7.009	FL	9.76
	A45S	213	Tube A	6 No. 15M Steel bars (3.65)	45	7.16	40	75.84	126.69	10.629	FL	34

^a The experimental results at ultimate load; DT = diagonal tension failure; SC = shear compression failure; FL = flexural failure.

^b At the top side of the tube.

Flexural-tension failure was the failure mode for six CFFT beams in this study. In contrast, the control specimens without transverse reinforcement and steel spiral experienced diagonal tension failure at the shear span and shear compression failure, respectively. The steel-reinforced CFFT beams experienced a gradual and ductile failure. The failure in the steel-reinforced CFFTs started by the tensile rupture in the FRP tube at their maximum tension moment zone. Complete failure in CFFT was noticed after the first and second break in the steel rebars at the tensile zone. Although the major failure mode noticed in the specimens was flexure driven, minor flexural-shear cracks in the concrete were developed. However, the concrete at the maximum compression zone remained intact. Due to these details, the author suggested that the partial confinement effect of the FRP tube on the concrete core increased the compressive strength of the concrete. On the other hand, FRP-reinforced CFFTs failed similarly to the steel-reinforced CFFTs. In this case, the failure started with the tensile rupture of the GFRP rebars, followed by the tensile rupture of the tube. Comparing the failure mode in the control specimens and CFFTs, the author concluded that the FRP tubes' contribution in terms of the presence of the longitudinal and circumferential fibers, the final failure mode changed from shear failure to a flexural-tension failure.

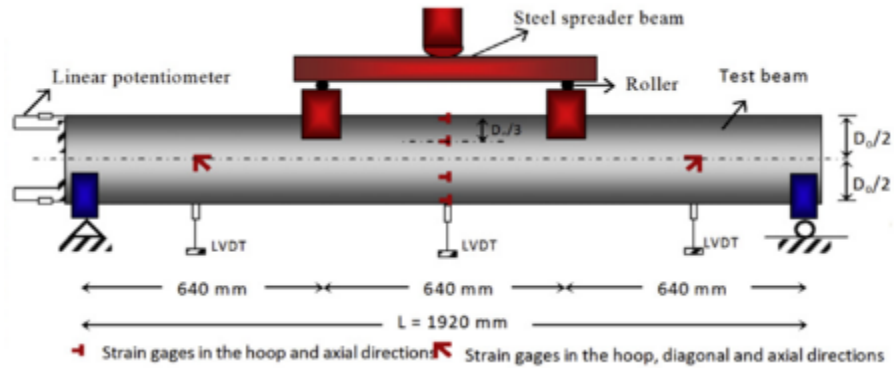


Figure 2-35. Test Setup and instrumentation (Mohamed and Masmoudi 2010)

The similar CFFTs reinforced with 30 and 45 MPa concrete did not exhibit any considerable change in their ultimate capacity. The steel-reinforced CFFTs filled with 30 and 45 MPa concrete did not show any increase in their capacity, whereas the FRP-reinforced CFFTs showed a minor 4.8% increase in their capacity when compared to 30 MPa and 45 MPa specimens. For all the CFFT specimens reinforced with steel and GFRP rebars, the ratio of strength between FRP reinforced CFFTs, and steel-reinforced CFFT beams was 60%, which was approximately equal to the cube root of axial stiffness ratio between GFRP and steel rebars. This study has observed that the thickness of GFRP tubes had a major influence on the strength, ductility, and deflection of the CFFTs. When compared between A30G and B30G, the increase in strength and ductility was 22.3% and 52%, respectively. This enhancement in the strength and ductility was observed due to the increase in reinforcement ratio of the GFRP tubes.

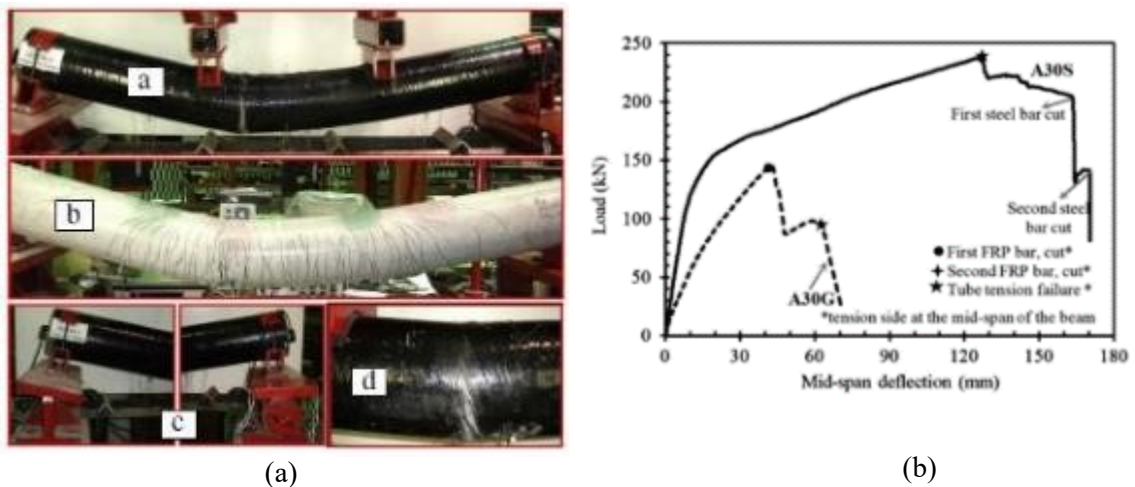


Figure 2-36. (a) Typical failure modes; (b) Load-deflection behavior (Mohamed and Masmoudi 2010)

Along with the experimental investigation, a simplified analytical method was developed in this study to predict the yield and resisting moments of the CFFT specimens corresponding to their failure modes. First, the analytical model was developed, idealizing Bernoulli's beam theory and based on the equations derived from linear elastic analysis. This model introduced a few variable factors considering the under-reinforced CFFT sections, assuming that the concrete does not reach its ultimate state. Next, an iterative theoretical moment equation was developed with three unknowns, strains, depth of neutral axis, and a factor representing the level of confinement gained from the interaction between FRP tube and concrete core of CFFT beams under flexural loads. Their analytical study established that the FRP tubes partially confined the concrete core in the CFFTs. Also, steel-reinforced CFFTs showed a higher level of confinement compared to FRP-reinforced CFFTs at ultimate. This confinement effect was further validated by the increase in the ultimate load capacity of steel-reinforced CFFT compared to their FRP-reinforced counterparts, which attributed to a higher confinement effect by the FRP tube on the concrete core. Finally, the cracking moment capacities were estimated using an equation that considered the elastic theory and was based on the gross sectional properties. This study introduced new values as modification factors for the equations based on their experimental and predicted cracking moment results. However, they suggested that the provided modification factors largely depend on FRP tubes' fiber architecture, orientation, and stiffness in the axial, hoop direction and require more experimental investigations.

Table 2-13. Experimental and Predicted Cracking Moments for RCFFT beams
(Mohamed and Masmoudi 2010)

Specimens ID	Crack moment, M_{cr} (kN m)					$M_{cr(exp)}/M_{cr(pred)}$			
	Experimental	ACI 318-08, ACI 440.1R-06, CSA S806-02	CSA S6-06	Fam [17]	Modified equation (new factor)	ACI 318-08, ACI 440.1R-06, CSA S806-02	CSA S6-06	Fam [17]	Modified equation (new factor)
A30S	6.75	4.40	2.93	7.34	6.9	1.53	2.30	0.92	0.98
A30G	5.09	3.32	2.21	5.54	5.2	1.53	2.30	0.92	0.98
B30G	5.55	3.40	2.26	5.67	5.33	1.63	2.46	0.98	1.04
A45G	5.82	3.89	2.59	6.48	6.09	1.50	2.25	0.90	0.96
B45G	6.24	3.96	2.64	6.60	6.21	1.58	2.36	0.94	1.00
A45S	7.53	4.9	3.31	8.29	7.79	1.54	2.27	0.91	0.97
	Average					1.55	2.32	0.93	0.99
	SD					0.05	0.07	0.19	0.03

2.4 INFERENCE FROM THE LITERATURE and RESEARCH GAP

There are no uncertainties surrounding FRP tubes' superior confining effect on improving the ultimate capacity of CFFT members. From the literature, it can be observed that a few major factors influence the behavior of CFFTs, internal reinforcement, shear-span to depth ratio, confining material, and composite action between components of CFFTs. The summary of the effect of these parameters on CFFTs are as follows:

- The introduction of internal reinforcement in terms of longitudinal rebars in the CFFTs significantly improves the strength and stiffness of the CFFT systems. With improving the structural aspect, internal reinforcement also improves the overall compositeness of the CFFT members by resisting excessive slip between the concrete core and the FRP tubes.
- The shear-span to depth ratio of the CFFT beam has a significant influence on its ultimate capacity and failure mode. Although short CFFT beams ($1 < a/D \leq 2.5$) sometimes generate web shear cracks in the concrete core, the CFFTs ultimately experience flexural failure. On the other hand, deep CFFT beams ($a/D \leq 1$) are more prone to experience shear failure by developing diagonal tensile cracks due to localized tensile stresses in the FRP tubes.
- The confinement effect generated by the FRP tube results in a superior structural system when compared to conventional transverse reinforcements such as steel ties, tubes, and steel spirals. The ultimate capacity, overall response, and the failure mode of CFFT greatly vary with respect to the FRP tube design parameters, such as thickness, fiber orientation, mechanical properties.
- The literature also showed that composite action between FRP tube and concrete core during loading condition plays a vital role in the overall behavior and the failure mode of CFFTs. The slip between concrete core and FRP tube during different loading intensities showed a reduction in the overall composite behavior of CFFTs, which might further influence the ultimate failure of the system.

The literature review shows the extensive studies performed to understand the shear and flexural behavior on CFFT with various fiber orientations, with or without internal reinforcement. Filament wound GFRP tubes with $\pm 55^\circ$ fiber orientation with respect to the

axial direction of the tube are commonly used in the piping, oil, and gas industries due to their effectiveness in resisting the internal pressure loads, which generates hoop stress to axial stress ratio of 2:1. For this reason, they are readily available for commercial applications. Hence from an economic standpoint, utilization of these GFRP tubes could be very beneficial for CFFT applications. However, only a handful of studies were conducted on CFFTs with $\pm 55^\circ$ fiber orientation, which hinders its widespread applications. Few studies on CFFTs with $\pm 55^\circ$ fiber orientation was performed to understand the behavior of deep and short CFFTs without internal reinforcement (Ahmad et al. 2008); performance of CFFTs under field close-in blast loading (Qasrawi et al. 2004); effect of tube damage on flexural strength of CFFTs (Lu and Fam 2020). However, no study was performed to explore the shear and flexural behavior of internal steel-reinforced CFFTs with $\pm 55^\circ$ fiber orientation. Hence, this research was conducted to gain a better understanding of the shear and flexural behavior of internally steel-reinforced short and deep CFFTs with $\pm 55^\circ$ fiber orientation.

2.5 FIELD APPLICATION OF CFFTS

With the advancement in construction industries in the twenty-first century, innovative and sustainable material systems, such as concrete-filled fiber-reinforced tubes (CFFT), gained significant popularity in field applications for marine infrastructures. The CFFT members can be used as bridge piers, fender piles, bridge decks, and girders. Few major field applications of CFFTs are discussed in this section.

Zaho et al. (2000) reported a field application of CFFTs with CFRP tubes as bridge girders to support the modular lightweight fiberglass bridge deck for the Kings Stormwater Channel Bridge, as shown in figure 2-37, located in California on the State Route 86 near the Salton Sea. The bridge has two spans that measure 10 m long and has a width of 13 m. This field application was possible due to an extensive investigation on the flexural behavior of full-scale bridge deck and girder components, which comprised a circular CFFT member combined with either conventional RC deck or a GFRP modular deck by Karbhari et al. (2000).



Figure 2-37. Kings Stormwater Channel Bridge (HPWREN, UCSD/CalTrans)

Fam et al. (2003) discussed various piling applications for CFFT in the marine environment. Most common applications include fender piling, which is used as a barrier to protect the pier. It absorbs and dissipates impact energy generated during the berthing of ships near ports. Dauphins, a group of piles, are placed close to the piers and wharves to guide and keep the vessels away from structures or serve as mooring points. The CFFT group piling can also be used as support to carry loads of light-duty piers and wharves. The group piling and dauphins can also be used as a protective layer for the bridge piers, and it will also help increase the strength and stiffness of the foundation.

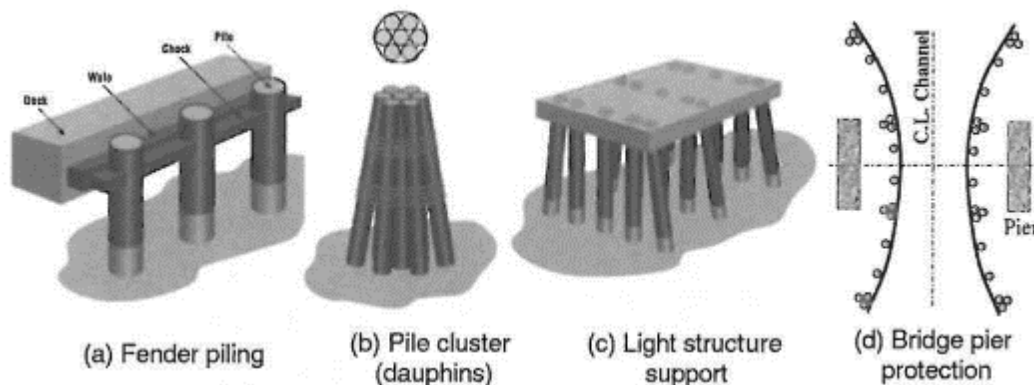


Figure 2-38. Various piling applications of CFFT: (a) Fender piling; (b) Dauphins; (c) Light structure support pile groups; (d) Bridge pier protection (Fam et al. 2003)

Fam et al. (2003) also reported eight selected field applications that utilized a total of 1554 CFFT members as marine piling along both coasts of the United States, as shown in figure 2-39. Although experiencing severe, harsh weather conditions such as severe hurricanes, regular inspection of structural performance has shown the composite piles in the field projects are performing well and still in service. Few of the projects include rehabilitation of Erie Canal in New York with the help of a total of 120 CFFT composite piles of 323 mm diameter and 16.2 m long, US Naval Station Ingleside project in Texas, which used a total of 180 CFFT piles of 367 mm diameter and 22 m long. In contrast, Belmar Municipal Marina in New Jersey, a commercial project, used a total of 140 CFFT piles of 323 m and 14.6 m long to pin the piers and hold the dock in position. The piles were primarily subjected to lateral loads in terms of 1.5 m ocean tides, and with this tidal movement, they also experienced harsh freeze-thaw cycles. Nevertheless, due to the high flexural capacity and corrosion resistance of the CFFT members, it made an excellent choice for this tidal basin project.



Figure 2-39. (a) Fender piles and dauphin clusters in Naval Station Ingleside Project;
(b) Structural piles in Belmar Municipal Marina Project (Fam et al. 2003)

CHAPTER 3 EXPERIMENTAL STUDY

3.1 GENERAL

In this chapter, the following sections will cover the experimental investigation on steel-reinforced concrete-filled GFRP tube specimens (CFFT). First, a brief section will discuss the components of the CFFT specimens and their properties. The following sections will outline a detailed explanation of the fabrication of the CFFT specimens, their instrumentation, and the testing procedure. Next, the test matrix will describe the eighteen CFFT specimens and their changing parameters, such as GFRP tubes, internal reinforcement ratios, and testing spans. Additionally, this chapter will discuss the failure mode of the specimens depending on their parameters. Finally, testing results from different specimen sets will be analyzed and compared for load vs. deflection, load vs. strain, and load vs. bond-slip behavior of the CFFT specimens and their ultimate moment capacity.

3.2 MATERIAL PROPERTIES

The materials used to prepare the CFFT test specimens includes GFRP tubes as confining material, steel rebars as internal longitudinal reinforcement, and concrete as infill.

3.2.1 GFRP Tubes

Three different kinds of GFRP tubes were used to prepare the CFFT specimens. The filament winding technique was used to produce the tubes. The GFRP pipes were manufactured using continuous roving of electrical/chemical resistant (ECR) glass fibers and a BIS-A vinyl-ester resin. The GFRP tubes had a fiber orientation of $\pm 55^\circ$ with respect to the longitudinal axis with an error of $\pm 2^\circ$. The fiber volume fraction of the tubes was 50.2%. Depending on their pressure rating, the tubes were categorized as P50, P100, and P150. The pressure rating mainly depended on the wall thickness of the GFRP tubes. With a constant inner diameter of 203.2 mm, the P50, P100, and P150 tubes had a wall thickness of 2.7 mm, 4.7 mm, and 6.7 mm, respectively.

The GFRP tubes were initially manufactured by RPS composites (Mahone Bay, NS, Canada). Some of the physical and mechanical properties of the GFRP tubes were provided by the manufacturer and a previous study by Betts et al. (2019). The tube parameters and properties are provided in the following table 3-1 and 3-2, respectively.

Table 3-1. Physical Properties of GFRP tubes as per the manufacturer and previous study

GFRP TUBE ID	Nominal Pressure Rating ^a		Inner Diameter (mm)	Outer Diameter (mm)	Tube Wall Thickness (mm)	Diameter to Thickness Ratio	Filament Wind Lay-Up (°) * ^b
	psi	kPa					
P50	50	345		208.6	2.7	75	[±55/+55] _s
P100	100	690	203.2	212.6	4.7	43	[±55] ₄
P150	150	1035		216.6	6.7	30	[±55] ₅

* Angle respect to longitudinal axis

^a Provided by RPS composites (Manufacturer)

^b From previous study by Betts et al. (2019)

Table 3-2. Mechanical Properties of GFRP tubes from a previous study by Betts et al. (2019)

GFRP TUBE ID	Inner Diameter (mm)	Tube Modulus (GPa)		Strength (MPa)	
		Compression	Tension	Compression	Tension
P50	203.2	11.50	-	73.33	-
P100	203.2	10.03	-	114.68	-
P150	203.2	8.32	-	117.20	-
P50	76	10.77	8.68	121.41	47.48
P150	76	9.04	10.68	128.86	70.76

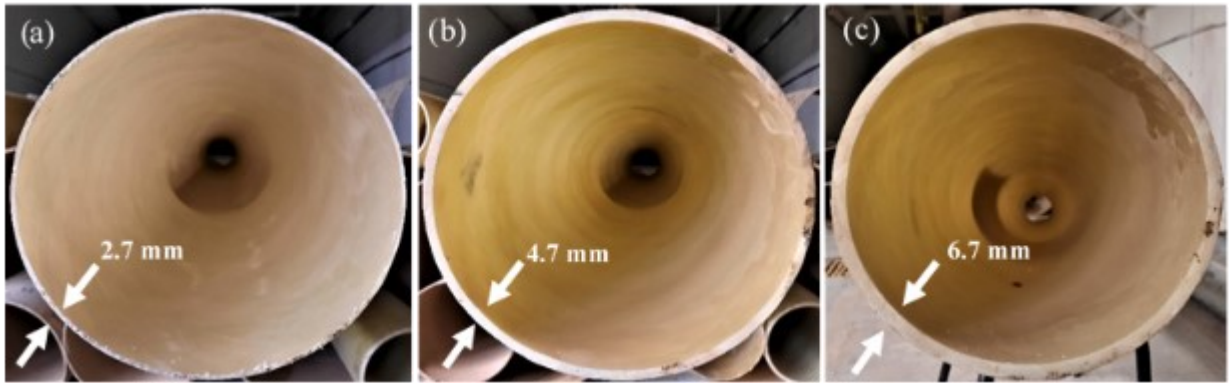


Figure 3-1. Variation in wall thickness of GFRP tubes: (a) P50; (b) P100; (c) P150

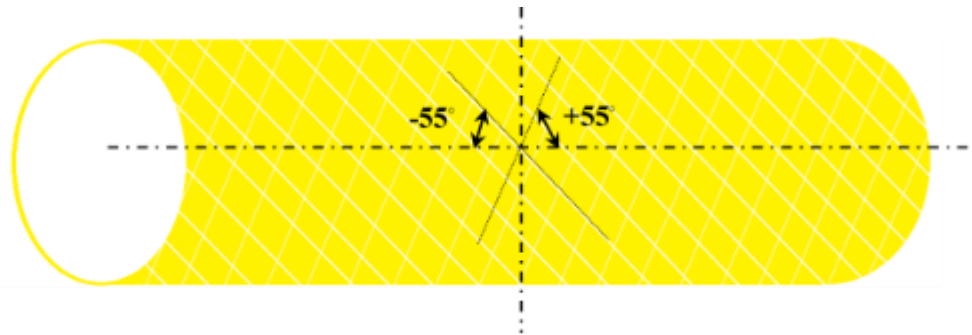


Figure 3-2. Schematic diagram of fiber orientation with respect to longitudinal axis

3.2.2 Concrete

The concrete was acquired from a local ready-mix concrete manufacturer. The concrete was prepared with a nominal aggregate size of 12.5 mm, and superplasticizers for better workability. The concrete mix had an average slump value of 228 mm. During the CFFT specimen casting day, nine number of 150 mm x 300 mm concrete cylinders were cast and cured under a similar condition with the CFFT test specimens to determine the compressive strength of the concrete.



Figure 3-3. Three stages of concrete compressive test: (a) Initial; (b) Intermediate; (c) Final

The nine concrete cylinders were tested in accordance with ASTM C39/39M-12 (2012) in three different phases during the CFFT specimen testing. A set of three concrete cylinders were tested in each of the initial, midway, and final stages of CFFT testing, respectively. The average compressive strength of the nine concrete cylinders was 40 MPa.

3.2.3 Steel Reinforcement

Two different types of steel rebars were used to prepare the CFFT specimens. Four numbers of 10M and three 15M steel rebars were tested following ASTM A615/615M-16 (2016) to determine the behavior and yield strength of the steel rebars. An Instron testing machine with a mechanical grip of 203.2 mm (8") was used to test the steel rebars under uniaxial tension. The steel rebar specimens were cut in the length of 1219.2 mm (48") for tensile testing and had a gauge length of 812.8 mm (32"). The rebar specimens were tested at a loading rate of 10 mm/min.

All four 10M steel rebar specimens showed similar stress vs. strain behavior. The 10M specimens showed initial elastic behavior followed by strain hardening region, final necking, and subsequent failure. As the 10M specimens did not show a clear yielding or a yield plateau, yield strengths of the 10M steel rebars were determined using the 2% offset method, shown in figure 3-5 (a).

15M rebar specimens, on the contrary, showed different stress vs. strain behavior compared to 10M rebar specimens. The 15M specimens showed an early elastic behavior followed by an apparent yield plateau, strain hardening region, and final failure. Figure 3-5 (b) exhibits the stress vs. strain behavior of 15M steel rebars.

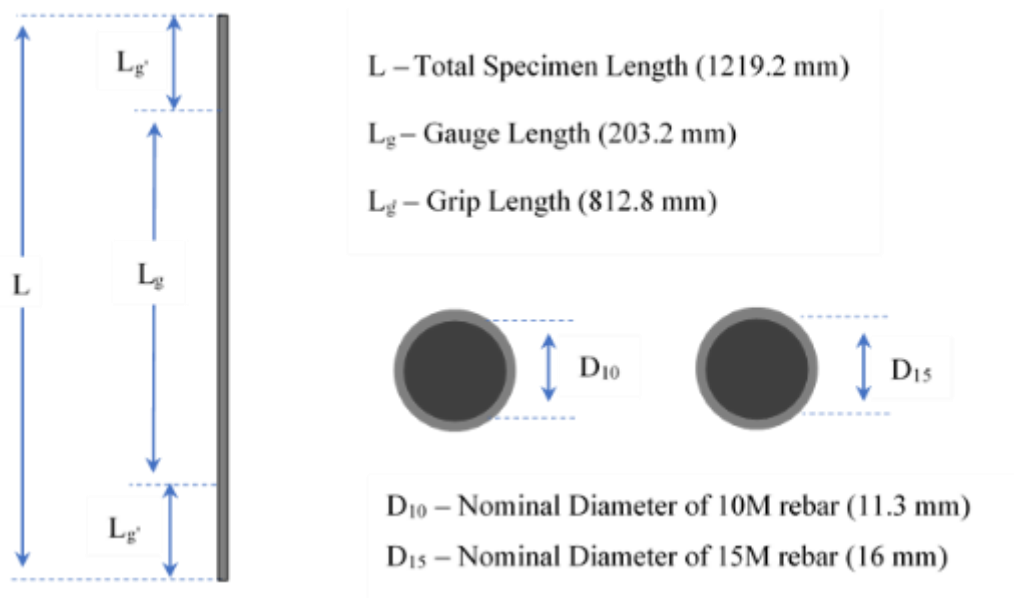


Figure 3-4. Schematics representation of tensile test of steel rebar specimens

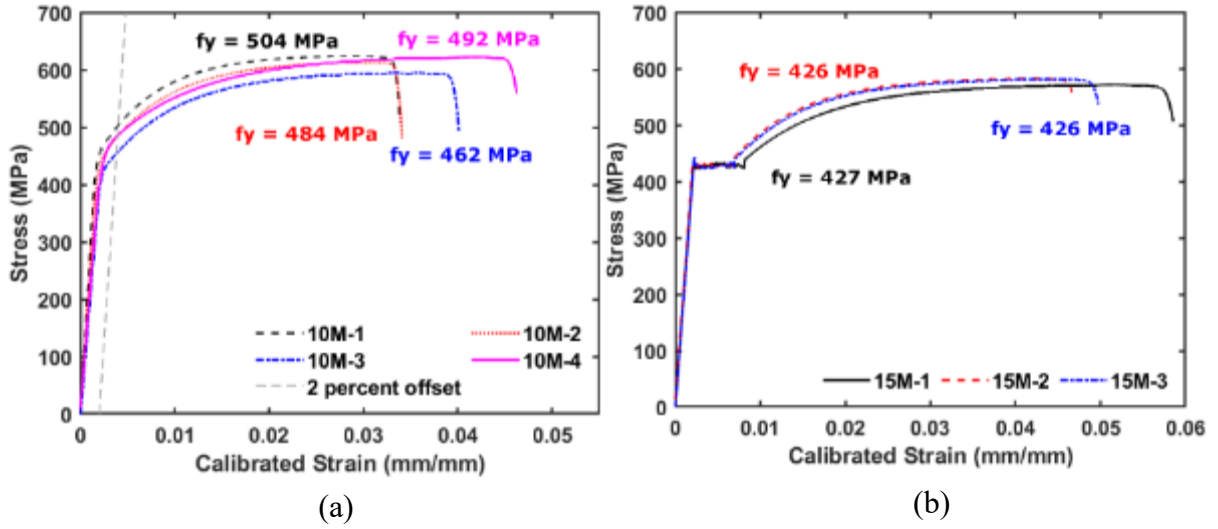


Figure 3-5. Tensile stress vs. strain behavior of steel rebars: (a) 10M; (b) 15M

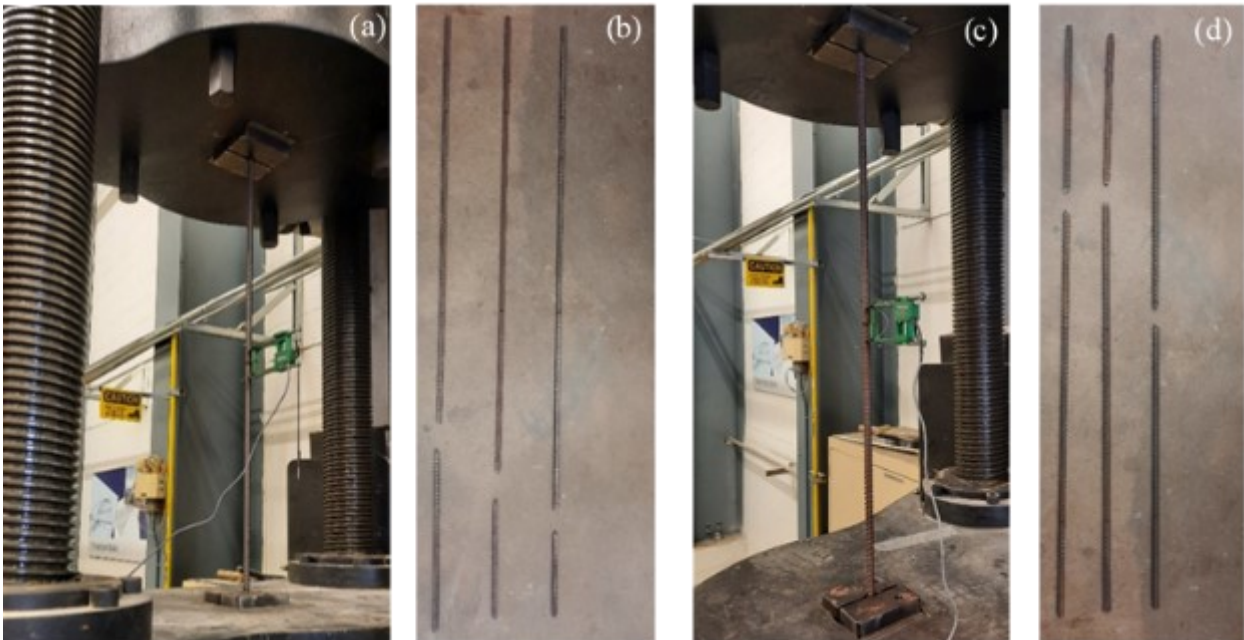


Figure 3-6. Uniaxial tensile test: (a) 10M rebar; (b) Failed 10M rebars; (c) 15M rebar; (d) Failed 15M rebars

The average yield strength of the 10M and 15M rebars were 485.5 MPa, and 426.3 MPa, respectively. The overall uniaxial tensile test results are stated in the following table 3-3.

Table 3-3. Experimental results of uniaxial tensile test of steel rebars

Steel Rebar Type	Steel Rebar ID	Nominal Diameter (mm)	Yield Strength (MPa)	Average Yield Strength (MPa)	Standard Deviation (MPa)
	10M - #1		504		
10M	10M - #2	11.3	484	485.5	17.7
	10M - #3		462		
	10M - #4		492		
	15M - #1		427		
15M	15M - #2	16	426	426.3	0.6
	15M - #3		426		

3.3 TEST MATRIX

To effectively understand and evaluate the overall behavior of CFFTs, extensive testing of CFFTs was carried out. In total, eighteen CFFT specimens were fabricated and tested under three different shear span to depth ratios. Three sets of six unique types of CFFT specimens were prepared from three different kinds of tubes and two different kinds of internal longitudinal steel rebars. Figure 3-7 shows six different kinds of CFFT and its typical cross-sections. Table 3-4 lists all types of CFFT specimens tested under three-point bending to fulfill the objectives mentioned in section 1.3. The specimen nomenclature was assigned with a systematic procedure, acknowledging the varying material properties and testing parameters. The specimen labeling has followed a pattern of “PX-Y-ADZ” to identify a particular specimen. In the label, “P” stands for pressure rating of the tube and the subsequent number “X” as its value in psi. The following term, “Y,” represents the type of internal longitudinal reinforcement. For example, “a” stands for 10M rebars, and “b” stands for 15M rebars. Finally, AD followed by “Z” represents the specimen’s shear span to depth ratio and its value.

Table 3-4. Test matrix for CFFT

Case Number	CFFT SPECIMEN ID	Shear Span to Depth Ratio (a/D _i)	Shear Span (a) in mm	Effective Span (C/C) from Support to Support (mm)	Internal Longitudinal Steel Reinforcement	
					Reinforcement Type	Reinforcement Ratio (%)
1	P50-a-AD0.5					
2	P100-a-AD0.5				#6-10M	1.85
3	P150-a-AD0.5	0.5	101.6	355.6		
4	P50-b-AD0.5					
5	P100-b-AD0.5				#6-15M	3.70
6	P150-b-AD0.5					
7	P50-a-AD1					
8	P100-a-AD1				#6-10M	1.85
9	P150-a-AD1	1	203.2	588.8		
10	P50-b-AD1					
11	P100-b-AD1				#6-15M	3.70
12	P150-b-AD1					
13	P50-a-AD2.25					
14	P100-a-AD2.25				#6-10M	1.85
15	P150-a-AD2.25	2.25	457.2	1066.8		
16	P50-b-AD2.25					
17	P100-b-AD2.25				#6-15M	3.70
18	P150-b-AD2.25					

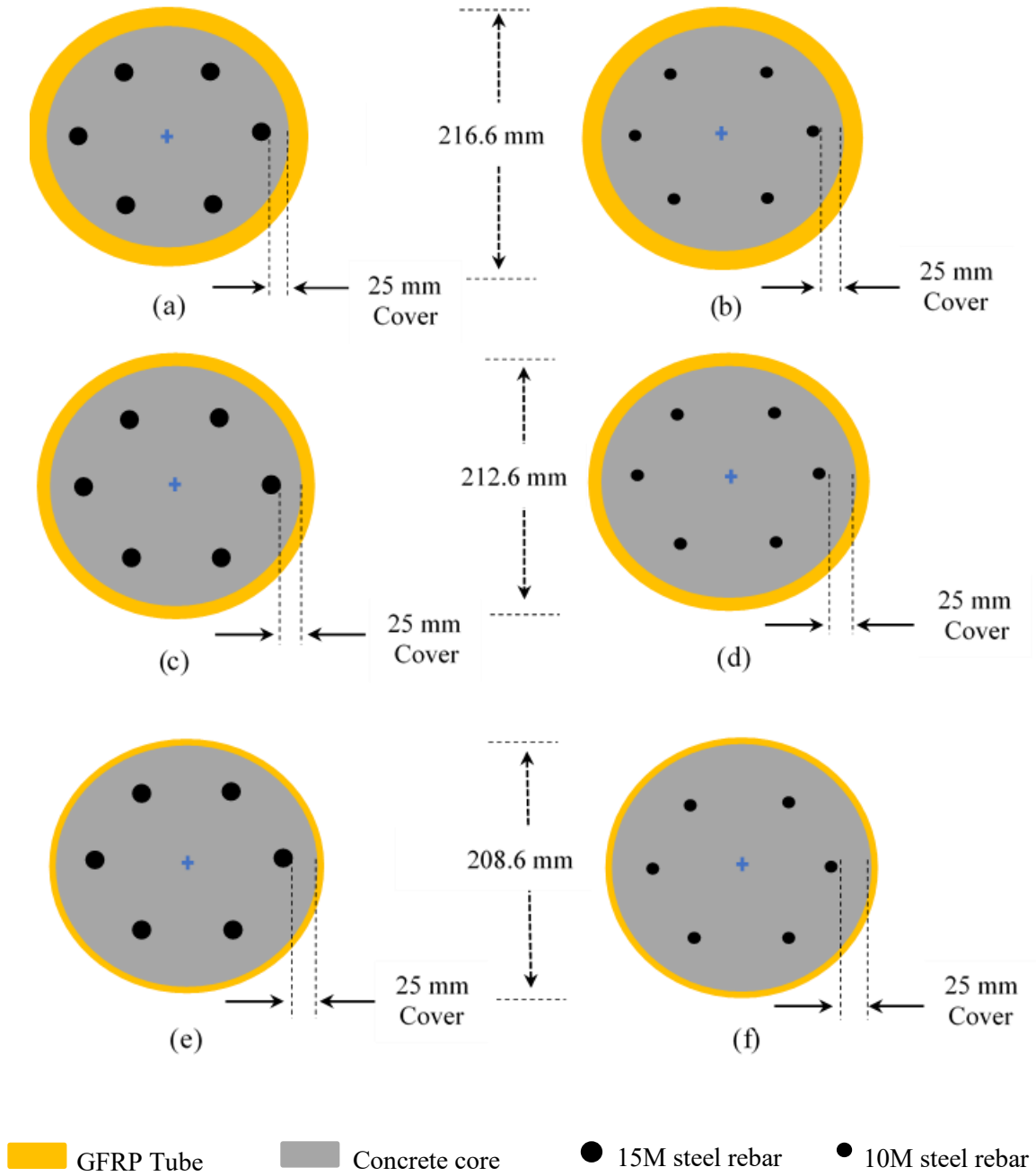


Figure 3-7. Layout of typical cross sections of CFFT specimen: (a) P150-15M; (b) P150-10M; (c) P100-15M; (d) P100-10M; (e) P50-15M; (f) P50-10M

3.4 SPECIMEN FABRICATION

The assembling and fabricating procedure for a total of eighteen CFFT specimens is shown in figure 3-8. All of the GFRP tubes were cut into a length of 1219.2 mm (48"). Initially, all eighteen hollow tubes were assembled on top of a plywood sheet to trace their location and wall thickness. A minimum clear cover of 25 mm between the rebar and inner wall of the tube was selected for all of the specimens, shown in figure 3-7. Next, depending upon the reinforcement type, the longitudinal rebar locations were drawn on the plywood sheet. The rebar locations on the plywood were then drilled depending on the rebar diameter. The traced plywood was then placed and fastened on top of a new plywood sheet and a wooden pallet. The hollow GFRP tubes were placed and fastened with the help of a rectangular wooden cage assembly. Similar to the bottom traced plywood, another plywood was traced for the top of the assembly as a lid and then cut with the help of an electric hand-saw shown in figure 3-8 (b). This procedure was planned and followed to ensure that the rebar location remained similar for all of the specimens, as there were no transverse reinforcement or stirrups were introduced to fix the rebar assembly. After preparing the cage with the hollow GFRP tubes, the steel rebars were placed depending on the specimen type and fastened with the help of tie wires and screws on the top plywood.

During the concrete casting, the concrete mix was poured from the top of the assembly. The concrete in the specimens was filled in three stages simultaneously. The extended rebars of the specimens were carefully vibrated for concrete compaction after each stage, as shown in figure 3-9 (b). After finishing the CFFT casting, nine additional cylinders were cast with the same batch of the concrete mix. The CFFT specimens, then surface finished to produce a smooth concrete surface, and the assembly was covered with a polythene sheet. Finally, the CFFT specimens and concrete cylinders were cured for a minimum of 28 days, so that concrete infill gained its design strength. After the curing process, the CFFT specimens were removed individually from the assembly for scheduled testing.

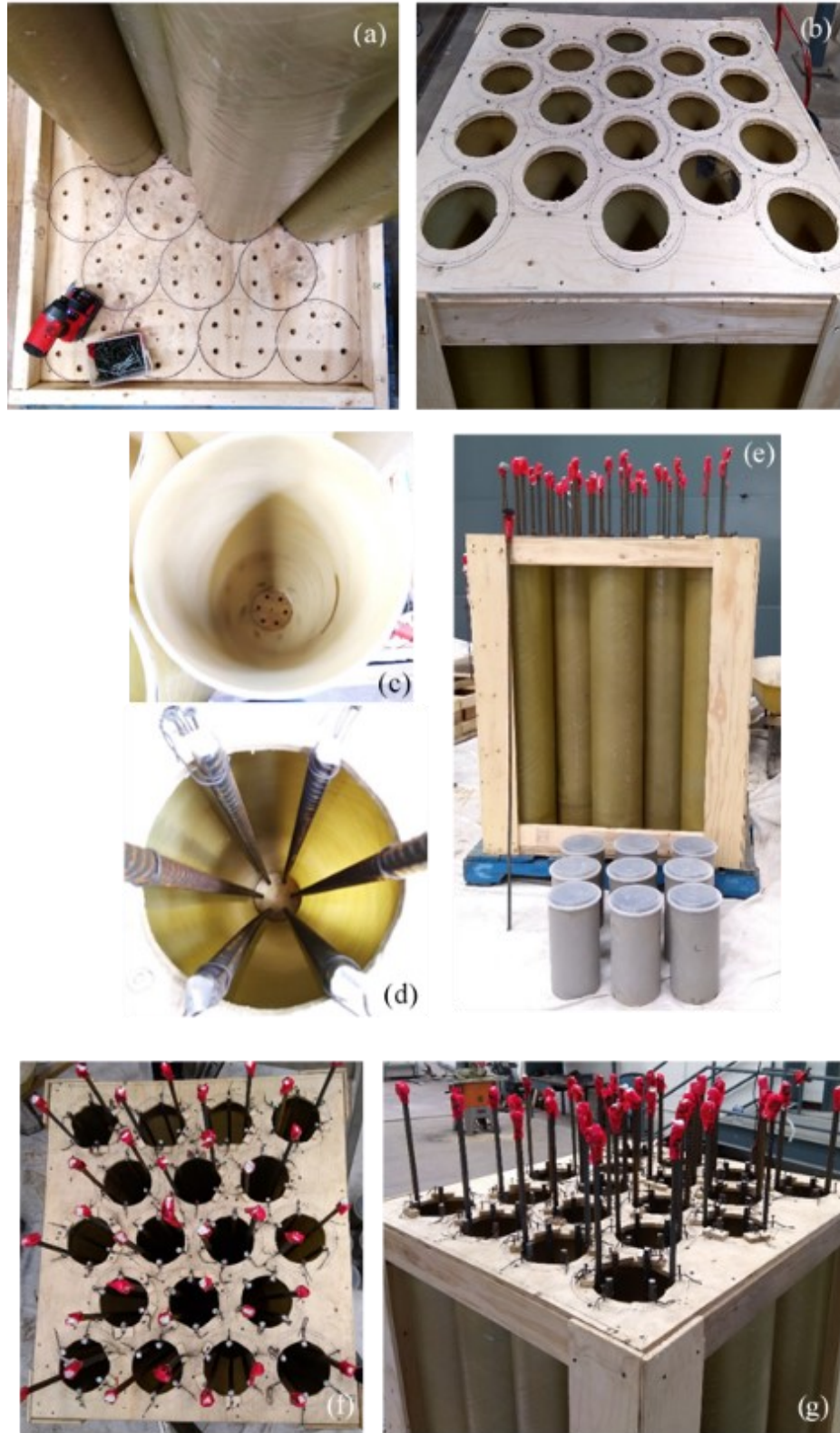


Figure 3-8. CFFT specimen fabrication: (a) Dimension layout; (b) Cage assembly; (c) Specimen before rebar installation; (d) Fixing of steel rebars; (e) Full assembly; (f) Top view of the full assembly; (g) Assembled formwork before concreting



Figure 3-9. CFFT specimen casting: (a) Concrete pouring; (b) Concrete compaction during specimen casting; (c) CFFT specimens ready for curing process; (d) Longitudinal view of CFFT; (e) Cross-sectional view of CFFT

3.5 INSTRUMENTATION and TEST SET-UP

Eighteen CFFT specimens were tested under three-point bending with a varying effective span of 355.6, 588.8, and 1066.8 mm, respectively. A generalized schematic diagram of the overall test set-up is illustrated in figure 3-10 (a). These spans were calculated and adopted based on the shear span to depth ratio of table 3-4. Semi-circular steel supports having a width of 76.2 mm (3") were used in the experimental set-up.

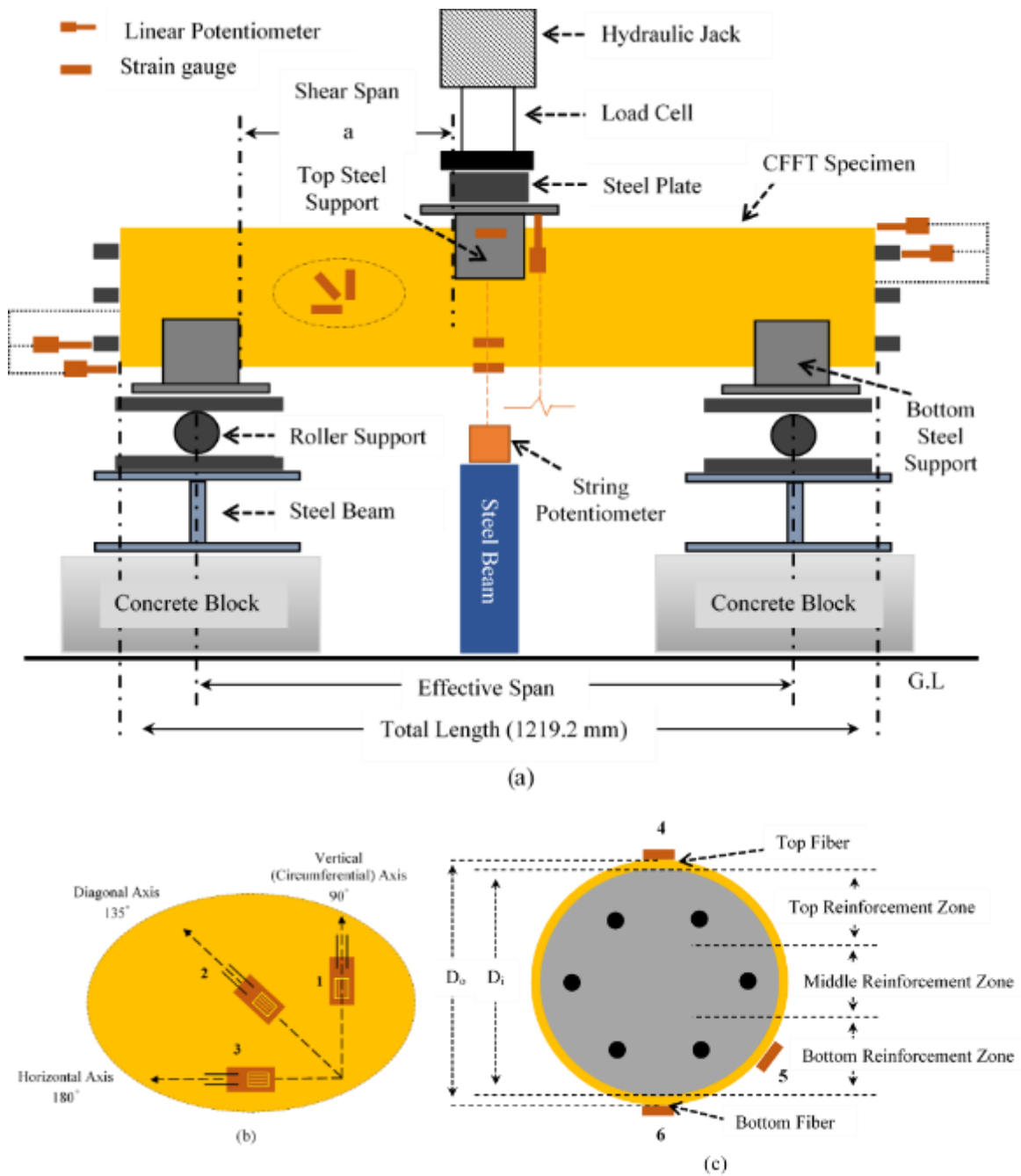


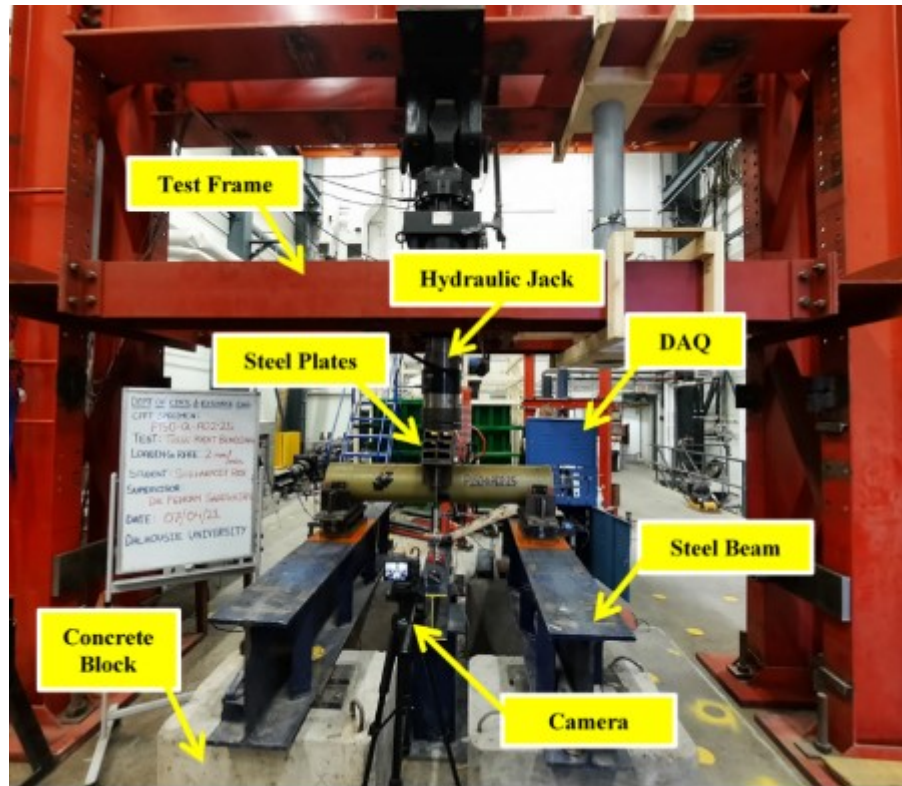
Figure 3-10. Schematic representation of test set-up and instrumentation details:

(a) Overall test set-up; (b) Orientation of strain rosette;

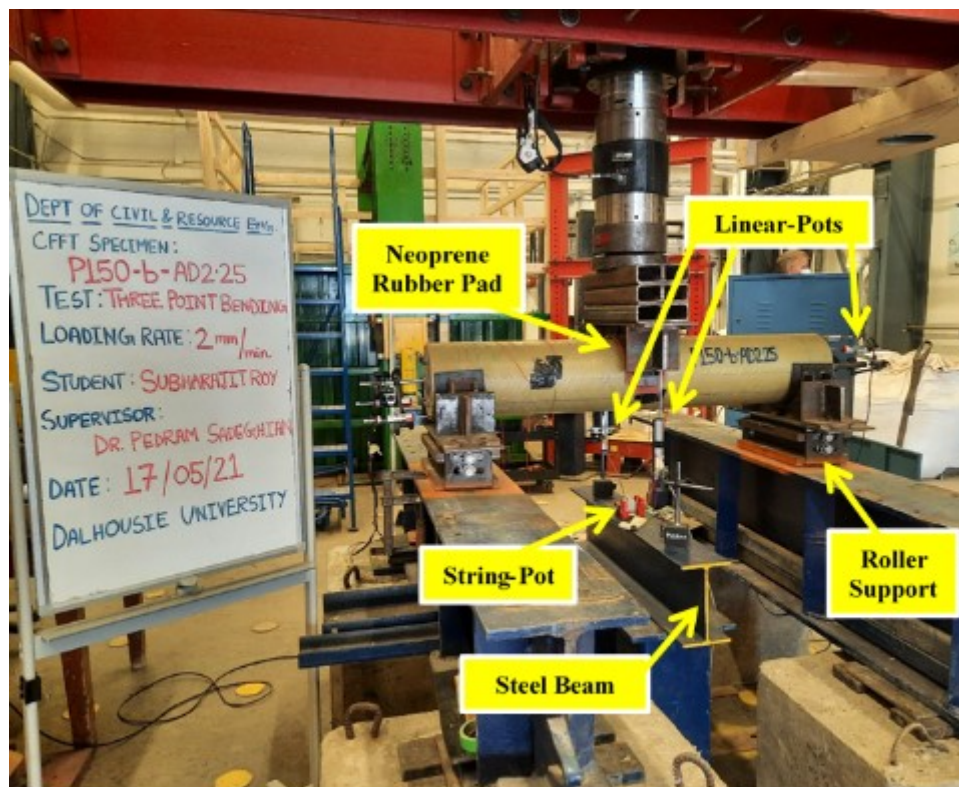
(c) Cross-sectional view of CFFT at mid-span

Neoprene rubber pads were placed between steel supports and CFFT specimens to reduce initial stress concentrations near the contact edge between the steel supports and CFFT. A 1 MN hydraulic actuator applied vertical perpendicular load to the CFFT specimen with a shear span to depth ratio of 1 and 2.25, respectively. For shorter span specimens with a shear span to depth ratio of 0.5 were tested using a 2 MN Instron 5590-HVL static hydraulic universal testing system. The concentrated vertical load was applied on the top steel support at the center of the CFFT specimen with a controlled and constant displacement rate of 2 mm/min using a load cell (except P150-b-AD1). All specimen instrumentation involved six electrical resistance strain gauges, six linear potentiometers, and a string potentiometer. Out of six strain gauges, three strain gauges (1,2,3) were attached as a strain rosette with a 45° rosette layout at the middle of the shear span as demonstrated in figure 3-10 (b). The strain rosette aimed to record the change in longitudinal, circumferential, and diagonal strains. To measure the changes in top compression, bottom tension, and bottom reinforcement zone strains, the rest of the three strain gauges (4,5,6) were applied at the top fiber, bottom fiber, and bottom reinforcement zone at the midspan of the CFFT specimen, respectively, as shown in figure 3-10 (c). All strain gauges were affixed to the outer surface of the CFFT specimens. The vertical displacement at the midspan was measured using two 105 cm (41") linear potentiometers and a 30.48 cm (12") string potentiometer. Two sets of 140 cm (55") linear potentiometers were mounted on both sides of the concrete core of CFFT to measure the bond-slip between the concrete core-steel rebar and concrete core-GFRP tube.

The linear potentiometers mounted on the left side of the specimen recorded the bond-slip between the concrete core-steel rebar and concrete core-GFRP tube at the bottom region. In contrast, the linear potentiometers on the specimen's right side recorded the bond-slip between concrete core-steel rebar and concrete core-GFRP tube at the top region of the specimen, as shown in figure 3-12 (a) and 3-12 (b). The test results, such as load increment, changes in strain values and displacement, etc., were monitored and recorded using a data acquisition system (DAQ), as illustrated in figure 3-11 (a).



(a)



(b)

Figure 3-11. Actual test set-up and instrumentation details: (a) Overall test set-up; (b) Test set-up and Instrumentation

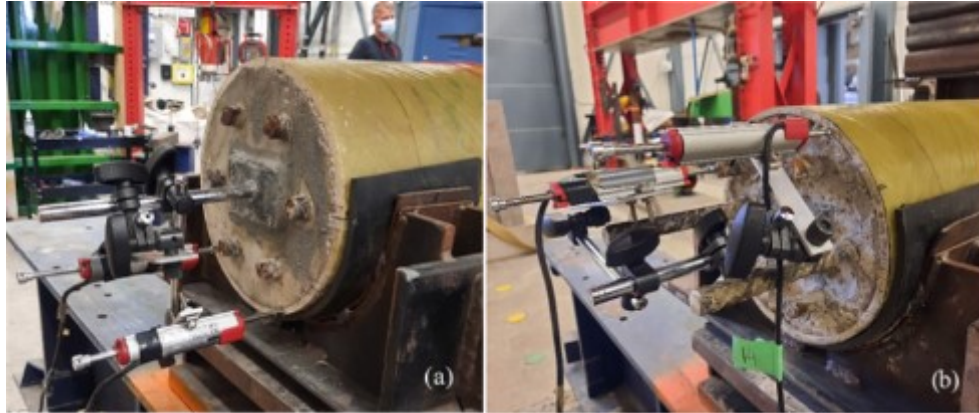


Figure 3-12. Instrumentation details for bond-slip: (a) Linear potentiometer arrangement (Left side of CFFT); (b) Linear potentiometer arrangement (Right side of CFFT)

3.6 TEST RESULTS and DISCUSSION

This section summarizes the experimental result acquired from the three-point bending tests of CFFT, as shown in figure 3-11. Table 3-5 presents ultimate load and ultimate moment carrying capacities for CFFT specimens. It also lists the mid-span deflection of CFFT specimens at their respective peak load. The ultimate moments and initial stiffnesses were derived from the load-deflection results. Finally, the results were analyzed in terms of overall load-deformation behavior with respect to the effect of shear span to depth ratio, effect of GFRP tube wall thickness, the effect of internal longitudinal steel reinforcement, ultimate moment capacity, moment-curvature behavior, and the final failure mode of the CFFT specimens.

Table 3-5. Summary of CFFT Specimens' test results

Case Number	CFFT SPECIMEN ID	Peak Load (kN)	Mid-Span Deflection at Peak Load (mm)	Peak Moment (M_u) at Mid-span (kN-m)	Initial Stiffness (kN/mm)	Failure Mode
1	P50-a-AD0.5	692.78	15.64	61.59	82.46	TR/CC**
2	P100-a-AD0.5	1089.07	17.91	96.82	105.82	TR/CC**
3	P150-a-AD0.5	1393.34	22.97	123.87	97.06	TR/CC**
4	P50-b-AD0.5	929.04	17.05	82.59	92.10	TR/CC**
5	P100-b-AD0.5	1328.69	17.84	118.12	113.67	TR/CC**
6	P150-b-AD0.5	1637.02	21.14	145.53	121.80	TR/CC**
7	P50-a-AD1	415.91	21.38	58.10	42.06	TR
8	P100-a-AD1	629.68	23.09	87.97	52.75	TR/CC**
9	P150-a-AD1	820.33	27.62	114.60	63.04	TR/CC**
10	P50-b-AD1	538.12	22.25	75.18	80.76	TR/CC**
11	P100-b-AD1	748.27	27.55	104.53	85.62	TR/CC**
12	P150-b-AD1*	854.54	31.22	119.38	86.59	TR/CC**
13	P50-a-AD2.25	199.10	45.81	53.10	16.01	TR
14	P100-a-AD2.25	278.69	51.85	74.33	19.85	TR
15	P150-a-AD2.25	367.19	64.23	97.99	19.05	TR
16	P50-b-AD2.25	248.27	46.48	66.21	22.33	TR
17	P100-b-AD2.25	338.95	63.17	90.40	22.66	TR
18	P150-b-AD2.25	413.13	37.42	110.18	40.28	TR/CC**

TR - Rupture in GFRP tube's tension region at mid-span.

CC - Cracking near compression region due to stress concentration around top support.

* - @ 0.5 mm/min loading rate.

** - Not visible during the test (hidden under top support and neoprene pad).

3.6.1 Failure Modes

Previous studies have shown that the CFFT under lateral flexural loads predominantly shows two major failure modes, shear failure, and flexural failure. The major parameter that affected the behavior and failure was mainly due to the confining tubes' different fiber orientation and material properties, the introduction of internal longitudinal reinforcement, and the shear span to depth ratio. In this study, irrespective of the testing parameters, all CFFT specimens exhibited similar failure patterns.

This particular section concentrates on the overall failure mode experienced by eighteen CFFT specimens depending on their shear span to depth ratio. Also, a comparison of the failure in the GFRP tube and the inner concrete core with similar CFFT was studied based on their three different shear-span to depth (a/D_i) ratios. All of the CFFT specimens failed in flexure by rupturing the GFRP tube in the tension region at the mid-span location, particularly under the applied load. During the tests, irrespective of their a/D_i ratio, all of the CFFT specimens showed similar failure behavior. The white stretch lines near the tension region in the GFRP tubes were instantaneously visible with the increase in the applied load on CFFTs'. Figure 3-13 (b) shows that these visible white lines on the GFRP tubes were developed in the same direction as the fiber oriented in the GFRP tube. The appearance of stretch lines was mainly due to the increase in the tensile stress at the tension region of the GFRP tube. The CFFT specimens experienced failure in the tension region at the mid-span directly under the load. The cracks in the bottom tension region at the GFRP tubes appeared close to the CFFT's ultimate capacity. The cracks predominantly originated from the bottom surface of the GFRP tube in CFFT and propagated toward the top at mid-span. This phenomenon was observed through loud audible matrix cracking and splitting the bottom surface of the tube. The CFFTs finally failed due to the tension rupture in the GFRP tube, as exhibited in figure 3-13 (d) and figure 3-14.

The CFFT specimens with the a/D_i ratio 0.5 and 1 experienced distinctive audible cracking, whereas the CFFTs with an a/D_i ratio of 2.25 did not experience a similar level of cracking noise. The initiation of audible cracking will be further discussed to a greater extent in the load-deflection behavior section.

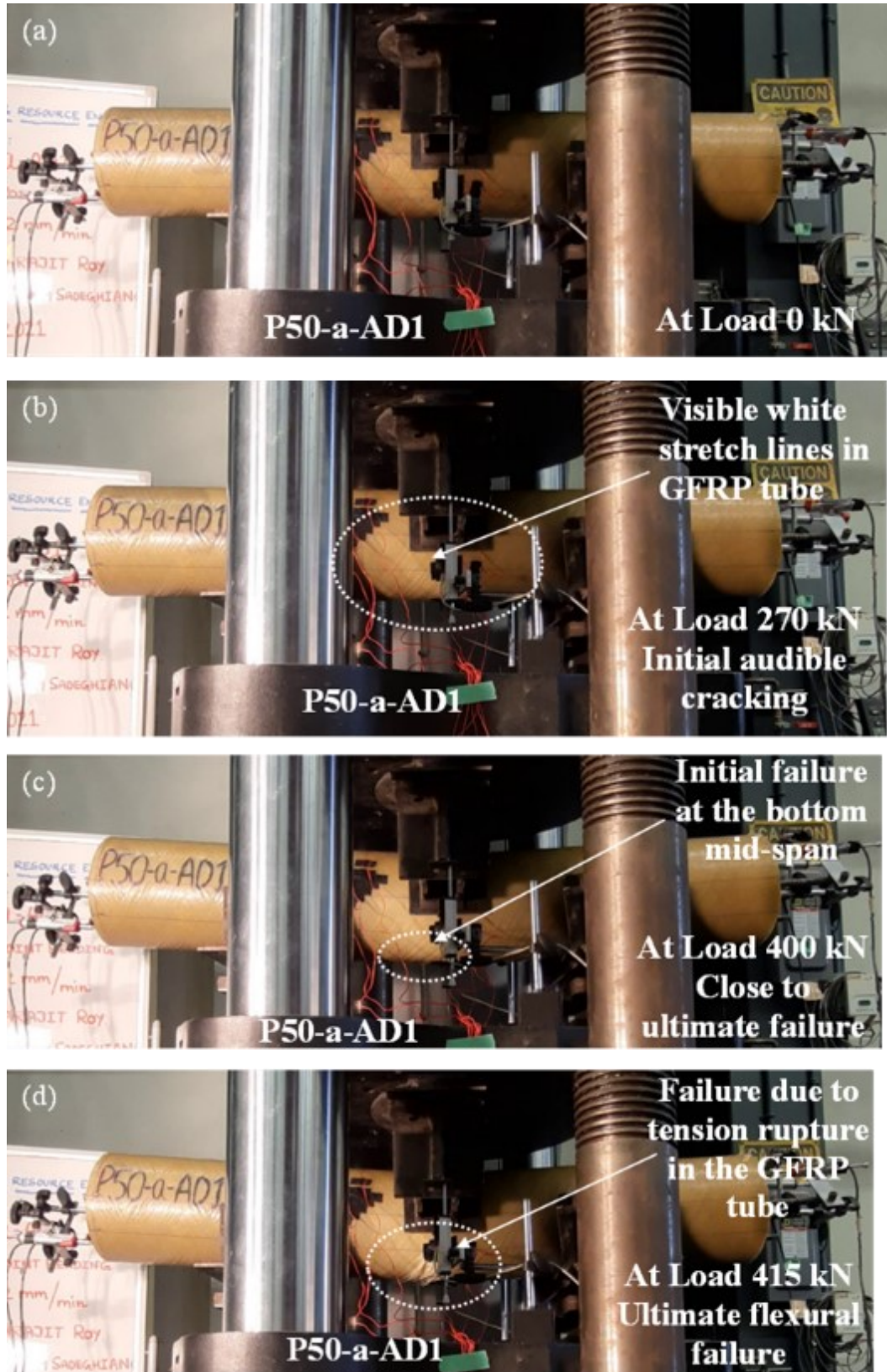


Figure 3-13. Test timelapse of the CFFT specimen P50-a-AD1: (a) At load about 0 kN; (b) At load about 270 kN; (c) At load about 400 kN; (d) At load about 415 kN

Although all tested CFFT specimens experienced flexural failure, which was the primary reason for the CFFTs' ultimate failure, the short-span CFFT specimens experienced compression cracks near the top steel support region. More specifically, the specimens reinforced with 15M steel rebars endured severe compression cracks around the top steel support, as shown in figures 3-14 (b) and 3-14 (e). The addition of neoprene rubber pads in between the steel supports and the test specimens significantly suppressed this problem to a certain extent. Out of all the short span specimens, the CFFT specimen P50-a-AD1 did not experience any compression cracks. In contrast, those specimens encountered a necking phenomenon, which possibly was an earlier stage for the compression crack development, as seen in figure 3-14 (a). Compared to short-span test specimens, apart from specimen P150-b-AD2.25, the longer span CFFT specimens did not experience any compression crack development under the top steel support. Figure 3-14 (g) shows minor compression crack development in the P150-b-AD2.25 CFFT specimen. Moreover, a trend was observed near the ultimate load capacity for the CFFT with the thinnest wall thickness. The CFFT specimens with P50 GFRP tube experienced an ultimate tensile rupture in the bottom tension surface at the mid-span by a crumbling manner with a distinctive audible cracking sound.

Furthermore, to understand the effect of shear span to depth ratio on the failure mode in the internal concrete core, P100 CFFT specimens which were internally reinforced with 10M steel rebars, were cut open. Figures 3-15, 3-16, and 3-17 exhibit a/D_i of 0.5, 1, and 2.25 CFFT specimens with an exposed concrete core, respectively. As seen from all three figures, the flexural failure pattern was similar in the GFRP tubes. The concrete core of CFFT specimens with a/D_i of 0.5, 1, and 2.25 experienced major flexural cracks at the bottom mid-span tension region, which propagated towards the compression zone. The minor web shear and flexural shear cracks were noticed in the CFFT specimens with a/D_i of 0.5 and 1. In contrast, the CFFT specimen with 2.25 did not develop any minor shear cracks but developed a few minor flexural cracks at the moment region.

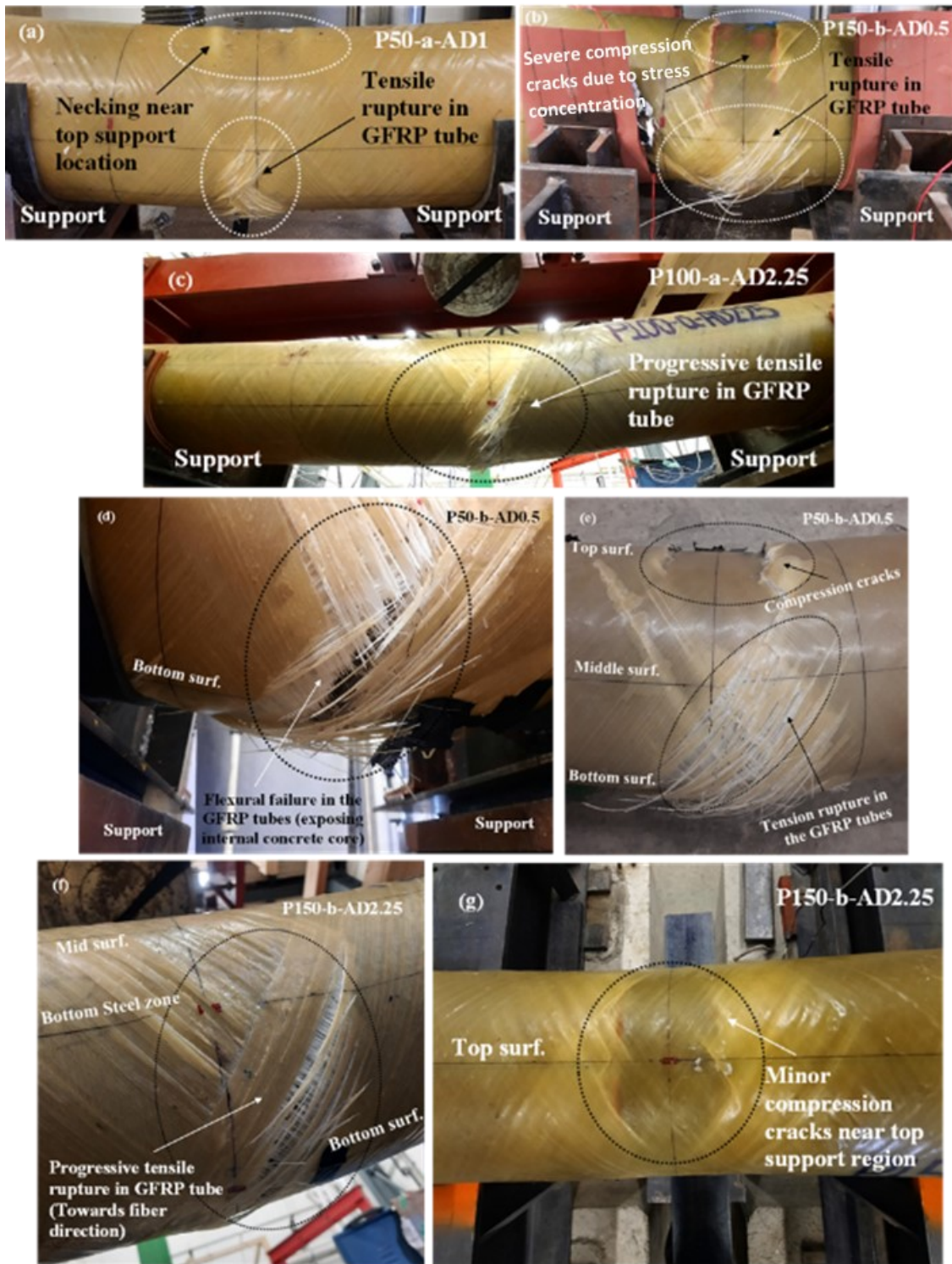


Figure 3-14. Various failure region of CFFT specimens: (a) P50-a-AD1; (b) P150-b-AD0.5; (c) P100-a-AD2.25; (d) Bottom surface of P50-b-AD0.5; (e) Front face of P50-b-AD0.5; (f) Bottom surface of P150-b-AD2.25; (g) Top surface of P150-b-AD2.25



Figure 3-15. Failure modes in P100-a-AD0.5 specimen: (a) Longitudinal cross-section of CFFT; (b) Inner concrete core and outer layer of GFRP tube; (c) Inner layer of GFRP tube

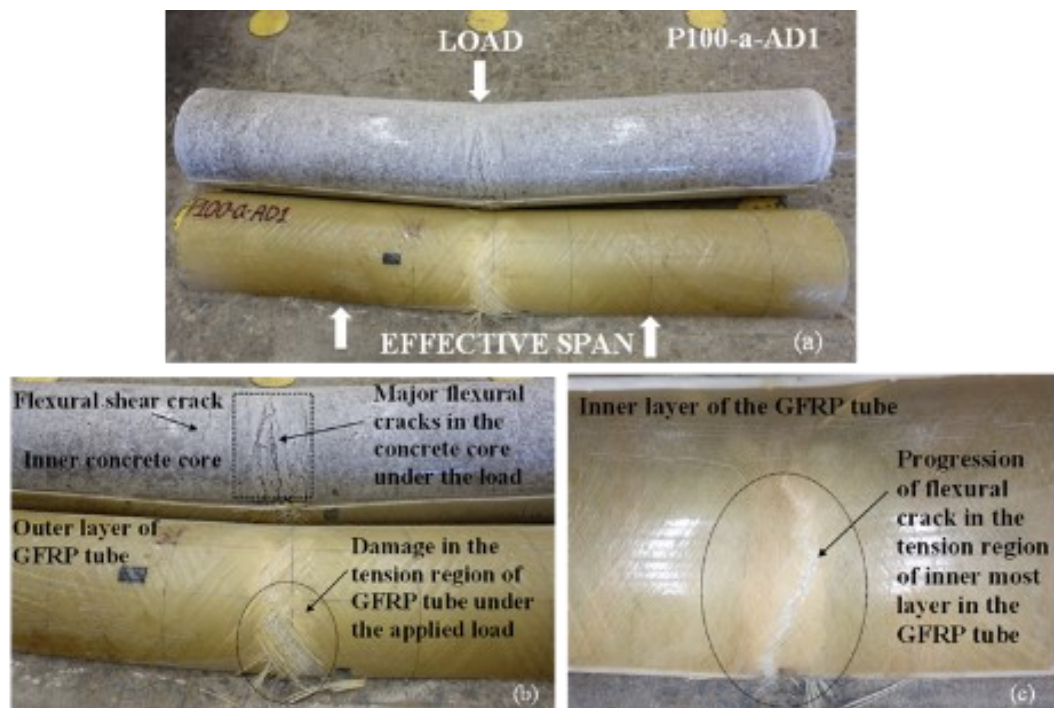


Figure 3-16. Failure modes in P100-a-AD1 specimen: (a) Longitudinal cross-section of CFFT; (b) Inner concrete core and outer layer of GFRP tube; (c) Inner layer of GFRP tube

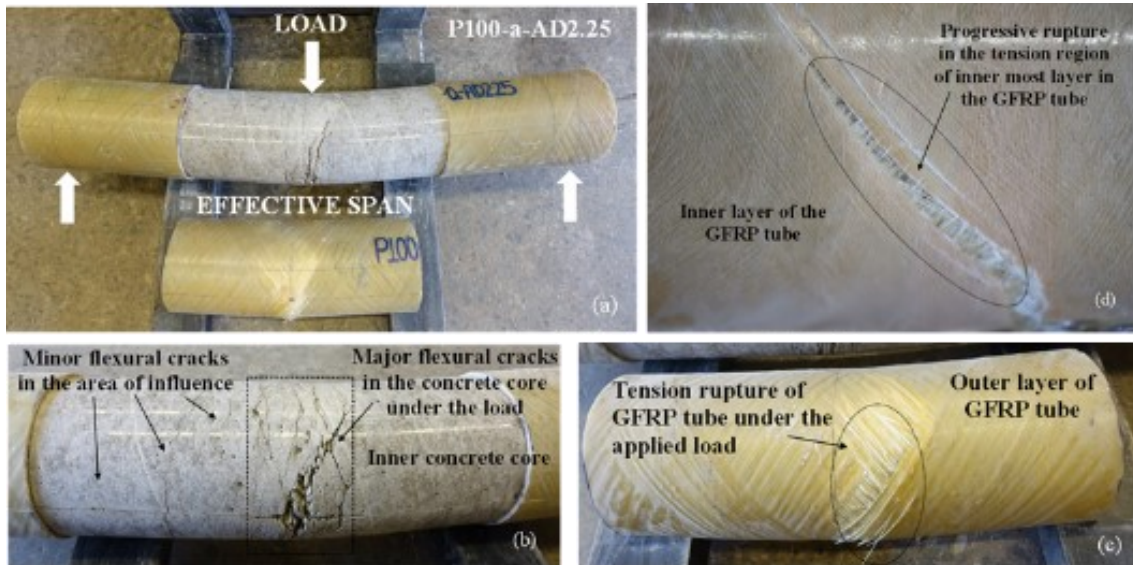


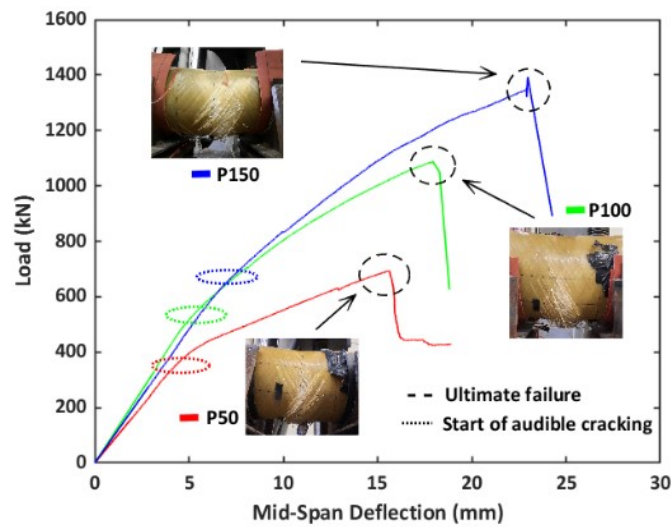
Figure 3-17. Failure modes in P100-a-AD2.25 specimen: (a) Longitudinal cross-section of CFFT; (b) Inner concrete core; (c) Outer layer of GFRP tube; (d) Inner layer of GFRP tube

3.6.2 Load-Deflection Behavior

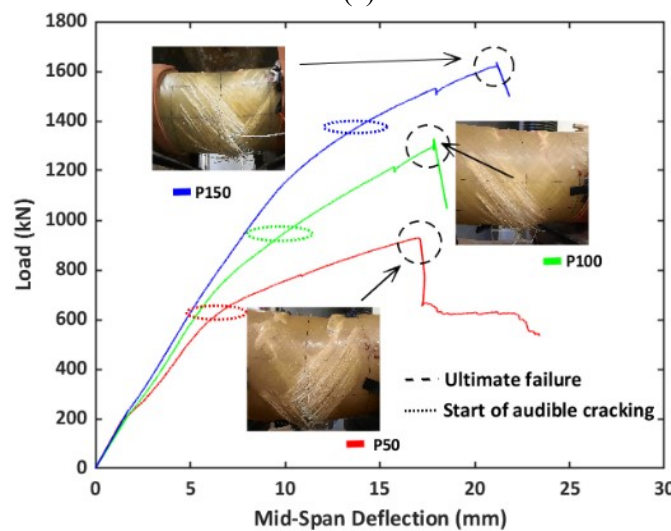
Load deflection behavior of a CFFT beam is an essential factor, considering that the CFFTs are primarily used as structural members such as bridge piers, fender piles, dauphins, etc. Therefore, the applied load at any given point in time during the three-point bend test was captured using a load cell. The corresponding change in mid-span deflection was measured with the help of two linear potentiometers (LP) and a string potentiometer (SP). The linear potentiometers attached to the top steel supports were mainly used to verify the data acquired through the string potentiometer.

Figures 3-18, 3-19, and 3-20 exhibit the load vs. mid-span deflection curves for eighteen CFFT specimens. The acquired mid-span deflection values from two LPs were averaged, which showed good confidence in the data acquired by the string potentiometer. Hence the averaged value of two linear potentiometers was considered and plotted against the load acquired from the DAQ. The deflection data recorded for the test specimen P150-b-AD2.25 showed an unusual load vs. mid-span deflection trend. Three of the deflection recording instruments for that test were not able to record a reliable data source. The issue arose due to a possible malfunction in the DAQ.

The following figures 3-18, 3-19, and 3-20 provide the load vs. mid-span deflection curves for the specimens with a/D_i of 0.5, 1, and 2.25, respectively. The load vs. mid-span deflection curves showed the overall nonlinear behavior of CFFT. The primary contributor to this nonlinearity of CFFT were the GFRP tubes, which have nonlinear behavior. The sudden drop in the load for the P150 specimen near 300 kN, as visualized in figure 3-19 (b), was due to the movement in the testing frame. Furthermore, the minor drops in the load for the P150 specimens around 85% of its ultimate capacity, as observed in figure 3-18 (b), 3-19 (b), and 3-20 (b), was speculated possibly due to the severe crushing experienced by the CFFT specimens at the compression region near the top steel support as exhibited in figure 14 (b), and figure 14 (g).



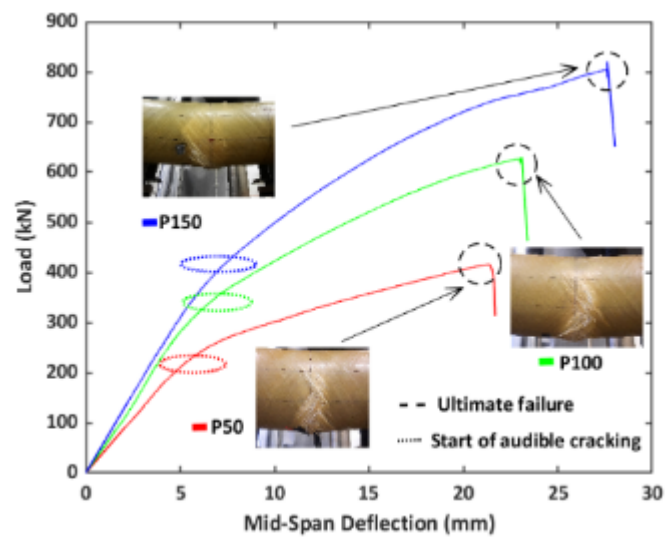
(a)



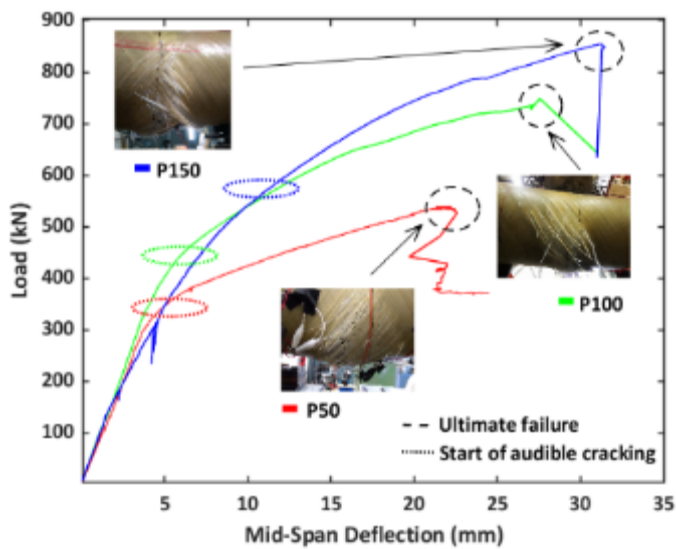
(b)

Figure 3-18. Load vs. Mid-span deflection for a/D_i of 0.5 specimens: (a) 10M; (b) 15M

The possible start of audible cracking in CFFT specimens was noticed during the tests. Overall, the CFFT specimens with the a/D_i of 0.5 and 1 produced a notable amount of audible cracking sound. In contrast, CFFT specimens with the a/D_i of 2.25 did not cause any significant cracking sounds. This initial audible cracking was observed for 15M and 10M specimens around 70% and 50% of their ultimate capacity, respectively. From the load vs. mid-span deflection curves, it is also identified that the commencement in the audible cracking occurred when the CFFT member transitioned from the linear phase to a nonlinear one.

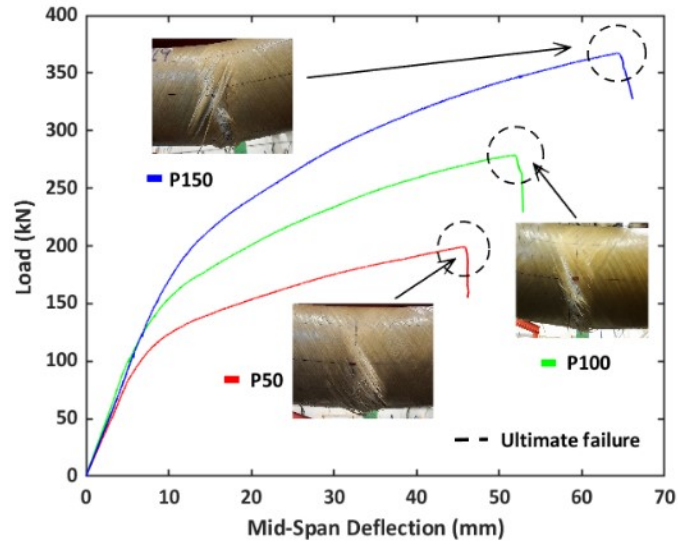


(a)

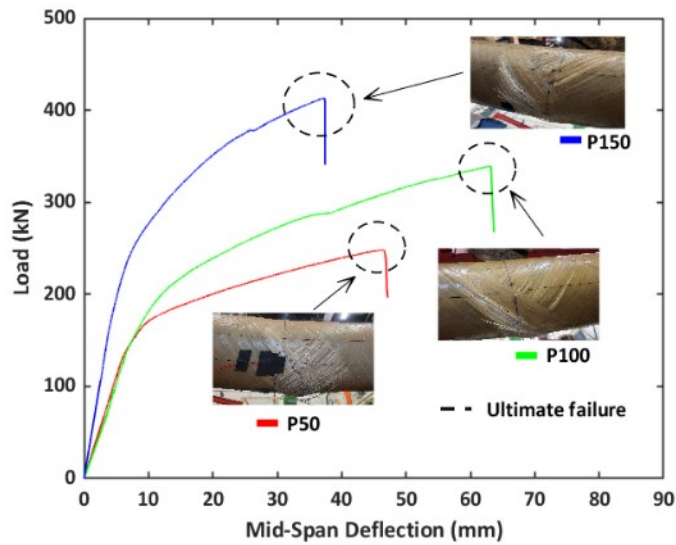


(b)

Figure 3-19. Load vs. Mid-span deflection for a/D_i of 1 specimens: (a) 10M; (b) 15M



(a)



(b)

Figure 3-20. Load vs. Mid-span deflection for a/D_i of 2.25 specimens: (a) 10M; (b) 15M

3.6.3 Effect of Shear Span to Depth Ratio

One of the influential parameters of this study was to understand the effect of the a/D_i ratio on the CFFT specimens. Therefore, the effect of the shear span to depth ratio is compared in terms of change in the load capacity and mid-span deflection of the test specimens. The overall increase in the load capacity is exhibited in figures 3-21 (a) and (b) for 10M and 15M steel-reinforced CFFT specimens, respectively.

All the CFFT specimens experienced an increase in their load capacity with the decrease in the a/D_i ratio; on the contrary, the mid-span deflection decreased. Therefore, the load capacity comparison between a/D_i ratio of 0.5 to 1, 1 to 2.25, and 0.5 to 2.25 for similar CFFT specimens had been drawn. P50-CFFT specimens reinforced with 10M rebars showed an increase in their load capacity close to 66%, 108%, and 247% compared to the above-stated ratios. Similarly, P50-CFFT specimens reinforced with 15M rebars showed an increase in their load capacity close to 72%, 117%, and 274%. P100-CFFT specimens reinforced with 10M steel rebars exhibited an increase in the load capacity around 74%, 126%, and 294%. In the case of P100-15M CFFT specimens, the load capacity increase was near 77%, 117%, and 292%. Finally, the P150-CFFT specimens reinforced with 10M steel rebars experienced an increase of about 70%, 123%, and 279%, and 15 M steel-reinforced specimens with the same GFRP tube showed an increase of 91%, 106%, and 296%, respectively.

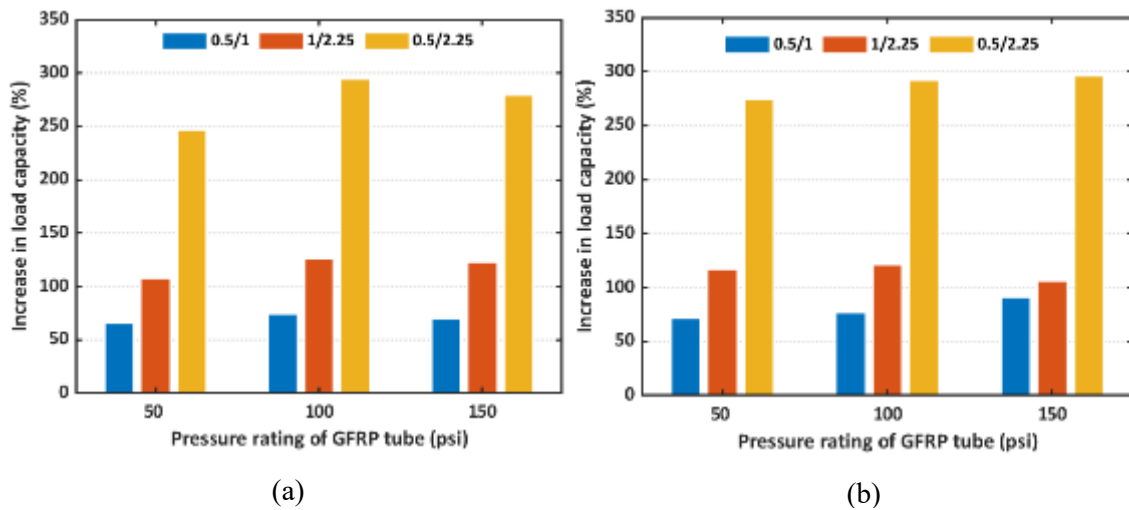


Figure 3-21. Influence of a/D_i ratios on the load capacity of CFFTs: (a) 10M; (b) 15M

A comparison between mid-span deflection has been drawn in the similar means to the load capacity for the CFFT specimens. The decreasing trend in the mid-span deflection for all CFFT was in a close range apart from P150-15M CFFT specimens. The decrease in deflection was in the range of 17% to 35%, 52% to 57%, and 63% to 72% for the a/D_i ratio of 0.5 to 1, 1 to 2.25, and 0.5 to 2.25, respectively. In contrast, the decrease in deflection for P150-15M specimens were 32%, 17%, and 44% for the a/D_i ratio of 0.5 to 1, 1 to 2.25, and 0.5 to 2.25, respectively. This anomaly in the trend was possibly due to the slower loading rate adopted during the test for the P150-b-AD2.25 specimen. Thus, the overall

comparison showed that as the a/D_i ratio decreases, the load capacity of the CFFT increases. This increase in capacity is mainly attributed due to the contribution of the GFRP tube and dowel action by the internal reinforcement.

3.6.4 Effect of Internal Longitudinal Reinforcement

This section explores the effect of the internal reinforcement on the load capacity of the CFFT specimens. Figure 3-22 (a), (b), and (c) shows the comparison in load-midspan deflection behavior of both 10M and 15M reinforced specimens with P50, P100, and P150 GFRP tubes, respectively.

The results showed that independent of the a/D_i ratio, the overall contribution of the internal reinforcement was higher for P50 CFFT specimens than the rest. The internal reinforcement contribution to the load capacity was in a descend for P100 CFFT and P150 CFFT specimens. The individual CFFT specimens were generally prepared with six internal rebars, but the contrast was mainly in their internal reinforcement ratio and the yield strengths. The 15M steel reinforced and 10M steel-reinforced CFFTs had an internal reinforcement ratio of 3.70% and 1.85%, respectively. The difference in the internal reinforcement showed its prominent influence on the ultimate load capacity and the overall load-deflection behavior of CFFT as the load capacity was comparatively high for 15M-CFFT specimens than 10M-CFFT specimens. For the a/D_i of 0.5, CFFT specimens with P50, P100, and P150 tubes had an ultimate load capacity increase of 34%, 21%, and 18%, respectively, when the internal longitudinal reinforcement ratio increased from 1.85% to 3.70%. This trend in the ultimate load capacity remained vastly identical for the CFFT specimens of a/D_i of 1 and 2.25. The P50, P100, and P150 CFFT specimens, when tested under a/D_i of 2.25, exhibited a load capacity increase of 25%, 22%, and 13%, respectively. In the case of the CFFT specimens tested under shear span to depth ratio of 1, a load capacity increase of 29% and 19% were observable for P50 and P100 specimens.

In contrast, the P150 CFFT specimen under the similar a/D_i , showed an increase of 5% in the load capacity when the internal reinforcement ratio increased from 1.85% to 3.70%. This anomaly in the load capacity trend could be speculated due to the difference in the loading rate used during the test. Thus, although all the CFFT specimens failed similarly

under various testing parameters, the effect of internal reinforcement is more critical in this case due to its significant impact that changed the load capacity and load-deflection behavior for the CFFT specimens.

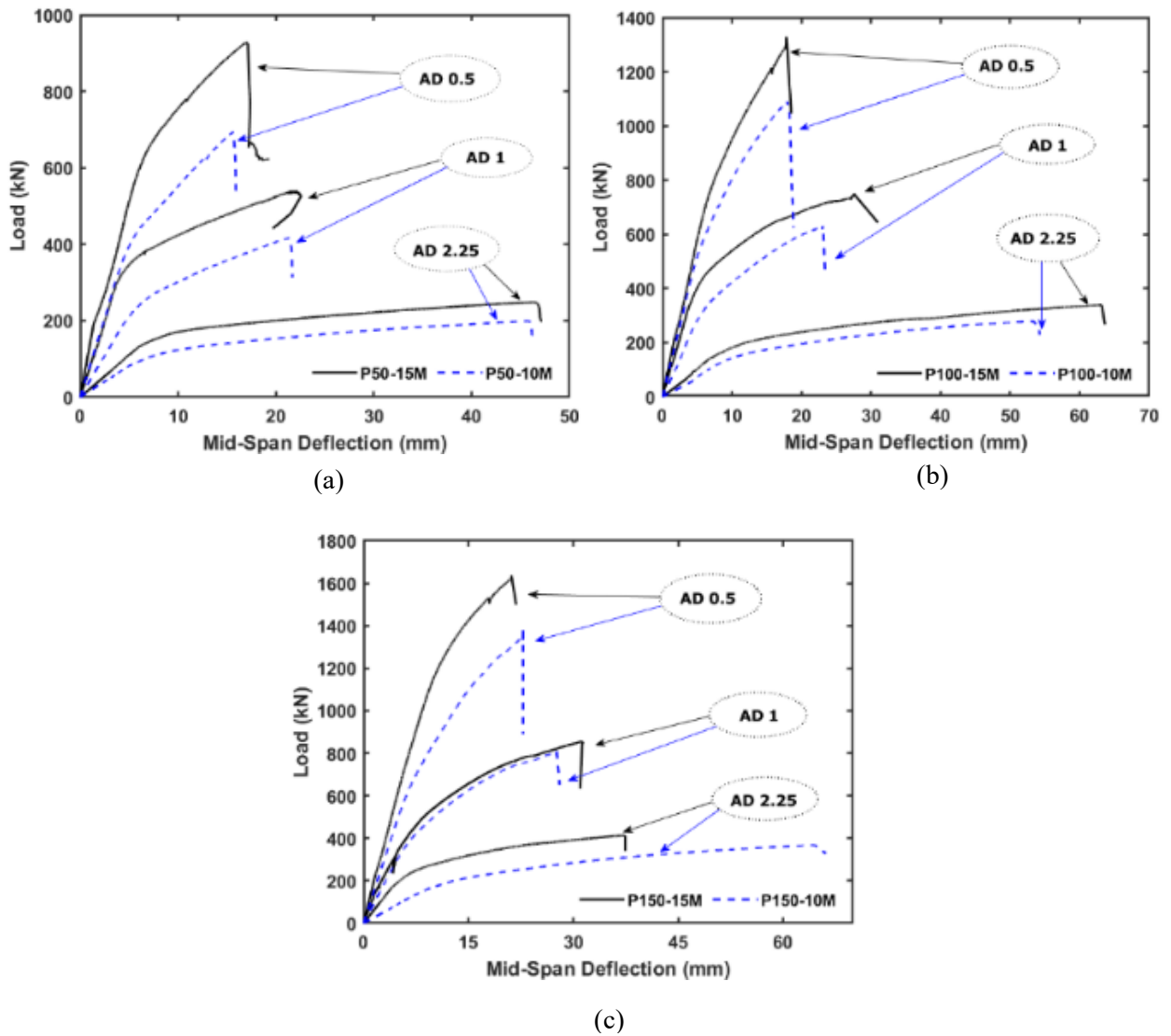


Figure 3-22. Effect of longitudinal reinforcement ratio on CFFTs: (a) P50; (b) P100; (c) P150

3.6.5 Effect of Pressure Rating

This section presents a comparison study on the effect of pressure rating of the GFRP on the behavior of CFFTs. The GFRP tubes with a constant inner diameter had three different pressure ratings, 50, 100, and 150 psi, directly related to their wall thickness. The P50, P100, and P150 GFRP tubes had an inner diameter to thickness ratio (D_i/t) of 75, 43, and 30, respectively, as provided in table 3-1. Figures 3-23 and 3-24 provide the effect of pressure rating in terms of the wall thickness of the GFRP tube on 10M and 15M-CFFT specimens, respectively. From the test results, it was evident that P150 tubes increased the CFFTs' ultimate load capacity significantly compared to P100 and P50 GFRP tubes. In addition, the percentage increase in the load capacity between P50 vs. P100 CFFT was higher when compared to P100 vs. P150 CFFTs for both 10M and 15M steel-reinforced specimens. This significant increase in ultimate load capacity between P50 and P100 CFFT specimens was perhaps due to the low amount of fibers present in the P50 GFRP tubes than it was supposed to have.

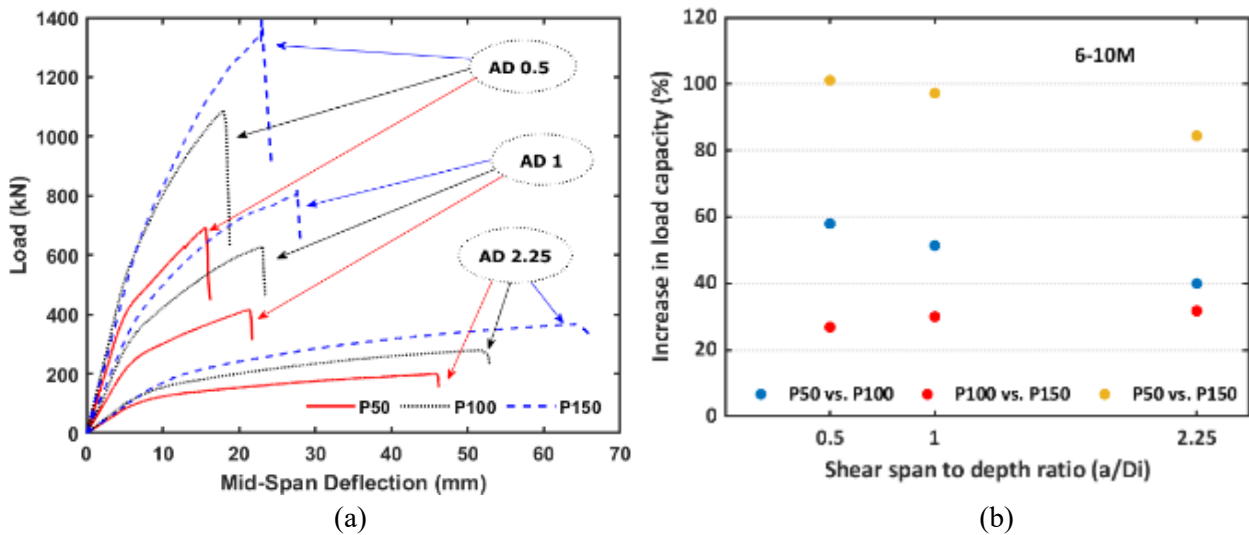


Figure 3-23. Effect of pressure rating of GFRP tubes on 10M steel-reinforced CFFTs:
 (a) Load-deflection behavior; (b) Percentage increase in load capacity

For CFFT specimens reinforced with 10M steel rebars tested under a/D_i of 0.5, the increase in load capacity was close to 101%, 58%, and 27% when compared between P50 vs. P150, P50 vs. P100, and P100 vs. P150 CFFT specimens, respectively. The 10M-CFFT specimens tested under a/D_i of 1 showed an increase in capacity around 97%, 51%, and 30% when compared to P50 vs. P150, P50 vs. P100, and P100 vs. P150 CFFT specimens, respectively. Similarly, when the specimens tested under a/D_i of 2.25 showed an increase of approximately 85%, 40%, and 32% when compared to P50 vs. P150, P50 vs. P100, and P100 vs. P150 CFFT specimens, respectively, as shown in figure 3-23 (b).

In the case of CFFT specimens reinforced with 15M steel rebars, the overall trend regarding the ultimate load capacity was similar to that of 10M steel-reinforced CFFTs, as shown in figure 3-24 (b). The specimens tested under a/D_i of 0.5 showed an increase in capacity around 76%, 43%, and 23% when compared to P50 vs. P150, P50 vs. P100, and P100 vs. P150 CFFT specimens, respectively. The specimens tested with an a/D_i of 2.25 experienced an increase in the ultimate load capacity of 67%, 36%, and 22% for P50 vs. P150, P50 vs. P100, and P100 vs. P150 CFFT specimens, respectively. In contrast, the similar specimens tested under a/D_i of 1 showed a load capacity increase of 59%, 39%, and 14% for P50 vs. P150, P50 vs. P100, and P100 vs. P150 CFFT specimens, respectively. Thus, the overall comparison of the result shows that the load capacity of CFFT increased with the increase in the inner diameter to thickness ratio (D_i/t) of the GFRP tube.

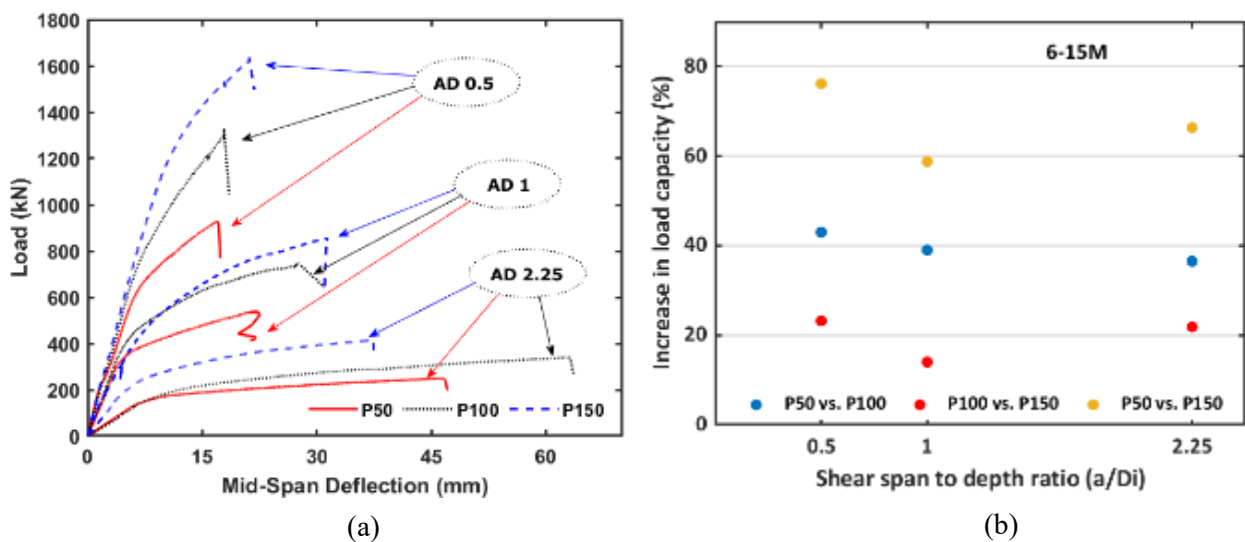


Figure 3-24. Effect of pressure rating of GFRP tubes on 15M steel-reinforced CFFTs:
 (a) Load-deflection behavior; (b) Percentage increase in load capacity

3.6.6 Moment Capacity

Figure 3-25 illustrates the overall moment capacity of the CFFT specimens, depending upon the GFRP tube's pressure rating. The moment capacity of the CFFTs was calculated with the help of their load capacity. Figures 3-25 (a) and 3-25 (b) showed that independent of the internal steel reinforcement, the CFFT with the greater GFRP tube wall thickness had a greater ultimate moment capacity.

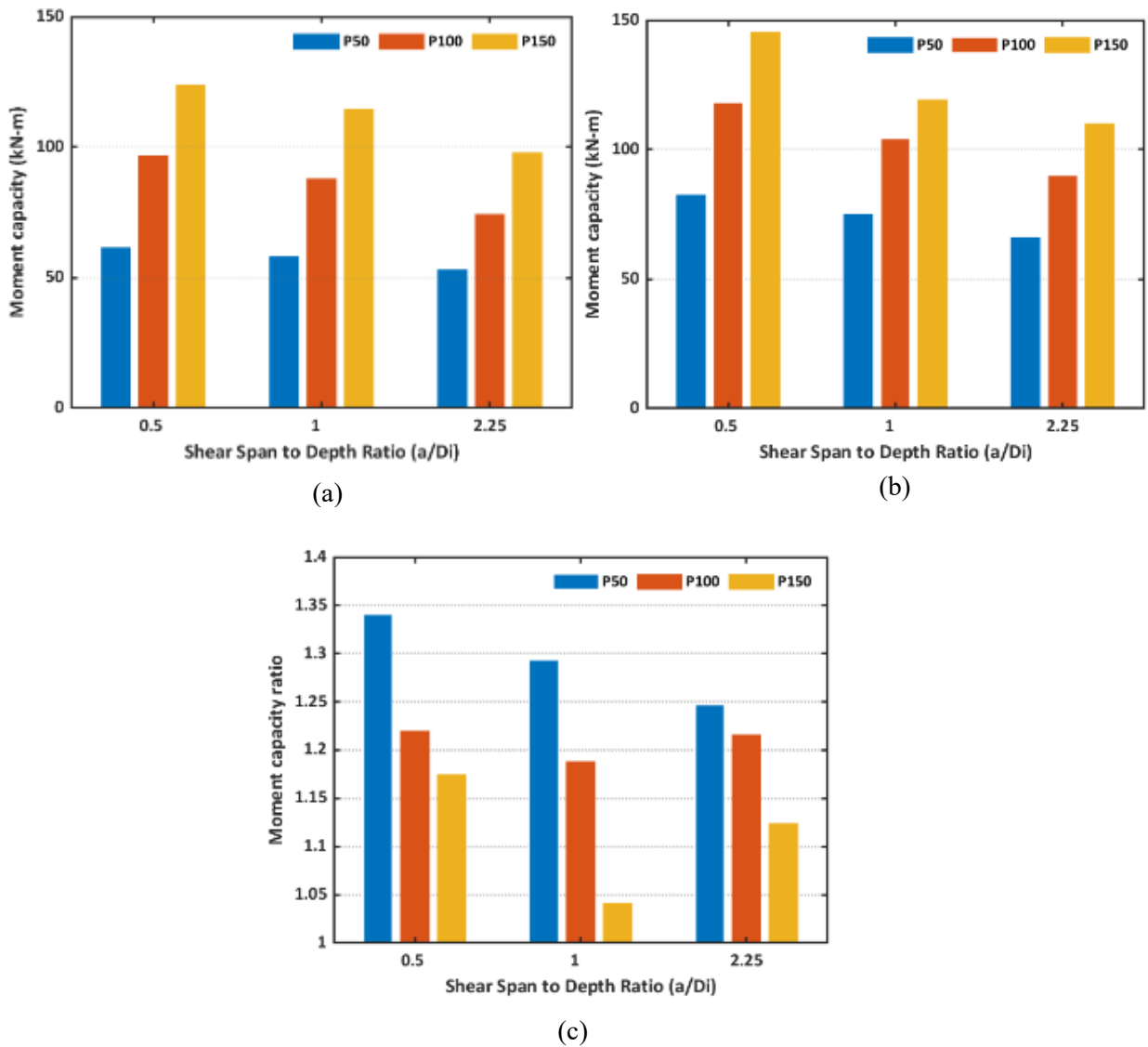


Figure 3-25. Effect of pressure ratings of GFRP tube on moment capacity of CFFTs:
 (a) 10M; (b) 15M; (c) Ratio of 15M and 10M specimens

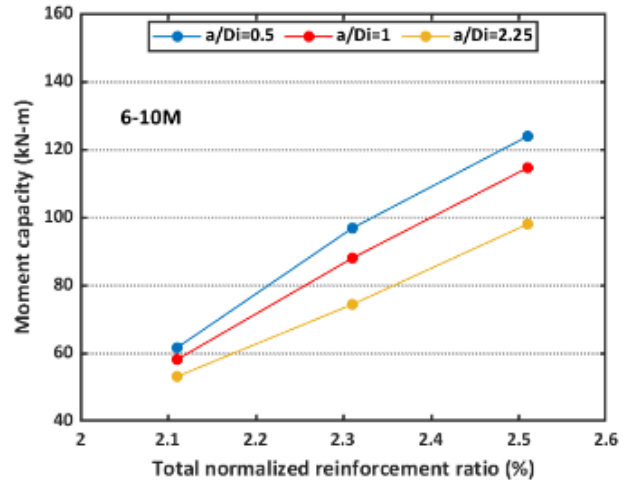
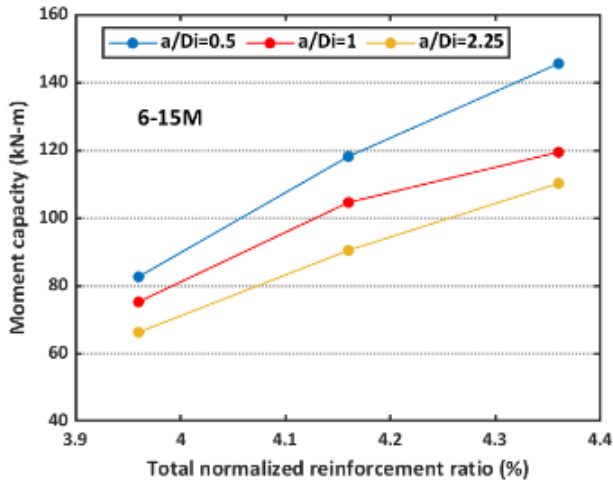
Table 3-6. Summary of CFFT Specimens' reinforcement ratio

Case Number	CFFT SPECIMEN ID	Steel Reinforcement Ratio	GFRP Tube Area (mm²)*	GFRP Reinforcement Ratio (%)	Normalized FRP to Steel Reinforcement Ratio (%)	Total Normalized Reinforcement Ratio (%)
1	P50-a-AD0.5		1742	5.37	0.26	2.11
2	P100-a-AD0.5	1.85	3103	9.57	0.46	2.31
3	P150-a-AD0.5		4405	13.58	0.66	2.51
4	P50-b-AD0.5		1742	5.37	0.26	3.96
5	P100-b-AD0.5	3.70	3103	9.57	0.46	4.16
6	P150-b-AD0.5		4405	13.58	0.66	4.36
7	P50-a-AD1		1742	5.37	0.26	2.11
8	P100-a-AD1	1.85	3103	9.57	0.46	2.31
9	P150-a-AD1		4405	13.58	0.66	2.51
10	P50-b-AD1		1742	5.37	0.26	3.96
11	P100-b-AD1	3.70	3103	9.57	0.46	4.16
12	P150-b-AD1		4405	13.58	0.66	4.36
13	P50-a-AD2.25		1742	5.37	0.26	2.11
14	P100-a-AD2.25	1.85	3103	9.57	0.46	2.31
15	P150-a-AD2.25		4405	13.58	0.66	2.51
16	P50-b-AD2.25		1742	5.37	0.26	3.96
17	P100-b-AD2.25	3.70	3103	9.57	0.46	4.16
18	P150-b-AD2.25		4405	13.58	0.66	4.36

*From previous study by Betts et al. (2020)

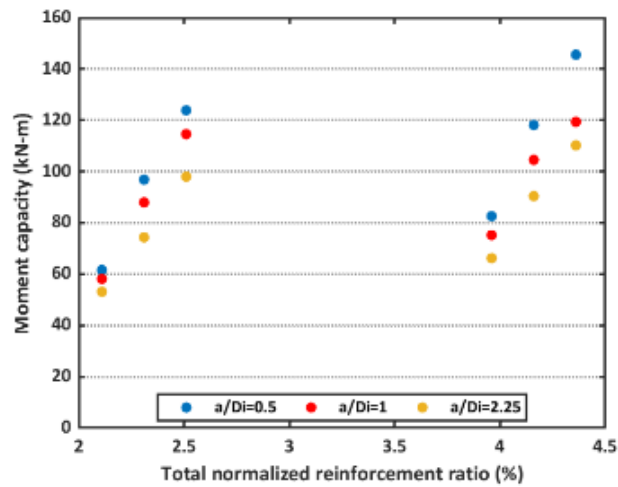
In other words, the pressure rating of the GFRP tube was directly comparable to the moment capacity of the CFFT specimens. As the GFRP reinforcement ratio increased with it, the moment capacity also increased. It is also observed that as the a/D_i decrease for the CFFTs, the moment capacity of the CFFTs increases. In general, the increase in the moment capacity was significant between a/D_i of 0.5 and 2.25 CFFT specimen when compared among successive a/D_i ratios of 0.5, 1, and 2.25. The percentage increase in the moment capacity was least when compared between the specimens of a/D_i 0.5 and 1. The only inconsistency in this ascending trend is observed for the specimens of the P150 CFFT group reinforced with 15M steel rebars. The moment capacity increase was 32% when compared between a/D_i of 0.5 and 2.25, showing a similar trend towards the rest. The moment capacity increase was 22% and 8% when compared between a/D_i of 0.5 and 1; and a/D_i of 1 and 2.25, respectively. This discrepancy in the result was perhaps due to specimen P150-b-AD1, which was tested under a lower loading rate. Furthermore, the internal steel reinforcement had a significant contribution towards the ultimate moment capacity of CFFTs. The contribution of steel reinforcement towards moment capacity was maximum for the P50 CFFT specimens. Altogether CFFTs reinforced with 15M steel rebars showed a considerable increase in moment capacity, particularly for the P50 CFFT tested under a/D_i of 0.5 showed an increase of 34% in their ultimate moment capacity.

Additionally, figure 3-26 shows the effect of combined normalized GFRP and steel reinforcement ratio on moment capacity based on the a/D_i ratios. Table 3-6 presents a summary of reinforcement ratios for CFFT specimens. P150 CFFT reinforced with 15M steel rebar and P50 CFFT specimens reinforced with 10M steel rebars had the highest and the lowest total normalized reinforcement ratio among the rest of the specimens, respectively. The effect on the moment capacity due to the difference in the reinforcement ratio was evident from figure 3-26, as the moment capacity of P150 CFFT with 15M steel-reinforced specimens was significantly higher than P50 CFFT with reinforced with 10M steel rebars. The increment effect of lower a/D_i ratio combined with normalized reinforcement ratio on moment capacity of CFFT can easily be perceived from figure 3-26 (c).



(a)

(b)



(c)

Figure 3-26. Effect of reinforcement ratio on moment capacity of CFFTs:

(a) 15M; (b) 10M; (c) Both 15M and 10M specimen

3.6.7 Load-Strain and Moment-Curvature

This section presents a brief overview of load vs. strain at mid-span, load vs. strain from strain rosette at the mid-shear span, and the moment-curvature response of the CFFTs subjected to three-point bending. Figures 3-27 (a) and 3-28 (a) exhibits load vs. mid-span strain for 10M steel-reinforced CFFT specimens tested under a/D_i of 1 and a/D_i of 0.5, respectively. Figures 3-27 (b) and 3-28 (b) shows load vs. mid-shear span strain from strain rosette for 10M steel-reinforced CFFT specimens tested under a/D_i of 1 and a/D_i of 0.5, respectively. Figures 3-27 (c) and 3-28 (c) illustrate the respective specimens' moment-curvature behavior.

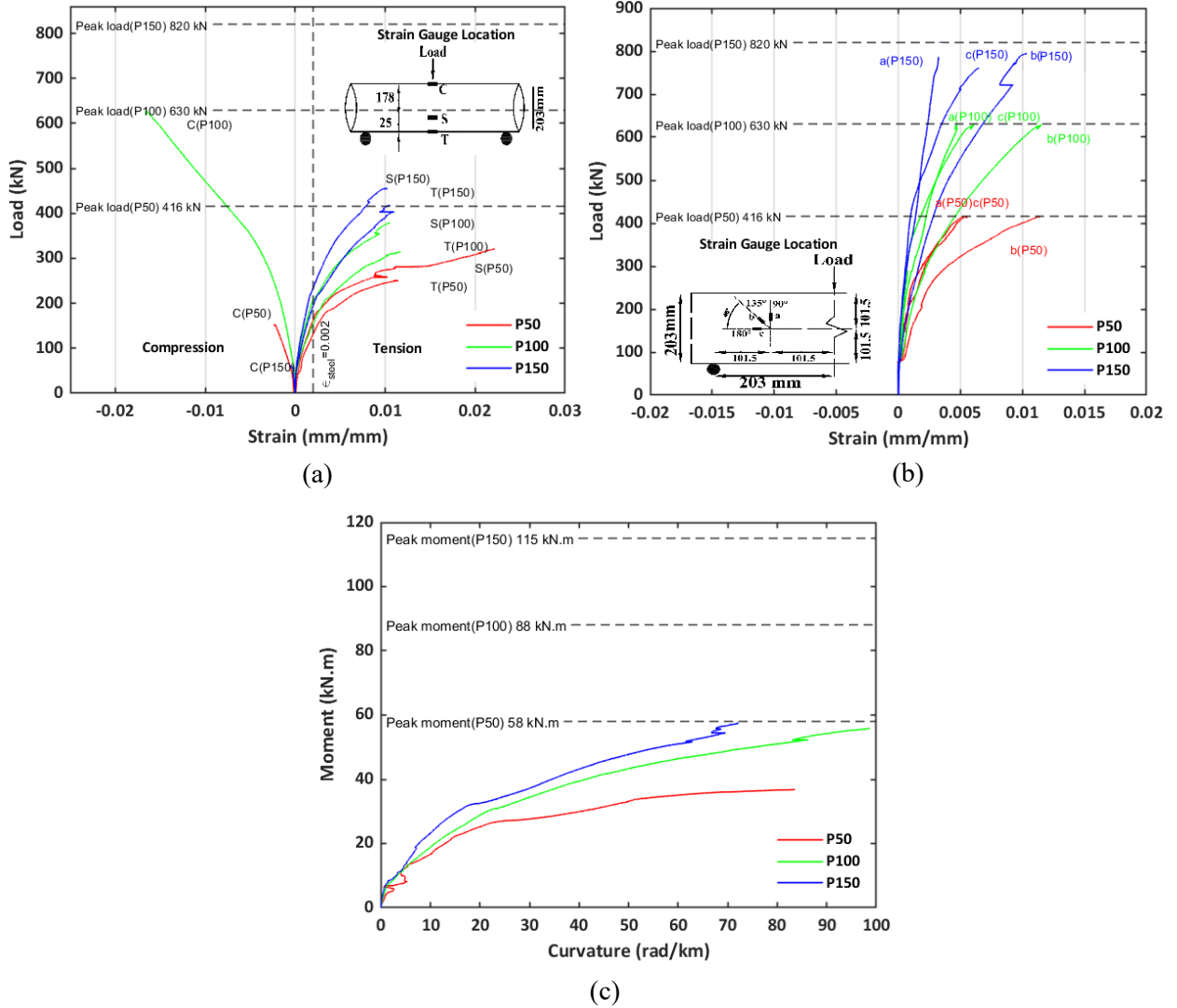


Figure 3-27. 10M steel-reinforced CFFT specimens with a/D_i of 1: (a) Load vs. mid-span strain; (b) Load vs. strain rosette; (c) Moment-curvature response at mid-span

The various acquired strain data from the tests was limited due to the strain gauges data limitation of ± 0.01 and the development of any damage near the strain gauge zones. Moment-curvature responses are not only essential for obtaining the flexural rigidity constant, it also provides the location of the neutral axis under various loading. The CFFT specimens had been assigned with three strain gauges in the top extreme compression fiber, bottom extreme tension fiber, and bottom steel reinforcement region, affixed to the outer surface on CFFT specimen at mid-span as shown in figure 3-10 (c). With the help of linear strain distribution relation for sectional analysis, the curvature for any particular load was calculated by joining a minimum of two strain gauge data points with a straight line and finding the arc tangent value of the gradient of the straight line (equation 3-1).

$$\varphi = \arctan(m) \dots\dots\dots 3-1$$

where,

φ is curvature at mid-span of the CFFT specimen (rad/km)

m is the gradient of the st. line, joining three (minimum two) strain values at compressive and tensile strain locations shown in figure 3-10 (c)

Due to the limitation in strain data, the complete moment-curvature relationship of CFFTs was not apprehended. From the processed data, the moment-curvature curve showed an early linear behavior. However, as the moment increased, the moment-curvature relation became a nonlinear one. The fluctuation in the moment-curvature curves was mainly due to the fluctuation in the acquired strain data during the testing. Additional load-strain and moment-curvature curves for the rest of the CFFTs were presented in APPENDIX-I.

Furthermore, the CFFT specimens were not failed in shear, so the requirement of calculating the principal tensile strain and the direction of principal tensile strain was not critical for this study. However, using strain transformation equations and the acquired strain data from the strain rosette, principal tensile strain and angle can be calculated. The transformation equations are listed as follows:

$$\varepsilon_p = \frac{\varepsilon_H + \varepsilon_V}{2} + \sqrt{\left(\frac{\varepsilon_H - \varepsilon_V}{2}\right)^2 + \left(\frac{\gamma_{xy}}{2}\right)^2} \dots\dots\dots 3-2$$

$$\gamma_{xy} = 2\varepsilon_D - (\varepsilon_H + \varepsilon_V) \quad \dots\dots\dots 3-3$$

$$\tan 2\theta = \frac{\gamma_{xy}}{\varepsilon_H - \varepsilon_V} \quad \dots\dots\dots 3-4$$

where,

ε_p is principal tensile strain; ε_H is longitudinal strain; ε_V is circumferential strain;

ε_D is diagonal strain; γ_{xy} is shear strain; θ is angle of the principal tensile strain

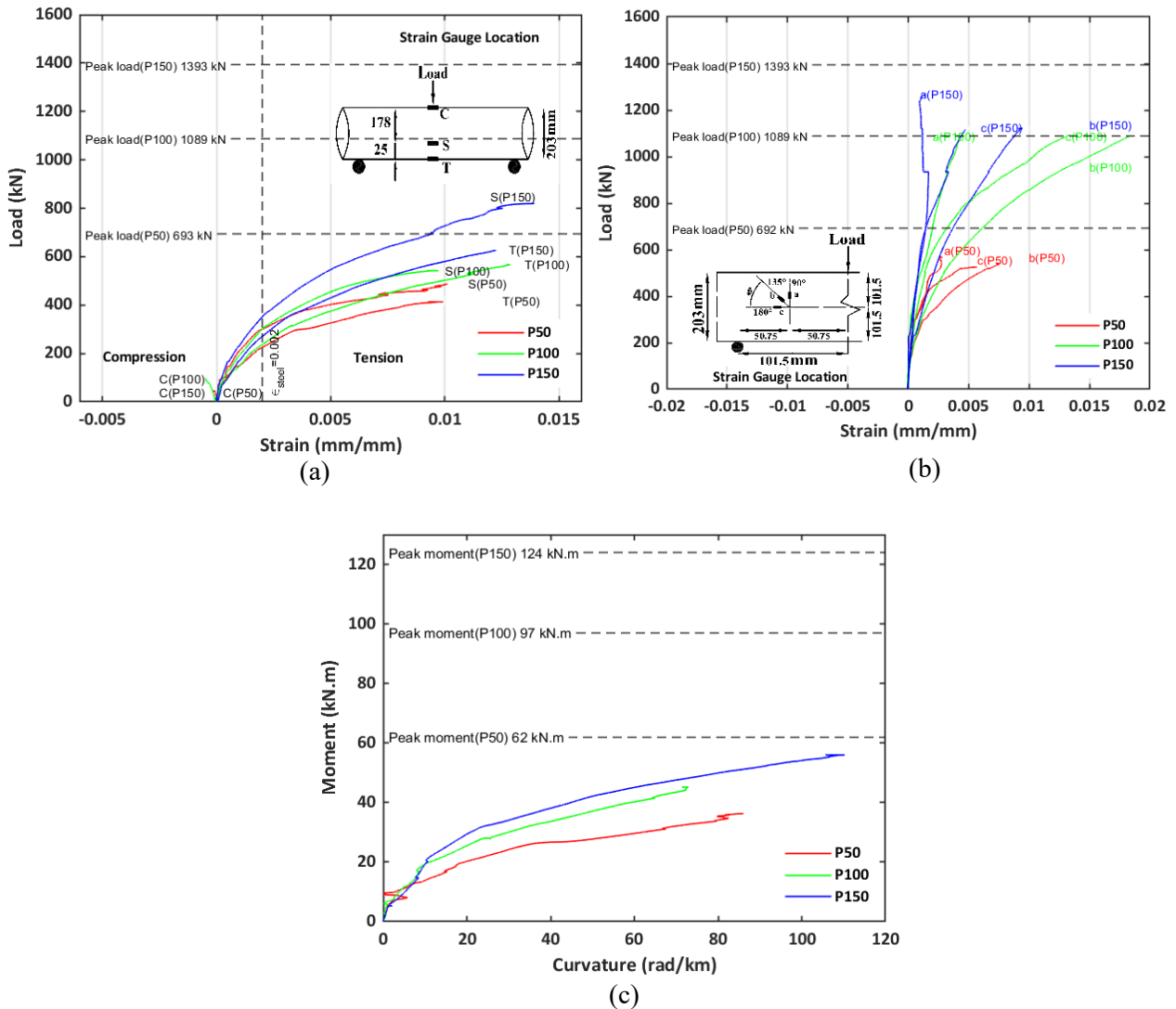


Figure 3-28. 10M steel-reinforced CFFT specimens with a/D_i of 0.5: (a) Load vs. mid-span strain; (b) Load vs. strain rosette; (c) Moment-curvature response at mid-span

3.6.8 Neutral Axis Depth and Compositeness

Figures 3-29 (a) and (b) show the neutral axis location at mid-span for the 10M steel-reinforced CFFT specimens tested under a/D_i of 1 and a/D_i of 0.5, respectively. The neutral axis depths were calculated and plotted in the curves until the availability of reasonable strain data at mid-span. Three strain data from the three affixed strain gauges at the mid-span, as shown in figure 3-10 (c), were considered for a particular load. Then, with the help of linear strain distribution relation for sectional analysis, the neutral axis depth for any particular load was calculated with the help of straight-line coefficients by joining a minimum of two strain gauge data points with a straight line and finally dividing the coefficients of the straight line (equation 3-5).

$$x = -\frac{c}{m} \quad \dots\dots\dots 3-5$$

where,

x is location of neutral axis

c is y-intercept of straight line

m is the gradient of straight line

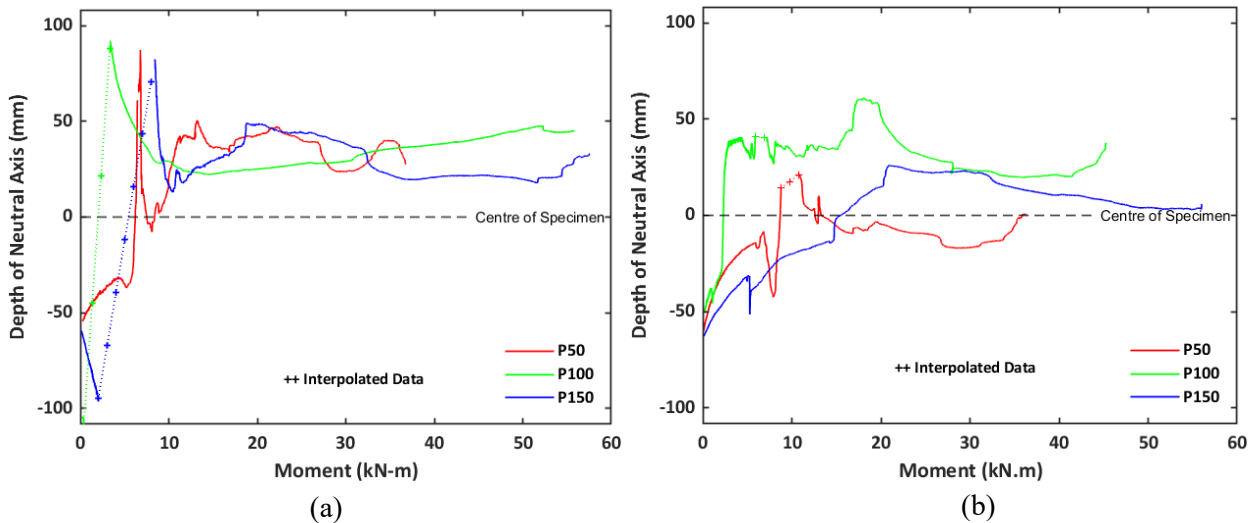


Figure 3-29. Location of neutral axis vs. moment at mid-span: (a) 10M steel-reinforced CFFTs with a/D_i of 1; (b) 10M steel-reinforced CFFTs with a/D_i of 0.5

The composite behavior between the components of the CFFT plays an essential role, and a previous study by (Fam and Rizkalla 2002) showed that slip between components of CFFT had some adverse effect on the CFFT behavior. The compositeness between different CFFT components was determined based on the measured slip between GFRP tube and concrete core; and steel rebar and concrete core. Figures 3-30 (a) and (b) exhibits slip between concrete core-steel rebar and concrete core-GFRP tube for the 10M CFFT specimens tested under a/D_i of 1, respectively. Also, figures 3-31 (a) and (b) show slip between concrete core-steel rebar and concrete core-GFRP tube for the 10M CFFT specimens tested under a/D_i of 0.5, respectively. In general, for most CFFT specimens, the slippage experienced between concrete core and GFRP tube was slightly higher than the concrete core and steel rebars. Although no bond-enhancing measures were taken during the specimen preparation, the maximum slip between the GFRP tube and concrete core was measured near the peak load at the right end of the P150-a-AD1 specimen. The recorded slip value was minimal (near 0.7 mm). These minor slip values further showed the enhanced composite action of the CFFT system, attributed mainly due to the presence of the internal steel rebar.

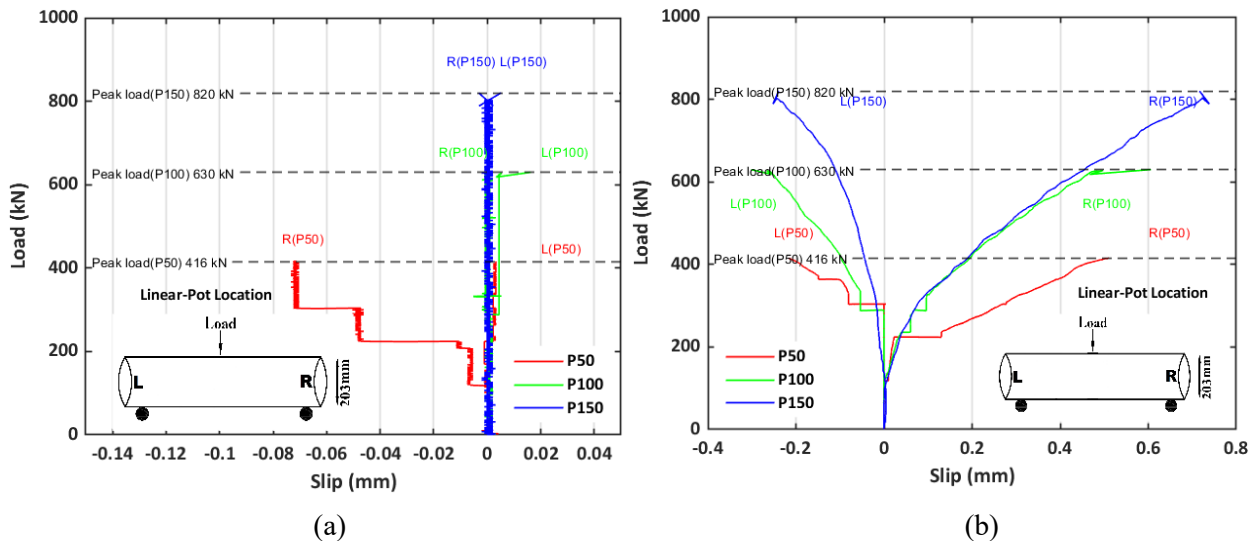


Figure 3-30. Compositeness of 10M steel-reinforced CFFTs with a/D_i of 1 based on slip:
 (a) Between concrete core-steel rebar; (b) Between concrete core-GFRP tube

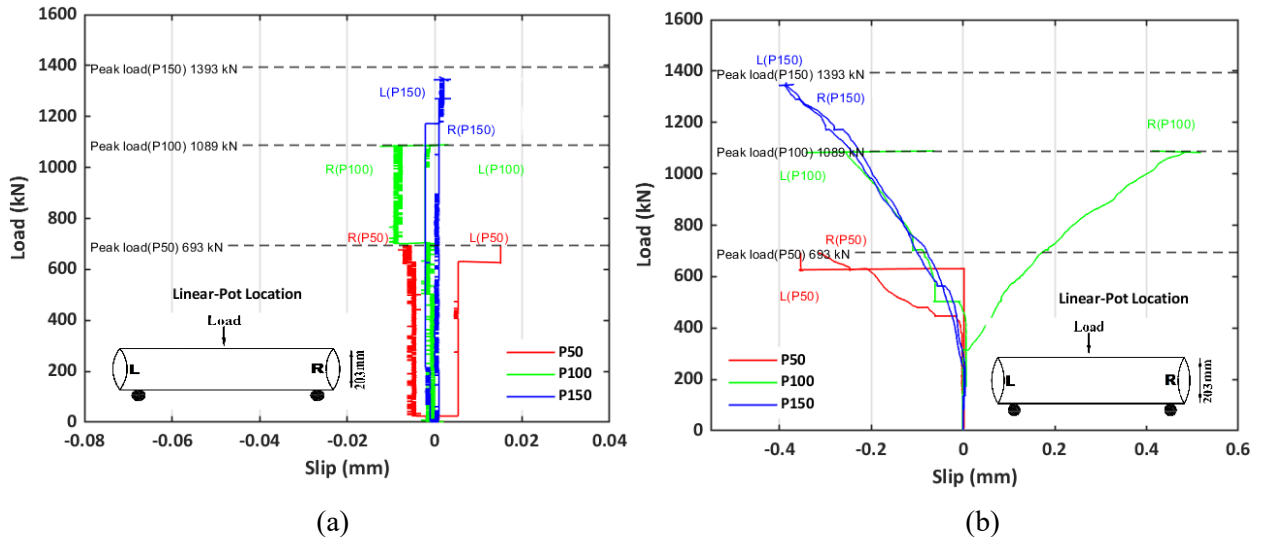


Figure 3-31. Compositeness of 10M steel-reinforced CFTs with a/D_i of 0.5 based on slip: (a) Between concrete core-steel rebar; (b) Between concrete core-GFRP tube

CHAPTER 4 FINITE ELEMENT MODELING

An analytical model was developed based on a simplified strut-tie model to estimate the ultimate load capacity of the CFFT members using truss analogy, geometric, and mechanical parameters of the GFRP tubes. Though it showed early signs of promise to predict the shear capacity of short-span CFFTs, the model encountered its limitation for increasing a/D_i ratios. Understanding and predicting the nonlinear behavior of the CFFTs is essential for designing the members used in structural applications. One of the critical elements of the CFFT is the FRP tubes as a confining member. Previously CFFT members were studied with various geometries (Ahmed et al. 2020; Ozbakkaloglu 2013; Fam et al. 2005; Lam and Teng 2003; Fam and Rizkalla 2002), material properties (Lu et al. 2019; Khan et al. 2017; Fam et al. 2007), and under different loading conditions (Qasrawi et al. 2015; ElGawady et al. 2010; Fam et al. 2003; Mirmiran and Shahawy 1997). Over the course of time, finite element modeling of CFFT gained popularity due to its ease and accuracy in predicting the nonlinear behavior of CFFT members. In addition, CFFT members have been studied previously using finite element (FE) modeling (Jawdhari et al. 2021; Abdelkarim and ElGawady 2014; Youssef et al. 2014; Fam and Son 2008). However, there is still a significant gap in the literature, as limited studies have been carried out on CFFT members with $\pm 55^\circ$ winding angle tubes under flexural loading using FE modeling.

This chapter describes the development of a quasi-static finite-element model for CFFTs and analyzes to understand the nonlinear behavior of CFFTs using the commercially available software program, LS-DYNA, version R10.0. Furthermore, the obtained results from the finite element models were compared with the extensive empirical data presented in Chapter 3.

4.1 MODEL DESCRIPTION

The quasi-static finite element model was developed, and the results were post-processed using commercially free pre and post-processing software LS-PrePost, and Notepad++ was used as a text and source code editor. The models were developed using both 2D and 3D elements for different parts. The developed FE problem was solved in LS-DYNA using the explicit solver. Although quasi-static FE models could be solved using implicit solver of LS-DYNA (guideline from Dynamore, 2018), due to explicit solver's ease of solving material nonlinearity, contact treatment, and a previous study (Jawdhari et al. 2020) factored in deciding the use of explicit solver for this study. Figure 4-1 (a) and (b) illustrates an isometric and cross-sectional view of a generalized CFFT model of a/D_i of 2.25, respectively.

4.1.1 GFRP Tube

The GFRP tubes were modeled using four-node laminated shell elements. These shell elements consider bending and shear deformation. The total number of elements and nodes for the GFRP tubes were 12800 and 12880, respectively. The elements had an aspect ratio of 0.92:1. Three different radii of 104.3, 106.3, and 108.3 mm were used to develop three different GFRP tubes, namely P50, P100, and P150, and the corresponding filament wound layup kept similar as presented in table 3-1. The GFRP tubes were modeled as part composite instead of section shell to stack multiple GFRP layers with different thicknesses and ply orientation and to activate laminated shell theory. The part composite method eliminates the integration rule definition, as it considers the position of integration points at the mid-point of the user-specified thicknesses and uses trapezoidal integration rule. The element formulation 2 or Belytschko-Tsay formulation was selected as the formulation of shell elements, which is also a default element formulation for the shell elements in LS-DYNA. The Belytschko-Lin-Tsay shell formulation is based on Reissner-Mindlin kinematic assumption, and it is an efficient formulation in terms of both time and cost. The shear correction factor is used to compensate for error arising due to constant transverse shear strains for the shell elements and is considered 1 in this study.

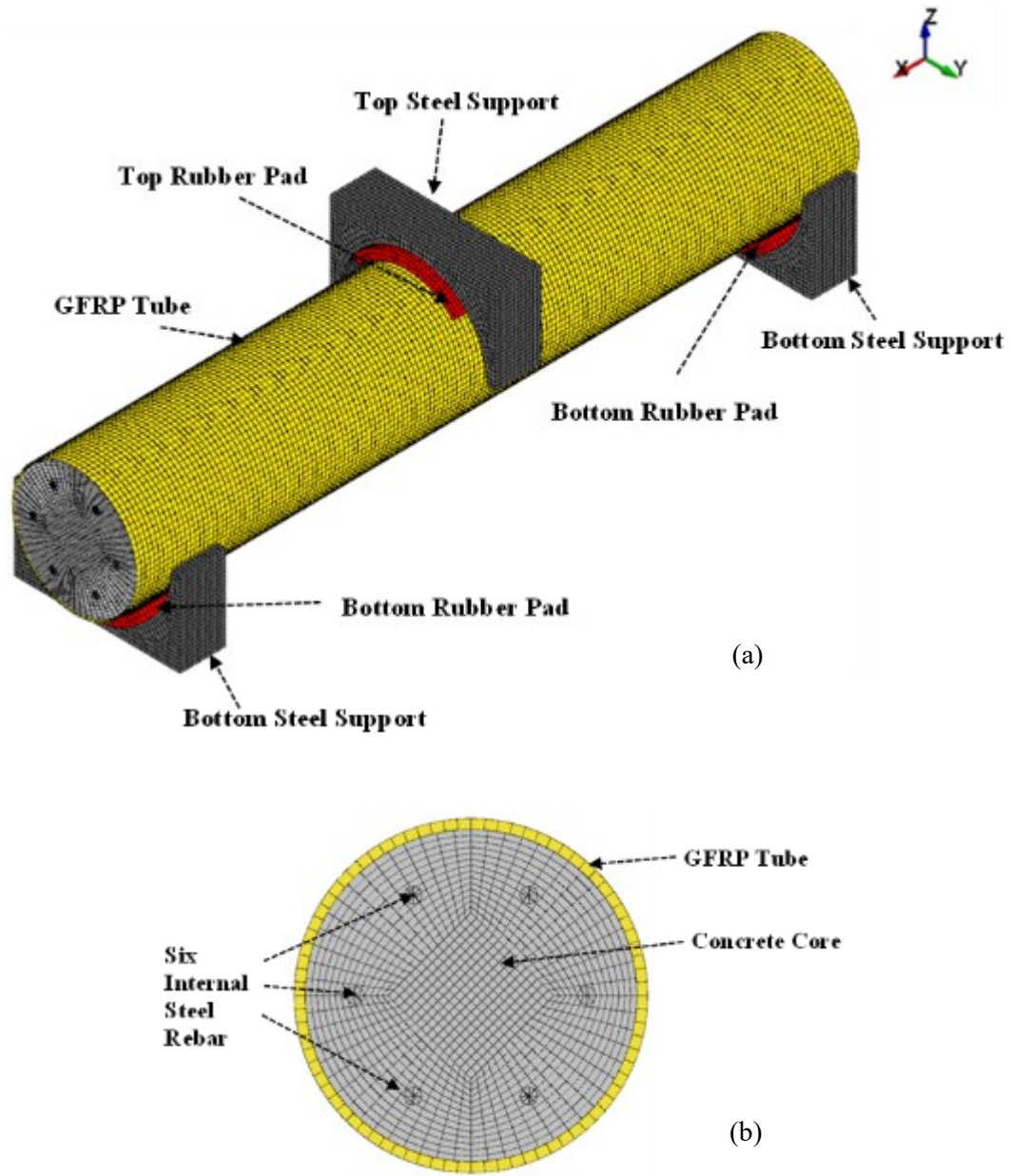


Figure 4-1. FE model of internally steel-reinforced CFFT with a/D_i of 2.25:
 (a) Isometric view; (b) Cross-sectional view

4.1.2 Concrete Core

The internal concrete core was modeled using eight-node hexahedron solid elements. The total number of elements and nodes for the concrete infill was 127800 and 132616, respectively. The internal concrete core radius was 101.6 mm, a constant for all CFFTs as all the GFRP tubes had the same inner diameter. The concrete core had an aspect ratio of 0.96:1 for the outermost element layer. The 3D solid elements for concrete core were modeled using element formulation 1 or constant stress solid element formulation. This formulation was chosen for solid elements as it allows the elements to undergo severe deformation and also due to its efficiency and accuracy.

4.1.3 Steel Reinforcement

The two types of internal steel rebars, namely 10M and 15M, were modeled using 2D elements. Both types of steel rebars had a clear cover of 25 mm in the model from the inner face of the GFRP tube. Figure 4-2 (a) and (b) shows both isometric and cross-sectional views of the rebar arrangement. The single steel rebar had 30 elements and 61 nodes. Element formulation 1 or Hughes-Liu with cross-section integration was selected as the element formulation for the beam elements, a default beam element formulation in LS-DYNA. In addition, a shear factor of 1 and 2x2 gauss quadrature integration rule was considered for modeling the beam elements, both of which are LS-DYNA defaults. Finally, the beam elements had a circular cross-section with 11.3 and 16 mm outer diameter for 10M and 15M rebars.

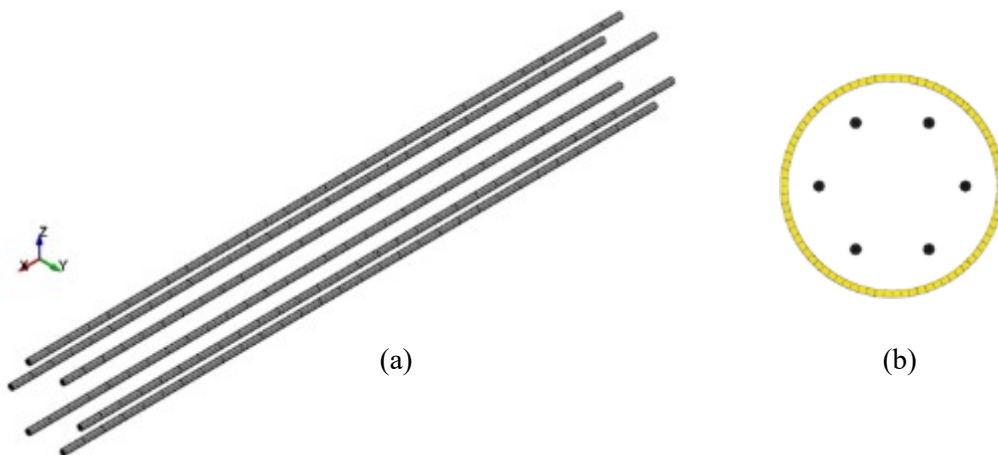


Figure 4-2. Steel rebar arrangement: (a) Isometric view; (b) Cross-sectional view

4.1.4 Auxiliary Parts

The auxiliary parts contain modeling of semi-circular steel supports and neoprene rubber pads. Both steel supports and neoprene pads in between the steel supports and CFFT were modeled using 3D solid elements. The supports and neoprene pads parts contained both hexahedron and pentahedron elements, generated due to the use of an automatic solid mesher with a constant element size of 6.5 mm. Each rubber pad part contained 960 elements and 1520 nodes, whereas the steel support consisted of 4044 elements and 5330 nodes. The width of the steel supports was kept as 76.2 mm (3”), similar to that of the experimental test setup, as seen in figure 3-11. The element formulation used for both steel supports and rubber pads was 1 or constant stress solid element formulation, similar to the modeling of the concrete core.

4.2 MATERIAL MODELS

The material modeling was the most challenging part of the FE analysis. Material models and their properties are the most influential factor for the FEA, which directly involves reproducing the nonlinear behavior of the CFFTs, as seen in Chapter 3.

4.2.1 GFRP Tube

This current study and previous studies (Betts et al. 2019; 2020) showed the nonlinear response of the CFFT and GFRP tube, respectively. Although MAT_054/055, ENHANCED COMPOSITE DAMAGE is a commonly used material model for composites. To capture this nonlinear behavior of the GFRP tube, material model MAT_058, LAMINATED_COMPOSITE_FABRIC was selected to model the GFRP tubes for this study. This particular damaged mechanics-based material model has the capability of modeling for unidirectional layers, woven fiber, and laminates with nonlinear pre-peak and post-peak softening of composite ply(s) (Cherniaev et al. 2018; Jawdhari et al. 2020). The material model MAT_058 uses Modified Hashin failure criteria (Chatla 2012) and incorporates three different failure surface types, namely, EQ. 0.0 or smooth failure surface for unidirectional layered composites, EQ. 1.0 and EQ. -1 or smooth and faceted failure surface, respectively, for complete laminates and fabrics.

In this study, EQ. 1.0 was selected as the failure surface type, and it assumes an interaction between normal and shear stresses for damage evolution in both fiber and transverse directions. The material coordinate system was defined with the help of the material axes option (AOPT) and component vector (v) in the MAT_058 material model. The angle-ply orientation $\pm 55^\circ$ layup was defined in the *PART_COMPOSITE as shown in figure 4-3. Table 4-1 shows material inputs for GFRP tubes from a previous study by Betts et al. (2019). These material modeling inputs were taken as a benchmark for this study. The model input parameters for GFRP tubes were separated into two sections, without stress limiting (SLIM) factors and with SLIM factors. The successive sections will be illustrating the mechanical property of GFRP lamina for material modeling.

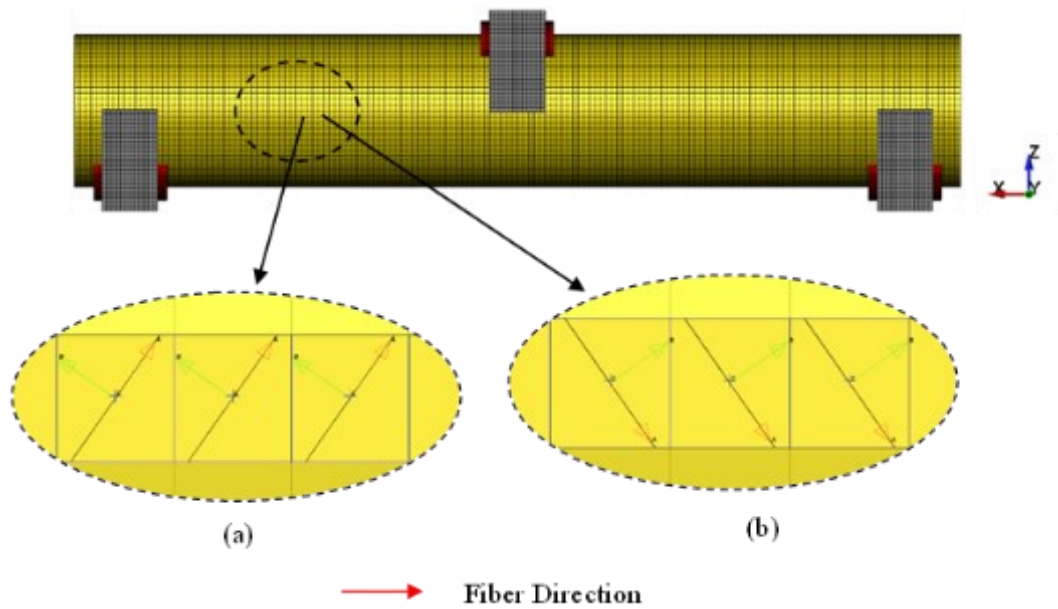


Figure 4-3. Composite ply orientation: (a) $+55^\circ$ layer; (b) -55° layer

Table 4-1. Mechanical properties of GFRP lamina (Betts et al. 2019)

Property	GFRP Lamina	
	Manufacturer Data	Modified Daniel & Ishai ($V_f = 50\%$)
Elastic modulus in fiber direction (E_1) in GPa	41.369	37.511
Elastic modulus in matrix direction (E_2) in GPa	8.991	9.496
Shear modulus (G_{12}) in GPa	3.228	3.915
Major Poisson's ratio (ν_{12})	0.278	0.28
Minor Poisson's ratio (ν_{21})		0.06
Tensile strength in fiber direction (X_T) in MPa		1036
Compressive strength in fiber direction (X_C) in MPa		564
Tensile strength in matrix direction (Y_T) in MPa		35
Compressive strength in matrix direction (Y_C) in MPa		116
In plane shear strength (S_C) in MPa		81

4.2.1.1 Without stress limiting factors

Due to the limited availability of strain data and other mechanical properties of GFRP lamina, 14 mechanical property values were defined in this model, which includes mass density, Young's moduli, Poisson's ratios, shear modulus, and strengths. The strength values from table 4-1 were increased to resist the premature failure in the GFRP tube in FEM. In this model. Non-physical parameters such as erosion strains, stress limit factors, and softening reduction factors, etc., were not defined in this model. The following table provides the material properties used for the GFRP tube modeling.

Table 4-2. Mechanical property inputs for MAT_058 without non-physical parameters

Property	Unit	GFRP Lamina	
		Manufacturer Data	Modified Data
Mass density (RO)	ton/mm ³	1.61 x 10 ⁻⁹	
Elastic modulus in longitudinal direction (E _A)	MPa	41.3 x 10 ³	
Elastic modulus in transverse direction (E _B)	MPa	9 x 10 ³	
Shear modulus (G _{AB} /G _{CA})	MPa	3.2 x 10 ³	
Shear modulus (G _{BC})	MPa		1.6 x 10 ³
Major Poisson's ratio (PR _{BA} /PR _{CA})*			0.28
Minor Poisson's ratio (PR _{CB})*			0.06
Tensile strength in longitudinal direction (X ^T)	MPa		3730
Compressive strength in longitudinal direction (X ^C)	MPa		1690
Tensile strength in transverse direction (Y ^T)*	MPa		35
Compressive strength in transverse direction (Y ^C)*	MPa		116
In plane shear strength (S ^C)	MPa		300

* From Betts et al. (2019)

4.2.1.2 With stress limiting factors

Similar to table 4-2, another set of material strength values were considered to model GFRP lamina. With this value provided in table 4-3, a few of the non-physical parameters were adopted, namely, SLIMT1, SLIMC1, SLIMT2, SLIMC2, and SLIMS. These are stress limiting factors for post-failure adjustment, which determines the residual strength following elastic damage of every laminate layer. The following relation could be used to calculate the minimum stress limit after stress maximum in the softening part.

$$\sigma_{\min} = \text{SLIM}_{xx} \cdot \text{Strength} \quad \dots\dots\dots 4-1$$

where,

σ_{\min} is the minimum stress in the composite post-failure

SLIM_{xx} is the corresponding stress limiting factor

The SLIM_{xx} factor values have a range, and it is between 0 to 1. From the relation 4-1, it could be observed that when the factor value is 0.8, any non-damaged element in the model will experience a strength reduction of 20% of their original element strength post-failure.

Table 4-3. Mechanical property inputs for MAT_058 with non-physical parameters

Property	Unit	GFRP Lamina	
		Manufacturer Data	Modified Data
Mass density (RO)	ton/mm ³	1.61 x 10 ⁻⁹	
Elastic modulus in longitudinal direction (E _A)	MPa	41.3 x 10 ³	
Elastic modulus in transverse direction (E _B)	MPa	9 x 10 ³	
Shear modulus (G _{AB} /G _{CA})	MPa	3.2 x 10 ³	
Shear modulus (G _{BC})	MPa		1.6 x 10 ³
Major Poisson's ratio (PR _{BA} /PR _{CA})*			0.28
Minor Poisson's ratio (PR _{CB})*			0.06
Tensile strength in longitudinal direction (X ^T)	MPa		2600
Compressive strength in longitudinal direction (X ^C)	MPa		850
Tensile strength in transverse direction (Y ^T)*	MPa		35
Compressive strength in transverse direction (Y ^C)*	MPa		116
In plane shear strength (S ^C)	MPa		250

* From Betts et al. (2019)

Table 4-4. Non-physical parameters for MAT_058

Parameter	Abbreviation	Value
Factor to determine the minimum stress limit after stress maximum (fiber tension)	SLIMT1	0.3
Factor to determine the minimum stress limit after stress maximum (fiber compression)	SLIMC1	0.8
Factor to determine the minimum stress limit after stress maximum (matrix tension)	SLIMT2	0.3
Factor to determine the minimum stress limit after stress maximum (matrix compression)	SLIMC2	0.8
Factor to determine the minimum stress limit after stress maximum (shear)	SLIMS	1

4.2.2 Concrete

The concrete infill was modeled using a nonlinear material model MAT_072R3, CONCRETE_DAMAGE_REL3. To define the complete material model, the MAT_072R3 model requires seven cards with an equation of state for pressure-volume strain response. This model has been previously used to model CFFTs (Jawdhari et al. 2020). The most significant aspect of the material model concrete Damage Model Release 3 is that it automatically generates parameters, such as damage and strain rate effects, confinement, shear dilation, and tensile fracture energy using a sole input of unconfined compressive strength of the concrete. The auto-generated parameters were written and stored in the “messag” file after the analysis. Due to the presence of limited experimental data, the automatic parameter generation trait of the model was used for this study. In addition, the non-physical unit conversion factors associated with the model were also considered. The mass density and Poisson’s ratio of the concrete were considered as 2.4×10^{-9} ton/mm³, and 0.2, respectively. The unconfined compressive strength of the concrete was adopted as 40 MPa according to the results provided in Chapter 3. The tensile strength of the concrete was considered as 3.8 MPa from the following relation by ACI 318-2014.

$$f_t = k(f_c')^n \dots\dots\dots 4-2$$

where,

f_c' is unconfined compressive strength of the concrete

k and n are constant coefficient and considered as 0.56, and 0.5 respectively (ACI 318-2014)

4.2.3 Steel Reinforcement

In order to capture the effect of internal reinforcement, the steel rebars were modeled using MAT_003, PLASTIC_KINEMATIC. It is a simple and very cost-effective model. For this study, four parameters were defined for modeling rebars. The mass density, elastic modulus, and Poisson's ratio were considered as 7.9×10^{-9} ton/mm³, 200×10^3 MPa, and 0.3, respectively. During the material testing, the average yield stress for the 10M steel rebars and 15M steel rebars were found to be 485.5 and 427.3 MPa and considered as 485 and 430 MPa for the model.

4.2.4 Auxiliary Materials

The auxiliary material consists of material modeling of semi-circular steel supports and neoprene rubber pads. The steel supports were modeled using MAT_001, ELASTIC, with the input parameter for mass density, elastic modulus, and Poisson's ratio as 7.9×10^{-9} ton/mm³, 200×10^3 MPa, and 0.3, respectively. The rubber pads beneath the supports were modeled as MAT_007, BLATZ-KO_RUBBER with a mass density and shear modulus of 1.1×10^{-9} ton/mm³, and 20 MPa, respectively. However, the actual material property of the supports and rubber pads used in this study was not known.

4.3 CONTACTS and BOUNDARY CONDITIONS

This section will illustrate the applied contact between different parts and boundary conditions in the finite element model.

4.3.1 Contacts

Each of the models consists of a total of nine parts, a GFRP tube, a concrete core, steel rebars arrangement, three semi-circular steel supports, and three rubber pads. The

automatic single surface contact was used for the hollow GFRP tube, a shell FEM part. This contact type is a penalty-based contact and considers shell thickness. The GFRP tube and inner concrete core were connected to each other via tied nodes to surface offset contact, as shown in figure 4-4. This is a contact type that uses a penalty-based formulation. With this contact option, the force and moment resultants are transferred to discrete spring elements between slave nodes and master segment, in this case, which was concrete nodes set and GFRP shell segment set, respectively. The static and dynamic coefficient of friction was considered as 0.5. The scale factors for both slave and master penalty stiffness (SFS and SFM) were kept as 1, which was the LS-DYNA default value. The load was applied to the top semi-circular steel support, which was placed on a rubber pad, and the rubber pads were in contact with CFFT and steel supports, as shown in figure 4-1 (a). Automatic surface to surface contacts was used between the steel supports and rubber pads and between rubber pads and CFFT. For these contacts, the static and dynamic coefficient of friction was assumed as 0.5. In the case of automatic surface to surface contacts, SOFT 1 option was selected on contact card A, and the scale factor for constraint forces (SOFSCF) was considered as 0.1. Setting SOFT as 1 caused the contact stiffness to be determined based on stability considerations by taking the timestep and nodal masses into account. The reason behind using this contact constraint formulation was due to both the dissimilarity between material stiffnesses (particularly soft foam material interacting with metals) and mesh densities.

Additionally, the internal steel rebars inside the concrete core were included explicitly using the constraint method (Dynamore, 2014). The constrained Lagrange in solid was used to couple the steel rebars to the concrete core of CFFT. The coupling direction (DIREC) was kept as 1, for which no coefficient of friction was required.

4.3.2 Boundary Conditions

A node-set was created using top surface nodes of the top steel support. The load on the node-set was defined using a prescribed motion set and with the help of a displacement curve, as shown in figure 4-5 (b). The top support location in the models was constant, whereas the location of the bottom supports was equidistant from the top support and changed according to the three different shear spans, 101.6, 203.2, and 457.2 mm,

respectively.

Figure 4-5 (a) shows the modeling of the roller-type supports. A roller-like behavior was simulated for the bottom steel supports with the help of the center nodes of the supports along the y-axis by allowing them to rotate about both the x and y-axis. The corner nodes along the same axis of the bottom support were only allowed to move about the x-axis. This was important because when transitional constrained about y-axis was not applied on those corner nodes, due to applied load, the whole model was experiencing an angular movement on the x-axis. In reality, during the test, the bottom semi-circular steel supports were mounted on top of roller supports, and steel plates were placed on top of the top steel support for equal distribution of the load, which was applied with a cylindrical load head. However, the above-stated boundary conditions were applied to the model for its simplicity and computational efficiency. Also, it was able to simulate similar environmental conditions as the actual test without significantly affecting the model results.

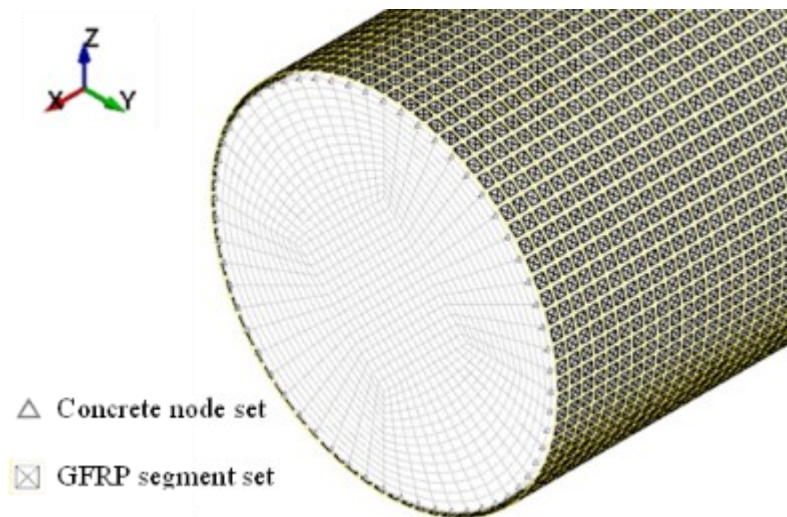


Figure 4-4. Tied contact between concrete core and GFRP tube

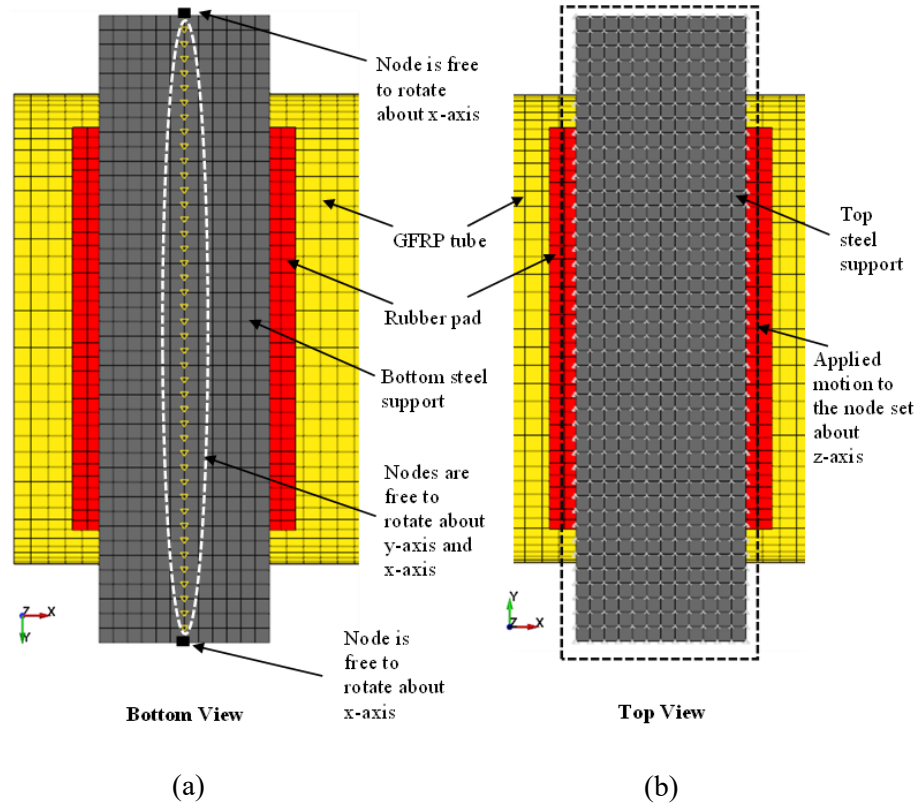


Figure 4-5. Modeling of boundary conditions: (a) SPC reaction supports;
(b) Prescribe motion set for top support

4.4 CONTROL PARAMETERS

The CFFT FE models encountered element hourglassing and stability issues during the analysis. Aside from the complications, a few additional factors were introduced to improve the precision of the FE model. The inclusion of stability parameters and the additional factors in the FE model will be discussed briefly in the following sections.

4.4.1 Hourglass

Hourglass shapes in FEM could be seen in the under-integrated solid and shell elements. However, beam elements were not susceptible to this problem. In this study, the FE models used ELFORM 1 for solid elements and ELFORM 2 for the shell elements, both of which were not fully integrated or a selective reduced integration formulation. Under subjected to pure bending, the reduced integrated elements could not detect strain and produce zero stress, leading to a zero-energy deformation mode in simulated results.

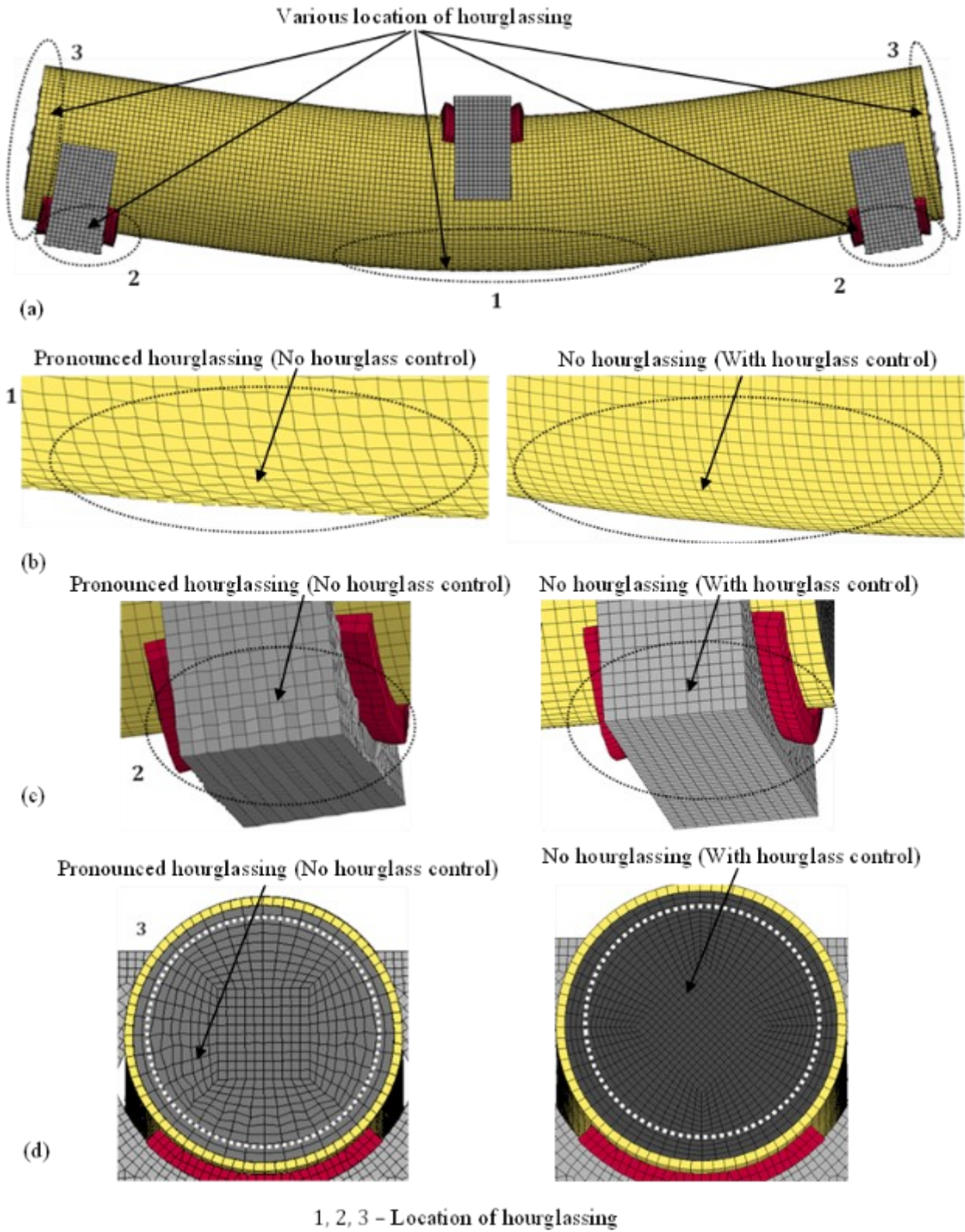


Figure 4-6. Hourglassing pattern and hourglass control in CFFT: (a) Various locations; (b) In GFRP tube; (c) In Steel supports; (d) In concrete core

Figure 4-6 illustrates comparisons between the hourglassing pattern in various locations (1, 2, and 3) with elements having no hourglass control vs. the effect of hourglass control mode in the FE model. The Flanagan-Belytschko stiffness hourglass control form was applied to control the hourglass-like phenomenon. Depending on the severity of the hourglass-like element shape in the analysis and comparing the hourglass energy with the internal energy of each FE part, different hourglass coefficients were adopted in different FE parts in the FE model. The hourglass coefficient (QM) for the GFRP tube was set as 0.005, and a default value for the hourglass coefficient for shell bending (QB) was kept as 0.1. The adopted hourglass coefficient for the concrete core was 0.075. In contrast, the hourglass coefficient for the rubber pads and the steel supports were set as 0.12 and 0.05, respectively. With the help of the above-stated hourglass controls, the hourglass modes were effectively inhibited while minimizing the non-physical stiffening of the FE parts in simulation results. The hourglass energy in the FE model was computed and included in the energy balance with the help of the hourglass energy calculation option (HGEN) in the control energy keyword. Finally, the effectiveness of the hourglass control was determined by comparing the hourglass energy of individual parts in the FE models to their internal energy. The maximum hourglass energy in the FE models was observed in the concrete and was less than 8% of their internal energy for P50 CFFTs.

4.4.2 Stability, Material and Contact

Additionally to the hourglassing, the FE model materials experienced negative volume and other stability issues due to large deformations in the soft materials such as rubber pads, different element sizes, materials, and sound speed. The above-stated complications in the FE model could be solved using two common methods, altering mass scaling and/or timestep. The idea behind mass scaling is to increase non-physical mass in the key location in the FE model in order to achieve a larger explicit timestep. However, for simplicity, the other method was adopted in the FE model to tackle the stability problems. The timestep to solve the FE problem was reduced to 0.5 using the scale factor for computed timestep (TSSFAC) in the control timestep keyword. The reduction in the timestep scale factor from the default value of 0.9 to 0.5 resulted in additional steps in completing the analysis, which then resulted in a longer run time of the analysis. However, the reduction in the timestep size did not gravely affect the analysis time and was practical enough to consider this

method.

The GFRP tube in the FE model, a composite shell material, might need to adopt a correction in terms of laminated shell theory. The laminated shell theory corrected the transverse shear stress to minimize the stress discontinuities between layers. This correction was applied for the thin laminated shells and activated by setting the LAMSHT value to 3 in the control shell keyword. Furthermore, the scale factor for the sliding interface penalties (SLSFAC) in the control contact keyword was set to a default value of 0.1. This resulted in the decrease in the contact stiffness for penalty-based contacts with SOFT set equal to 0, which was the contact between the GFRP tube and the concrete core.

4.5 MODEL ASSUMPTIONS and LIMITATIONS

The FE model was developed based on two critical assumptions, GFRP tube architecture, and material inputs, to analyze the behavior of CFFT members under flexural loading. Figure 4-7 exhibits the GFRP tube architecture irrespective of the filament wound laminae thickness and the overall tube thickness. For modeling simplicity, the filament wound laminae thickness was assumed to be the overall section thickness of the tube, including the thickness of the resin coat and the liner. Therefore, the thickness of each lamina was considered to be the section thickness divided by the number of laminae.

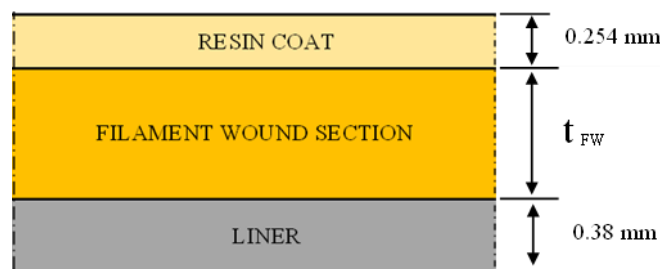


Figure 4-7. GFRP tube architecture (Measurement provided in Betts et al. 2019)

The available material data were limited in this study for both GFRP tube and concrete. The material model used for the GFRP tubes, MAT_058, comprises nine cards, out of which seven cards are essential. Those seven cards include moduli, Poisson's ratios, various stress and strain values and their factors, failure surface types, strength values, and non-physical parameters, which depend on the material properties. The manufacturer

provided the material properties, such as elastic and shear moduli. The strength values were assumed and modified with the help of a previous study by Betts et al. (2019). In the case of modeling the concrete, MAT_072R3 material model, the average compressive strength was considered for all different CFFT models. Also, the majority of the concrete modeling was highly dependent on the auto-generated parameters.

Aside from the above-stated assumptions, mesh sensitivity analysis was not performed for the FE model. Hence the computational efficiency of the model remains an untested factor. Furthermore, the control parameters discussed in section 4.4 were also dependent on the different mesh sizes.

4.6 MODEL VERIFICATION

The section summarizes the comparison and verification of the developed FE models with and without stress limiting factors by comparing load-deflection, load-strain, moment-curvature behavior, and the failure modes using the experimental results.

4.6.1 Model Without Stress Limiting Factors

The FE models developed in this study, ignoring the SLIM factors, were verified using the experimental results presented in Chapter 3. Table 4-5 provides the comparison of peak load, mid-span deflection at peak load, and initial stiffness between the FE models and experimental results. The average test-model ratio for predicting the peak load and mid-span deflection at peak load are 0.86 and 1, respectively. The test-model ratio for the initial stiffness is 0.71, which suggests an overprediction by the model. This initial stiffness overprediction in the model possibly arises due to the model assumptions discussed in section 4.5, particularly the mechanical properties and architecture of the GFRP tubes. Figures 4-10, 4-14, and 4-18 show the overall nonlinear behavior of CFFTs by comparing the load-deflection diagrams from the test and the FE model. Whereas figures 4-11, 4-15, and 4-19 exhibit the comparison of strain prediction and behavior between model and test. Figures 4-12, 4-16, and 4-20 exhibits the comparison of moment-curvature behavior between model and test. Although due to insufficient experimental strain results, a conclusive verdict could not be made on the strain and moment-curvature behavior, the initial comparison from the available data shows a promise.

Table 4-5. Verification of FE Models without SILM factors Using Test Data

CFFT SPECIMEN ID	Peak Load (kN)			Mid-Span Deflection at Peak Load (mm)			Initial Stiffness (kN/mm) ¹		
	Test	Model	Test- Model Ratio	Test	Model	Test- Model Ratio	Test	Model	Test- Model Ratio
P50-a-AD0.5	693	868	0.80	15.6	10.3	1.51	82.5	118.1	0.70
P100-a-AD0.5	1089	1243	0.88	17.9	15.5	1.15	105.8	126.3	0.84
P150-a-AD0.5	1393	1510	0.92	23.0	19.4	1.19	97.1	130.1	0.75
P50-b-AD0.5	929	1045	0.89	17.1	13.0	1.32	92.1	133.8	0.69
P100-b-AD0.5	1329	1398	0.95	17.8	17.5	1.02	113.7	136.5	0.83
P150-b-AD0.5	1637	1651	0.99	21.1	19.2	1.10	121.8	139.9	0.87
P50-a-AD1	416	529	0.79	21.4	21.1	1.01	42.1	78.0	0.54
P100-a-AD1	630	734	0.86	23.1	26.4	0.88	52.8	85.1	0.62
P150-a-AD1	820	903	0.91	27.6	26.6	1.04	63.0	87.98	0.72
P50-b-AD1	538	646	0.83	22.3	22.9	0.97	80.8	90.4	0.89
P100-b-AD1	748	868	0.86	27.6	28.2	0.98	85.6	93.7	0.91
P150-b-AD1	854	1009	0.85	31.2	28.5	1.09	86.6	97.1	0.89
P50-a-AD2.25	199	261	0.76	45.8	68.4	0.67	16.0	28.4	0.56
P100-a-AD2.25	279	373	0.75	51.9	65.3	0.79	19.9	31.4	0.63
P150-a-AD2.25	367	430	0.85	64.2	72.4	0.89	19.1	36.9	0.52
P50-b-AD2.25	248	302	0.82	46.5	60.6	0.77	22.3	38.9	0.57
P100-b-AD2.25	339	417	0.81	63.2	60.9	1.04	22.7	43.4	0.52
P150-b-AD2.25	413	458	0.90	37.4	70.5	0.53	40.3	52.4	0.77
Mean			0.86			1.00			0.71
Standard Deviation			0.06			0.23			0.14
COV (%)			8			23			19

¹ Initial stiffnesses were calculated between deflections of 1 mm and 5 mm

Aside from the experimental and model comparison of the mid-span strain of the extreme compression fiber, extreme tension fiber, and the strain at the outer layer of the GFRP tube at the bottom rebar region, the load-strain diagrams also show the tensile strain at the bottom steel rebar at mid-span from the FE model. Furthermore, from the load-strain diagrams, it can be observed that the yielding of the bottom steel rebars initiates the nonlinearity in the load-deflection behavior of the CFFTs. This phenomenon further substantiates the contribution of the GFRP tube's nonlinear behavior and confinement effect to CFFTs.

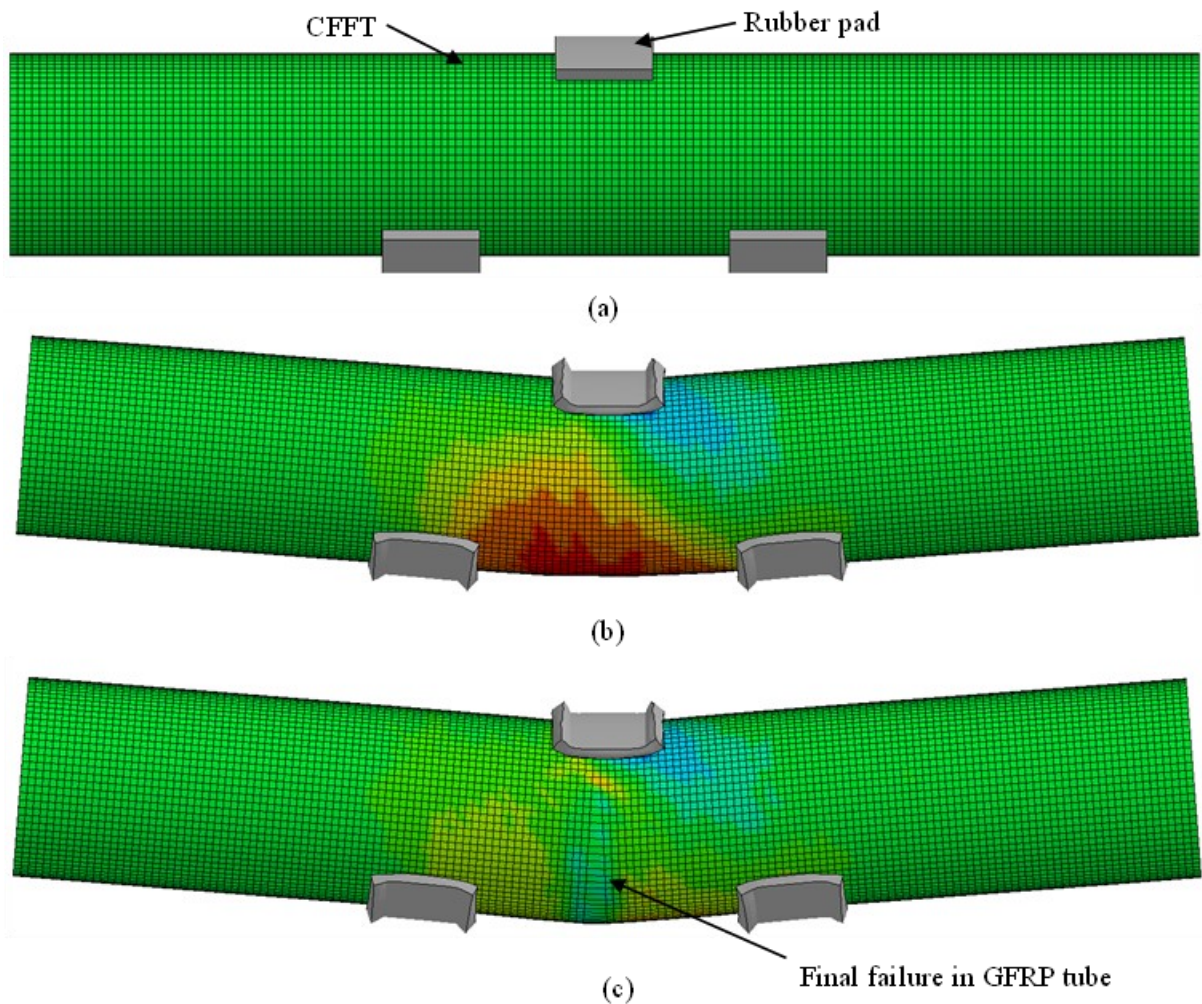


Figure 4-8. Progression of failure in CFFT model without stress limiting factors:
 (a) Before applied load; (b) Stress concentration in GFRP tube before failure; (c) Tension failure – sudden load-drop in the load-midspan deflection curve

Additionally, to validate the failure mode of CFFT, damage in the GFRP tube and concrete core between experimental outcomes and FE models was visually compared. Figures 4-8 (b) and 4-8 (c), exhibit the progression of stress concentration in the GFRP tube of CFFT and the ultimate failure of P100-a-AD0.5 CFFT specimens, respectively. Independent of the testing parameters, all FE models without stress limiting factors failed in a similar manner, as shown in figure 4-8. The red-colored elements in figure 4-8 (b) portrayed the stress concentration in the bottom tension region of the GFRP tube at the midspan. Final failure in the model occurred by stretching in the elements at the tension region of the GFRP tubes in the CFFTs, which corresponded to the sudden drop in the load after reaching the ultimate capacities of the CFFT in the load-mid-span deflection diagrams. Figures 4-9, 4-13, and 4-17 exhibit a comparison study between experimental failures and model simulation of the damage in the GFRP tube and concrete core of the CFFTs. Apart from capturing the stress concentration in the GFRP tube and the ultimate failure in the CFFT, figures 4-9 (b), 4-13 (b), and 4-17 (b) shows that the FE model was successfully captured the major flexural crack development at the bottom mid-span in the concrete core of the CFFT specimens by inspecting the strain values of the contour plots. The red areas in figures 4-9 (b), 4-13 (b), and 4-17 (b) represent the damage progression of the concrete core, which started at the bottom tension region in the concrete core and propagated towards the compression region.

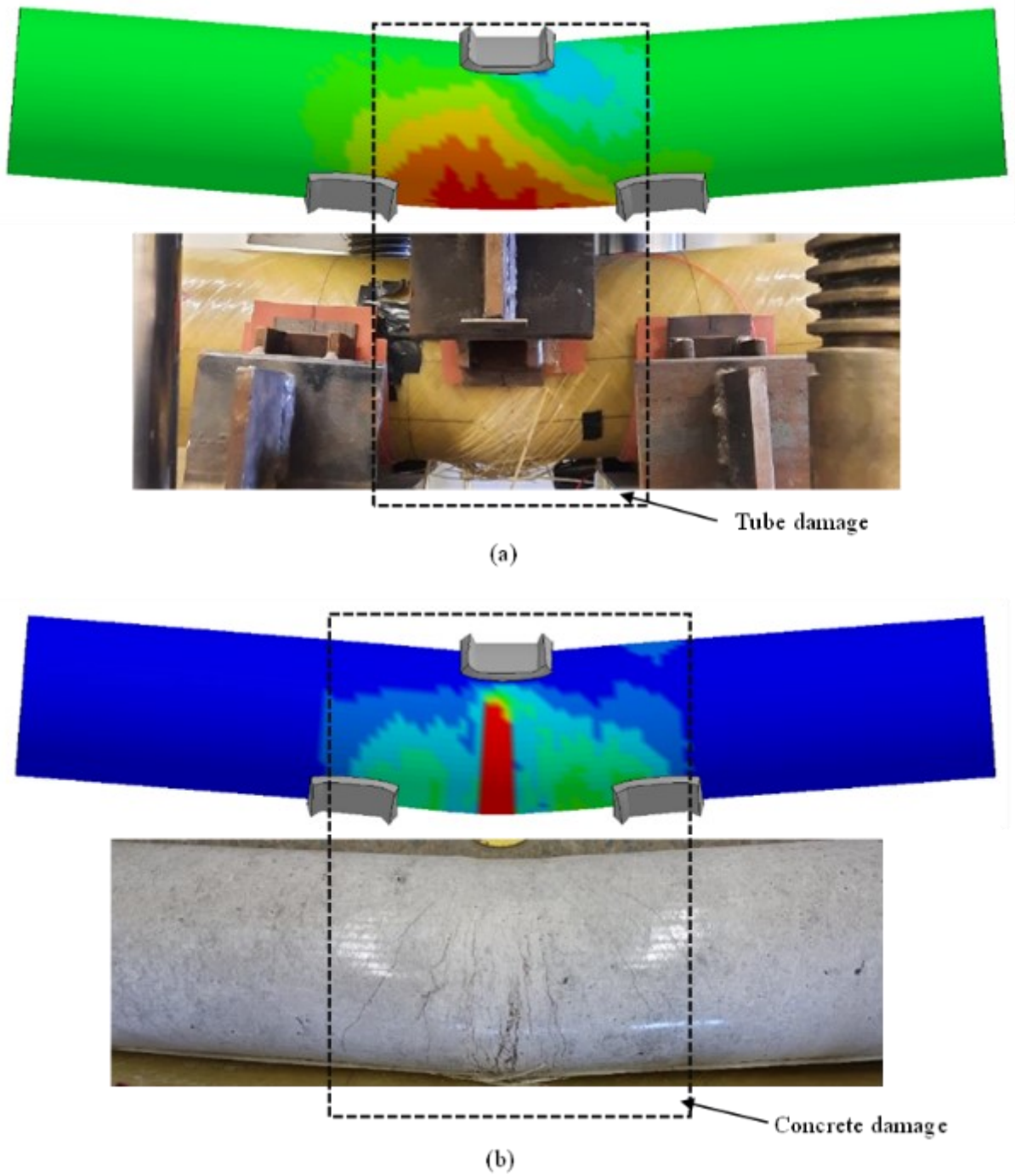


Figure 4-9. Visual comparison of P100-a-AD0.5 CFFT specimen: (a) Simulation of failure in GFRP tube; (b) Simulation of damage in concrete

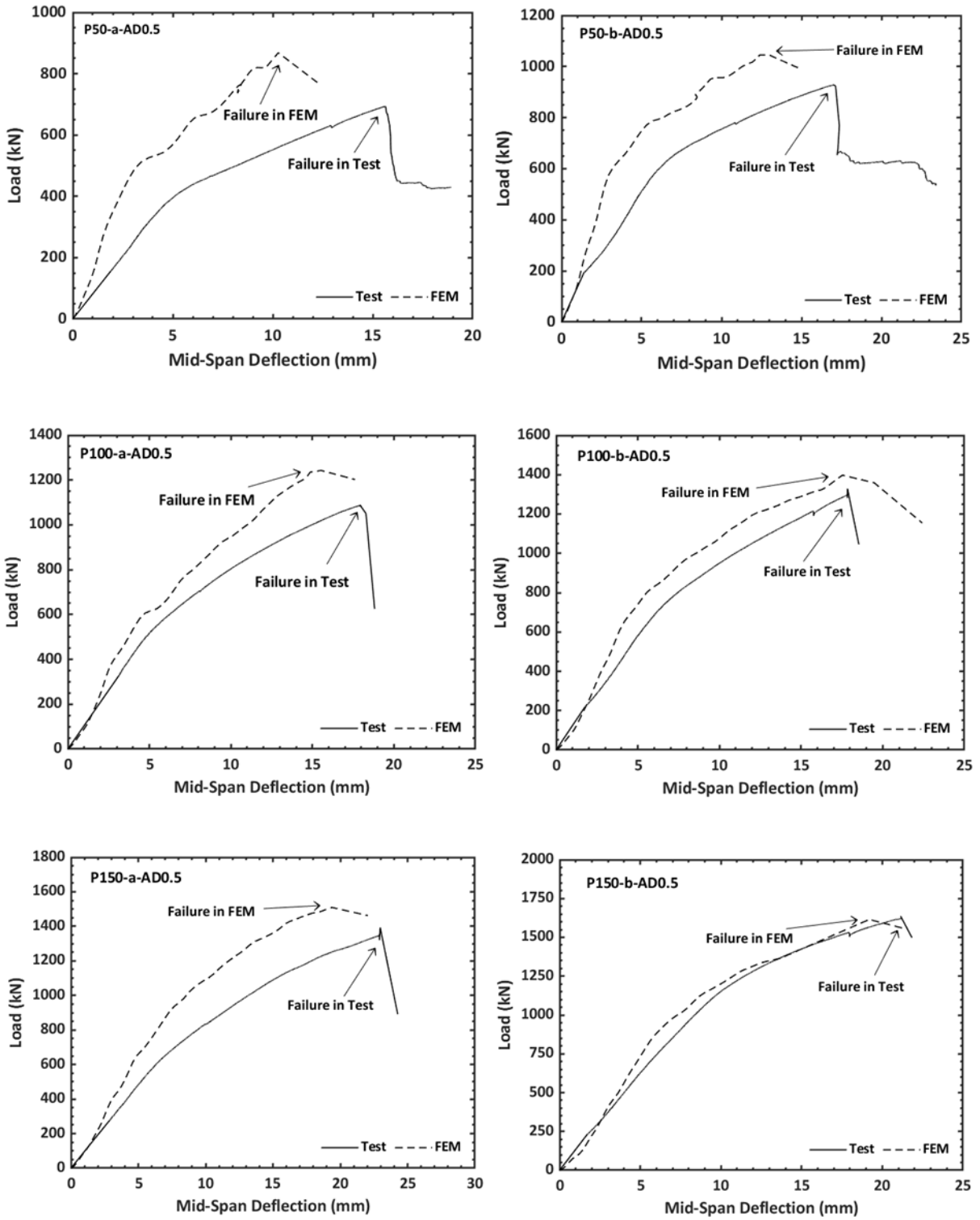


Figure 4-10. Load versus mid-span deflection verification: a/D_i of 0.5 CFFT FE models

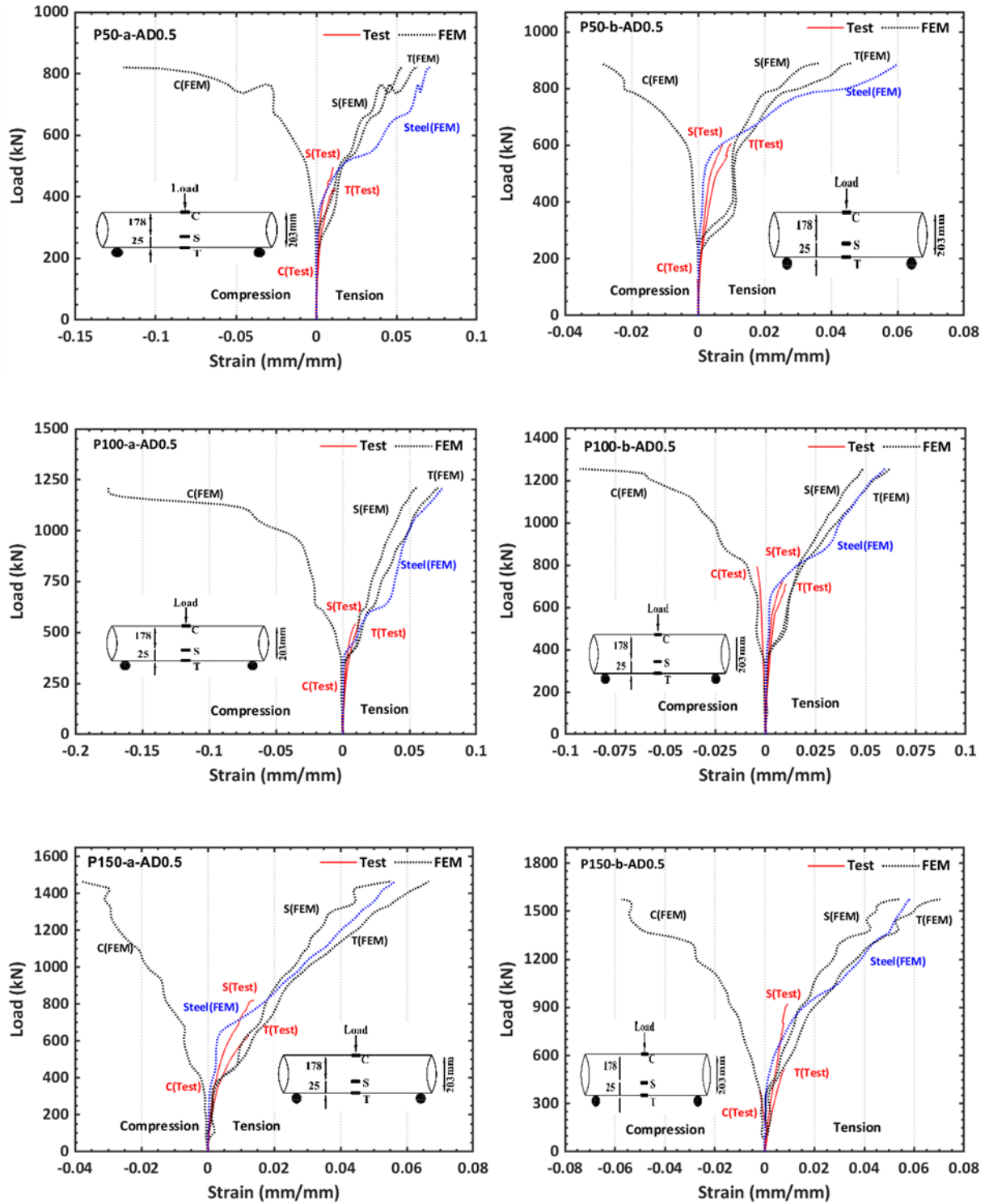


Figure 4-11. Load versus strain verification: a/D_1 of 0.5 CFFT FE models

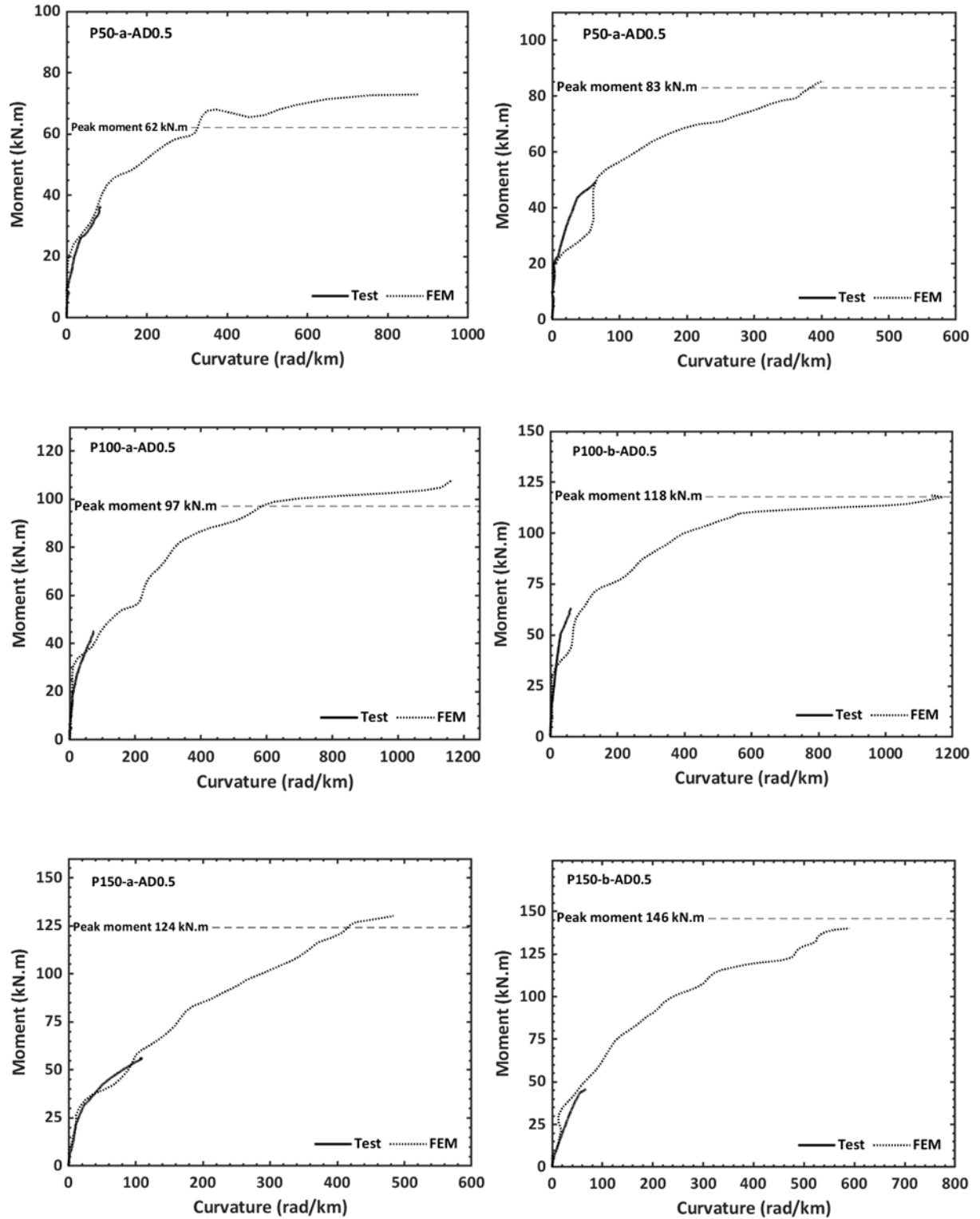


Figure 4-12. Moment versus curvature verification: a/D_i of 0.5 CFST FE models

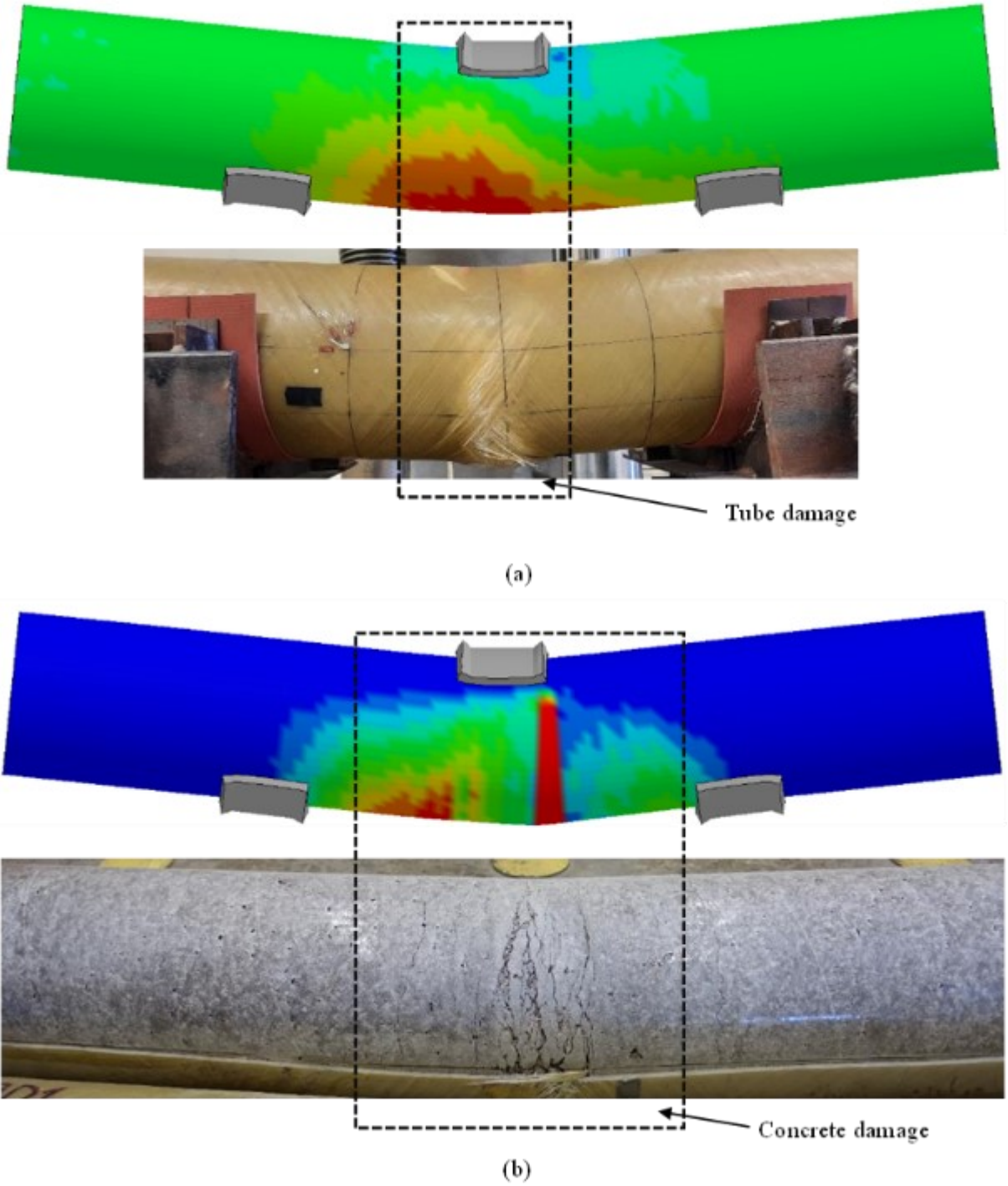


Figure 4-13. Visual comparison of P100-a-AD1 CFFT specimen: (a) Simulation of failure in GFRP tube; (b) Simulation of damage in concrete

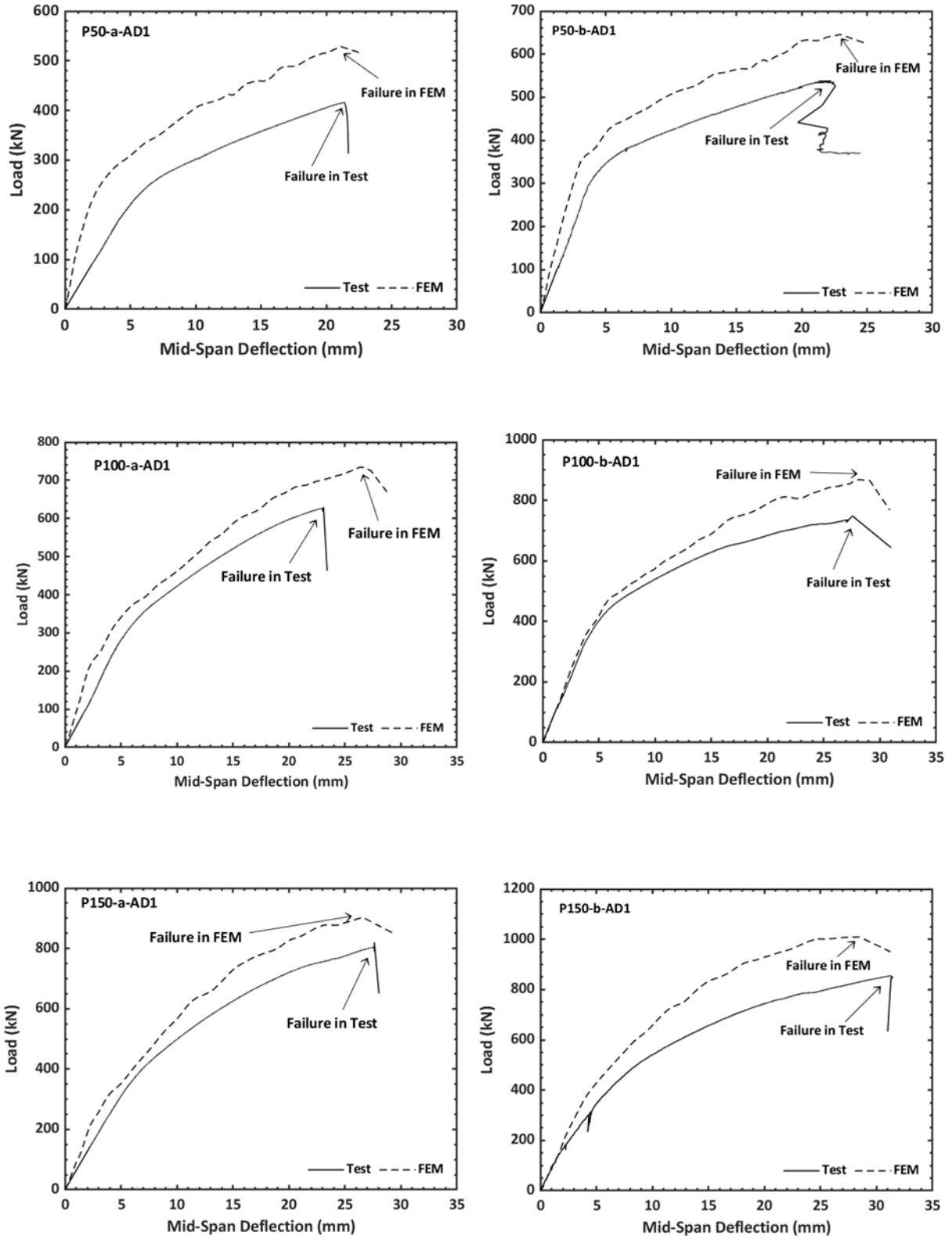


Figure 4-14. Load versus mid-span deflection verification: a/D_i of 1 CFFT FE models

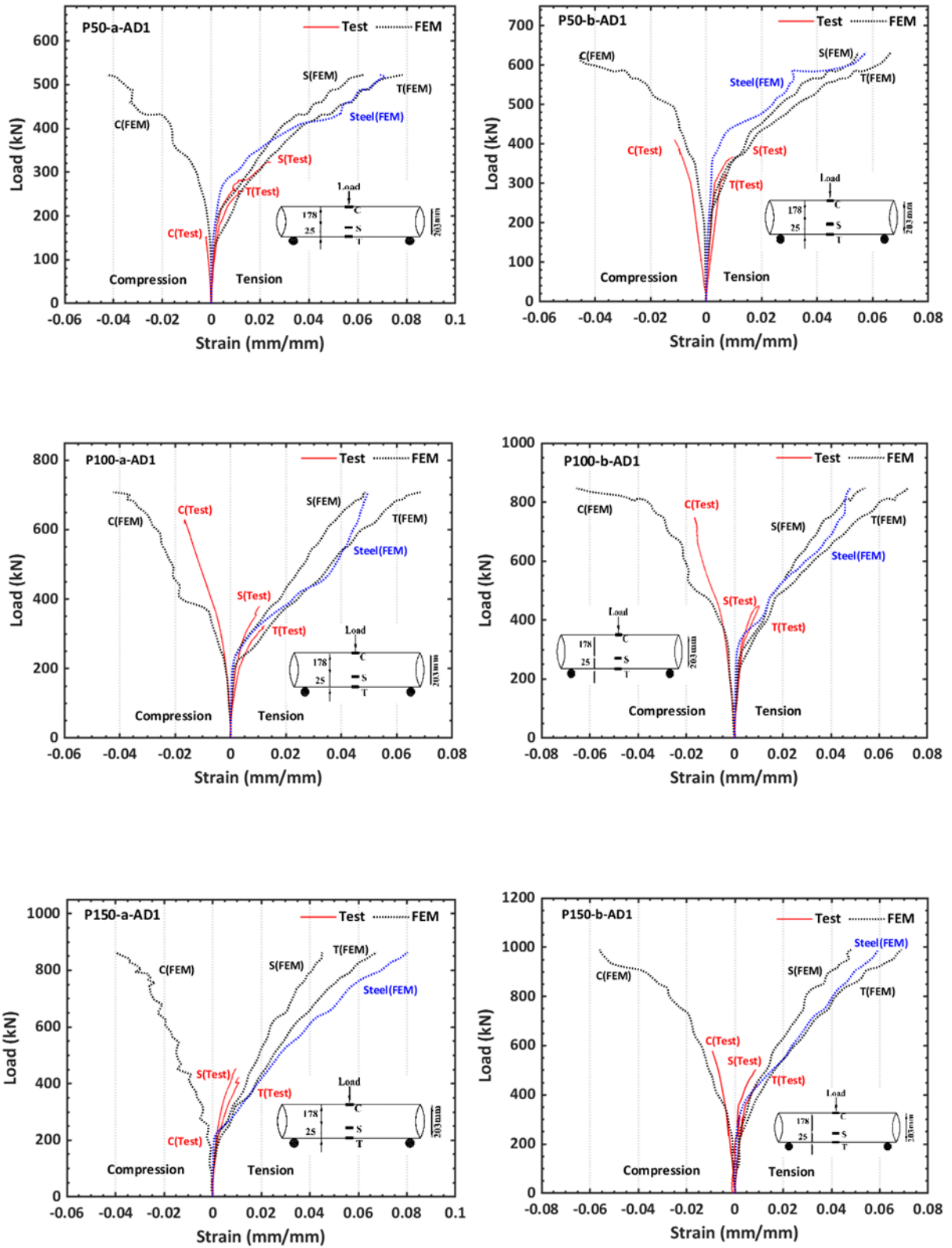


Figure 4-15. Load versus strain verification: a/D_i of 1 CFFT FE models

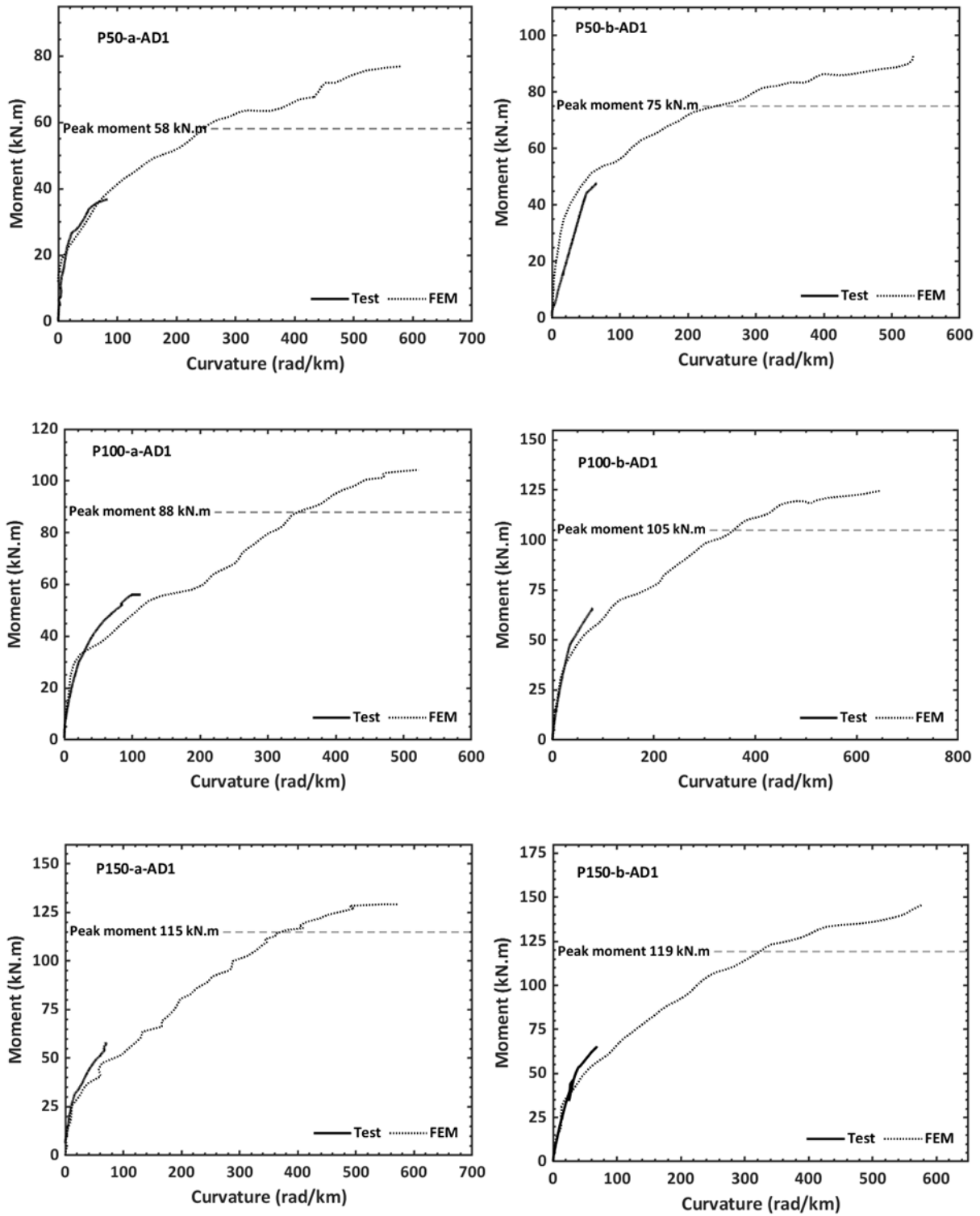
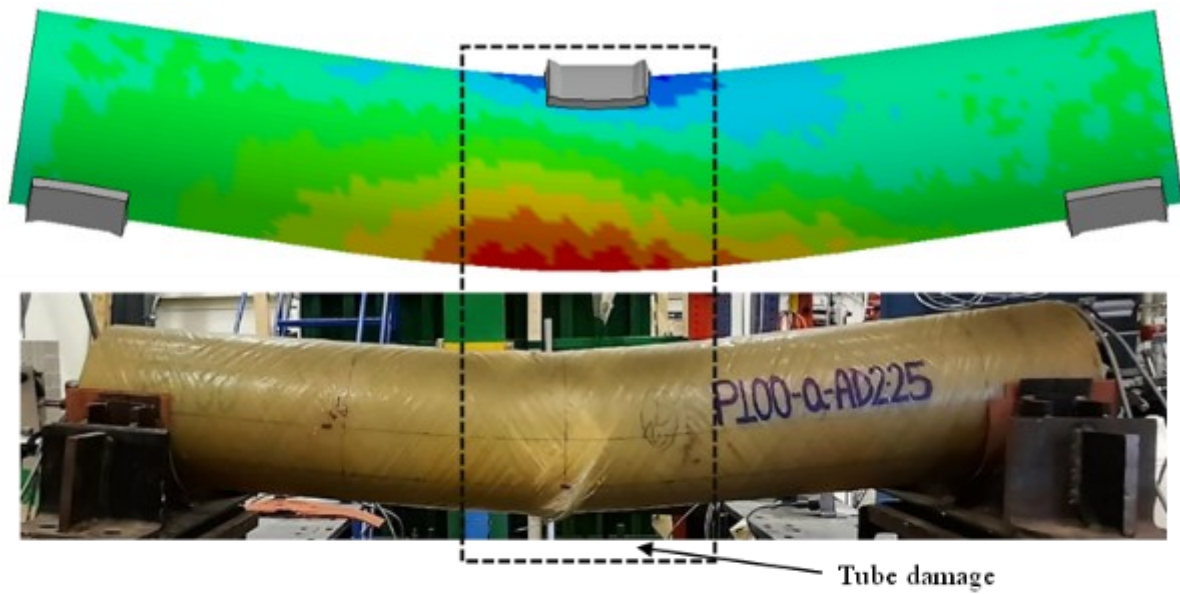
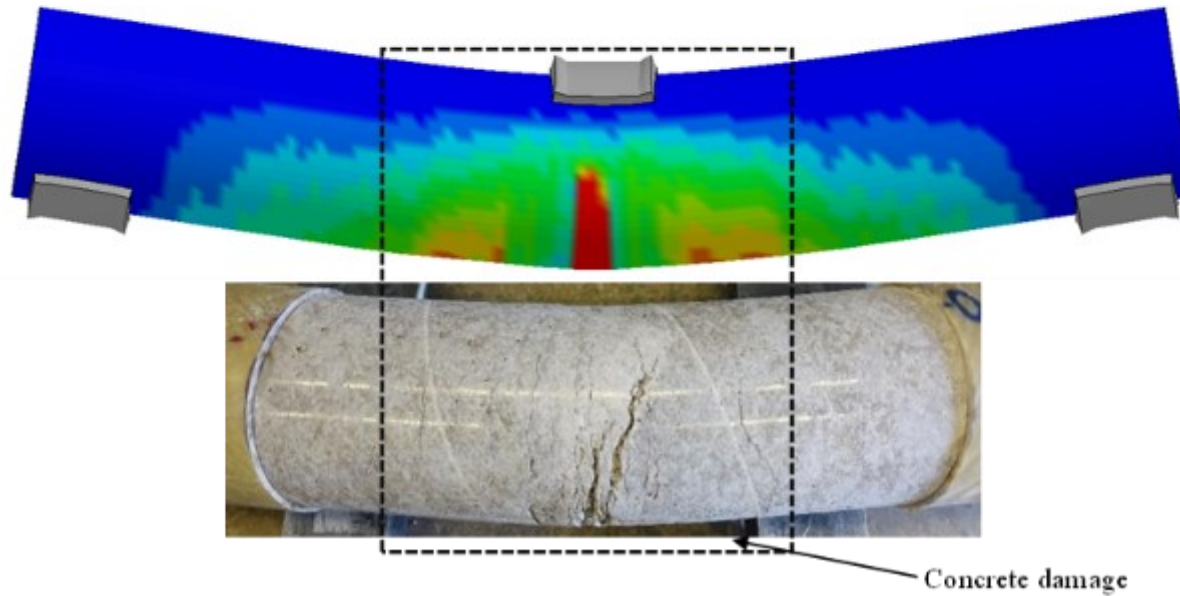


Figure 4-16. Moment versus curvature verification: a/D_i of 1 CFFT FE models



(a)



(b)

Figure 4-17. Visual comparison of P100-a-AD2.25 CFFT specimen: (a) Simulation of failure in GFRP tube; (b) Simulation of damage in concrete

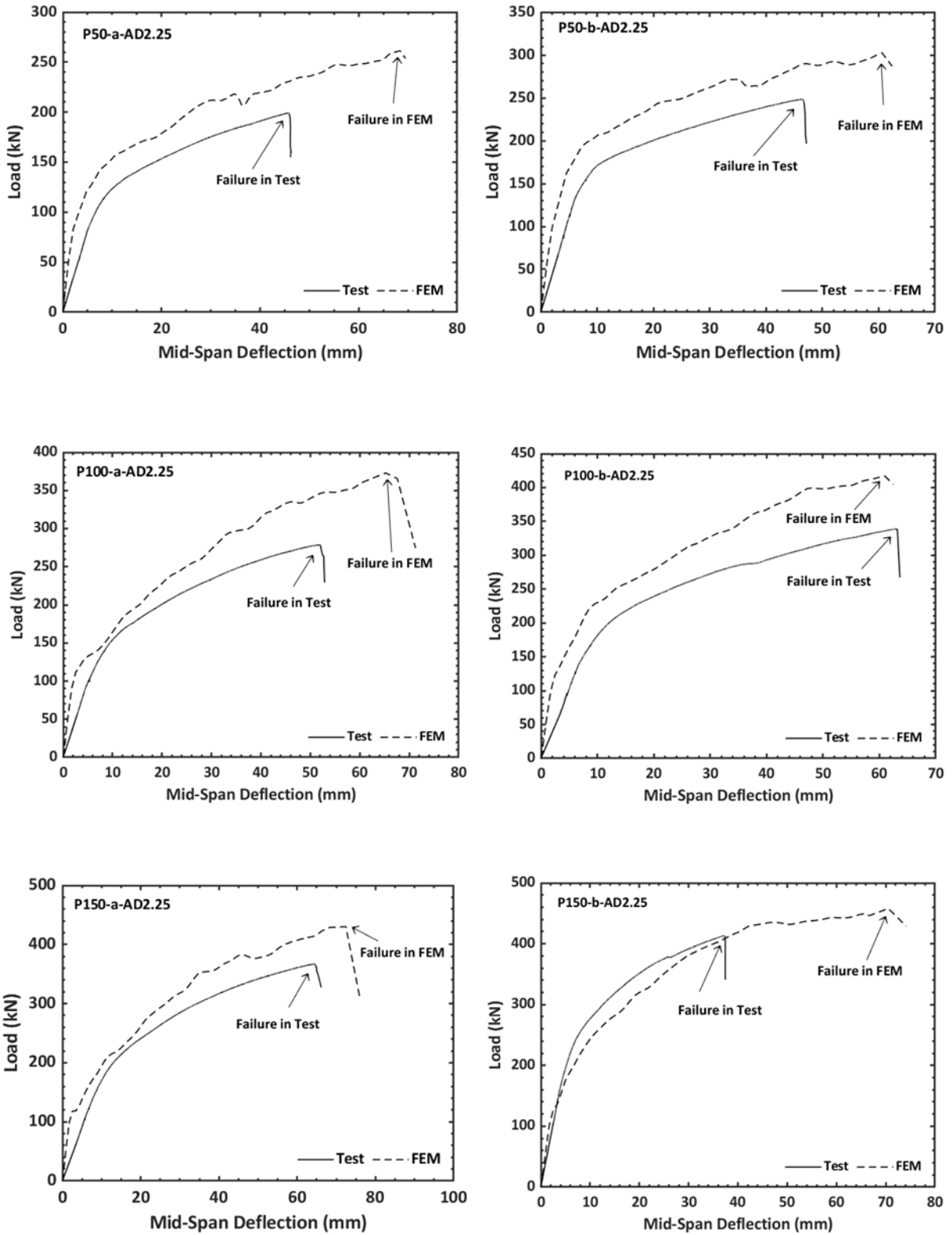


Figure 4-18. Load versus mid-span deflection verification: a/D_i of 2.25 CFFT FE models

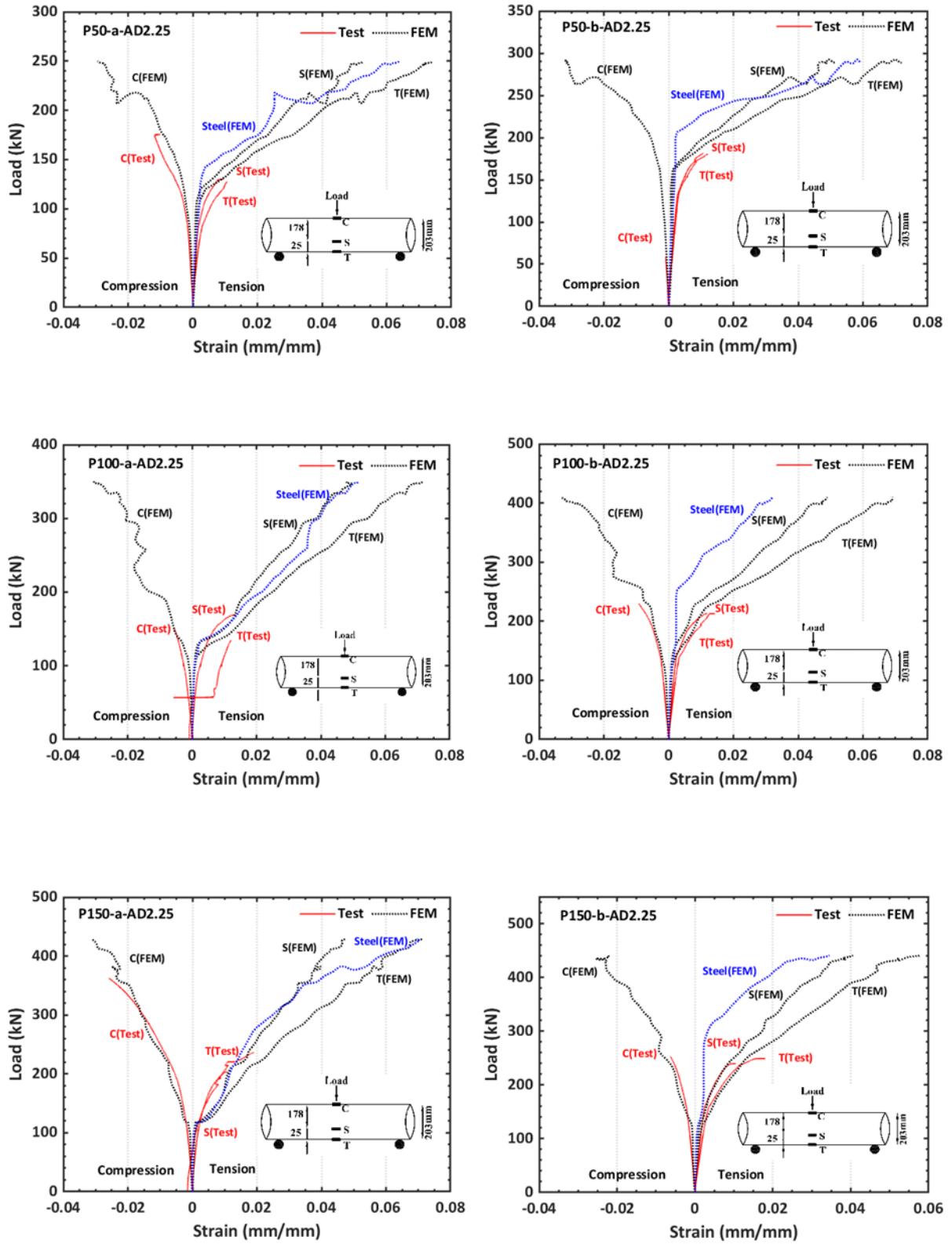


Figure 4-19. Load versus strain verification: a/D_i of 2.25 CFRT FE models

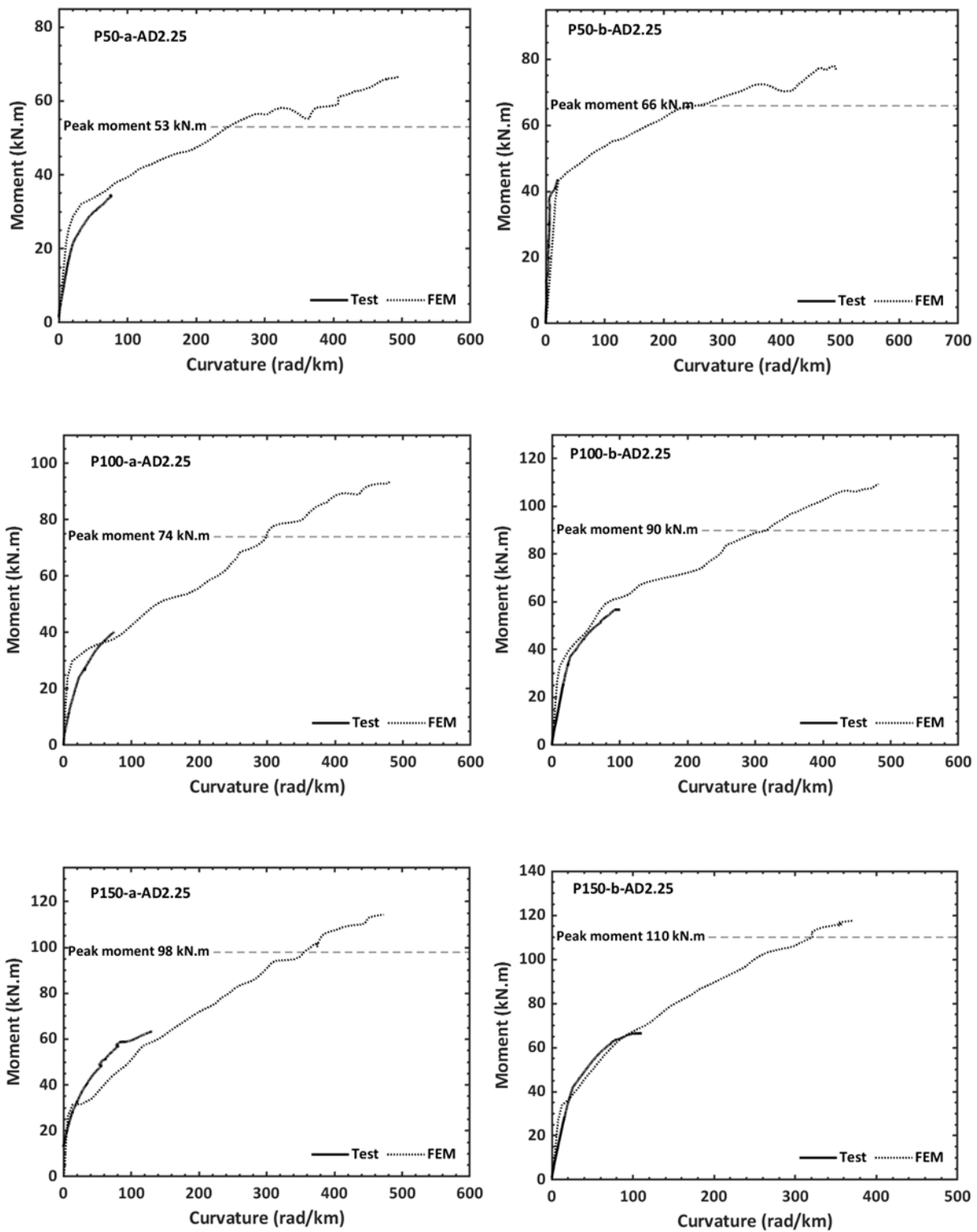


Figure 4-20. Moment versus curvature verification: a/D_i of 2.25 CFFT FE models

Overall, the comparison between experimental and FE models without SLIM factors showed that the developed FE model was successful in predicting the nonlinear behavior, failure mode, ultimate load capacities with an average error of 14%, mid-span deflection correspond to the ultimate load capacity of CFFTs. Also, from table 4-5, it could be noticed that the result prediction from the P50-CFFT FE models had a higher difference which further affected the overall average of the results. One of the probable causes of the inaccuracies related to the P50-CFFT models might be aroused due to the behavior and the mechanical properties of the P50-GFRP tubes, as a study by Betts et al. (2019) related the P50 hollow GFRP tubes showed a similar inconsistency while predicting its behavior. The standard deviation and the coefficient of variation for the ultimate load capacities of all CFFT specimens were 0.06 and 8%, respectively. In contrast, the standard deviation and the coefficient of variation (COV) for the mid-span deflections corresponding to ultimate load capacity were 0.23 and 23%, respectively, primarily due to the higher inaccuracies for the P50-CFFT specimens and P150-b-AD2.25 specimen. The test-model ratio of mid-span deflection for the P150-b-AD2.25 specimen was 0.53. This high discrepancy in the ratio was primarily due to the error in the instrumentation during the experiment, which was discussed previously in Chapter 3.

4.6.2 Model With Stress Limiting Factors

In addition to the FE models discussed in section 4.6.1, the FE models were modified, particularly the GFRP tube material model. As illustrated in tables 4-3 and 4-4, non-physical parameters such as SLIM factors were added to the material model, and modifications in the mechanical properties were made by reducing longitudinal strengths to inspect any improvement in the prediction on the behavior of the CFFTs. Finally, the results from the modified FE models were verified using the experimental results presented in Chapter 3. Table 4-6 provides the comparison of peak load, mid-span deflection at peak load, and initial stiffness between the FE models and experimental results.

Table 4-6. Verification of FE Models with SILM factors Using Test Data

CFFT SPECIMEN ID	Peak Load (kN)			Mid-Span Deflection at Peak Load (mm)			Initial Stiffness (kN/mm) ¹		
	Test	Model	Test- Model Ratio	Test	Model	Test- Model Ratio	Test	Model	Test- Model Ratio
P50-a-AD0.5	693	797	0.87	15.6	12.2	1.28	82.5	115.6	0.71
P100-a-AD0.5	1089	1133	0.96	17.9	12.4	1.44	105.8	122.9	0.86
P150-a-AD0.5	1393	1359	1.03	23.0	14.8	1.55	97.1	135.4	0.72
P50-b-AD0.5	929	986	0.94	17.1	11.4	1.50	92.1	135.5	0.68
P100-b-AD0.5	1329	1292	1.03	17.8	13.5	1.32	113.7	153.1	0.72
P150-b-AD0.5	1637	1497	1.09	21.1	14.6	1.45	121.8	165.8	0.73
P50-a-AD1	416	472	0.88	21.4	15.1	1.42	42.1	84.4	0.50
P100-a-AD1	630	693	0.91	23.1	18.6	1.24	52.8	92.0	0.57
P150-a-AD1	820	859	0.95	27.6	19.7	1.40	63.0	94.4	0.67
P50-b-AD1	538	599	0.90	22.3	20.9	1.07	80.8	90.8	0.89
P100-b-AD1	748	787	0.95	27.6	18.1	1.52	85.6	91.2	0.94
P150-b-AD1	854	937	0.91	31.2	19.3	1.62	86.6	95.0	0.91
P50-a-AD2.25	199	233	0.85	45.8	73.4	0.62	16.0	28.9	0.55
P100-a-AD2.25	279	331	0.84	51.9	60.5	0.86	19.9	31.0	0.64
P150-a-AD2.25	367	394	0.93	64.2	63.4	1.01	19.1	37.8	0.51
P50-b-AD2.25	248	290	0.86	46.5	52.2	0.89	22.3	39.1	0.57
P100-b-AD2.25	339	386	0.88	63.2	65.7	0.96	22.7	44.2	0.51
P150-b-AD2.25	413	446	0.93	37.4	47.5	0.79	40.3	52.9	0.76
Mean			0.93			1.22			0.69
Standard Deviation			0.07			0.30			0.14
COV (%)			7			25			20

¹ Initial stiffnesses were calculated between deflections of 1 mm and 5 mm

The average test-model ratio for prediction of peak loads and corresponding mid-span deflection at the peak loads are 0.93, and 1.22 respectively. The test-model ratio for the initial stiffness is 0.69. Figures 4-23, 4-27, and 4-31 exhibit the overall nonlinear behavior of CFFTs and compare the load-deflection behavior between tests and FE models. Figures 4-24, 4-28, and 4-32 show the strain behavior comparison between tests and FE models. Figures 4-25, 4-29, and 4-33 exhibits the comparison of moment-curvature between the tests and FE models. In general, the FE models were successful in capturing the nonlinear behavior of the CFFT and can be observed in load-deflection diagrams. Due to the limited strain results from the experiments, a convincing comparison study was not feasible between the strain behavior and the moment-curvature behavior of the CFFTs. Nevertheless, the strain and moment-curvature diagrams show that the models were successfully predicted the initial strain and moment-curvature behavior.

Furthermore, the failure mode of the CFFT from the FE model simulation showed that all CFFT FE models, independent of testing parameters, experienced a tensile rupture in the bottom face of the CFFT at the mid-span. Figure 4-21 (a), (b), and (c) represents the progression of failure in the P100-a-AD0.5 CFFT model. The red-colored elements in figure 4-21 (b) represents stress concentration at the bottom tension face of the GFRP tube in CFFT. Though these CFFT models' failure mode was similar to the failure experienced by the CFFT models without SLIM factors, the intensity of the failure was different. When comparing figures 4-8 (c) and 4-21 (c), it is evident that as the CFFT models reached the ultimate load capacity, the GFRP tube in the CFFT failed and lost its capacity entirely at the bottom tension region for models without SLIM factors.

In contrast, the failure in the GFRP tubes was not as severe as the previous one for the CFFT models with SLIM factors. This phenomenon can be further observed when comparing the load-deflection behavior between two different models. The models without SLIM factors experienced a sudden drop and complete loss in the load capacity, whereas those with SLIM factors experienced a significant load drop but did not experience a complete loss in their capacity. This phenomenon directly resulted from adding stress limiting factors (SLIM) in the GFRP tube material model, which helped retain some strength in the GFRP tube post-failure. However, the post-peak behavior of CFFTs was not accounted for in this study. Hence in-depth investigation on the SLIM factor coefficient was not considered.

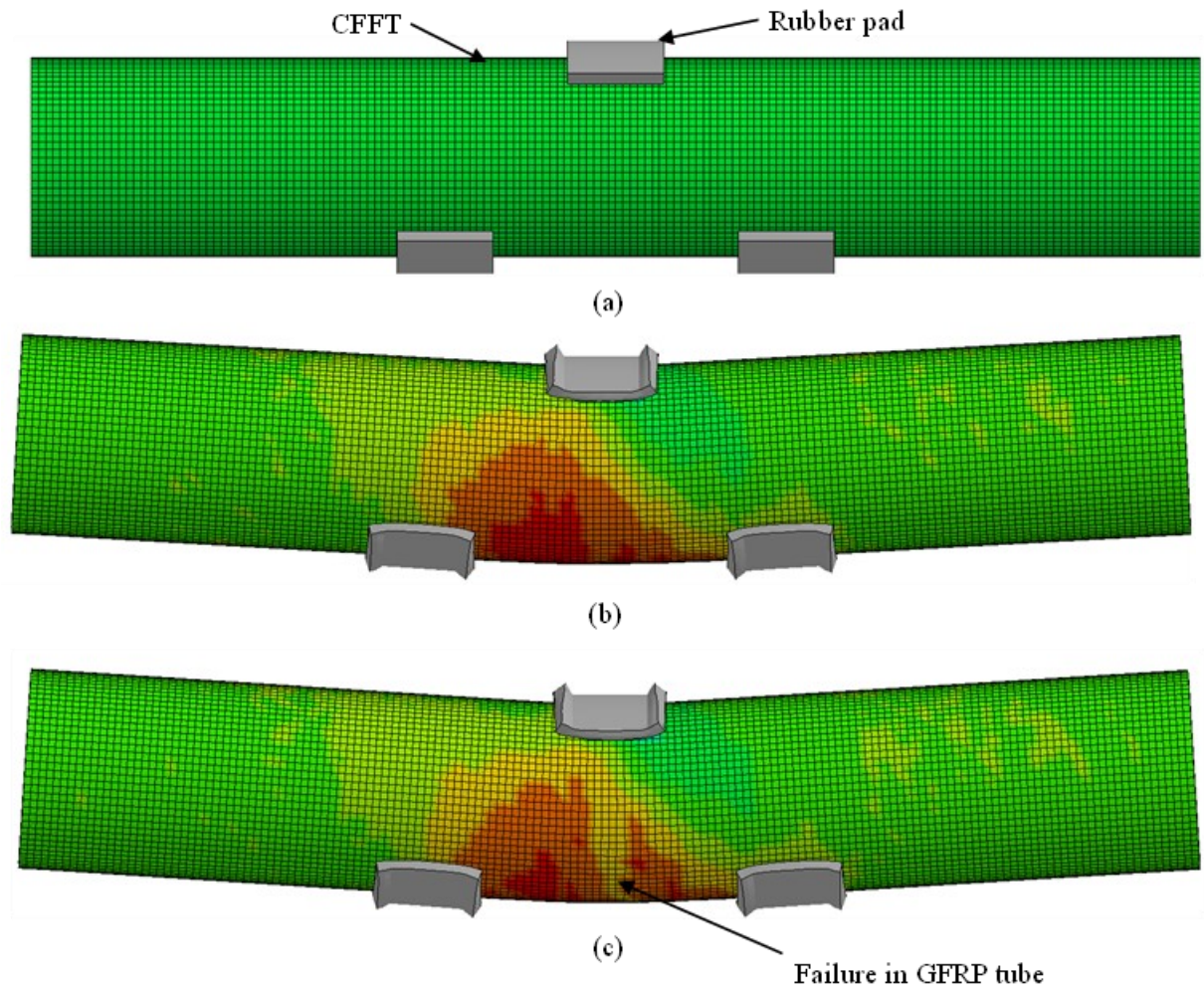


Figure 4-21. Progression of failure in CFFT model with stress limiting factors:
 (a) Before applied load; (b) Stress concentration in GFRP tube before failure; (c) Tension failure – sudden load-drop in the load-midspan deflection curve

Figures 4-22, 4-26, and 4-30, exhibit a comparison study between experimental failures and model simulation of the damage in the GFRP tube and concrete core of the P100-a-AD0.5, P100-a-AD1, and P100-a-AD2.25 CFFT models, respectively. Apart from capturing stress concentration and damage in the GFRP tubes, the FE models were successfully captured the damage development in the inner concrete core of the CFFT specimens. In addition, the FE models were able to accurately replicate the flexural cracks generated in the actual test specimens. While inspecting the strain values in the concrete

core from the contour plots, figures 4-22 (b), 4-26 (b), and 4-30 (b), the red areas portray the major flexural cracks and their progression in the concrete core of CFFTs, which started at the bottom tension region in the concrete core at the mid-span.

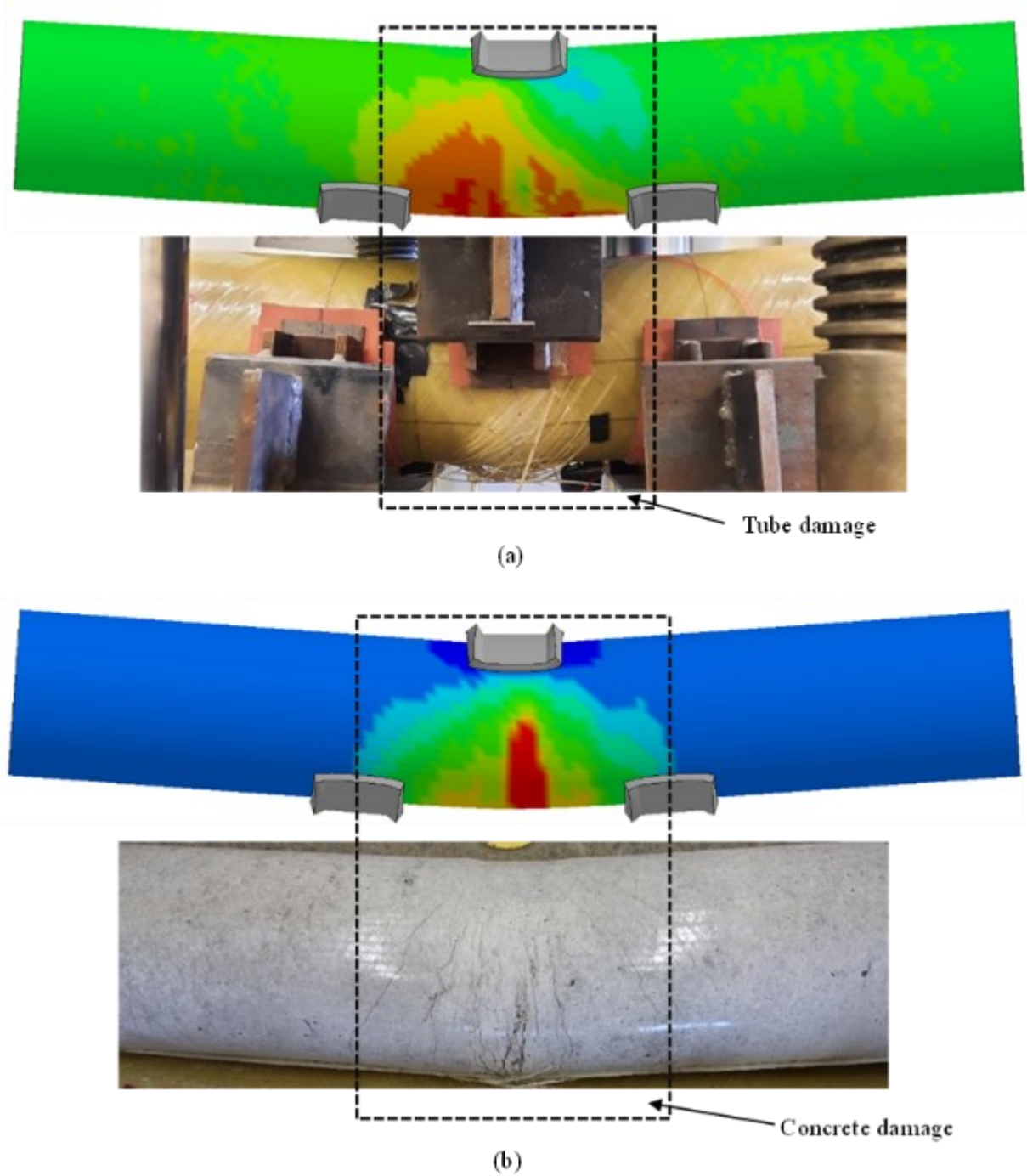


Figure 4-22. Visual comparison of P100-a-AD0.5 CFFT specimen: (a) Simulation of failure in GFRP tube; (b) Simulation of damage in concrete

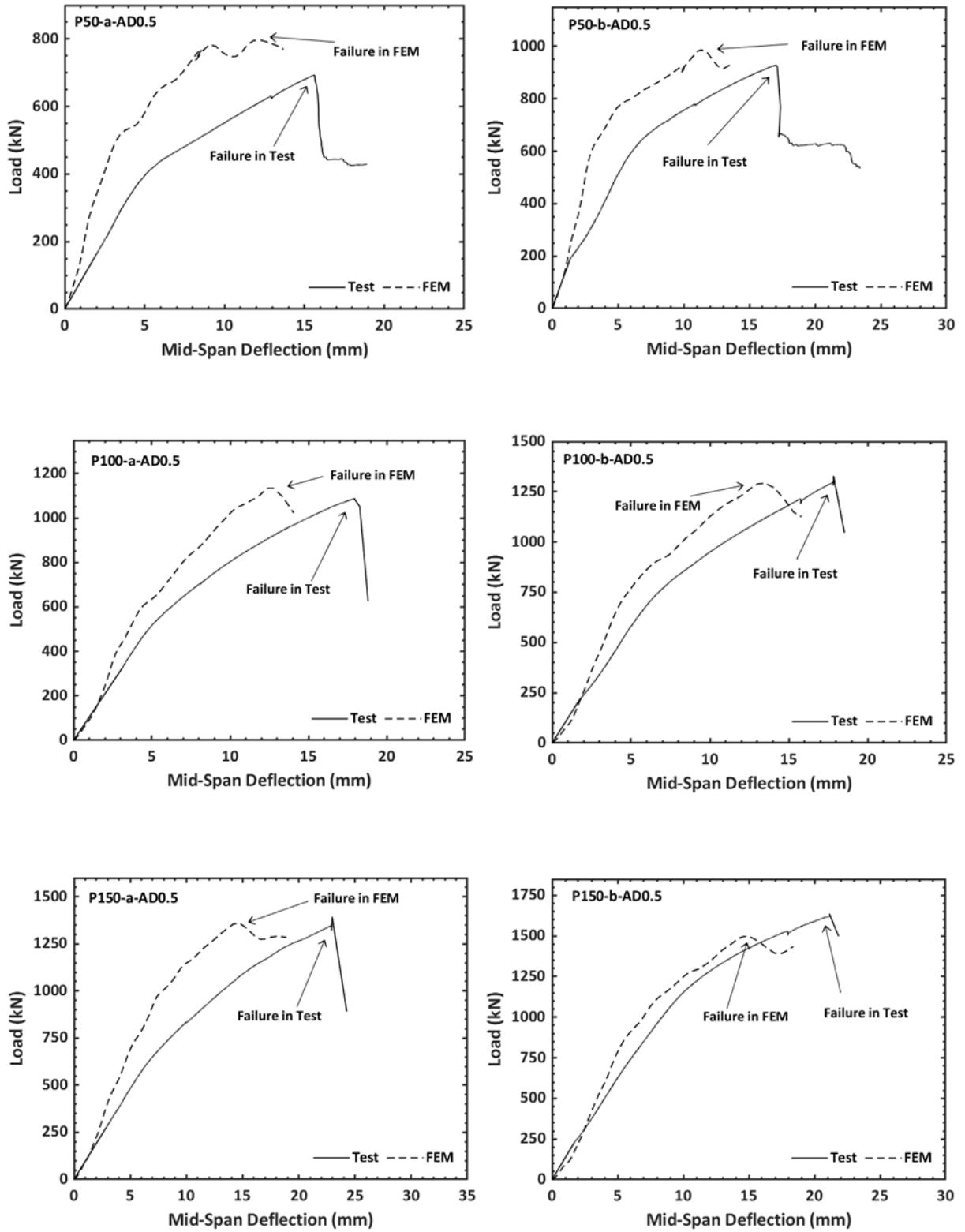


Figure 4-23. Load versus mid-span deflection verification: a/D_i of 0.5 CFFT FE models

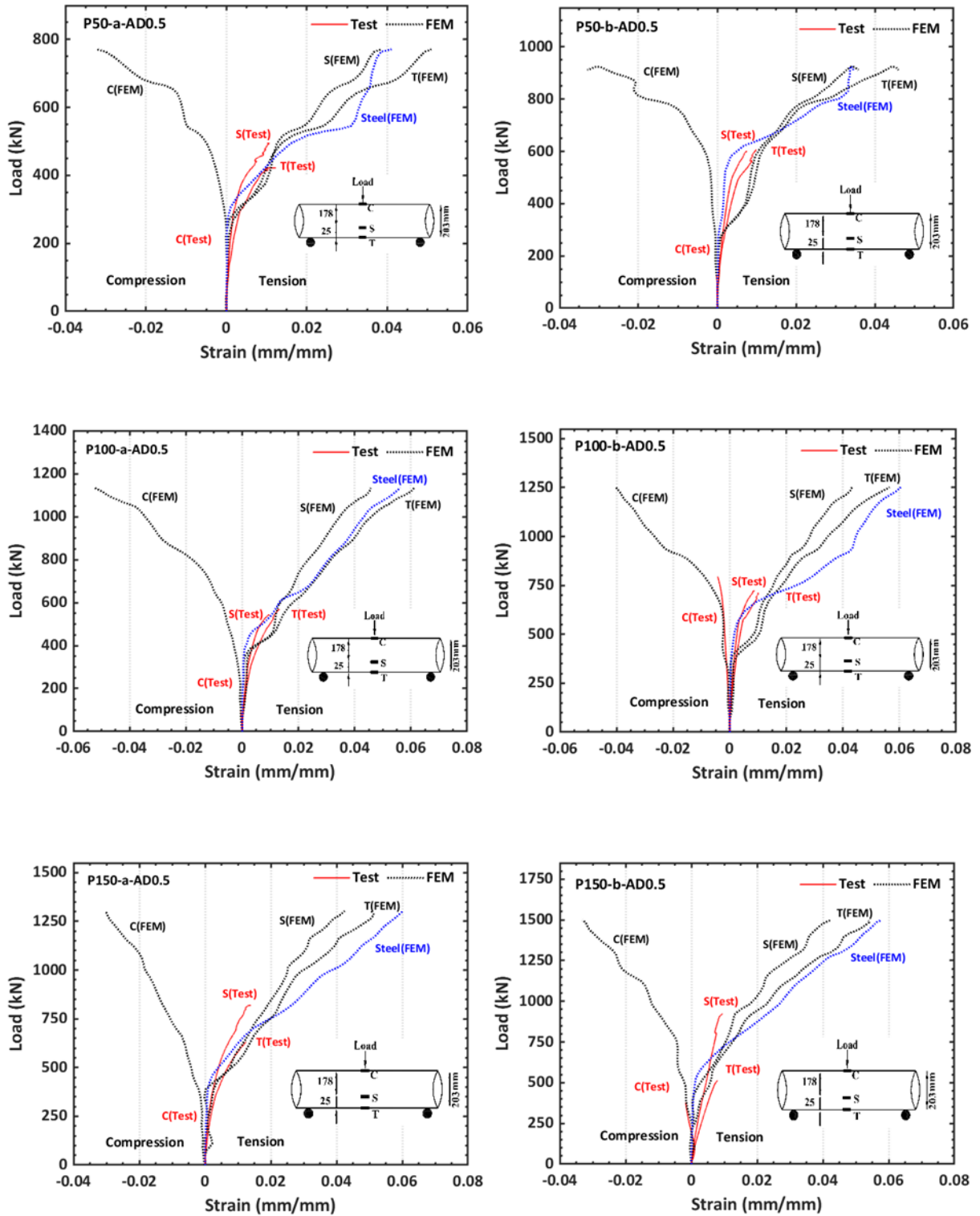


Figure 4-24. Load versus strain verification: a/D_i of 0.5 CFST FE models

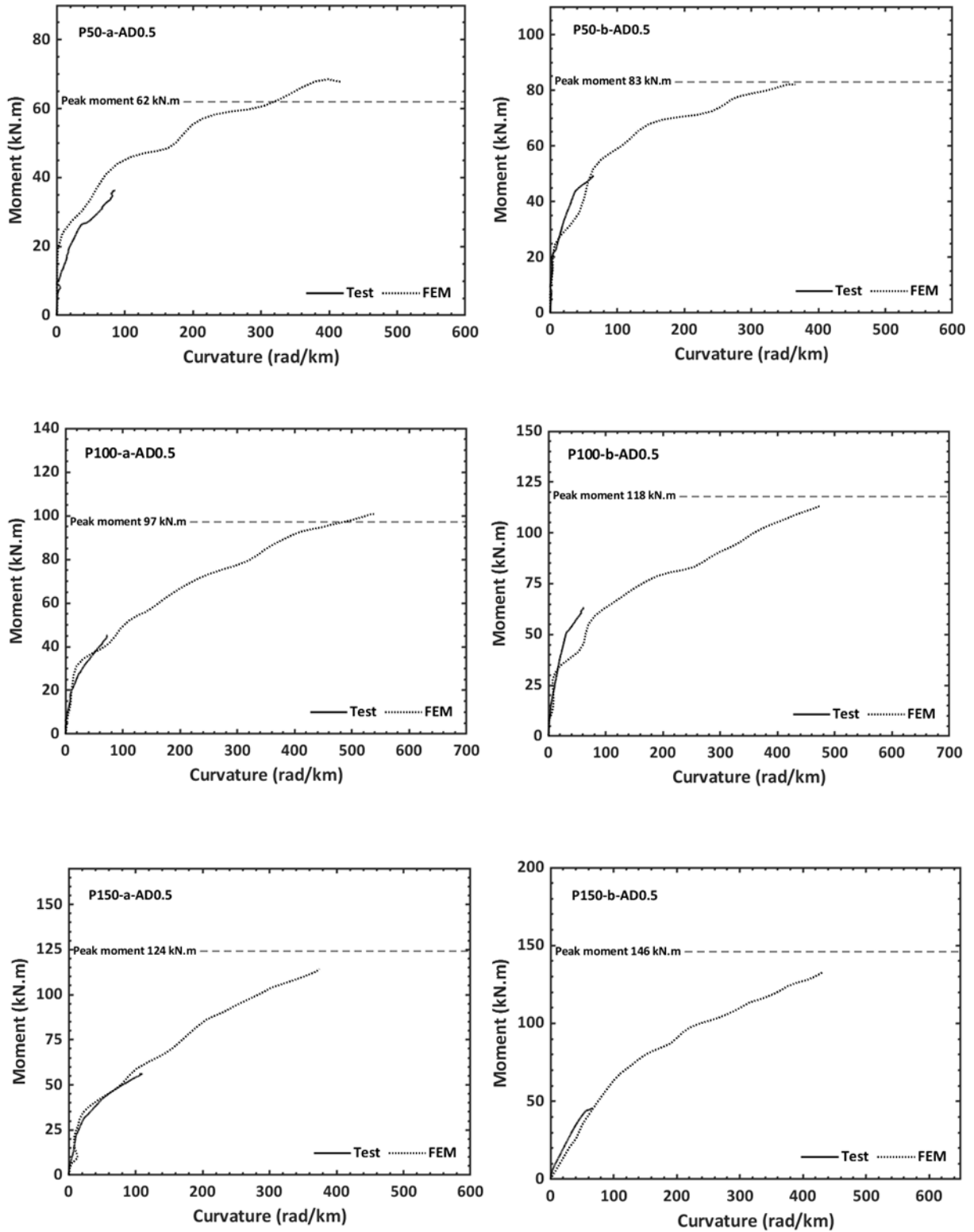
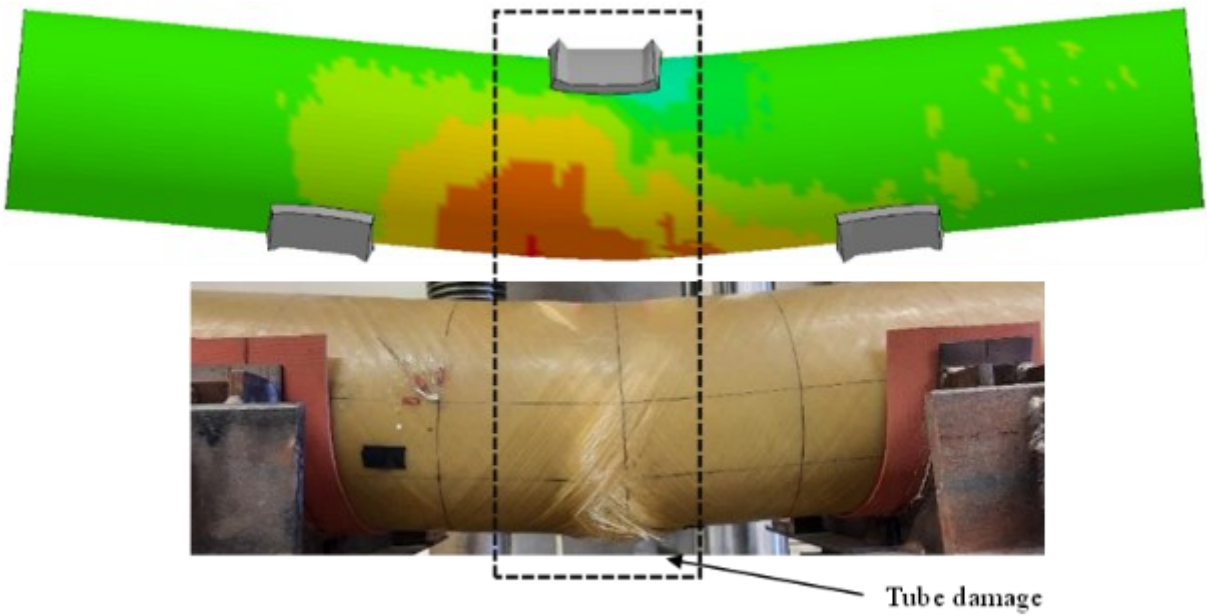
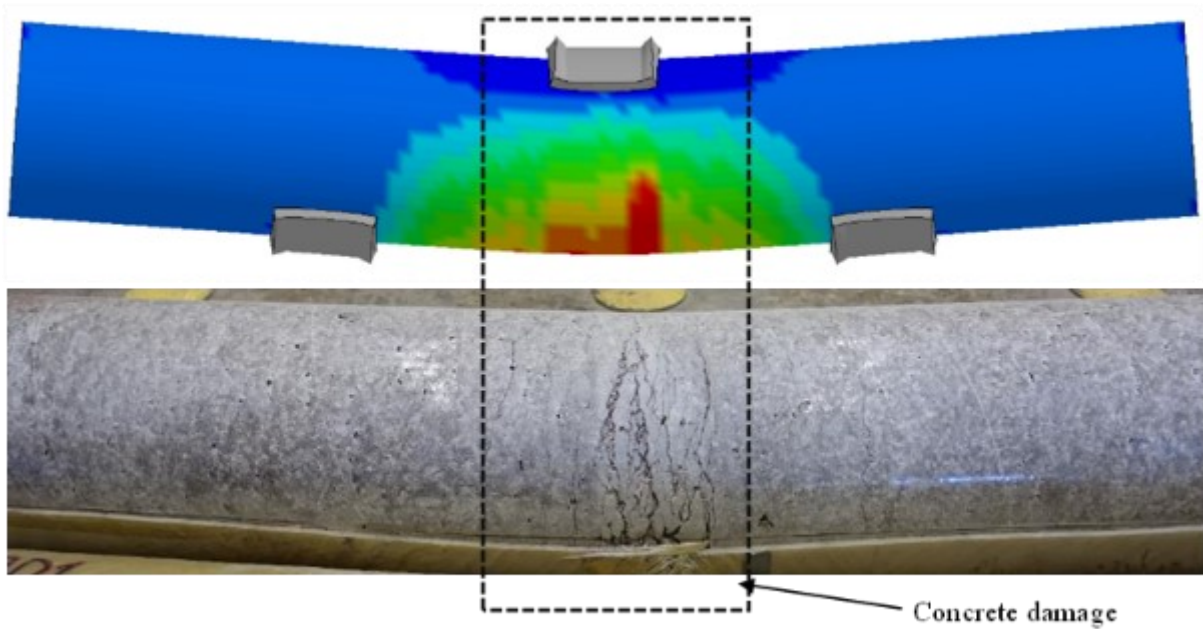


Figure 4-25. Moment versus curvature verification: a/D_i of 0.5 CFFT FE models



(a)



(b)

Figure 4-26. Visual comparison of P100-a-AD1 CFFT specimen: (a) Simulation of failure in GFRP tube; (b) Simulation of damage in concrete

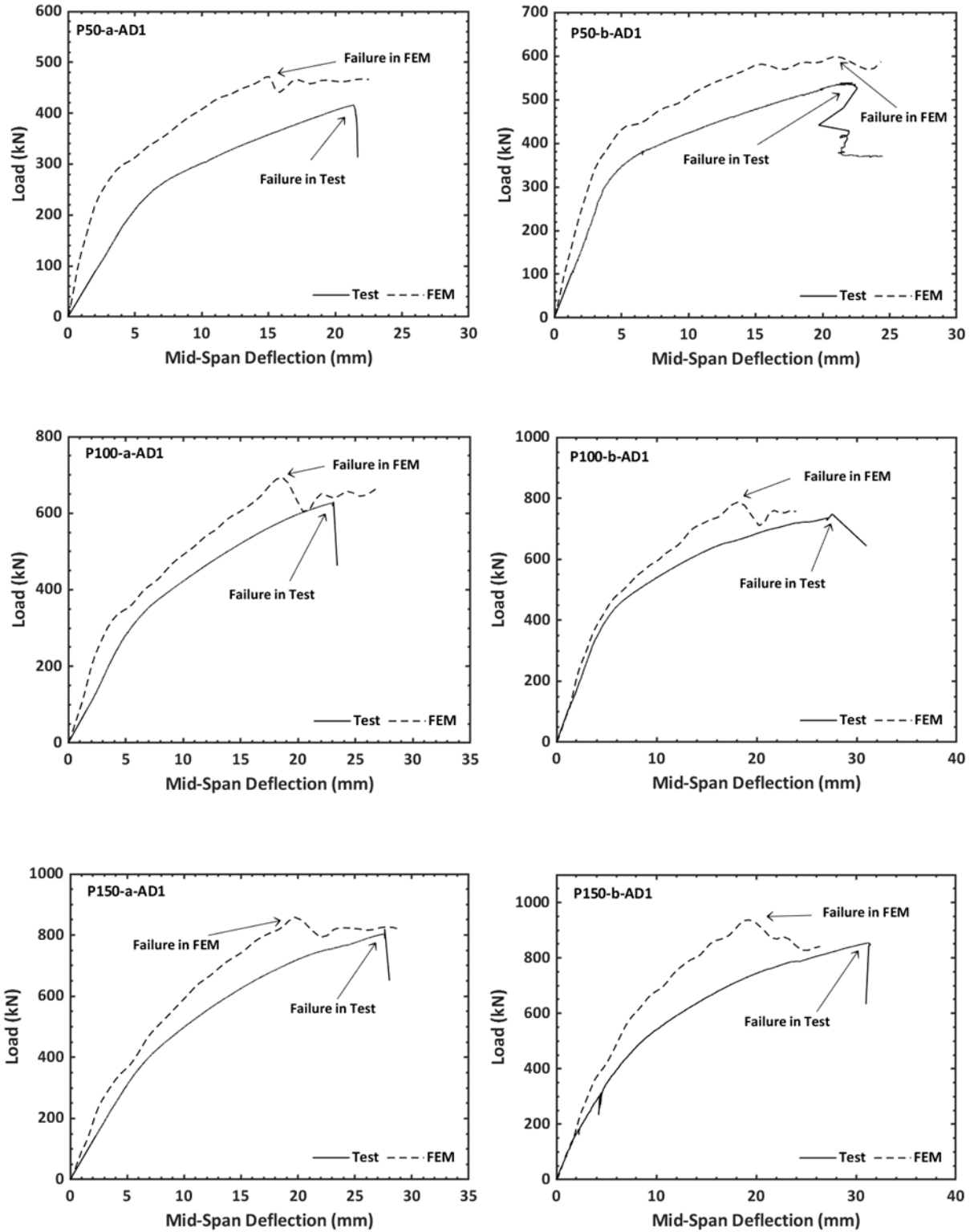


Figure 4-27. Load versus mid-span deflection verification: a/D_i of 1 CFFT FE models

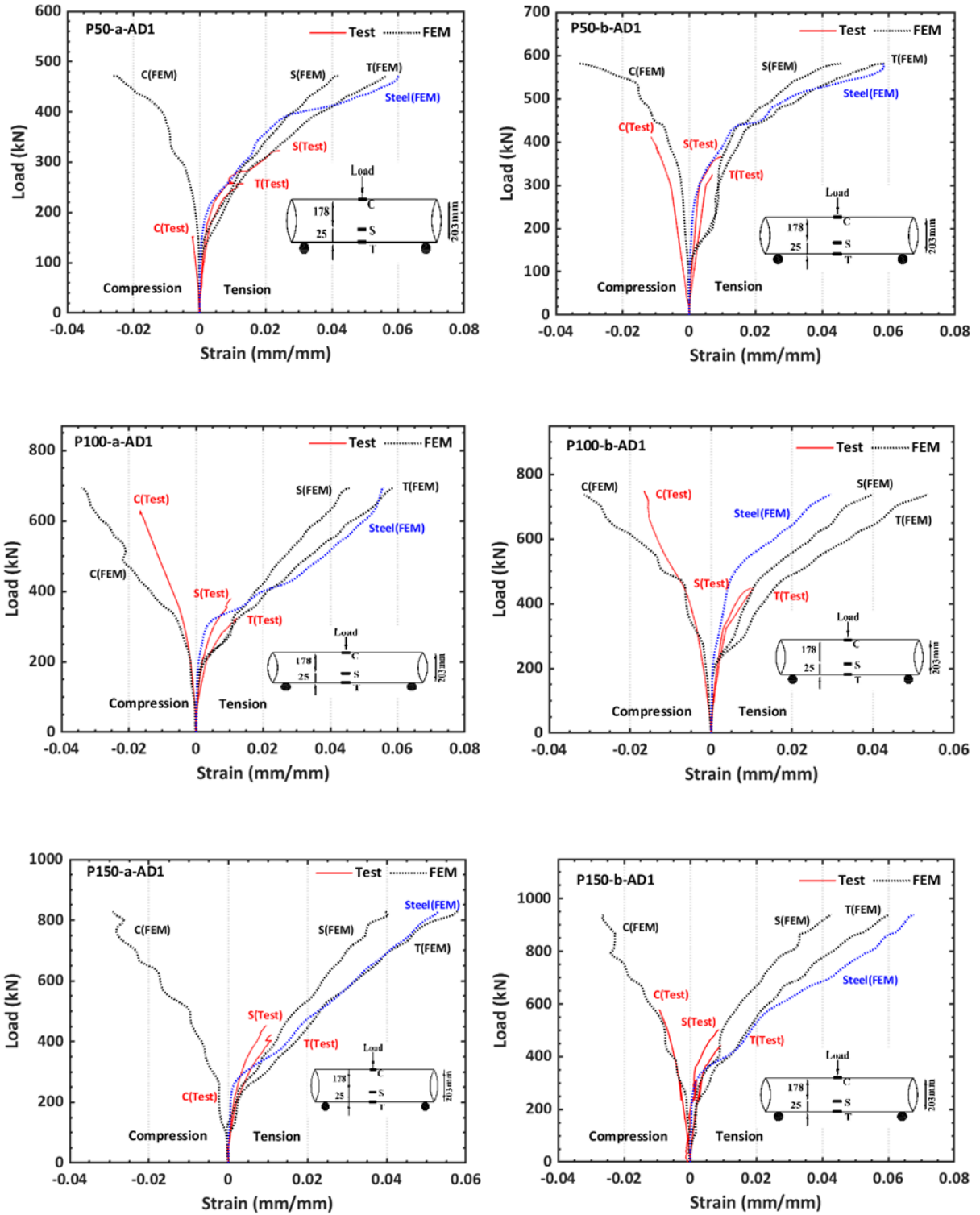


Figure 4-28. Load versus strain verification: a/D_i of 1 CFFT FE models

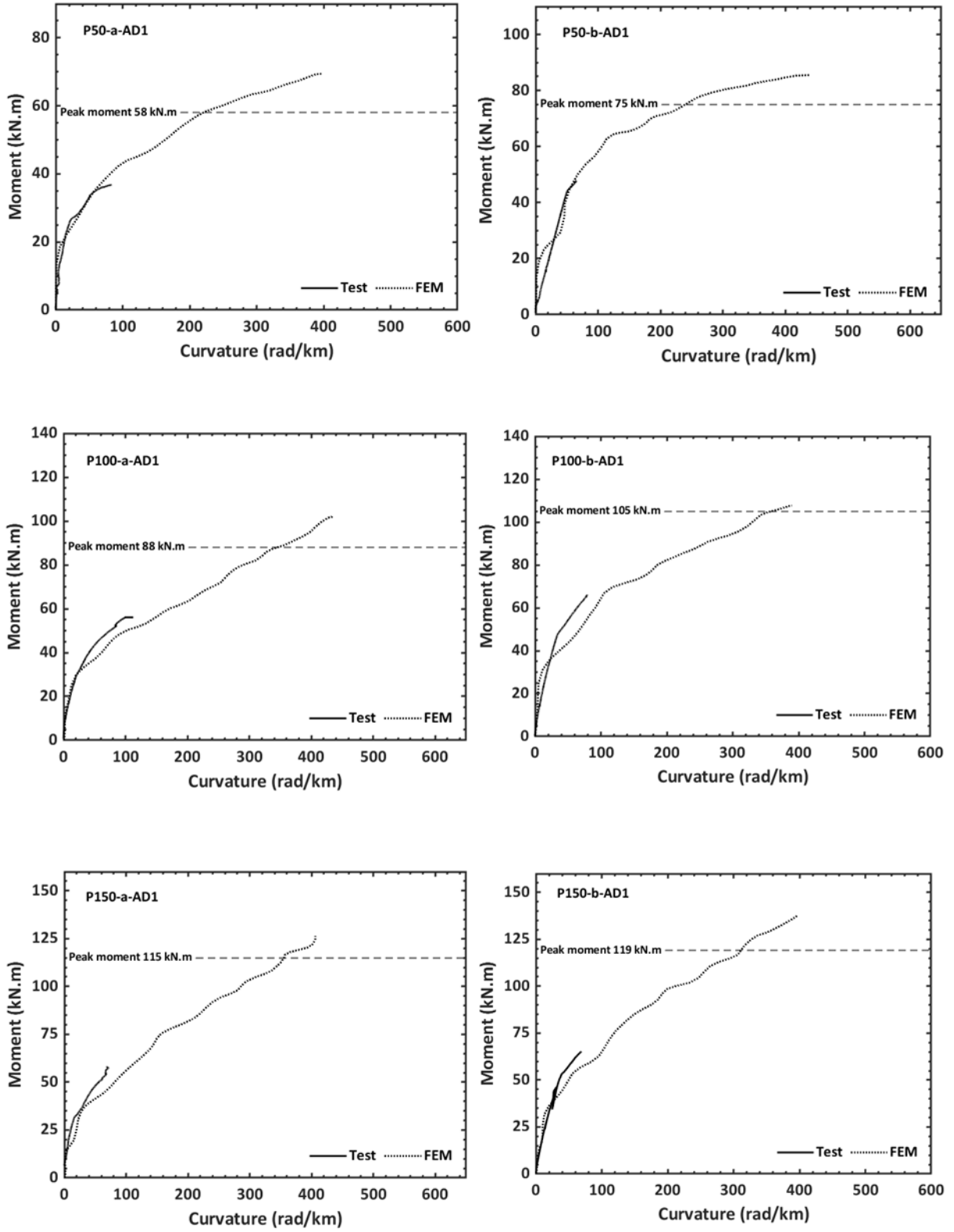
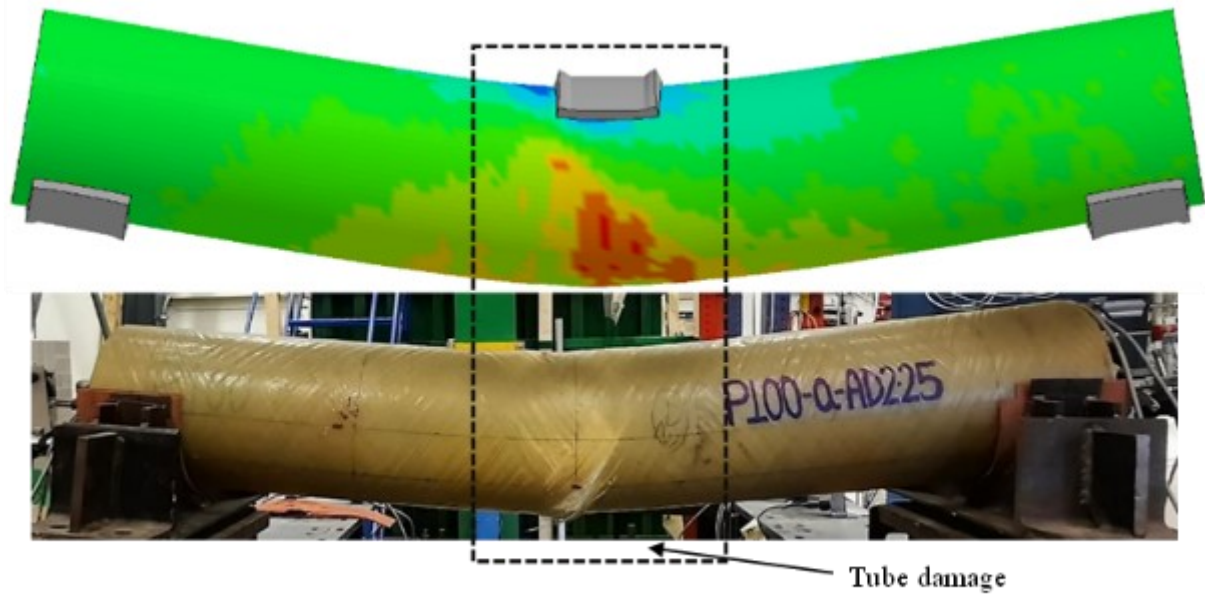
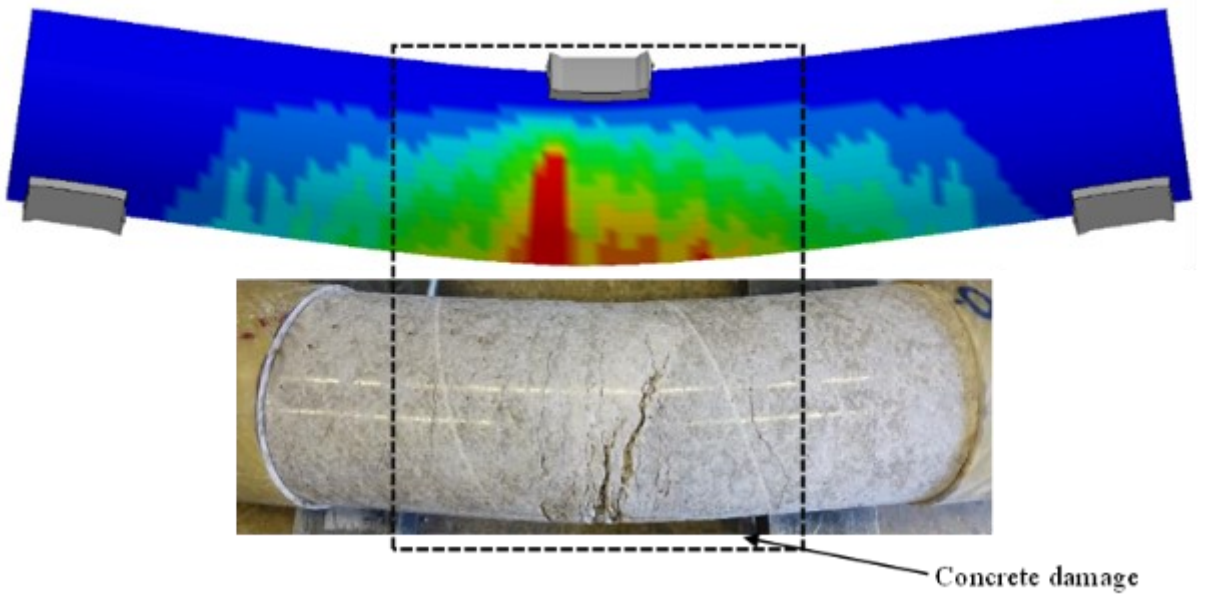


Figure 4-29. Moment versus curvature verification: a/D_i of 1 CFFT FE models



(a)



(b)

Figure 4-30. Visual comparison of P100-a-AD2.25 CFFT specimen: (a) Simulation of failure in GFRP tube; (b) Simulation of damage in concrete

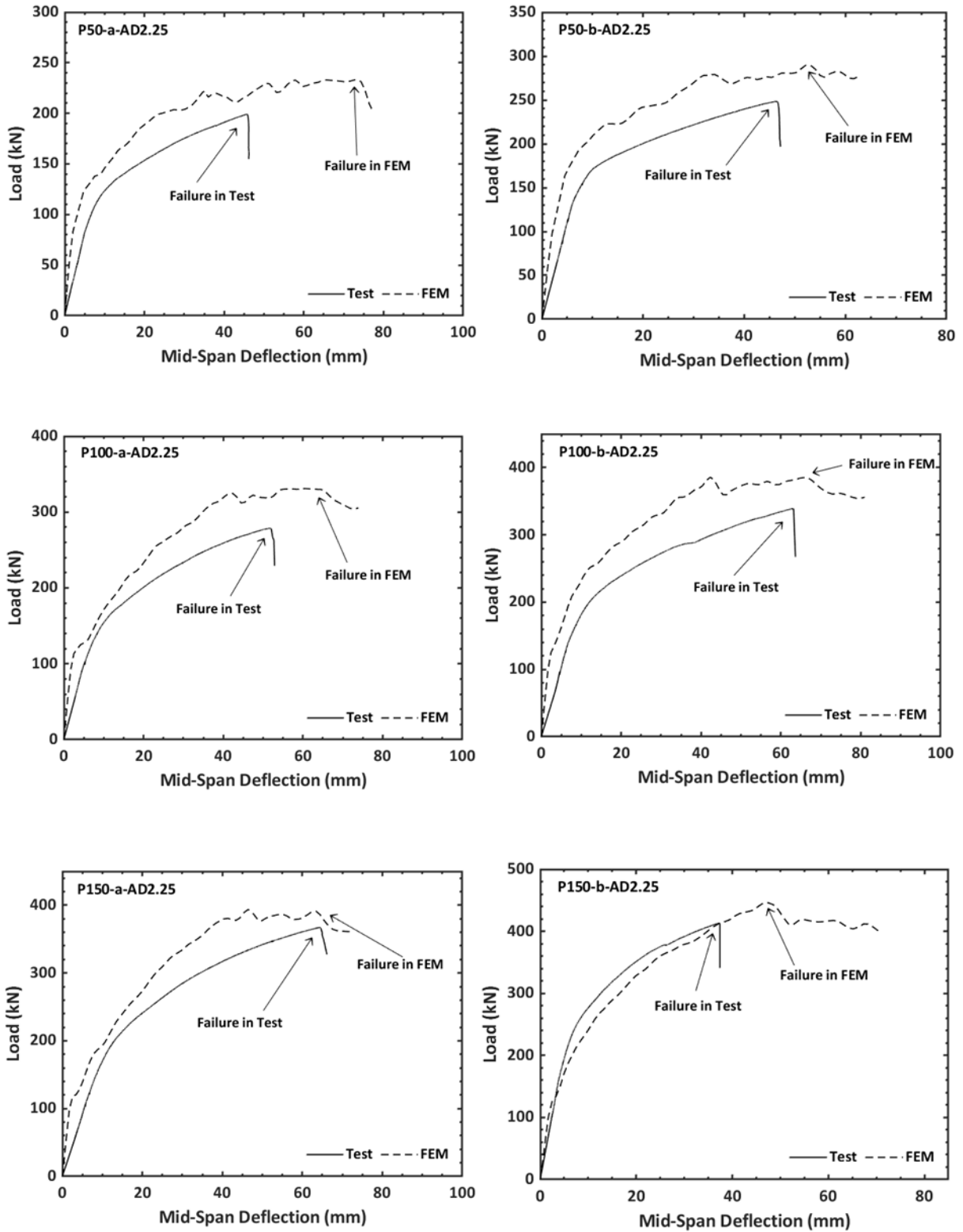


Figure 4-31. Load versus mid-span deflection verification: a/D_i of 2.25 CFFT FE models

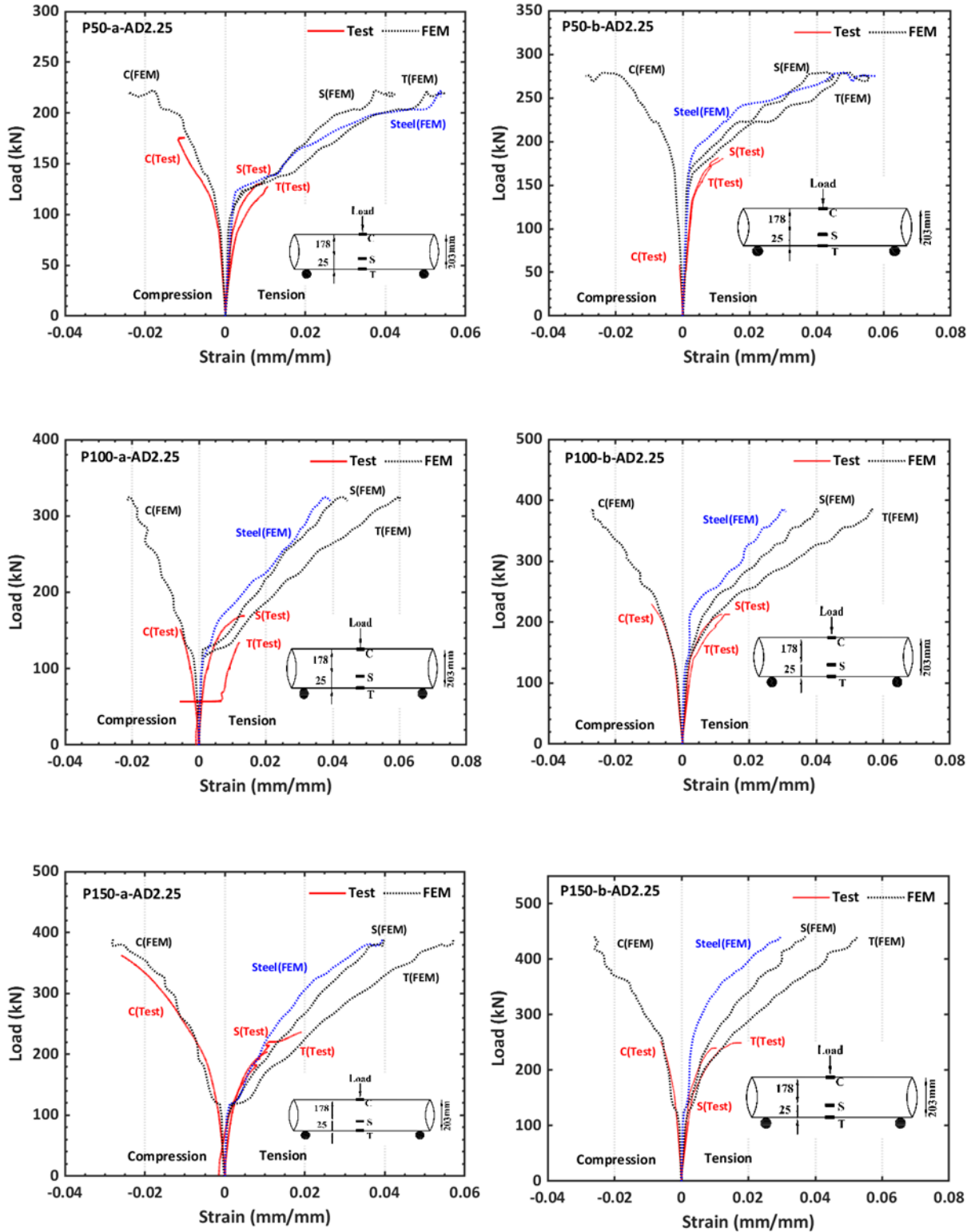


Figure 4-32. Load versus strain verification: a/D_i of 2.25 CFST FE models

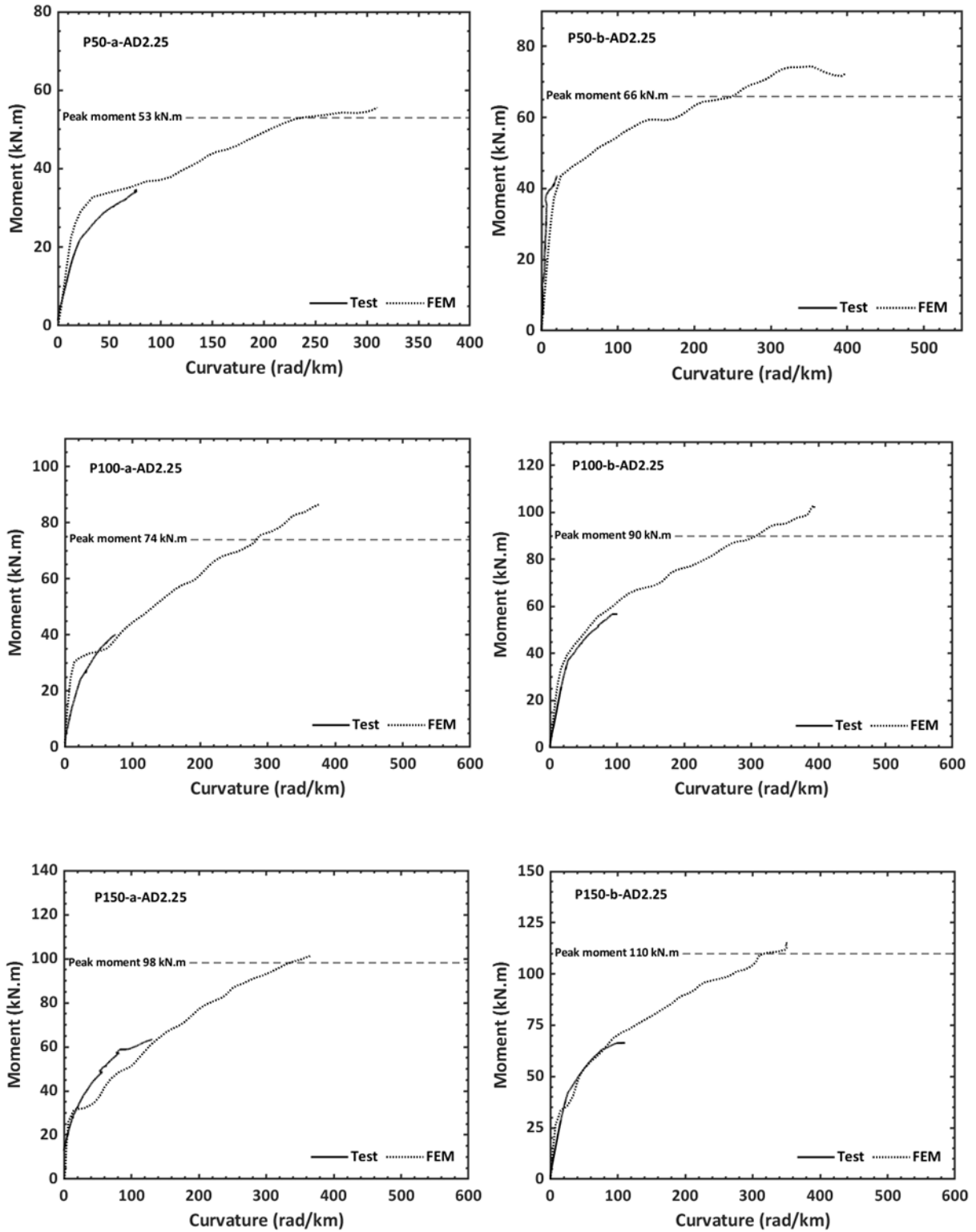


Figure 4-33. Moment versus curvature verification: a/D_i of 2.25 CFFT FE models

In general, the comparison between the test and model result showed an average error in ultimate load capacity prediction of 7%, with a standard variation and coefficient of variation of 0.07 and 7%, respectively. Although the models with SLIM factors on an average overpredict the ultimate load capacity, this is a significant improvement compared to the load capacity prediction by the models without SLIM factors. This improvement might not be directly related to the addition of SLIM factors but rather a consequence of the reduction in the longitudinal values strengths of the GFRP tube. The comparison also showed an average error of 22%, an underprediction in the mid-span deflection by the model with a standard variation and coefficient of variation of 0.3 and 25%, respectively. This discrepancy in the prediction of mid-span deflection could be correlated to the reduction in the longitudinal strength of the GFRP tube material model. From table 4-6, it was also noticed that the average test-model ratio for initial stiffness was 0.69, with a standard variation and coefficient of variation of 0.14 and 20%, a similar result when compared to the average acquired from the model without SLIM factors. The similar overprediction in the initial stiffness by both models, with and without SLIM factors, further substantiates that the contrast in the prediction aroused due to the model's assumptions, particularly the moduli and GFRP tube architecture. Overall, the comparison results between tests and FE models showed that the models were successful in predicting the nonlinear behavior, failure mode, ultimate load capacities, load-strain, and moment-curvature behavior of CFFTs.

CHAPTER 5 CONCLUSIONS AND RECOMMENDATIONS

5.1 CONCLUSIONS

The presented research aimed to explore the shear and flexural behavior and failure modes of reinforced concrete-filled fiber-reinforced-polymer tubes (CFFTs) to confirm their structural capabilities in the field of sustainable infrastructure. This research also provides a platform for developing a reliable design procedure to lay a foundation for future works and design recommendations. In order to achieve these goals, a total of eighteen steel-reinforced CFFT beam specimens were prepared and tested under three-point bending with changing parameters. The experimental parameters included: three types of GFRP tubes in terms of wall thickness; type of internal steel reinforcement in terms of reinforcement ratio; and three different shear span to depth ratios, namely 0.5, 1, and 2.25. Additionally, a finite element model was developed with the help of LS-DYNA to capture the nonlinear behavior of CFFTs and validate the experimental results. Based on the experimental and FEA study, the following conclusions are drawn:

- All eighteen CFFT beams tested as a part of this study failed due to flexure. The CFFT beams ultimately failed by rupturing the bottom tension region of the GFRP tubes at mid-span. Unlike some CFFTs reported in the literature, deep CFFTs with $\pm 55^\circ$ GFRP tubes, particularly when tested under shear span to depth ratio (a/D_i) of 0.5, were not susceptible to shear failure. This resistance towards shear failure was primarily due to the presence of fibers in the $\pm 55^\circ$ direction with respect to the longitudinal axis of the GFRP tubes, which prevented any development of diagonal fracture in the GFRP tubes.
- The GFRP tubes used in this study had a constant inner diameter and three varying tube wall thicknesses related to their different pressure capacities. CFFTs with GFRP tubes of three different nominal pressure ratings, P50, P100, and P150, had inner diameter to wall thickness ratios (D_i/t) of 75, 43, and 30, respectively. The results exhibited that the overall ultimate capacity of CFFTs was increased with the increase in pressure rating of the GFRP tubes. However, irrespective of the other test parameters, the percentage increase in the ultimate load capacity between

P50 and P100 CFFTs was much higher when compared to the difference between P100 and P150 CFFTs.

- Effect of two different internal steel reinforcement ratios of 1.85% and 3.70% in CFFT specimens exhibited that the ultimate load capacity, stiffness, and ductility of the CFFTs increased with the increase in the internal reinforcement ratio. The increase in load capacity due to the increased reinforcement ratio was higher for P50 CFFT specimens when compared to P100 and P150 CFFTs. The load capacity increase due to the increase in internal steel reinforcement ratio in CFFTs was in descending order for P50, P100, and P150 CFFT specimens.
- The ultimate capacity of the similar CFFT specimens increased as the shear span to depth ratio (a/D_i) decreased. This phenomenon was mainly due to the formation of compression struts in the CFFT beams between the load and the supports. In addition, the CFFT specimens tested under a/D_i of 0.5 and 1 revealed the presence of flexural-shear and web shear crack patterns in their concrete core. This crack pattern development further substantiates the compression strut formation claims. The load capacity increase in CFFTs with the decrease in a/D_i ratio was maximum among the P150 CFFT specimens followed by P100 and P50 CFFT specimens.
- Overall, the ultimate moment capacity of the CFFT members, increased with an increase in their total normalized reinforcement ratio. However, the GFRP tube pressure ratings, in terms of their wall thickness and internal steel reinforcement ratios, also separately had a significant influence on the ultimate moment capacity of CFFTs.
- With no bond enhancement measures in place, the maximum slip of less than 0.7 mm was recorded between the GFRP tube and concrete core for the P150-a-AD1 specimen during the entire loading history of the CFFT tests. This result further indicated superior composite action between components in the CFFT members.
- The developed finite element models in this study were reasonably successful in predicting the overall nonlinear behavior, capacity, and failure mode of all CFFT specimens.
- The FE models with SLIM factors in the GFRP material model showed higher accuracy in predicting the load capacity of the CFFT specimens. The improvement

in prediction from those models was a consequence of the changes made in the mechanical properties of the GFRP tubes rather than the introduction of SLIM factors. Although, the SLIM factors could be an influential parameter for modeling the post-peak behavior of the CFFTs.

5.2 RECOMMENDATIONS FOR FUTURE STUDIES

This research addressed the shear and flexural behavior of CFFTs with $\pm 55^\circ$ fiber orientation. In addition to the conclusion drawn based from the experimental study and finite element model, the following future recommendations are suggested to further expand on the research of CFFTs with $\pm 55^\circ$ fiber orientation:

- Studying the effect on CFFTs with $\pm 55^\circ$ fiber orientation under combined axial-flexural loading for developing axial load-moment interaction diagrams.
- Analyze the mechanical performance of steel-reinforced CFFTs with $\pm 55^\circ$ fiber orientation under dynamic loading conditions to understand load-bearing behavior further.
- Study the effect of cyclic loading on the CFFT members to analyze the fatigue limit.
- Refining the finite element model to incorporate accurate GFRP tube architecture and non-physical parameters for GFRP tube such as SLIM factors, ERODS, SOFT.
- Additional research on the materials should be conducted to address the limitation in material properties of GFRP tube and concrete to improve the material models for finite element models.
- Develop a complete design guideline, readily available to engineers for a wide range of field applications of CFFTs.

BIBLIOGRAPHY

- Abdelkarim, O. I., and ElGawady M. A. (2014). “Analytical and Finite-Element Modeling of FRP-Concrete-Steel Double-Skin Tubular Columns.” *Journal of Bridge Engineering*, ASCE, Vol. 20, No. 8, B4014005, pp. 1-12.
- ACI. (2014). – “ACI 318, Building Code Requirements for Structural Concrete and Commentary.”
- Ahmad, I., Zhu, Z., and Mirmiran, A. (2008). “Behavior of Short and Deep Beams Made of Concrete-Filled Fiber-Reinforced Polymer Tubes.” *Journal of Composites for Construction*, ASCE, Vol. 12, No. 1, pp. 102-110.
- Ahmed, A. A., Hassan, M., and Masmoudi, R. (2020). “Flexural Performance of Unbonded Posttensioned Rectangular Concrete Filled FRP Tube Beams.” *Journal of Composites for Construction*, ASCE, 24(5):04020058, pp.1-16.
- ASTM. (2016). – “ASTM A615/A615M, Standard Specification for Deformed and Plain Carbon-Steel Bars for Concrete Reinforcement.”
- ASTM. (2017). – “ASTM A370, Standard Test Methods and Definition for Mechanical Testing of Steel Products.”
- ASTM. (2012). – “ASTM C39/39M, Standard Test Method for Compressive Strength of Cylindrical Concrete Specimens.”
- ASTM. (2018). – “ASTM C33/C33M, Standard Specification for Concrete Aggregates.”
- ASTM. (2018). – “ASTM C1611/C1611M, Standard Test Method for Slump Flow of Self-Consolidating Concrete.”
- Betts, D., Sadeghian, P., and Fam, A. (2019). “Investigation of the stress-strain constitutive behavior of $\pm 55^\circ$ filament wound GFRP pipes in compression and tension.” *Composites Part B*, Elsevier Ltd., 172(2019), 243-252.
- Betts, D., Sadeghian, P., and Fam, A. (2020). “Experimental and analytical investigations of the flexural behavior of hollow $\pm 55^\circ$ filament wound GFRP tubes.” *Thin-Walled Structures*, Elsevier Ltd., Vol. 159, 107246, pp. 1-13.
- Burgueño, R., and Bhide, K. M. (2006). “Shear Response of Concrete-Filled FRP Composite Cylindrical Shells,” *Journal of Structural Engineering*, ASCE, 132(6), 949-960.

- Canadian Infrastructure Report Card (CIRC, 2019) – Monitoring the State of Canada’s Core Public Infrastructure.
- Chatla, P. (2012). “LS-Dyna for Crashworthiness of Composite Structures.” Master of Science thesis, University of Cincinnati, USA.
- Cherniaev, A., Butcher, C., and Montesano, J. (2018). “Predicting the axial crush response of CFRP tubes using three damage-based constitutive models.” *Thin-Walled Structures*, Elsevier Ltd., 129(2018): 349-364.
- Cole, B., and Fam, A. (2006). “Flexural Load Testing of Concrete-Filled FRP Tubes with Longitudinal Steel and FRP Rebar.” *Journal of Composites for Construction*, ASCE, Vol. 10, No. 2, pp. 161-171.
- CSA. (2014). – “CSA S6, Canadian Highway Bridge Design Code.”
- Davol, A., Burgueño, R., and Seible, F. (2001). “FLEXURAL BEHAVIOR OF CIRCULAR CONCRETE FILLED FRP SHELLS.” *Journal of Structural Engineering*, ASCE, 127(7), pp. 810-817.
- Daniel, I. M., and Ishai, O. (1994). *Engineering Mechanics of Composite Materials*, Oxford University Press, New York.
- Dynamore. (2018). “Guideline for implicit analyses using LS-DYNA.” Dynamore.
- ElGawady, M., Booker, A. J., and Dawood, H. M. (2010). “Seismic Behavior of Posttensioned Concrete-Filled Fiber Tubes.” *Journal of Composites for Construction*, ASCE, Vol. 14, No.5, pp. 616-628.
- Fam, A. Z., and Rizkalla, S. H. (2002). “Flexural Behavior of Concrete-Filled Fiber-Reinforced Polymer Circular Tubes.” *Journal of Composites for Construction*, ASCE, 1090-0268, Vol. 6, No. 2, pp. 123-132.
- Fam, A., Flisak, B., and Rizkalla, S. (2003). “Experimental and analytical modeling of concrete-filled fiber-reinforced polymer tubes subjected to combined bending and axial loads.” *ACI Structural Journal*, Vol. 100(4), pp. 499-509.
- Fam, A., Greene, R., and Rizkalla, S. (2003). “Field Applications of Concrete-Filled FRP Tubes for Marine Piles.” *Field Application of FRP Reinforcement: Case Studies*, ACI, SP-215-9, pp. 161-180.
- Fam, A., Schnerch, D., and Rizkalla, S. (2005). “Rectangular Filament-Wound Glass Fiber Reinforced Polymer Tubes Filled with Concrete under Flexural and Axial Loading: Experimental Investigation.” *Journal of Composites for Construction*, ASCE, Vol. 9(1), pp. 25-33.

- Fam, A., and Cole, B. (2007). "Tests on reinforced-concrete-filled, fiber-reinforced-polymer circular tubes of different shear spans." *Canadian Journal of Civil Engineering*, Vol. 34(3), pp. 311-322.
- Fam, A., Cole, B., and Mandal, S. (2007). "Composite tubes as an alternative to steel spirals for concrete members in bending and shear." *Construction and Building Materials*, Elsevier Ltd., Vol. 21(2), pp. 347-355.
- Fam, A., and Son, J. (2008). "Finite element modeling of hollow and concrete-filled fiber composite tubes in flexure: Optimization of partial filling and a design method for poles." *Engineering Structures*, Elsevier Ltd., 30(2008): 2667-2676.
- Foundation Wharves Halifax, Infrastructure Projects, Develop Nova Scotia from <https://developns.ca/projects/infrastructure-projects-provincial-stimulus-funding/marine-infrastructure-projects-baddeck-mahone-bay/>
- Jawdhari, A., Fam, A., and Sadeghian, P. (2020). "MODELING THE NONLINEAR RESPONSE OF ± 55 ANGLE-PLY GFRP TUBE USED IN CFFT APPLICATIONS." *8th International Conference on Advanced Composite Materials in Bridges and Structures*, Sherbrooke, Quebec, Canada.
- Kings Stormwater Channel Bridge, UCSD and CalTrans Connect Sensors on Kings Stormwater Channel Bridge to HPWREN from <http://hpwren.ucsd.edu/news/021115.html>
- Karbhari, V.M., Seible, F., Burgueño, R., Davol, A., Wernli, M., and Zhao, L. (2000). "Structural Characterization of Fiber-Reinforced Composite Short- and Medium -Span Bridge Systems." *Applied Composite Materials*, Kluwer, 7(2), pp. 151-182.
- Khan, Q. S., Sheikh, M. N., and Hadi, M. N.S. (2017). "Concrete Filled Carbon FRP Tube (CFRP-CFFT) columns with and without CFRP reinforcing bars: Axial-flexural interactions." *Composites Part B*, Elsevier Ltd., Vol. 133, pp. 42-52.
- Lam, L., and Teng, J.-G. (2003). "Design-oriented Stress-Strain Model for FRP-confined Concrete in Rectangular Columns." *Journal of Reinforced Plastics and Composites*, Sage Publications, Vol. 22, No. 13, pp. 1149-1186.
- Lu, C., Onge, J. St., and Fam, A. (2020). "Damage Threshold of Near-Cross-Ply Tubes Used in Concrete-Filled FRP Tubes Loaded in Flexure." *Journal of Composites for Construction*, ASCE, Vol. 24(2):04019063, pp. 1-13.
- Lu, C., and Fam, A. (2020). "The effect of tube damage on flexural strength of $\pm 55^\circ$ angle-ply concrete-filled FRP tubes." *Construction and Building Materials*, Elsevier Ltd., 240, 117948, pp. 1-11.

- Mirmiran, A., and Shahawy, M. (1997). "BEHAVIOR OF CONCRETE COLUMNS CONFINED BY FIBER COMPOSITES." *Journal of Structural Engineering*, ASCE, Vol. 123, No. 5, pp. 583-590.
- Mirmiran, A., Samaan, M., Cabrera, S., and Shahawy, M. (1998). "Design, manufacture and testing of a new hybrid column." *Construction and Building Materials*, Elsevier Ltd., Vol. 12, No. 1, pp. 39-49.
- Moser, R., Holland, B., Kahn, L., Singh, P., and Kurtis, K. (2011). "Durability of Precast Prestressed Concrete Piles in Marine Environment: Reinforcement Corrosion and Mitigation Part 1." *Office of Materials and Research Georgia Department of Transportation, GODT Research Project No. 07-30, Task Order No. 02-55*.
- Mohamed, H. M., and Masmoudi, R. (2010). "Flexural strength and behavior of steel and FRP-reinforced concrete-filled FRP tube beams." *Engineering Structures*, Elsevier Ltd., Vol. 32, No. 11, pp. 3789-3800.
- Ozbakkaloglu, T. (2013). "Concrete-Filled FRP Tubes: Manufacture and Testing of New Forms Designed for Improved Performance." *Journal of Composites for Construction*, ASCE, Vol. 17(2), pp. 280-291.
- Ozbakkaloglu, T., and Vincent, T. (2014). "Axial Compressive Behavior of Circular High-Strength Concrete-Filled FRP Tubes." *Journal of Composites for Construction*, ASCE, Vol. 18, No. 2: 04013037, pp. 1-11.
- Piling Canada Projects from <http://www.pilingcanada.ca/articles/projects>
- Popovics, S. (1973). "A numerical approach to the complete stress-strain curve of concrete." *Cement and Concrete Research*, Elsevier Ltd., Vol 3, Issue 5, pp. 583-599.
- Qasrawi, Y., and Fam, A. (2008). "Flexural Load Tests on New Spun-Cast Concrete-Filled Fiber-Reinforced Polymer Tubular Poles." *ACI Structural Journal*, Technical Paper, V. 105, No. 6, November-December 2008, pp. 750-759.
- Qasrawi, Y., Heffernan, P. J., and Fam, A. (2015). "Performance of Concrete-Filled FRP Tubes under Field Close-in Blast Loading." *Journal of Composites for Construction*, ASCE, Vol. 19, No. 4, 04014067, pp. 1-12.
- Qasrawi, Y., Heffernan, P. J., and Fam, A. (2015). "Dynamic behaviour of concrete filled FRP tubes subjected to impact loading." *Engineering Structures*, Elsevier Ltd, Vol. 100, pp. 212-225.
- QuakeWrap, Inc., Pier and Wharf Construction III from <https://quakewrap.com/pdfs/Pile-Buck-Timber-Repair-Featuring-PileMedic-Web.pdf>

- Schwer, L. (2014). "Modeling Rebar: The forgotten Sister in Reinforced Concrete Modeling." *Dynamore*.
- Shawkat, W., Fahmy, W., and Fam, A. (2007). "Cracking patterns and strength of CFT beams under different moment gradients." *Composite Structures*, Elsevier Ltd., Vol. 84(2), pp. 159-166.
- Timoshenko, S. P., and Gere, J. M. (1972). *Mechanics of materials*, Van Nostrand, New York, 128–130.
- Youssf, O., ElGawady, M. A., Mills, J. E., and Ma, X. (2014). "Finite element modelling and dilation of FRP-confined concrete columns." *Engineering Structures*, Elsevier Ltd., 79(2014): 70-85.
- Zhao, L., Burgueño, R., Rovere, H.L., Seible, F., and Karbhari, V.M. (2000). "Preliminary evaluation of the hybrid tube bridge system." Report No. TR-2000/4, *Dept. of Structural Engineering, University of California*, San Diego, CA, pp. 1-56.
- Zhao, M.Z., Lehman, D.E., and Roeder, C. W. (2021). "Modeling recommendations for RC and CFST sections in LS-Dyna including bond slip." *Engineering Structures*, Elsevier Ltd., 229(2021):111612, pp. 1-20.

APPENDIX A: EXPERIMENTAL TEST DATA

Appendix A presents experimental test results of all 18 CFFTs, which were not included in Chapter 3.

- Section A.1. presents load vs. mid-span strains of the outer layer of GFRP tube of tested CFFT specimen in three different locations at mid-span. (C: Top compression fiber; S: In bottom tension-steel rebar zone; T: Bottom tension fiber)
- Section A.2. presents load vs. strain results from the strain gauge rosette arrangement, which was mounted at the mid-shear span ($a/2$) of the CFFTs. (a: 90° or hoop direction, b: 135° or diagonal direction, c: 180° or longitudinal direction)
- Section A.3. presents moment vs. curvature results obtained from load and strain data. (Due to inconclusive experimental strain data of P50-b-AD2.25, the curvature results were not plotted)
- Section A.4. presents N.A. depth vs. moment results. (N.A. depths were truncated where results were inconclusive)
- Section A.5. presents load vs. slip recorded between GFRP tube and concrete core. (Location of the LPs; L: Left side of the CFFT at the bottom region of the GFRP tube, R: Right side of the CFFT at the top region of the GFRP tube)
- Section A.6. presents load vs. slip recorded between steel rebars and concrete core. (Location of the LPs; L: Left side of the CFFT at a top compression steel rebar, R: Right side of the CFFT at a bottom tension-steel rebar)

A.1. LOAD vs. MID-SPAN STRAIN RESULTS

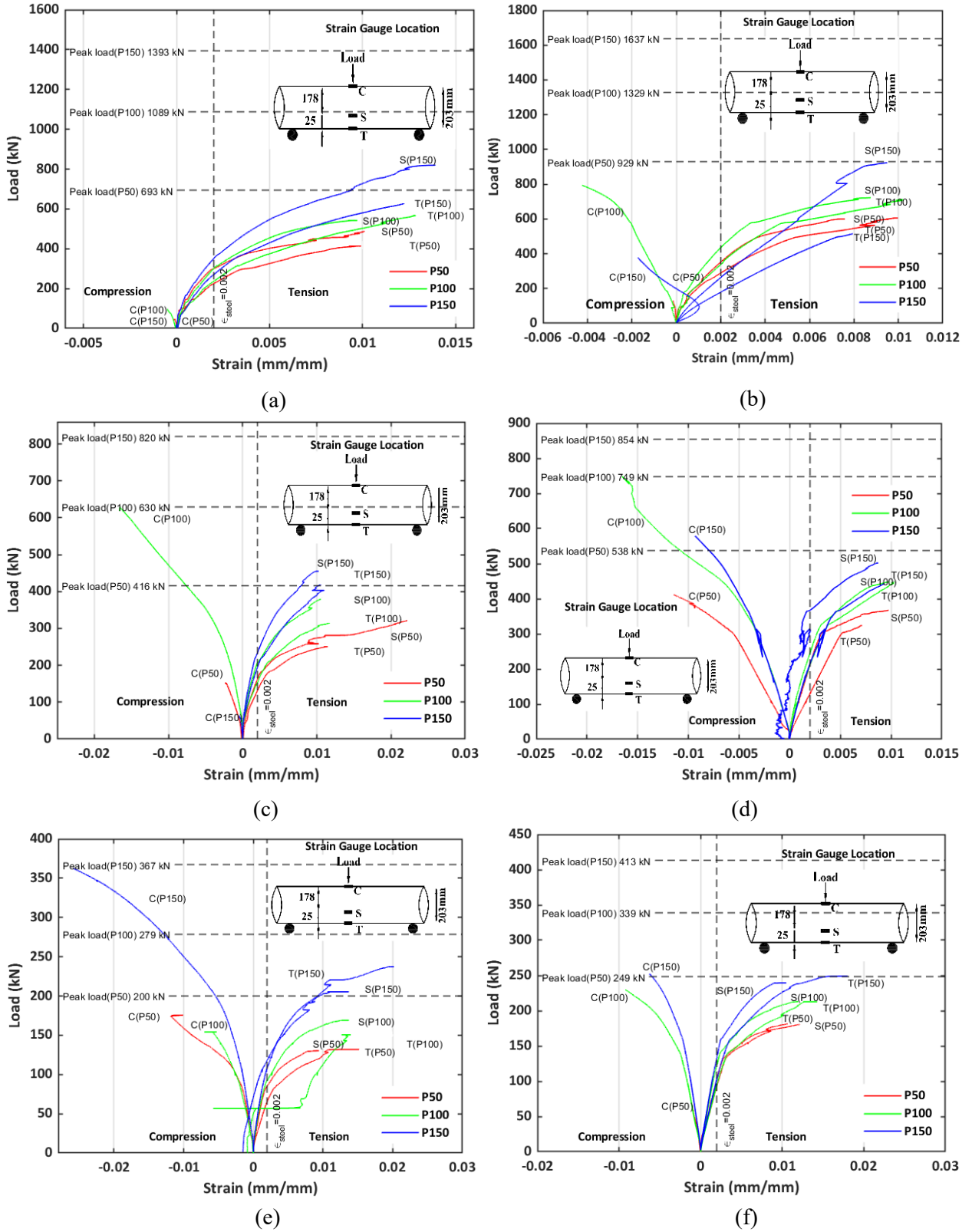


Figure A.1. Load vs. mid-span strains for CFFT specimens: (a) a-AD0.5; (b) b-AD0.5; (c) a-AD1; (d) b-AD1; (e) a-AD2.25; (f) b-AD2.25

A.2. LOAD vs. STRAIN ROSETTE RESULTS

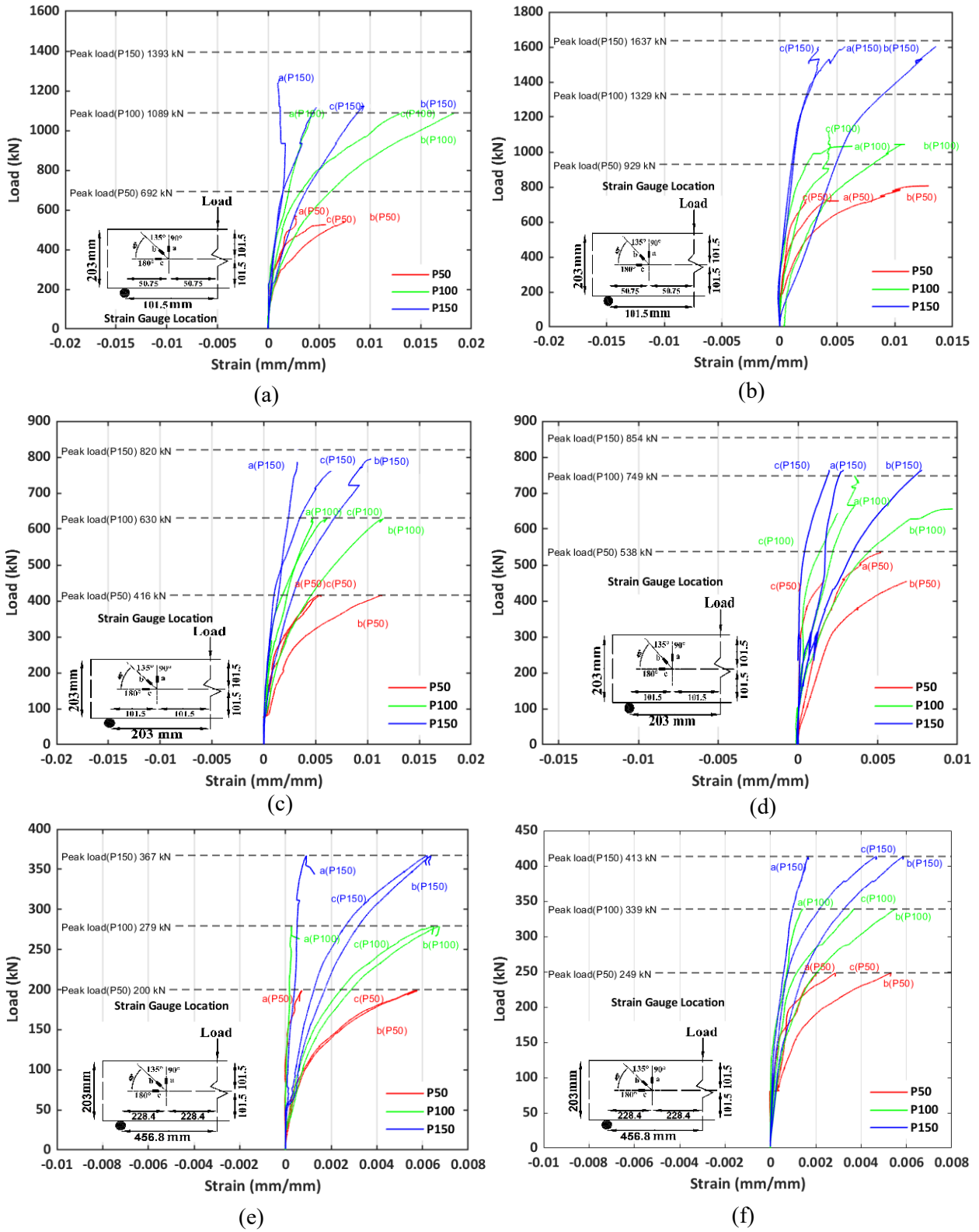


Figure A.2. Load vs. strain rosette for CFFT specimens: (a) a-AD0.5; (b) b-AD0.5; (c) a-AD1; (d) b-AD1; (e) a-AD2.25; (f) b-AD2.25

A.3. MOMENT vs. CURVATURE RESULTS

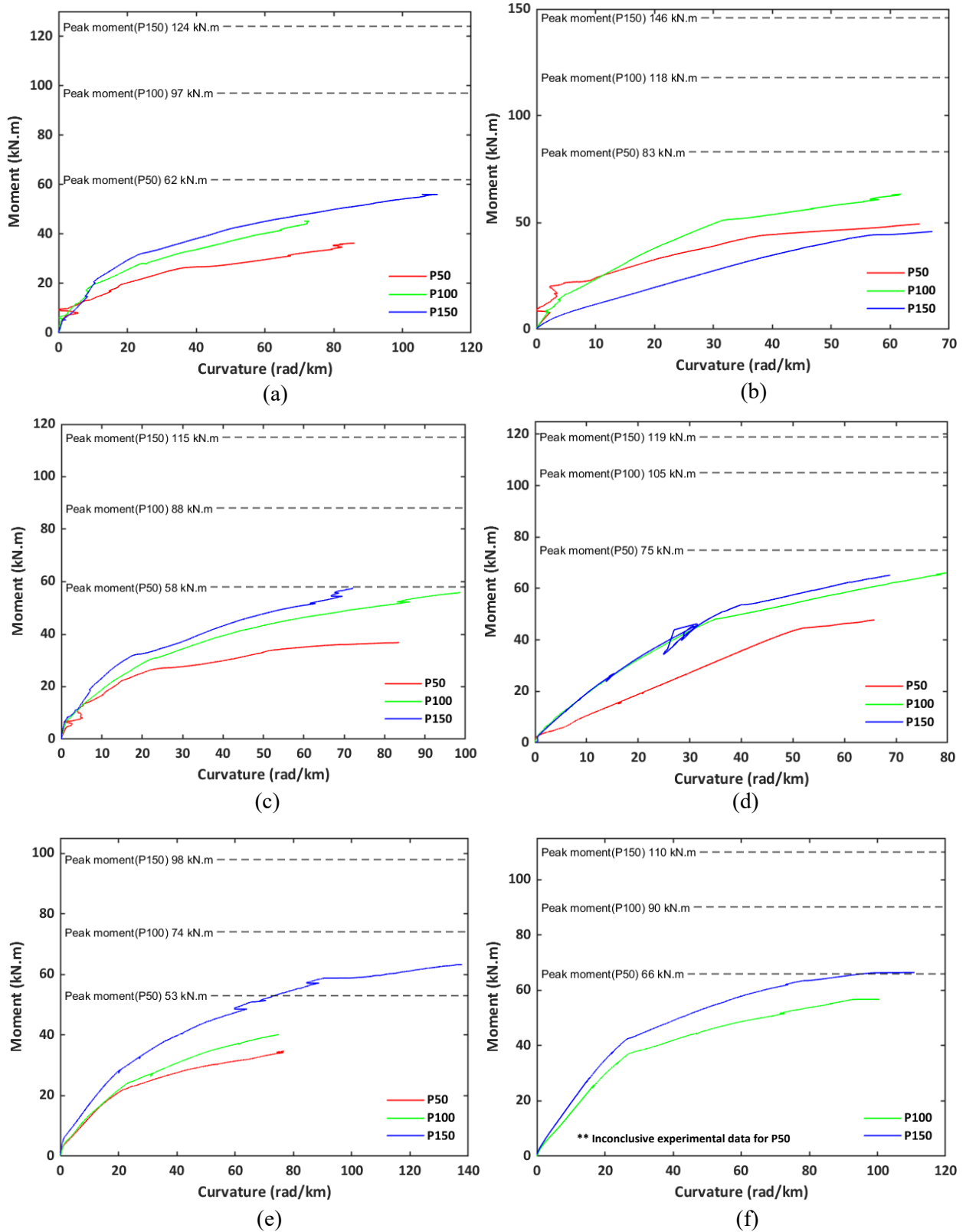


Figure A.3. Moment vs. curvature for CFFT specimens: (a) a-AD0.5; (b) b-AD0.5; (c) a-AD1; (d) b-AD1; (e) a-AD2.25; (f) b-AD2.25

A.4. NEUTRAL AXIS DEPTH vs. MOMENT RESULTS

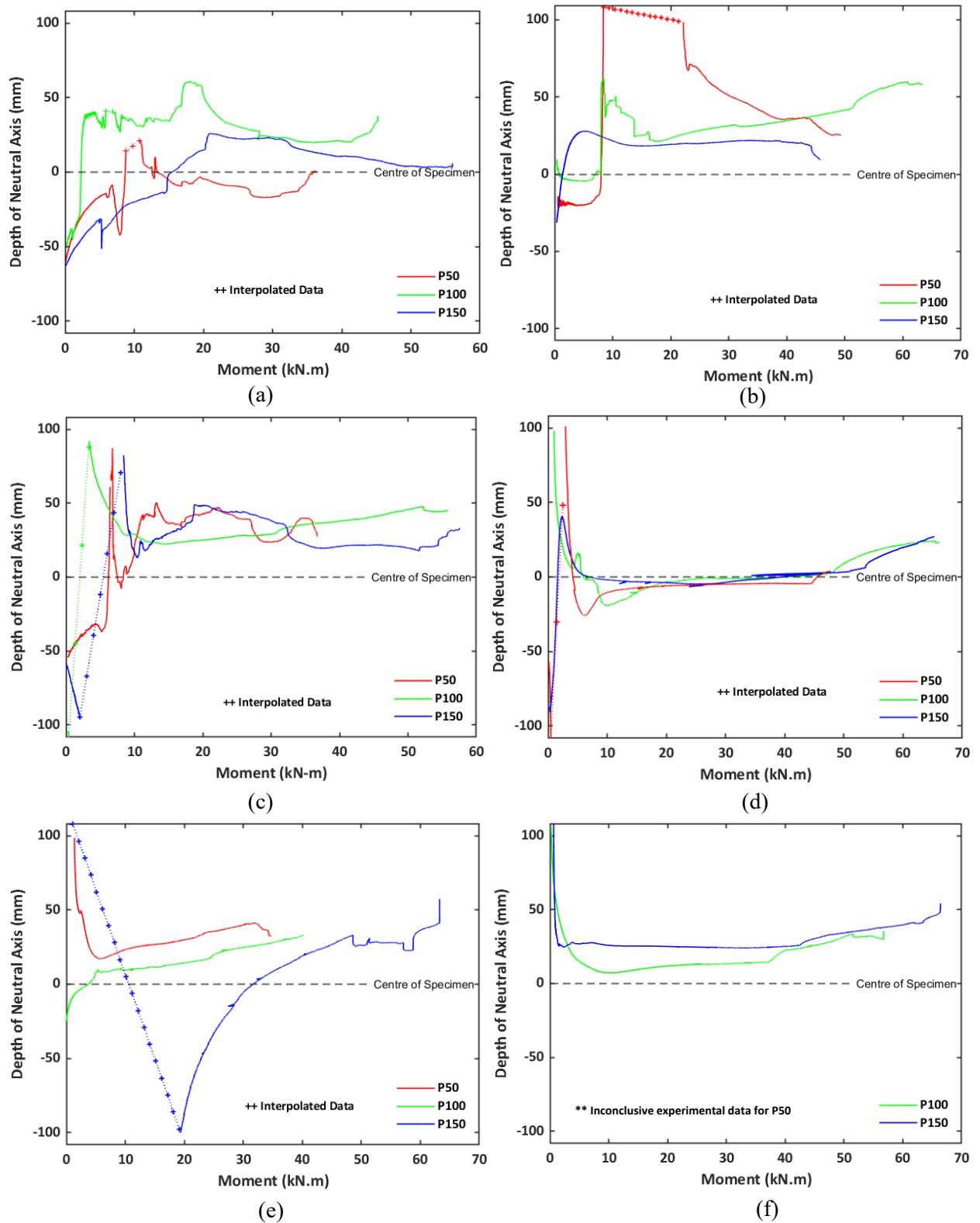


Figure A.4. N.A depth vs. moment for CFFT specimens: (a) a-AD0.5; (b) b-AD0.5; (c) a-AD1; (d) b-AD1; (e) a-AD2.25; (f) b-AD2.25

A.5. LOAD vs. SLIP BETWEEN GFRP TUBE and CONCRETE

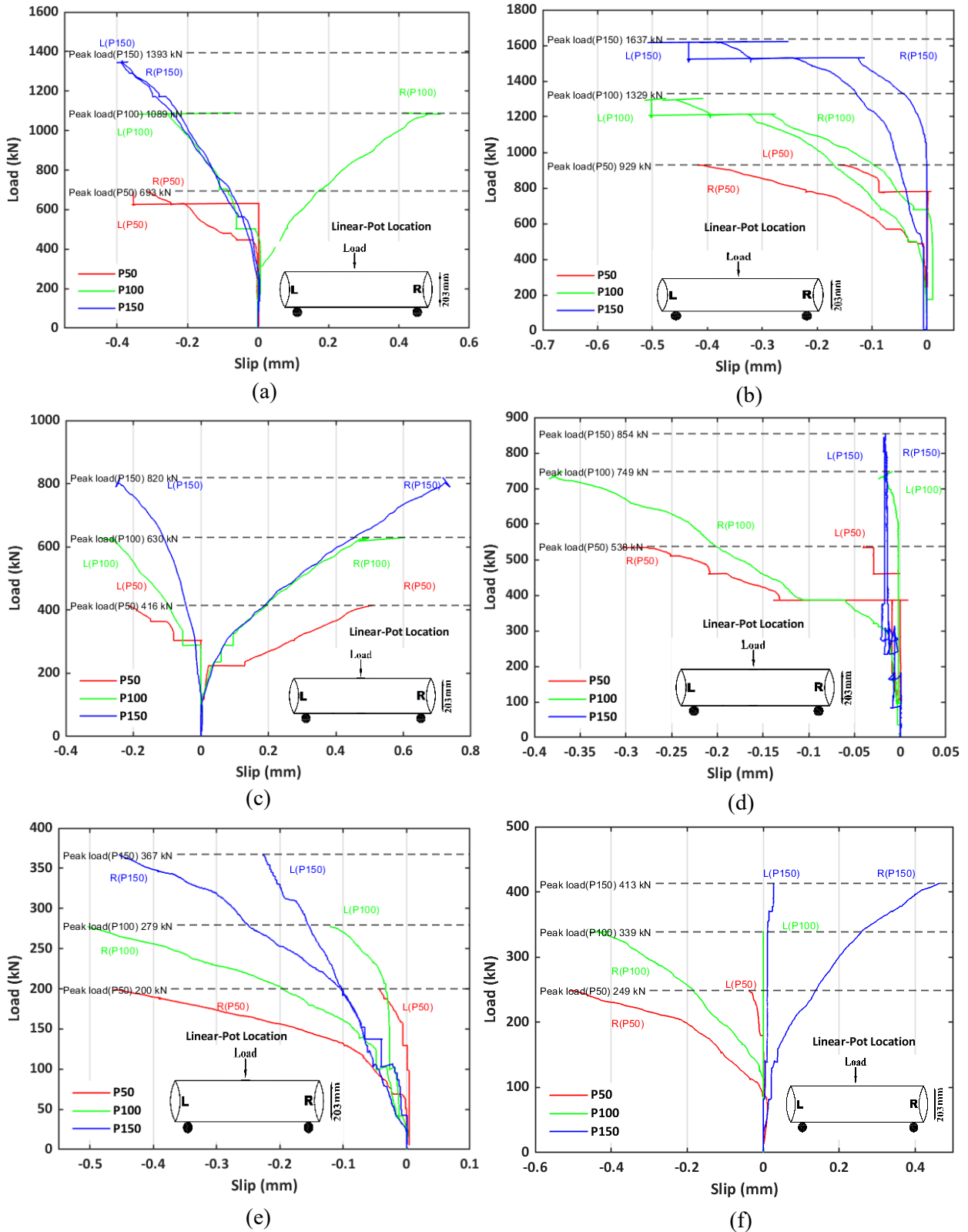


Figure A.5. Load vs. slip between GFRP tube and concrete for CFFT specimens: (a) a-AD0.5; (b) b-AD0.5; (c) a-AD1; (d) b-AD1; (e) a-AD2.25; (f) b-AD2.25

A.6. LOAD vs. SLIP BETWEEN CONCRETE and STEEL REBARS

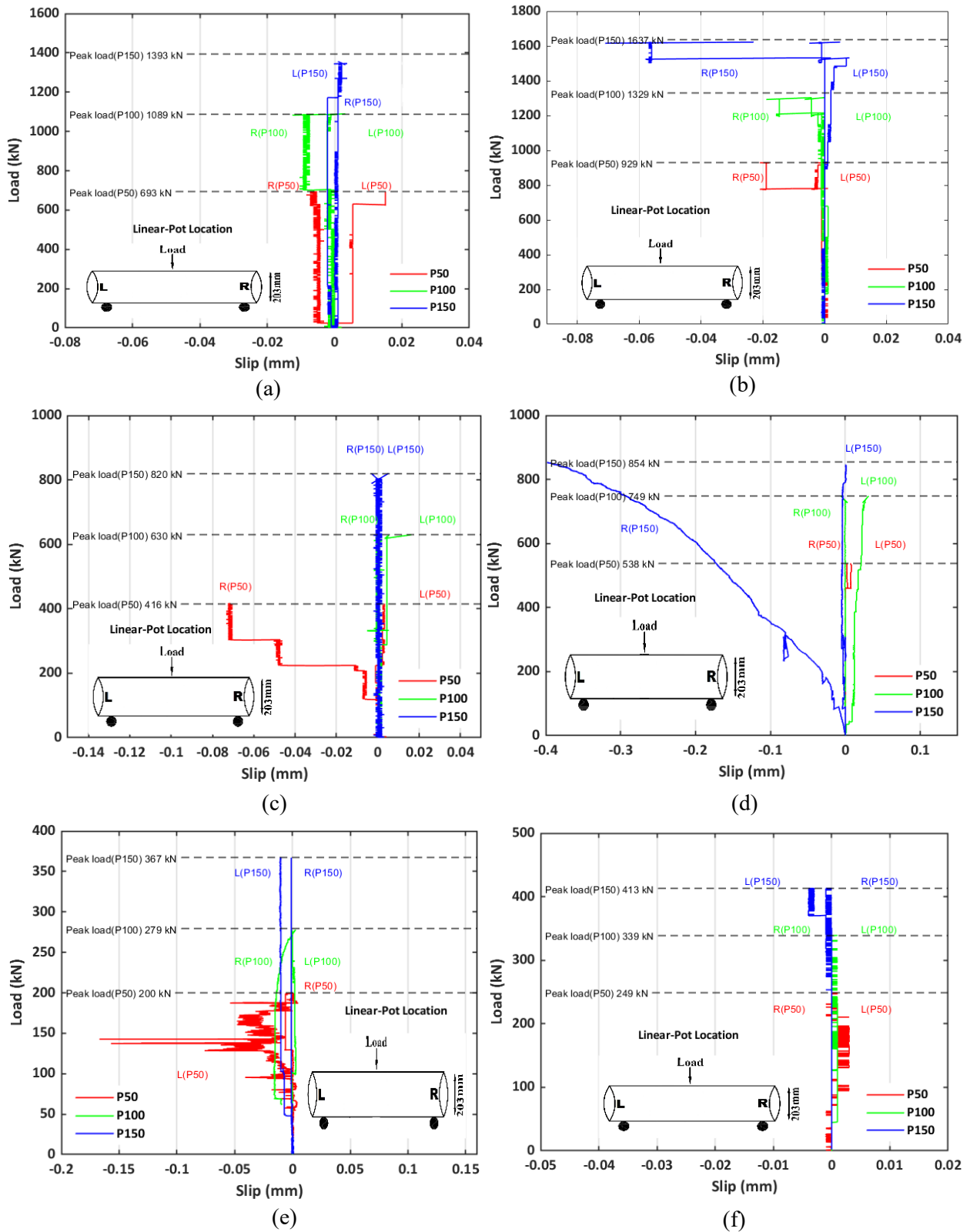


Figure A.6. Load vs. slip between concrete and steel rebars for CFFT specimens: (a) a-AD0.5; (b) b-AD0.5; (c) a-AD1; (d) b-AD1; (e) a-AD2.25; (f) b-AD2.25

APPENDIX B: SAMPLE LS-DYNA MATERIAL and CFFT CODES

B.1. GFRP TUBE MODELING CODE

B.1.1. Part Composite Card for GFRP tubes

```
----- P50 GFRP TUBE
*PART_COMPOSITE
$#                                     title
P50_GFRP_TUBE
$#   pid   elform   shrf   nloc   marea   hgid   adpopt   ithelfrm
      1     2       1.0    0.0    0.0     1     0       0
$#   mid1  thick1   b1     tmid1  mid2    thick2  b2       tmid2
      1     0.9    55.0    0     1     0.9    -55.0    0
      1     0.9    55.0    0     0     0.0    0.0     0
```

```
----- P100 GFRP TUBE
*PART_COMPOSITE
$#                                     title
P100_GFRP_TUBE
$#   pid   elform   shrf   nloc   marea   hgid   adpopt   ithelfrm
      1     2       1.0    0.0    0.0     1     0       0
$#   mid1  thick1   b1     tmid1  mid2    thick2  b2       tmid2
      1     1.175  55.0    0     1     1.175  -55.0    0
      1     1.175  55.0    0     1     1.175  -55.0    0
```

```
----- P150 GFRP TUBE
*PART_COMPOSITE
$#                                     title
P150_GFRP_TUBE
$#   pid   elform   shrf   nloc   marea   hgid   adpopt   ithelfrm
      1     2       1.0    0.0    0.0     1     0       0
$#   mid1  thick1   b1     tmid1  mid2    thick2  b2       tmid2
      1     1.34   55.0    0     1     1.34   -55.0    0
      1     1.34   55.0    0     1     1.34   -55.0    0
      1     1.34   55.0    0     0     0.0     0.0     0
```

B.1.2. Material Card for GFRP tubes without SLIM factors

```
*MAT_LAMINATED_COMPOSITE_FABRIC_TITLE
GFRP_Composite
$#   mid   ro       ea       eb       (ec)   prba   tau1   gamma1
      11.61000E-9  41300.0  9000.0  0.0    0.28   0.0   0.0
$#   gab   gbc       gca   slimt1  slimc1  slimt2  slimc2  slims
 3200.0  1600.0  3200.0  0.0    0.0    0.0    0.0    0.0
$#   aopt  tsize   erods   soft    fs       epsf   epsr   tsmd
 3.0     0.0    0.0    0.0    1.0    0.0    0.0    0.9
$#   xp    yp       zp     a1      a2      a3     prca   prcb
 0.0    0.0    0.0    0.0    0.0    0.0   0.28  0.06
$#   v1    v2       v3     d1      d2      d3     beta   beta
 0.0    0.0    1.0    0.0    0.0    0.0   0.0
$#   ellc  ellt    e22c   e22t    gms
 0.0    0.0    0.0    0.0    0.0
$#   xc    xt       yc     yt      sc
 1690.0  3730.0  116.0  35.0   300.0
$#   lcxc  lcxt    lcyc   lcyt    lcsc   lctau  lcgam  dt
 0       0       0       0       0       0       0       0.0
$#   lce11c  lce11t  lce22c  lce22t  lcgms
 0       0       0       0       0
```

B.1.3. Material Card for GFRP tubes with SLIM factors

```

*MAT_LAMINATED_COMPOSITE_FABRIC_TITLE
GFRP_Composite
$#      mid      ro      ea      eb      (ec)      prba      tau1      gamma1
      11.61000E-9  41300.0  9000.0  0.0      0.28      0.0      0.0
$#      gab      gbc      gca      slimt1   slimc1   slimt2   slimc2   slims
      3200.0     1600.0   3200.0   0.3      0.8      0.3      0.8      1.0
$#      aopt      tsize   erods    soft     fs       epsf     epsr     tsmd
      3.0        0.0      0.0      0.0      1.0      0.0      0.0      0.9
$#      xp        yp       zp       a1       a2       a3       prca     prcb
      0.0        0.0      0.0      0.0      0.0      0.0      0.28     0.06
$#      v1        v2       v3       d1       d2       d3       beta
      0.0        0.0      1.0      0.0      0.0      0.0      0.0
$#      e11c     e11t     e22c     e22t     gms
      0.0        0.0      0.0      0.0      0.0
$#      xc        xt       yc       yt       sc
      850.0     2600.0  116.0   35.0   250.0
$#      lcxc     lcxt     lcyc     lcyt     lcsc     lctau    lcgam    dt
      0         0        0        0        0        0        0        0.0
$#      lcellc   lcellt   lce22c   lce22t   lcgms
      0         0        0        0        0

```

B.2. CONCRETE MODELING CODE

```

*MAT_CONCRETE_DAMAGE_REL3_TITLE
Concrete
$#      mid      ro      pr
      22.40000E-9  0.2
$#      ft      a0      a1      a2      b1      omega    alf
      3.8      -40.0   0.0     0.0     0.0     0.0     0.0
$#      slambda  nout    edrop   rsize   ucf     lcrate   locwidth  npts
      0.0      2.0     0.0     0.03937 145.0   -1       0.0      0.0
$#      lambda1  lambda2  lambda3  lambda4  lambda5  lambda6  lambda7   lambda8
      0.0      0.0     0.0     0.0     0.0     0.0     0.0     0.0
$# lambda09  lambda10  lambda11  lambda12  lambda13  b3      a0y      a1y
      0.0      0.0     0.0     0.0     0.0     0.0     0.0     0.0
$#      eta1     eta2     eta3     eta4     eta5     eta6     eta7     eta8
      0.0      0.0     0.0     0.0     0.0     0.0     0.0     0.0
$#      eta09    eta10    eta11    eta12    eta13    b2      a2f      a2y
      0.0      0.0     0.0     0.0     0.0     0.0     0.0     0.0

```

B.3. 15 M STEEL REBAR MODELING CODE

```

*MAT_PLASTIC_KINEMATIC_TITLE
Steel_Rebar_15M
$#      mid      ro      e      pr      sigy     etan     beta
      37.90000E-9  200000.0  0.3     430.0   0.0     0.0
$#      src      srp      fs      vp
      0.0      0.0     0.0     0.0

```


B.4. 10 M STEEL REBAR MODELING CODE

```
*MAT_PLASTIC_KINEMATIC_TITLE
Steel_Rebar_10M
$#      mid      ro      e      pr      sigy      etan      beta
      37.90000E-9  200000.0  0.3  485.0      0.0      0.0
$#      src      srp      fs      vp
      0.0      0.0      0.0      0.0
```

B.5. STEEL SUPPORT MODELING CODE

```
*MAT_ELASTIC_TITLE
Steel_Supports
$#      mid      ro      e      pr      da      db      not used
      47.90000E-9  200000.0  0.3  0.0      0.0      0
```

B.6. RUBBER PAD MODELING CODE

```
*MAT_BLAZ-KO_RUBBER_TITLE
Rubber_pad
$#      mid      ro      g      ref
      51.10000E-9  20.0      0.0
```

B.7. SAMPLE LS-DYNA CODE FOR P50-b-AD0.5 SPECIMEN

```
$# LS-DYNA Keyword file created by LS-PrePost(R) V4.3.20 - 09Jan2018
$# Created on Nov-05-2021 (21:20:46)
*KEYWORD
*TITLE
$Three-Point Bending using LS-DYNA Explicit Solver
$KEYWORD MEMORY=600M NCPU=8
$# title
CFFT MODEL: P50-b-AD0.5
*CONTROL_CONTACT
$#  slsfac  rwpnal  islchk  shlthk  penopt  thkchg  orien  enmass
      0.1      0.0      1      0      1      0      1      0
$#  usrstr  usrfric  nsbcs  interm  xpene  ssthk  ecdt  tiedprj
      0      0      0      0      4.0      0      0      0
$#  sfric  dfrc  edc  vfc  th  th_sf  pen_sf
      0.0      0.0      0.0      0.0      0.0      0.0      0.0
$#  ignore  frceng  skiprwg  outseg  spotstp  spotdel  spothin
      0      0      0      0      0      0      0.0
$#  isym  nserod  rwgaps  rwgdth  rwksf  icov  swradf  ithoff
      0      0      1      0.0      1.0      0      0.0      0
$#  shldg  pstiff  ithcnt  tdcnof  ftall  unused  shltrw
      0      0      0      0      0      0.0
*CONTROL_ENERGY
$#  hgen  rwen  slnten  rylen
      2      2      1      1
*CONTROL_SHELL
$#  wrpang  esort  irnxx  istupd  theory  bwc  miter  proj
      20.0      0      -1      0      2      2      1      0
$#  rotasc1  intgrd  lamsht  cstyp6  tshell
      1.0      0      3      1      0
$#  psstupd  sidt4tu  cntco  itsflg  irqquad  w-mode  stretch  icrq
      0      0      0      0      2      0.0      0.0      0
```

```

$# nfail1 nfail4 psnfail keepcs delfr drcpsid drcprm
      0      0      0      0      0      0      1.0
*CONTROL_TERMINATION
$# endtim endcyc dtmin endeng endmas
      0.1      0      0.0      0.01.000000E8
*CONTROL_TIMESTEP
$# dtinit tssfacs isdo tslimt dt2ms lctm erode ms1st
      0.0      0.5      0      0.0      0.0      0      0      0
$# dt2msf dt2mslc imslc unused unused rmscl
      0.0      0      0      0      0      0.0
*DATABASE_GLSTAT
$# dt binary lcur ioopt
      0.001      0      0      1
*DATABASE_MATSUM
$# dt binary lcur ioopt
      0.001      0      0      1
*DATABASE_SPCFORC
$# dt binary lcur ioopt
      0.001      0      0      1
*DATABASE_BINARY_D3PLOT
$# dt lcdt beam npltc psetid
      0.001      0      0      0      0
$# ioopt
      0
*DATABASE_EXTENT_BINARY
$# neiph neips maxint strflg sigflg epsflg rltflg engflg
      6      6      3      1      1      1      1      1
$# cmpflg ieverp beamip dcomp shgce stssz n3thdt ialemat
      0      0      1      1      1      1      2      1
$# nintsld pkp_sen sclp hydro msscl therm intout nodout
      0      0      1.0      0      0      0
$# dtdt resplt neipb
      0      0      0
*BOUNDARY_PRESCRIBED_MOTION_SET_ID
$# id heading
      1Applied_Load
$# nsid dof vad lcid sf vid death birth
      3      3      2      1      1.0      01.000000E28      0.0
*BOUNDARY_SPC_SET_ID
$# id heading
      1Reaction_Nodes
$# nsid cid dofx dofy dofz dofrx dofry dofrz
      1      0      0      0      1      0      0      0
*SET_NODE_LIST_TITLE
Support_Reaction
$# sid da1 da2 da3 da4 solver
      1      0.0      0.0      0.0      0.0MECH
[LIST OF NODES NOT SHOWN]
*BOUNDARY_SPC_SET_ID
$# id heading
      2Corner_Nodes
$# nsid cid dofx dofy dofz dofrx dofry dofrz
      2      0      0      1      1      0      0      0
*SET_NODE_LIST_TITLE
Corner_Nodes_Support
$# sid da1 da2 da3 da4 solver
      2      0.0      0.0      0.0      0.0MECH
[LIST OF NODES NOT SHOWN]
*CONTACT_AUTOMATIC_SINGLE_SURFACE_ID
$# cid title
      1Internal_Contact_GFRP Tube
$# ssid msid sstyp mstyp sboxid mboxid spr mpr

```

\$#	1	0	3	0	0	0	0	0	0
	fs	fd	dc	vc	vdc	penchk	bt	dt	
	0.5	0.5	0.0	0.0	0.0	0	0.01.00000E20		
\$#	sfs	sfm	sst	mst	sfst	sfmt	fsf	vsf	
	1.0	1.0	0.0	0.0	1.0	1.0	1.0	1.0	
*CONTACT_AUTOMATIC_SURFACE_TO_SURFACE_ID									
\$#	cid								title
2Contact_Top Steel Support_and Top Rubber Pad									
\$#	ssid	msid	sstyp	mstyp	sboxid	mboxid	spr	mpr	
	4	5	3	3	0	0	0	0	
\$#	fs	fd	dc	vc	vdc	penchk	bt	dt	
	0.5	0.5	0.0	0.0	0.0	0	0.01.00000E20		
\$#	sfs	sfm	sst	mst	sfst	sfmt	fsf	vsf	
	1.0	1.0	0.0	0.0	1.0	1.0	1.0	1.0	
\$#	soft	sofscl	lcidab	maxpar	sbopt	depth	bsort	frcfreq	
	1	0.1	0	1.025	2.0	2	0	1	
*CONTACT_AUTOMATIC_SURFACE_TO_SURFACE_ID									
\$#	cid								title
3Contact_Top Rubber Pad_GFRP Tube									
\$#	ssid	msid	sstyp	mstyp	sboxid	mboxid	spr	mpr	
	5	1	3	3	0	0	0	0	
\$#	fs	fd	dc	vc	vdc	penchk	bt	dt	
	0.5	0.5	0.0	0.0	0.0	0	0.01.00000E20		
\$#	sfs	sfm	sst	mst	sfst	sfmt	fsf	vsf	
	1.0	1.0	0.0	0.0	1.0	1.0	1.0	1.0	
\$#	soft	sofscl	lcidab	maxpar	sbopt	depth	bsort	frcfreq	
	1	0.1	0	1.025	2.0	2	0	1	
*CONTACT_AUTOMATIC_SURFACE_TO_SURFACE_ID									
\$#	cid								title
4Contact_GFRP Tube_Right Rubber Pad									
\$#	ssid	msid	sstyp	mstyp	sboxid	mboxid	spr	mpr	
	1	7	3	3	0	0	0	0	
\$#	fs	fd	dc	vc	vdc	penchk	bt	dt	
	0.5	0.5	0.0	0.0	0.0	0	0.01.00000E20		
\$#	sfs	sfm	sst	mst	sfst	sfmt	fsf	vsf	
	1.0	1.0	0.0	0.0	1.0	1.0	1.0	1.0	
\$#	soft	sofscl	lcidab	maxpar	sbopt	depth	bsort	frcfreq	
	1	0.1	0	1.025	2.0	2	0	1	
*CONTACT_AUTOMATIC_SURFACE_TO_SURFACE_ID									
\$#	cid								title
5Contact_GFRP Tube_Left Rubber Pad									
\$#	ssid	msid	sstyp	mstyp	sboxid	mboxid	spr	mpr	
	1	9	3	3	0	0	0	0	
\$#	fs	fd	dc	vc	vdc	penchk	bt	dt	
	0.5	0.5	0.0	0.0	0.0	0	0.01.00000E20		
\$#	sfs	sfm	sst	mst	sfst	sfmt	fsf	vsf	
	1.0	1.0	0.0	0.0	1.0	1.0	1.0	1.0	
\$#	soft	sofscl	lcidab	maxpar	sbopt	depth	bsort	frcfreq	
	1	0.1	0	1.025	2.0	2	0	1	
*CONTACT_AUTOMATIC_SURFACE_TO_SURFACE_ID									
\$#	cid								title
6Contact_Right Rubber pad_Right Steel Support									
\$#	ssid	msid	sstyp	mstyp	sboxid	mboxid	spr	mpr	
	7	6	3	3	0	0	0	0	
\$#	fs	fd	dc	vc	vdc	penchk	bt	dt	
	0.5	0.5	0.0	0.0	0.0	0	0.01.00000E20		
\$#	sfs	sfm	sst	mst	sfst	sfmt	fsf	vsf	
	1.0	1.0	0.0	0.0	1.0	1.0	1.0	1.0	
\$#	soft	sofscl	lcidab	maxpar	sbopt	depth	bsort	frcfreq	
	1	0.1	0	1.025	2.0	2	0	1	
*CONTACT_AUTOMATIC_SURFACE_TO_SURFACE_ID									
\$#	cid								title
7Contact_Left Rubber Pad_Left Steel Support									
\$#	ssid	msid	sstyp	mstyp	sboxid	mboxid	spr	mpr	
	9	8	3	3	0	0	0	0	
\$#	fs	fd	dc	vc	vdc	penchk	bt	dt	

```

0.5      0.5      0.0      0.0      0.0      0      0.01.00000E20
$#      sfs      sfm      sst      mst      sfst      sfmt      fsf      vsf
1.0      1.0      0.0      0.0      1.0      1.0      1.0      1.0      1.0
$#      soft     sofsc1  lcidab  maxpar   sbopt    depth    bsort    frcfrq
1        0.1      0        1.025   2.0      2        0        1
*CONTACT_TIED_NODES_TO_SURFACE_OFFSET_ID
$#      cid                                     title
8Contact_GFRP Tube_Concrete Core
$#      ssid     msid     sstyp   mstyp   sboxid   mboxid   spr      mpr
4        1        4        0       0        0        0        0
$#      fs       fd       dc      vc      vdc     penchk   bt      dt
0.5      0.5      0.0     0.0     0.0     0        0.01.00000E20
$#      sfs      sfm      sst     mst     sfst    sfmt     fsf     vsf
1.0      1.0      0.0     0.0     1.0     1.0     1.0     1.0
*SET_NODE_LIST_TITLE
Concrete_Outer_Surface
$#      sid      da1      da2      da3      da4      solver
4        0.0    0.0     0.0     0.0MECH
[LIST OF NODES NOT SHOWN]
*SET_SEGMENT_TITLE
GFRP_Tube_Surface
$#      sid      da1      da2      da3      da4      solver
1        0.0    0.0     0.0     0.0MECH
[LIST OF SEGMENTS NOT SHOWN]
*PART_COMPOSITE
$#                                     title
P50_GFRP_TUBE
$#      pid     elform   shrf     nloc     marea    hgid     adpopt   ithelfrm
1        2        1.0     0.0     0.0     1        0        0
$#      mid1    thick1   b1       tmid1    mid2     thick2   b2       tmid2
1        0.9    55.0    0        1        0.9     -55.0    0
1        0.9    55.0    0        0        0.0     0.0     0
*PART
$#                                     title
Concrete_Core
$#      pid     secid    mid     eosid    hgid     grav     adpopt   tmid
2        2        2        0        2        0        0        0
*SECTION_SOLID_TITLE
Solid_Elements
$#      secid   elform   aet
2        1        0
*MAT_CONCRETE_DAMAGE_REL3_TITLE
Concrete
$#      mid     ro      pr
22.40000E-9  0.2
$#      ft      a0      a1      a2      b1      omega    alf
3.8      -40.0   0.0     0.0     0.0     0.0     0.0
$#      slambda  nout    edrop   rsize   ucf     lcrate   locwidth  npts
0.0      2.0    0.0     0.03937 145.0   -1        0.0     0.0
$#      lambda1  lambda2  lambda3  lambda4  lambda5  lambda6  lambda7  lambda8
0.0      0.0    0.0     0.0     0.0     0.0     0.0     0.0
$# lambda09  lambda10 lambda11 lambda12 lambda13 b3      a0y     a1y
0.0      0.0    0.0     0.0     0.0     0.0     0.0     0.0
$#      eta1     eta2     eta3     eta4     eta5     eta6     eta7     eta8
0.0      0.0    0.0     0.0     0.0     0.0     0.0     0.0
$#      eta09    eta10    eta11    eta12    eta13    b2      a2f     a2y
0.0      0.0    0.0     0.0     0.0     0.0     0.0     0.0
*HOURLASS_TITLE
Concrete_Core
$#      hgid     ihq      qm      ibq      q1      q2      qb/vdc   qw
2        5        0.075   0        1.5     0.06    0.1     0.1

```

```

*PART
$#
Steel_Rebar_15M
$#   pid      secid      mid      eosid      hgid      grav      adpopt      tmid
      3        3        3        0        0        0        0        0
*SECTION_BEAM_TITLE
Steel_Rebar_15M
$#   secid      elform      shrf      qr/irid      cst      scoor      nsm
      3        1        1.0      2        1        0.0      0.0
$#   ts1      ts2      tt1      tt2      nsloc      ntloc
      16.0      16.0      0.0      0.0      0.0      0.0
*MAT_PLASTIC_KINEMATIC_TITLE
Steel_Rebar_15M
$#   mid      ro      e      pr      sigy      etan      beta
      37.90000E-9      200000.0      0.3      430.0      0.0      0.0
$#   src      srp      fs      vp
      0.0      0.0      0.0      0.0
*PART
$#
Top_Steel_Support
$#   pid      secid      mid      eosid      hgid      grav      adpopt      tmid
      4        2        4        0        4        0        0        0
*MAT_ELASTIC_TITLE
Steel_Supports
$#   mid      ro      e      pr      da      db      not used
      47.90000E-9      200000.0      0.3      0.0      0.0      0
*HOURLASS_TITLE
Steel_Supports
$#   hgid      ihq      qm      ibq      q1      q2      qb/vdc      qw
      4        5      0.05      0      1.5      0.06      0.1      0.1
*PART
$#
Top_Rubber_Pad
$#   pid      secid      mid      eosid      hgid      grav      adpopt      tmid
      5        2        5        0        5        0        0        0
*MAT_BLATZ-KO_RUBBER_TITLE
Rubber_pad
$#   mid      ro      g      ref
      51.10000E-9      20.0      0.0
*HOURLASS_TITLE
Rubber_Pads
$#   hgid      ihq      qm      ibq      q1      q2      qb/vdc      qw
      5        5      0.12      0      1.5      0.06      0.1      0.1
*PART
$#
Right_Steel_Support
$#   pid      secid      mid      eosid      hgid      grav      adpopt      tmid
      6        2        4        0        4        0        0        0
*PART
$#
Right_Rubber_Pad
$#   pid      secid      mid      eosid      hgid      grav      adpopt      tmid
      7        2        5        0        5        0        0        0
*PART
$#
Left_Steel_Support
$#   pid      secid      mid      eosid      hgid      grav      adpopt      tmid
      8        2        4        0        4        0        0        0
*PART
$#
Left_Rubber_Pad
$#   pid      secid      mid      eosid      hgid      grav      adpopt      tmid
      9        2        5        0        5        0        0        0
*HOURLASS_TITLE
GFRP Tube
$#   hgid      ihq      qm      ibq      q1      q2      qb/vdc      qw

```

```

1          5          0.005          0          1.5          0.06          0.1          0.1
*MAT_LAMINATED_COMPOSITE_FABRIC_TITLE
GFRP_Composite
$#  mid      ro      ea      eb      (ec)      prba      tau1      gamma1
    11.61000E-9  41300.0  9000.0  0.0  0.28  0.0  0.0
$#  gab      gbc      gca      slimt1      slimc1      slimt2      slimc2      slims
    3200.0  1600.0  3200.0  0.0  0.0  0.0  0.0  0.0
$#  aopt      tsize      erods      soft      fs      epsf      epsr      tsmd
    3.0  0.0  0.0  0.0  1.0  0.0  0.0  0.9
$#  xp      yp      zp      a1      a2      a3      prca      prcb
    0.0  0.0  0.0  0.0  0.0  0.0  0.28  0.06
$#  v1      v2      v3      d1      d2      d3      beta
    0.0  0.0  1.0  0.0  0.0  0.0  0.0
$#  e11c      e11t      e22c      e22t      gms
    0.0  0.0  0.0  0.0  0.0
$#  xc      xt      yc      yt      sc
    1690.0  3730.0  116.0  35.0  300.0
$#  lcxc      lcxt      lcyc      lcyt      lcsc      lctau      lcgam      dt
    0  0  0  0  0  0  0  0.0
$#  lce11c      lce11t      lce22c      lce22t      lcgms
    0  0  0  0  0
*DEFINE_CURVE_TITLE
Displacement_Curve_For_Load
$#  lcid      sidr      sfa      sfo      offa      offo      dattyp      lcint
    1  0  1.0  -1.0  0.0  0.0  0  0
[CURVE DATA NOT SHOWN]
*SET_NODE_LIST_TITLE
Applied_Load
$#  sid      da1      da2      da3      da4      solver
    3  0.0  0.0  0.0  0.0MECH
[LIST OF NODES NOT SHOWN]
*CONSTRAINED_LAGRANGE_IN_SOLID_TITLE
$#  cupid      title
    1Constrained_Between_Concrete_Core_and_Steel_Rebar
$#  slave      master      sstyp      mstyp      nquad      ctype      direc      mcoup
    3  2  1  1  0  2  1  0
$#  start      end      pfac      fric      frcmin      norm      normtyp      damp
    0.01.00000E10  0.1  0.0  0.5  0  0  0.0
$#  cq      hmin      hmax      ileak      pleak      lcidpor      nvent      blockage
    0.0  0.0  0.0  0  0.1  0  0  0
$#  iboxid      ipenchk      intforc      ialesof      lagmul      pfacmm      thkf
    0  0  0  0  0.0  0  0.0
*ELEMENT_SOLID
$#  eid      pid      n1      n2      n3      n4      n5      n6      n7      n8
    12801  2  12881  12897  12898  12882  13977  13993  13994  13978
[FULL LIST OF SOLID ELEMENTS NOT SHOWN]
*ELEMENT_SHELL
$#  eid      pid      n1      n2      n3      n4      n5      n6      n7      n8
    1  1  1  2  82  81  0  0  0  0
    2  1  2  3  83  82  0  0  0  0
[FULL LIST OF SHELL ELEMENTS NOT SHOWN]
*ELEMENT_BEAM
$#  eid      pid      n1      n2      n3      rt1      rr1      rt2      rr2      local
    156960  3  763007  763008  763009  0  0  0  0  2
    156961  3  763008  763010  763011  0  0  0  0  2
[FULL LIST OF BEAM ELEMENTS NOT SHOWN]

```

```

*NODE
$#  nid          x          y          z          tc          rc
     1          0.0        102.95         0.0          0          0
     2          0.0        102.6326       8.077364       0          0

```

[FULL LIST OF NODE-LOCATION NOT SHOWN]

*END

B.8. AUTO GENERATED CONCRETE PARAMETERS IN LS-DYNA

```

-----
Updated Release III K&C concrete model
by K&C/Javier Malvar (9/99 updated 4/12)
based on LRDA/K&C f3dm16w.f (8/7/95)
LS-DYNA Release III of Mat072 by
Len Schwer (May 04) & Y.Wu (April, 12)
-----
pressure phi    0.00000E+00    5.00000E-01
pressure phi    1.33333E+01    6.42500E-01
pressure phi    3.06667E+01    6.37453E-01
pressure phi    1.20000E+02    7.53000E-01
pressure phi    3.38000E+02    1.00000E+00
f c fyc ft      =    4.00000E+01    1.79416E+01    3.80000E+00
Ec              =    2.99379E+04
$----- MATERIAL CARDS -----
-
$ LS-DYNA Keyword Generated Input for Release III
$ [Default values = K&C generic f'c=6580 psi concrete]
*MAT_Concrete_Damage_Rel3
$ MATID RO PR
 72 2.400E-09 2.000E-01
$ ft A0 A1 A2 B1 OMEGA A1F
3.800E+00 1.182E+01 4.463E-01 2.020E-03 1.600E+00 5.000E-01 4.417E-01
$ sLambda NOUT EDROP RSIZE UCF LCRate LocWidth
NPTS
1.000E+02 2.000E+00 1.000E+00 3.937E-02 1.450E+02 1.000E+00 2.540E+01
1.300E+01
$ Lambda01 Lambda02 Lambda03 Lambda04 Lambda05 Lambda06 Lambda07
Lambda08
0.000E+00 8.000E-06 2.400E-05 4.000E-05 5.600E-05 7.200E-05 8.800E-05 3.200E-
04
$ Lambda09 Lambda10 Lambda11 Lambda12 Lambda13 B3 A0Y
A1Y
5.200E-04 5.700E-04 1.000E+00 1.000E+01 1.000E+10 1.150E+00 8.928E+00 6.250E-
01
$ Eta01 Eta02 Eta03 Eta04 Eta05 Eta06 Eta07
Eta08
0.000E+00 8.500E-01 9.700E-01 9.900E-01 1.000E+00 9.900E-01 9.700E-01 5.000E-
01
$ Eta09 Eta10 Eta11 Eta12 Eta13 B2 A2F
A2Y
1.000E-01 0.000E+00 0.000E+00 0.000E+00 0.000E+00 1.350E+00 2.958E-03 6.438E-
03

```

```

$----- EOS-8 CARDS -----
-
$ Generated EOS 8 (Tabulated Compaction)
*EOS_Tabulated_Compaction
$   EOSID      Gamma      E0      Vol0
      72 0.000E+00 0.000E+00 1.000E+00
$   VolStrain01      VolStrain02      VolStrain03      VolStrain04
VolStrain05
      0.00000000E+00 -1.50000001E-03 -4.30000015E-03 -1.00999996E-02 -3.05000003E-
02
$   VolStrain06      VolStrain07      VolStrain08      VolStrain09
VolStrain10
      -5.13000004E-02 -7.25999996E-02 -9.43000019E-02 -1.73999995E-01 -2.08000004E-
01
$   Pressure01      Pressure02      Pressure03      Pressure04
Pressure05
      0.00000000E+00 2.49482231E+01 5.43871269E+01 8.73187790E+01
1.65905685E+02
$   Pressure06      Pressure07      Pressure08      Pressure09
Pressure10
      2.50230667E+02 3.55013214E+02 5.43122803E+02 3.17091919E+03
4.84993457E+03
$           Multipliers of Gamma*E
      .000000000E+00 .000000000E+00 .000000000E+00
      .000000000E+00 .000000000E+00 .000000000E+00
$   BulkUnld01      BulkUnld02      BulkUnld03      BulkUnld04
BulkUnld05
      1.66321484E+04 1.66321484E+04 1.68650000E+04 1.77132383E+04
2.10729316E+04
$   BulkUnld06      BulkUnld07      BulkUnld08      BulkUnld09
BulkUnld10
      2.44492578E+04 2.78089531E+04 3.03536719E+04 6.82916016E+04
8.31607422E+04
$-----

```